

**Large deformation and crystallisation
properties of process optimised cocoa
butter emulsions**

by

Vincenzo di Bari

A thesis submitted to the University of Birmingham

for the degree of DOCTOR OF PHILOSOPHY

Microstructure Group

School of Chemical Engineering

College of Physical and Engineering Sciences

University of Birmingham

May 2015

UNIVERSITY OF
BIRMINGHAM

University of Birmingham Research Archive

e-theses repository

This unpublished thesis/dissertation is copyright of the author and/or third parties. The intellectual property rights of the author or third parties in respect of this work are as defined by The Copyright Designs and Patents Act 1988 or as modified by any successor legislation.

Any use made of information contained in this thesis/dissertation must be in accordance with that legislation and must be properly acknowledged. Further distribution or reproduction in any format is prohibited without the permission of the copyright holder.

Abstract

The objectives of the research presented in this thesis were: (1) optimise the processing conditions for the production of water-in-cocoa butter emulsions; (2) understand the role of water droplets on the large deformation behaviour and crystallisation properties of emulsified systems. Results showed that a scraped surface heat exchanger could be used to produce tempered emulsions with a small average droplet size ($\sim 3 \mu\text{m}$). In all systems stability was provided by the emulsifier and fat crystals forming a network both in the bulk and at the interface of the water droplets.

Characterisation of the large deformation properties of emulsions showed that the elastic behaviour remained constant at low aqueous phase percentages while the strength at fracture decreased. This result suggests that water droplets act as stress-concentrator elements, which is probably due to their partial sintering with the bulk network.

Results of crystallisation experiments have shown that the effect of droplets on kinetics of crystallisation depends on the degree of supercooling: only at relatively high temperatures (15, 20 °C) the dispersed droplets increased the kinetics of crystallisation compared to bulk cocoa butter (CB). With respect to polymorphic evolution, emulsified systems evolved faster toward more stable forms than bulk CB at all temperatures.

To my Family

Homo faber fortunae suae

Acknowledgments

I would like to thank Prof. Ian Norton for giving me the chance of being part of ‘microstructure’ research group. During the last four years I have had the opportunity to develop and grow as researcher and for this I will be forever grateful. I am also grateful to Dr Jennifer Norton and Dr Antonio Sullo for their help, support and advices.

I would like to thank Cargill for funding the PhD project and in particular Dr Paul Smith, Dr Danièle Karleskind, and Dr Piet Bogaert for their interest in the project and constant support. I would also like to thank Prof. Peter Lillford and Prof. Clive Marshman for the many useful discussions throughout the PhD. I would like to express my gratitude to Steve Ablett for his help and support during the completion of the NMR work and patience with me.

A special huge thank goes to Miss Lynn Draper not only for the help and support at the university but also for the care for me as a person: I will never forget how much you have done for me in these years. I am also extremely grateful to Mr Robert Sharp: your help and true friendship have made my days at Birmingham much more enjoyable.

I am very grateful to Dr Richard Greenwood for allowing me to be the “honorary EngD”: being part of that family has been a great experience and has allowed me to meet many brilliant researchers. I would like also to thank Prof. Mark Simmons for all of his help, especially in the hardest moments when nobody else seemed to be able to help.

I would like to say thanks a lot to the friends from the “coffee club” and “kebab club”: Federico, James, Tony, Bill, Dan, *etc.* All have been great friends during these years.

A special thank goes to people I have met outside Chemical Engineering that have become my family: Fabrizio and Nancy, Sabrina, Giulia, Bianca and her family, Asia and Matteo, Nadine and many others.

A special thought is for Emmanuelle Costard...

A special thank goes to zio Elio: our weekly conversations and your encouragement and advices have helped me to grow a lot.

Finally, I would like to thank my parents and my sister for their encouragement and constant support: this is for you!!!

Table of Contents

Chapter 1. Introduction	1
1.1. Background	1
1.2. Thesis objectives	3
1.3. Thesis structure	4
Chapter 2. Literature review	6
2.1. Fat crystallisation	7
2.1.1. General aspects of lipids and fat crystallisation	7
2.1.1.1. Supersaturation	8
2.1.1.2. Nucleation	10
2.1.1.3. Crystal growth	12
2.1.2. Fat polymorphism	13
2.1.3. Structure of fat crystal networks	19
2.1.3.1. Mechanical behaviour of fat crystal networks	21
2.1.4. Models describing fat isothermal crystallisation	23
2.1.4.1. Avrami model	23
2.1.5. Cocoa butter: composition and crystallisation behaviour	26
2.2. Emulsions and Emulsification	32
2.2.1. Emulsion definition and classification	32
2.2.2. Emulsifiers	36
2.2.2.1. Surfactants	36
2.2.2.2. Pickering stabilisation	39
2.2.3. Emulsions formation	42
2.2.4. Emulsion physical instability	44
2.2.4.1. Gravitational separation	45

2.2.4.2.	Flocculation.....	46
2.2.4.3.	Coalescence and partial coalescence.....	46
2.2.4.4.	Ostwald ripening.....	47
2.2.4.5.	Phase inversion.....	48
2.2.5.	Fat crystals stabilised emulsions.....	48
2.2.5.1.	Pickering stabilisation via interfacial crystallisation.....	53
2.2.5.2.	Water-in-cocoa butter emulsions.....	57
2.3.	Conclusions and outlook.....	58
Chapter 3.	Materials and Methods.....	60
3.1.	Introduction.....	61
3.2.	Materials.....	61
3.2.1.	Lipid phase.....	61
3.2.1.1.	Cocoa butter.....	61
3.2.1.2.	Polyglycerol Polyricinoleate.....	62
3.2.2.	Aqueous Phase.....	62
3.3.	Methods.....	62
3.3.1.	Margarine line.....	62
3.3.1.1.	Coarse emulsions preparation.....	66
3.3.1.2.	Tempering-emulsification process: theory and set-up.....	67
3.3.2.	Nuclear Magnetic Resonance.....	69
3.3.2.1.	Theory of low field pulsed NMR (pNMR).....	69
3.3.2.2.	Bruker Minispec Spectrometer.....	72
3.3.2.3.	Droplet size measurement.....	73
3.3.2.1.	Solid Fat Content measurement: direct and indirect method.....	76
3.3.2.2.	Method development for SFC measurements.....	78
3.3.2.3.	Solid fat content (SFC) determination.....	86
3.3.2.4.	Crystallisation kinetics.....	89

3.3.3.	Differential Scanning Calorimetry (DSC).....	90
3.3.3.1.	Melting behaviour of processed CB systems	92
3.3.3.2.	Stop-and-return thermal analysis	93
3.3.4.	Wilhelmy plate interfacial tension measurements.....	99
3.3.5.	Uniaxial compression analysis	100
3.3.5.1.	Casting of the samples for mechanical analysis.....	100
3.3.5.2.	Compression analysis.....	102
3.3.6.	Microstructure visualisation	105
3.3.6.1.	Bright- field and Polarised light microscopy	105
3.3.6.2.	Cryogenic-Scanning Electron Microscopy	106
3.3.7.	Conductivity measurement	106
Chapter 4.	Effect of processing and formulation on the microstructural properties of water-in-cocoa butter emulsions.....	107
4.1.	Introduction.....	108
4.2.	Results and discussion	110
4.2.1.	Effect of processing condition on emulsion droplet size.....	110
4.2.1.1.	Use of Margarine line: Effect of SSHE rotational speed on droplet size	112
4.2.1.2.	Use of Margarine line: Effect of PS rotational speed on droplet size...	114
4.2.1.3.	Effect of SSHE alone on emulsion droplet size	116
4.2.1.4.	Effect of residence time on average droplet size.....	123
4.2.1.5.	Effect of the SSHE outlet Temperature on the final droplet size.....	125
4.2.1.6.	Data model fitting.....	127
4.2.2.	Effect of processing conditions on CB polymorphic form.....	130
4.2.3.	Effect of process and formulation on emulsion droplet size	136
4.2.3.1.	Production of emulsions with higher dispersed phase percentage	136
4.2.3.2.	Effect of emulsifier concentration on emulsion production and stabilisation	139

4.2.3.3. Cryo-SEM visualisation of emulsions	144
4.3. Conclusions.....	148
Chapter 5. Effect of microstructure on the large deformation behaviour of cocoa butter systems	150
5.1. Introduction.....	151
5.2. Results and discussion	153
5.2.1. Large deformation behaviour of bulk cocoa butter	153
5.2.2. Effect of water percentage on the large deformation behaviour of water-in-cocoa butter emulsions.....	163
5.2.3. Effect of dispersed phase droplet size on the large deformation behaviour of water-in-cocoa butter emulsions.....	177
5.2.4. Large deformation behaviour as function of compressive rate	182
5.3. Conclusions.....	189
Chapter 6. Crystallisation in water-in-cocoa butter emulsions	191
6.1. Introduction.....	192
6.2. Results.....	194
6.2.1. Overview of the crystallisation study	194
6.2.2. Emulsions: formulation and droplet size	195
6.2.3. Crystallisation at 5 °C.....	196
6.2.4. Crystallisation at 10 °C.....	204
6.2.5. Crystallisation at 15 °C.....	210
6.2.6. Crystallisation at 20 °C.....	217
6.3. Discussion	223
6.3.1. Effect of water droplets on kinetics of crystallisation	224
6.3.2. Effect of water droplets on polymorphic evolution.....	225
6.4. Conclusions.....	230
Chapter 7. Conclusions and future recommendations.....	232
7.1. Conclusions.....	233

7.1.1. Effect of processing and formulation on the microstructural properties of water-in-cocoa butter emulsions	233
7.1.2. Effect of microstructure on the large deformation behaviour of cocoa butter systems	234
7.1.3. Crystallisation in water-in-cocoa butter emulsions	236
7.2. Future recommendations.....	238

List of Figures

Figure 2.1: Schematic of the three basic polymorphs found in fats. Image taken from Sato (2001).....	15
Figure 2.2: Double (a) and triple (b) chain length structure. Image taken from Sato <i>et al.</i> , (1999).....	17
Figure 2.3: Free energy of activation (ΔG_n^\ddagger) and free energy of nucleation for the three basic polymorphs. Image taken from Marangoni (2002).....	19
Figure 2.4: Schematic representation of polymorphic evolution in fats. Image modified from Sato <i>et al.</i> (1999).....	19
Figure 2.5: Hierarchical model for fat crystal networks. The characteristic length scales have been added to help the discussion. Image taken from Tang and Marangoni (2007).....	20
Figure 2.6: Highly schematic representation of a surfactant: the hydrophilic head is represented as a circle separated and the hydrophobic tail is depicted as a rod. More complex structures can be found in real systems.	37
Figure 2.7: Schematic representation of the position of a particle at the interface according to its hydrophobicity. Image taken from Binks (2002).	41
Figure 2.8: Representation of the destabilisation mechanisms occurring in emulsions. Image taken from Fredrick <i>et al.</i> , (2010).....	45
Figure 3.1: (a) Image of the SSHE shaft with the blades mounted on it. (b) Schematic design of the shaft, blades and jacket of the SSHE containing the dimensions of the elements. Full and dashed arrows represent flow of the emulsion and jacket water, respectively. (c) Dimensions of the SSHE in a cross section: $\phi 50\text{mm}$ is the cross section diameter; $\phi 30\text{mm}$ is the diameter of the inner cavity where emulsification occurs; $\phi 10\text{mm}$ is the gap distance between the internal and external jacket walls. Illustration modified from Norton and Fryer, 2012.	63
Figure 3.2: (a) Image of the PS shaft showing the pins. (b) Schematic design of the shaft, blades and jacket of the SSHE containing the dimensions of the elements. Full and dashed arrows represent flow of the emulsion and jacket water, respectively. (c) Dimensions of the PS in a cross section: $\phi 80\text{mm}$ is the cross section diameter; $\phi 40\text{mm}$ is the diameter of the inner cavity where emulsification occurs; $\phi 20\text{mm}$ is	

the gap distance between the internal and external jacket walls. Illustration modified from Norton and Fryer, 2012.....	64
Figure 3.3: Schematic representation of the processing set up. The continuous arrows represent the flow of the emulsions, the dashed arrows the flow of the water into the jackets to control temperature and the “T” represents points where the temperature was monitored. The dashed box around the SSHE indicates a process based on the use of this mixer only. Schematic is not in scale.	66
Figure 3.4: Processing set-up adopted on emulsification. See text for details.	69
Figure 3.5: Visualisation of a Hahn Spin-Echo sequence. Each step of the experiment is indicated by a letter, for explanation see text. Image taken from Bruker minispec manuals.	74
Figure 3.6: Schematic representation of the stimulated echo sequence. The first 90° pulse and the second two pulses are depicted as grey rectangles and the field gradient pulses are indicated by the dotted arrows. The spin-echo signal is depicted at right-hand side of the sequence. For “filter” and symbols explanations see text. Image taken from van Duynhoven <i>et al.</i> (2007).	75
Figure 3.7: Schematic of a relaxation curve after a 90° pulse. L is the signal produced by the liquid components. The characteristic time point of signal detection (70 μ s) is also shown.....	78
Figure 3.8: NMR signal intensity as function of SFO mass. A linear response occurs for a mass up to ~0.5 g.	80
Figure 3.9: NMR signal intensity as function of SFO standards at two values of <i>ns</i> : 4 (diamonds) and 16 (squares).	81
Figure 3.10: Calibration points for 2 (triangle) and 10 s (square) RD. The R ² and equation refer to the 10 s RD calibration.	82
Figure 3.11: Example of sample used to measure the temperature profile (A); general set-up for real-time temperature recording (B, C).	88
Figure 3.12: (a) Solid fat content (SFC) evolution curve over time for bulk cocoa butter crystallised at 5°C; (b) corresponding double logarithmic transformation (Section 3.3.2.4.). In 3.12b the full diamond represents the whole transformed curve while the white square represent the portion of the curve used to calculate the Avrami parameters using linear fitting (a detailed explanation for the chosen interval is provided in Section 6.2.3.).	90

- Figure 3.13: Schematic illustration of the time-temperature profile applied for the “stop-and-return” method. Sample is initially melted at 50 °C for 5 minutes, followed by cooling to the desired T_{Cr} and isothermal hold for a defined time (Δt). Finally the sample is re-melted. The cycle was be repeated several times.95
- Figure 3.14: Example of deconvolution analysis of a melting curve of a CB sample obtained following a 120 minutes isothermal holding at 20 °C. The red, blue, and yellow line represents the experimental, theoretical, and baseline curve, respectively. Each green line represents the polymorph referred by the Roman numeral; the “relative mass fraction” of each polymorph is referred in the legend. Arrows indicate the extremes of integration for total enthalpy calculation.97
- Figure 3.15: Example of specimens of 20% emulsion after 24h at 20 °C. The arrows indicated portions where sample contraction is well visible. 102
- Figure 3.16: Representation of the characterising parameters used in uniaxial compression analysis. (B) Magnification of the portion of the curve used for E_{app} calculation. 105
- Figure 4.1: Average $d_{3,2}$ of emulsions containing (A) 10% and (B) 20% (wt%) aqueous phase; average free water content (%) of emulsions containing (C) 10% and (D) 20% aqueous phase. All emulsions contain 1% PGPR (wt%) overall. Diamonds and circles represent emulsions produced using a N_{PS} of 170 and 1345 rpm, respectively. Error bars are one standard deviation of triplicates (where no visible, error bars are smaller than symbols). 114
- Figure 4.2: Average droplet size ($d_{3,2}$) of emulsions containing (A) 10% and (B) 20% (wt%) aqueous phase; average free water content (%) of emulsions containing (C) 10% and (D) 20% aqueous phase. All emulsions contain 1% PGPR (wt%) overall. Squares and triangles represent emulsions produced using a N_{SSHE} of 490 and 930 rpm, respectively. Error bars are one standard deviation of triplicates (where no visible, error bars are smaller than symbols). 115
- Figure 4.3: (A) average $d_{3,2}$ and (B) free water (%) of emulsions containing 10 and 20% (wt%) aqueous phase as function of N_{SSHE} . All emulsions contain 1% PGPR (wt%) overall. Error bars represent plus and minus one standard deviation of triplicates (where no visible, error bars are smaller than symbols). 116
- Figure 4.4: Micrographs of 20% aqueous phase emulsions produced using the SSHE at four rotational speeds (indicated in the image). 118

Figure 4.5: Average $d_{3,2}$ (◆) and free water % (◇) of 20% (wt%) aqueous phase emulsions as function of the SSHE T_{out} . All emulsions contain 1% PGPR (wt%) overall. Error bars represent one standard deviation of triplicates.	126
Figure 4.6: $d_{3,2}$ values as function of tip speed for emulsion containing 20% (wt%) dispersed phase and produced at different T_{out} . All emulsions contain 1% PGPR (wt%) overall. Results are average of triplicates and error bars represent one standard deviation (where no visible, error bars are smaller than symbols).....	129
Figure 4.7: Melting curves of 10 (left) and 20% (right) aqueous phase emulsions produced using various combinations of SSHE and PS rotor rates: A – B, C – D, and G - H correspond to a set up where both units are at 170, 500, and 1345 rpm, respectively. E – F have been obtained with SSHE at 1315 rpm and PS at 170 rpm. For clarity the used shear combinations are referred for each curve together with the percentage of dispersed phase.....	133
Figure 4.8: Melting curves of 20% aqueous phase emulsions produced using the SSHE only at four rotational speed: 170 rpm (A), 490 rpm (B), 930 rpm (C), and 1315 rpm (D).....	135
Figure 4.9: Effect of dispersed phase percentage (Φ_m , %) on (A) droplet size ($d_{3,2}$) and (B) free water content for emulsions produced using the SSHE alone (diamonds) or the full margarine line (white triangles). All emulsions contain 1% PGPR (wt%) overall. Error bars represent one standard deviation of triplicates (where no visible, error bars are smaller than symbols).	137
Figure 4.10: Effect of PGPR concentration ([PGPR]) on (a) droplet size ($d_{3,2}$) and (b) free water content at one day (full circles) and at one month after production (empty circles). Error bars represent one standard deviation of triplicates (where no visible, error bars are smaller than symbols).	141
Figure 4.11: Water-cocoa butter oil interfacial tension as function of time at different PGPR concentration (symbols are explained in the legend).....	142
Figure 4.12: Cryo-SEM visualisation of 20% aqueous phase emulsions with 0% PGPR. Water droplets appear encased within the fat crystal network.	144
Figure 4.13: Micrographs of emulsions containing 0% (a), 0.1% (b), 1% (c), and 2% (d) PGPR. Droplets are surrounded by a crystalline shell (black arrows) within a fat network (blue arrows).	145

Figure 4.14: Micrographs of broken water droplets as a result of sample preparation providing an evidence for interfacial “shell” thickness. The thickness values have been estimated using the Cryo-SEM microscope software.	147
Figure 5.1: Melting profile of statically and sheared crystallised CB.	155
Figure 5.2: Example of stress (σ_E)-strain curve (ϵ_E) for statically and sheared crystallised CB.	155
Figure 5.3: Image of a test specimen before and after compression.	157
Figure 5.4: Micrograph of a test specimen while failure is occurring.	157
Figure 5.5: (a) Apparent Young’s (E_{app}) and (b) bulk modulus (BM) for statically and sheared crystallised CB. Error bars are plus/minus one standard error of the mean.	158
Figure 5.6: Average (a) stress ($\sigma_{failure}$) and (b) strain ($\epsilon_{failure}$) to failure for statically and sheared crystallised CB. Error bars are plus/minus one standard error of the mean.	161
Figure 5.7: Microstructural visualisation of CB (a) statically and (b, c, d) sheared crystallised. A granular microstructure was common to both systems. For sheared CB microstructures with a granular centre and surrounded by a featherlike arrangement were also observed (C, D).	162
Figure 5.8: Melting profile of CB systems (at 5 °C/min). Each endotherm corresponds to the sample indicated in the legend and have all been normalised per gram of CB.	166
Figure 5.9: PLM visualisation of a 20% and 30% water-in-cocoa butter emulsion.	166
Figure 5.10: Apparent Young’s modulus (E_{app} , ▲) and Bulk modulus (BM , Δ) for CB systems with increasing water mass fraction. Error bars are plus/minus one standard error of the mean. Solid lines serve only to guide reader’s eye.	167
Figure 5.11: (a) Stress (◆) and strain (◇) to fracture and (b) work to fracture (■) expressed as function of aqueous phase percentage. Error bars are plus/minus one standard error of the mean.	170
Figure 5.12: Cryo-SEM of a 20% (wt%) water-in-cocoa butter emulsion (scale bar = 100 μ m).	172
Figure 5.13: Cryo-SEM image of a 20% (wt%) water-in-cocoa butter emulsion (scale bar = 20 μ m). Water droplets (covered by a continuous crystalline shell) and the cocoa butter (CB) matrix are indicated in the figure.	173

Figure 5.14: Detail of a water droplet for a (A) 20%, (B) 30%, and (C) 40% aqueous phase emulsion (w/w basis).	174
Figure 5.15: melting behaviour of emulsions produced at four SSHE rotational speeds. Endotherms correspond to samples with an average $d_{3,2}$ of (from top to bottom) 14, 8.1, 4, and 3.5 μm , respectively. Endotherms have been normalised per gram of CB.	178
Figure 5.16: Apparent Young's modulus (E_{app} , \blacktriangle) and bulk modulus (BM, Δ) as function of the average droplet size ($d_{3,2}$, μm). Error bars represent one standard error of the mean. Solid lines serve only to guide reader's eye.	179
Figure 5.17: (a) True stress (\blacklozenge) and strain (\diamond) to failure expressed as function of average droplet size $d_{3,2}$ (μm). (b) Specific work to failure as function of $d_{3,2}$ (\blacksquare) and free water (\square). Error bars represent plus/minus one standard error of the mean.	180
Figure 5.18: Apparent Young's modulus (E_{app}) as function of compressive rate. Bulk cocoa butter (\diamond), 20% aqueous phase (\square) and 40% aqueous phase (Δ). Error bars are plus/minus one standard error of the mean.	183
Figure 5.19: Bulk modulus (BM) as function of compressive rate. Bulk cocoa butter (\diamond), 20% (wt%) aqueous phase (\square) and 40% (wt%) aqueous phase (Δ). Error bars are plus/minus one standard error of the mean.	184
Figure 5.20: (a) fracture stress, (b) fracture strain, (c) work to fracture as function of compressive rate for bulk cocoa butter (\diamond), 20% (wt%) aqueous phase (\square) and 40% (wt%) aqueous phase (Δ). Error bars are plus/minus one standard error of the mean.	186
Figure 6.1: (a) SFC curves, (b) enthalpy of fusion per gram of CB, and (c) main melting peak temperatures for bulk CB (\diamond), 20% (Δ) and 40% (\circ) aqueous phase emulsions, and CB containing 1% PGPR (\square) at 5 °C. Error bars represent one standard deviation of triplicates and where not shown is within symbol size.	198
Figure 6.2: Average melting curves for CB systems crystallised at 5 °C at all holding times. The time point corresponding to each melting curve and the CB system are referred in the figure.	201
Figure 6.3: Polymorphic evolution of CB systems crystallised at 5 °C. Form II, III, and IV are represented by diamond, square, and triangles, respectively. Lines serve only to guide the reader's eye: solid, dotted, and dashed lines correspond to Form II, III, and IV, respectively.	203

Figure 6.4: (a) SFC curves, (b) enthalpy of fusion, and (c) melting peak temperatures for CB (\diamond), 20% (Δ) and 40% (\circ) aqueous phase emulsions, respectively, at 10 °C as isothermal crystallisation temperature. Error bars represent the standard deviation and where not shown are smaller than symbols.....	205
Figure 6.5: Average melting curves for CB systems crystallised at 10 °C at nine holding times. The time point corresponding to each melting curve and the CB system are referred in the figure.	207
Figure 6.6: Polymorphic evolution of CB systems crystallised at 10 °C. Form II, III, IV, and V are represented by diamond, square, triangles, and circles, respectively. Lines serve only to guide the reader’s eye: solid, dotted, dashed, and dashed-dotted line is for Form II, III, IV, and V, respectively.....	208
Figure 6.7: (a) SFC curves, (b) enthalpy of fusion, and (c) melting peak temperatures for CB (\diamond), 20% (Δ) and 40% (\circ) aqueous phase emulsions, respectively, at 15 °C as isothermal crystallisation temperature. Error bars represent the standard deviation and where not shown are smaller than symbols.....	212
Figure 6.8: Average endothermic curves for CB systems crystallised at 15 °C at all the selected holding times. The time point corresponding to each melting curve and the investigated system are referred in the figure.	214
Figure 6.9: Polymorphic evolution of CB systems crystallised at 15 °C. Form II, III, IV, and V are represented by diamond, square, triangles, and circles, respectively. Lines serve only to guide the reader’s eye: solid, dotted, dashed, and dashed-dotted line is for Form II, III, IV, and V, respectively.....	216
Figure 6.10: SFC curves (a), enthalpy of fusion (b) and melting peak temperatures (c) for CB (\diamond), 20% (Δ) and 40% (\circ) aqueous phase emulsions, and 1% PGPR in CB (\square), respectively, at 20 °C as isothermal crystallisation temperature. Error bars represent the standard deviation and where not shown are smaller than symbols.	218
Figure 6.11: Average endothermic curves for CB systems crystallised at 20 °C at all the selected holding times. The time point corresponding to each melting curve and the investigated system are referred in the figure.	222
Figure 6.12: Polymorphic evolution of CB systems crystallised at 20 °C. Form II, III, IV, and V are represented by diamond, square, triangles, and circles, respectively. Lines serve only to guide the reader’s eye: solid, dotted, dashed, and dashed-dotted line is for Form II, III, IV, and V, respectively.....	223

List of Tables

Table 2.1: Nomenclature, subcell form, and characteristic short spacing lines for the three basic polymorphs in fats (Chapman, 1962; Larsson, 1966).....	16
Table 2.2: Values of Avrami exponent (n) for different growth morphology and nucleation types.	25
Table 2.3: Polymorphic forms and proposed corresponding melting ranges of cocoa butter (CB) solid phases according to literature.....	27
Table 2.4: Long and short spacing values (Å) and chain length structure of CB polymorphic forms published in literature (for simplicity only strong lines are reported).....	28
Table 3.1: Rotor level and corresponding rotor rate and tips speed for SSHE and PS. In bold there are the combinations used. Values of rotor rate have been measured using a rotation-speed laser sensor (Compact instrument, UK).	65
Table 3.2: SFO weighed masses and corresponding amounts measured by the NMR at different recycle delay (RD) values.	83
Table 3.3: Values of tau spacing (τ) and corresponding sampling window used on calibration.	84
Table 3.4: Values of weighted and measured SFO. The NMR signal intensity is also reported.	84
Table 3.5: Samples masses of SFO-water mixtures measured by NMR. The SFO/water ratios have been also compiled.	85
Table 3.6: Total liquid content measured by NMR for water-SFO mixtures.....	86
Table 3.7: Polymorph and corresponding melting peak and range used for the deconvolution analysis Melting peak and range correspond to parameters b and c in equation 3.13.....	99
Table 4.1: $d_{3,2}$ and free water (%) values (standard deviation given in brackets) as a function of SSHE and PS rotational speed for emulsions containing 20% water at three time points.....	119
Table 4.2: Values of $\Delta d_{3,2}$ (in μm) for emulsions containing 10 and 20% aqueous phase and produced using either the SSHE alone (at four rotor speeds) or in series with the PS working at two rotor speeds (N_{PS}). According to equation 4.1, positive and	

negative values denote an increase and decrease in $d_{3,2}$, respectively, as a result of using the PS.....	121
Table 4.3: $d_{3,2}$ and free water values, (standard deviation given in brackets) as a function of SSHE and PS rotational speed, for emulsions containing 20% water experiencing different time lengths and combinations of shearing.	124
Table 4.4: Melting properties of water-in-cocoa butter emulsions.....	132
Table 5.1: Average droplet size $d_{3,2}$ (μm), free water (%), and SFC (%) for bulk CB and emulsions containing 10, 20, 30, and 40% (wt%) aqueous phase (plus/minus one standard error of the mean).	165
Table 5.2: rotor rate and microstructural parameters of emulsions produced at different rotor rate.....	177
Table 6.1: Droplet characteristics of emulsions prior to crystallisation and after re-crystallisation experiment.	196
Table 6.2: Avrami parameters and R^2 of the fitting for SFC data obtained on isothermal crystallisation at 10 °C of CB systems.....	206
Table 6.3: Avrami parameters and R^2 of the fitting for SFC data obtained on isothermal crystallisation at 15 °C of CB systems.....	213
Table 6.4: Avrami crystallisation parameters and R^2 of the fitting for SFC data obtained on isothermal crystallisation at 20 °C of CB systems.....	219

List of Abbreviations

CB	Cocoa Butter
DSC	Differential Scanning Calorimetry
DSD	Droplet Size Distribution
FID	Free Induction Decay
MPa	Mega-Pascal = 10^6 Pa
NMR	Nuclear Magnetic Resonance
O/W	Oil-in-water emulsions
Pa	Pascal
pfgNMR	Pulsed Field Gradient NMR
PLM	Polarised light microscopy
PS	Pin Stirrer
RF	Radio Frequency
SFC	Solid Fat Content
SSHE	Scraped Surface Heat Exchanger
TAG	Triacylglycerol
W/O	Water-in-oil emulsions
XRD	X-ray Diffraction

List of Symbols

\sim	Approximately
ΔG	Gibbs free energy content
ΔG^\ddagger	Activation free energy
ΔP	Laplace pressure
Φ	Dispersed phase volume fraction
Φ_m	Dispersed phase mass fraction
$d_{3,3}$	Volume weighted mean diameter
$d_{3,2}$	Surface weighted mean diameter
σ	Width or standard deviation of droplet size distribution
T_1	Spin-Lattice relaxation time
T_2	Spin-Spin relaxation time
τ	Tau spacing
δ	Length of one PFG
G	Intensity of one PFG
Δ	Time between two consecutive PFG
T_m	Melting Temperature
T_{Cr}	Crystallisation Temperature
n	Avrami exponent
k	Avrami constant
$t_{1/2}$	Half time of crystallisation

Chapter 1. Introduction

1.1. Background

The important link between human health and consumed foods has long been recognised. In this context, obesity is a condition characterised by a severe excess of body weight and body fat which has been shown to correlate with the development of cardiovascular diseases and Type II Diabetes. Obesity has been associated with a life-style characterised by limited activity and the consumption of high energy-dense foods, and it is recognised to be a growing problem in the Western world; therefore, strategies are needed to reduce this condition. One approach to try and reduce the risk of obesity is development of “low calorie-low fat” alternatives to standard products, so to reduce energy intake. However “low fat” alternatives are usually less liked by consumers (Norton *et al.*, 2006). Furthermore, the development of these alternatives raises questions from a microstructural design and formulation engineering point of view. The possibility of developing healthier alternatives to full fat products begins with understanding the role played by different ingredients and the relationships existing between process-formulation engineering and material science as well as consumer-food interactions. The most common strategy applied in the food industry to reduce energy content in foods consists of replacing fat with aqueous based systems. This approach often aims to modify the so called “microstructure” of food products (size range between 1 to 200 μm). Low fat spreads (fat content $\leq 60\%$) are a common example of this type of approach. In these water-in-oil emulsions the continuous crystalline fat phase provides the solid-like structure and traps the aqueous phase dispersed in the form of small droplets (Heertje,

1993). Low fat spreads that are both stable and liked by the consumer result from the optimisation of (1) lipid component characteristics (which provide stability and structure on crystallisation), (2) formulation technology (e.g. use of emulsifiers to control destabilisation and release flavour compounds), and (3) processing route. More recently, the use of emulsion technology to reduce fat content in chocolate has been proposed. This sets bigger challenges than those faced for low-fat spreads as chocolate has a more complex microstructure. It consists of a suspension of hydrophilic solids (sugar and cocoa particles in dark chocolate, totalling >60%, wt%) suspended in a semi-solid fat phase (mainly cocoa butter >30%, wt%) that contains emulsifiers (primarily phospholipids) to stabilise the suspension and facilitate processing. Furthermore, to be accepted by consumers, chocolate fat phase has to be crystallised into a specific polymorphic state (form V) via a process known as *tempering*. Form V provides stability on storage and the desired sensorial properties (mouthfeel, snap, and glossiness). It is easy to understand that the accomplishment of the goal of a low-fat chocolate faces both process and microstructural-formulation challenges as well as from a mechanical-sensorial point of view. Ideally, the emulsification process should be easily integrated into the standard chocolate manufacturing procedure (as any substantial modification may create a barrier to the use of this technology) and emulsions should be tempered and stable in order to allow further processing. From a mechanical-sensorial point of view, the replacement of part of the fat with water is expected to result in differences in comparison with a full fat chocolate, primarily in terms of texture, which may lead to failure in the acceptance of the product. Furthermore, the possibility of incorporating stable water droplets within the CB matrix also depends on the crystallisation behaviour of the emulsions during and after processing. The possibility of using water-in-cocoa butter emulsions as a novel ingredient

to reduce chocolate fat content has been proposed for the first time by Norton *et al.* (2009, 2012). Although these authors showed that water-in-cocoa butter emulsions represent a promising route for the development of a low-fat chocolate, questions stand with respect to process optimisation and the factors determining emulsions crystallisation and stabilisation. Other questions regard the expected different mechanical properties of the final product and the possibility to meet the desired texture-mouthfeel sensations.

1.2. Thesis objectives

In order to further advance the current understanding of the relationship between process-formulation conditions and microstructural properties of water-in-cocoa butter emulsions, three main objectives were determined:

- 1 To investigate the effect of a range of processing and formulation conditions on the microstructure and stability of water-in-cocoa butter emulsions, in order to optimise emulsion production;
- 2 To characterise the large deformation mechanical behaviour of cocoa butter and water-in-cocoa butter emulsions;
- 3 To understand the effect of water droplets on the crystallisation behaviour of cocoa butter systems.

To achieve these goals, experiments were designed to first optimise emulsion production, considering droplet size and cocoa butter polymorphism as the main microstructural properties. The characterisation of the mechanical behaviour at large deformation provides understanding of the droplets-matrix interaction and the role of water droplets on the mechanical properties of emulsions. The study of the crystallisation behaviour of

emulsions highlights the role of the interface on phase transitions and polymorphic behaviour.

1.3. Thesis structure

Chapter 2 presents a comprehensive literature review of phase transition and structural organisation in lipid systems. Cocoa butter static crystallisation is discussed in detail. The main aspect of emulsion formation and mechanism instability are briefly described and particular attention is given to fat crystals stabilised emulsions. The chapter ends by discussing the recent advancements in lipid crystallisation in emulsified systems.

Chapter 3 provides a detailed description of the materials and methods used to produce and characterise the emulsions. The method developed to characterise the solid fat content in emulsions is described in detail as well as the methods used to characterise the mechanical behaviour and polymorphic phase transition of these systems.

Chapter 4 presents the results of the investigation of processing conditions and formulation on the microstructural properties of water-in-cocoa butter emulsions, leading to process optimisation.

Chapter 5 initially describes the large deformation behaviour of bulk cocoa butter using uniaxial compression test. Thereafter, the discussion focuses on comparing the mechanical behaviour of water-in-cocoa butter emulsions with the bulk fat phase. The effect of water percentage and droplet size is investigated. The role of compressive rate on the mechanical response is discussed.

Chapter 6 contains the results of the crystallisation study of the cocoa butter systems. The NMR method developed in Chapter 3 is applied to determine crystallisation kinetics, while deconvolution analysis of endotherms is used to characterise polymorphism.

Chapter 7 summarises the main findings of the research discussed in the results chapters and highlights future studies.

Chapter 2. Literature review

This chapter presents an overview of the current knowledge in the field of colloidal dispersions relevant to the objectives of this thesis. In the first part the main aspects concerning fat crystallisation, fat crystal networks and their mechanical properties are discussed. The second part of the chapter discusses emulsions formation and mechanisms of instability. The final part focuses on fat crystal stabilised emulsions as a type of Pickering stabilisation. The recent advancements regarding the phenomena of interfacial crystallisation in emulsions are also discussed. It should be considered that the fields of crystallisation and emulsification are very broad; therefore, the literature reviewed is selective rather than comprehensive.

2.1. Fat crystallisation

2.1.1. General aspects of lipids and fat crystallisation

The word “fat” is generally used to indicate lipid systems existing in a solid state at ambient temperature ($\sim 25\text{ }^{\circ}\text{C}$), compared to “oils” which are liquid at the same temperature (Marangoni *et al.*, 2012). Although fats are solid polycrystalline materials, they always contain liquid oil trapped within the network (Marangoni *et al.*, 2012). A *crystal* is a material made up of elementary units arranged in a well ordered geometrical packing fashion to attain a minimum in their free energy content (Walstra, 2002).

Fats generally consist mainly of complex mixture of triacylglycerols and some minor lipid components (Himawan *et al.*, 2006; Sato and Ueno, 2011). Triglycerides or triacylglycerols are non-polar neutral molecules containing a glycerol backbone linked with three fatty acids *via* an ester bond. The three hydroxyl groups on the glycerol backbone are identified with the code “sn-1, 2, or 3” (*sn*: stereo-specifically numbered) and the three bonded fatty acids indicated by the letters R_1 , R_2 , and R_3 . The type, length as well as the degree of unsaturation of the hydrocarbon chains can change among fats, affecting their crystallisation behaviour. When the three fatty acids are the same, triglycerides are called “monoacid”, otherwise they are referred to as “mixed-acid” (Sato, 2001). The carbon atoms forming the chain are arranged in a “zig-zag” manner which affects the subsequent three dimensional packing of the molecules in the solid state (Section 2.1.2.). Several reviews on the different features of crystallisation and polymorphism of fats have been published in the literature (Timms, 1984; Himawan *et al.*, 2006; Sato, 2001, Sato *et al.*, 2013). These reviews should be considered for a more detailed description of crystallisation and polymorphic transition in lipid systems.

Lipids can exist in a liquid or solid-like state, or more commonly as a mixture of the two depending on temperature and pressure (Sato *et al.*, 2013). The general change in the physical state from liquid to solid is called *crystallisation*. The liquid-to-solid transitions considered in this thesis refer to transformations occurring at atmospheric pressure (101 kPa). The physical state of fats can vary greatly ranging from liquid oil to plastic dispersion, until obtaining a hard brittle solid depending on temperature (assuming constant pressure) (Timms, 1984). At any temperature, one characterising parameter is represented by the amount of crystalline material and defined as *Solid Fat Content (SFC)*: the fraction of solid material over the total lipid content in the system. In general, differences in the physical state imply differences in the physical properties of the materials. Some of the physical properties are discussed in the following sections.

Fat crystallisation is usually divided into three main stages: supersaturation, nucleation, and crystal growth, although only the latter two steps imply the formation of a new solid phase within the liquid one. It should be considered that many changes occur toward and after the end of the crystallisation process (when the SFC content remains fairly constant) including: nucleation and crystallisation of new crystals, Ostwald ripening of large crystals at the expense of small crystals, oil and small crystal migration, polymorphic transitions and “network sintering”, i.e. development of solid bridges between fat crystals (Johansson and Bergenstål, 1995a).

2.1.1.1. Supersaturation

In solution (or melt), the crystallisation of a component can occur when supersaturation with respect to that component is reached. In a saturated solution (a system where solute and crystals are in thermodynamic equilibrium), supersaturation is achieved only if the activity of the crystallising component is higher than in the solution (and, therefore, in the

solid) (Kloek *et al.*, 2000a). Under this condition, the chemical potential difference ($\Delta\mu$) between the supersaturated liquid and the solid is the thermodynamic driving force for crystallisation (Himawan *et al.*, 2006). Mathematically the $\Delta\mu$ is given by:

$$\Delta\mu = R T \ln\beta \quad (\text{Eq. 2.1}),$$

where, R is the gas constant (8.314 J/K/mol), T is the absolute temperature of crystallisation (in Kelvin degree (K)), and $\ln\beta$ is the supersaturation. The parameter β is the superaturation ratio given by:

$$\beta = [c] / [c^*] \quad (\text{Eq. 2.2}),$$

where, $[c]$ is the total concentration of the crystallising specie in solution at supersaturation and $[c^*]$ is the solubility limit of the solute at the determined temperature and pressure (Kloek *et al.*, 2000a; Marangoni *et al.*, 2012).

Fat crystallisation is a complex phenomenon, usually promoted by a decrease in temperature (Walstra, 2002). The complexity of the phenomenon can be understood considering that fats are mixtures of many different TAGs types varying in chemical structures and physical properties. In these multi-component systems, the high melting points TAGs become supersaturated with respect to the liquid oil phase represented by the low melting point TAGs (Loisel *et al.*, 1998a). In the case of fats, supersaturation conditions are usually achieved by cooling the melt below the melting temperature (T_m), i.e. the temperature above which the SFC is zero (Himawan *et al.*, 2006). The process of lowering temperature is known as “melt supercooling” and for a molten system its “degree of supercooling (ΔT)” is defined as:

$$\Delta T = T_m - T_{cr} \quad (\text{Eq. 2.3}),$$

where, T_m and T_{Cr} are the melting and crystallisation temperature, respectively. The value of ΔT at which the crystallisation is first observed depends on physicochemical properties of the lipid phase (chemical composition, presence of impurities, physical structure: bulk vs emulsified) and processing parameters (cooling rate, application of shear, etc) (McClements, 2005). For mono-component lipid systems, where the TAGs have similar chemical structure, the chemical potential difference for crystallisation can be described in terms of supercooling and Equation 2.1 assumes the following form (Sato *et al.*, 2013):

$$\Delta\mu = \frac{\Delta T \times \Delta H_m}{T_m} \quad (\text{Eq. 2.4}),$$

where, ΔH_m is the melting enthalpy (J/mol) and ΔT is the degree of supercooling. A supersaturated melt is said to be in a *metastable* state and for such system the transformation from liquid to solid is a thermodynamically favourable process as the free energy of the liquid state is higher than that of the solid state (McClements, 2012a). Although below the T_m crystallisation is expected to occur, a system can exist in a supercooled state for a significant amount of time before crystallisation starts. This is due to the presence of activation energy barriers associated with the freedom of TAGs molecules in the melt, i.e. they can assume many conformations, thus increasing the difficulty of finding the correct alignment and packing into stable crystal nuclei (Marangoni *et al.*, 2012, McClements, 2012a). If the right conditions are met, crystallisation starts *via* nucleation and continues *via* crystal growth.

2.1.1.2. Nucleation

For fat crystallisation to occur, it is essential to develop stable nuclei that can subsequently grow. A nucleus is an assembly of molecules organised to form a crystal lattice which does not re-dissolve in solution and grows into a crystal (Cook and Hartel,

2010). The nucleation behaviour of a melt depends on several factors including the molecular nature of the crystallising lipid, the application of external forces, cooling rate, and the presence of foreign materials. Nucleation is generally divided into two main groups: *homogeneous* and *heterogeneous*.

Homogeneous nucleation is the process by which molecules spontaneously associate with each other after collision and form small ordered molecular clusters, which then grow to form crystals. TAGs homogeneous nucleation generally obeys the Gibbs-Thompson model and its detailed mathematical description can be found in the literature (Marangoni *et al.*, 2012; McClements, 2012a; Povey, 2014). Homogeneous nucleation requires a higher degree of supercooling than heterogeneous nucleation as molecules have to encounter each other in the right orientation and have to remain in contact long enough to grow into clusters and then nuclei. *Heterogeneous nucleation* occurs when nuclei originate from impurities (foreign particles, surfaces, or pre-existing crystals) (Cook and Hartel, 2010). By providing (heterogeneous) surfaces, impurities decrease the activation energy associated with nucleation thus making the formation of nuclei a more thermodynamically favourable process than in bulk melt. Heterogeneous nucleation is further divided in two types: (1) *Primary heterogeneous nucleation*: it occurs when the impurities (dust, air bubbles, walls of mixers) are chemically different from the crystallising component; (2) *secondary heterogeneous nucleation* occurs when the impurities are represented by crystals or their fragments which share the same chemical structure of the crystallising component (McClements, 2012a). This type of nucleation occurs in scraped surface heat exchangers (see Chapter 4). It can be easily understood that the type of nucleation process plays a critical role on the overall fat crystallisation phenomenon. Furthermore, TAGs can nucleate in different polymorphs according to the

degree of supercooling and processing conditions (Marangoni *et al.*, 2012; Sato *et al.*, 2013), where polymorphs can be considered different solid arrangements of the same molecules (Section 2.1.2.). In real situations, heterogeneous nucleation is the predominant nucleating process and α form (the least stable) is the main polymorph formed as its activation energy of formation is much lower than that required for the other polymorphs (Marangoni *et al.*, 2012). Finally, it should be considered that some foreign molecules existing in the melt may delay the crystallisation process (for example some emulsifiers). Different molecules and reasons have been discussed in the literature (see McClements, 2012a), but they will not be considered in this thesis.

2.1.1.3. *Crystal growth*

The nucleation step is readily followed by *crystal growth* (Marangoni *et al.*, 2012), although often these processes occur simultaneously. Crystal growth occurs when TAGs molecules adsorb to the surface of nuclei directly from the melt after having diffused to the crystal-liquid interface (Walstra, 2002). Crystal growth rate depends on a series of parameters namely diffusion of crystallising and non-crystallising molecules to and away, respectively, from the crystal surface, integration of the new molecules into the existing structure and removal of latent heat of crystallisation (Cook and Hartel, 2010). Given the number of processes occurring concurrently, and the fact that different faces of fat crystals can grow at different rates, the construction of a model describing the crystal growth phenomenon is difficult (McClements, 2012a). In lipid systems it is recognised that the adsorption of a new molecule onto a growing crystal surface is the limiting step at high temperature whereas at low temperature molecular diffusion to and from the solid-liquid interface limits the growth due to increased bulk viscosity (Hartel, 2001).

2.1.2. Fat polymorphism

Polymorphism is a property typical of crystallising compounds and refers to their ability to exist in different crystalline forms (Sato and Ueno, 2011). Different solid forms of the same crystallising material are referred to as “polymorphs”, “polymorphic transformations or modifications”, or simply “forms”.

This property of fats has been recognised for over a century and suggested by the existence of multiple melting peaks for the same TAGs crystallised under different conditions (Chapman, 1962, Timms, 1984). Two types of polymorphism exist: enantiotropic and monotropic polymorphism. In the case of *enantiotropic polymorphism* at a given temperature and pressure range, each polymorph is stable (Himawan *et al.*, 2006).

Monotropic polymorphism is the most common polymorphism in fats and the name derives from the fact that all polymorphs are *metastable*, but one. The unstable polymorphs always tend to transform toward the only thermodynamically stable modification over time. In fats three main polymorphs are recognised to exist, each of which is characterised by a specific arrangement of the aliphatic chains of the TAG molecules (Timms, 1984) (Fig. 2.1) and identified with Greek letters α (alpha), β' (beta prime), β (beta) in increasing order of thermodynamic stability, density, and melting point (Marangoni *et al.*, 2012). Together with differences in the physical properties, the different conformation of the molecules is responsible for the different thermodynamic properties of the three polymorphic forms (i.e. the free energy content) (McClements, 2012a).

To better understand polymorphism it should be considered that different levels of organisation can be identified within fat crystals networks. At a nanoscale level, TAGs

are long chain molecules able to assume two types of conformation on crystallisation: (1) a *tuning fork* arrangement where the fatty acid residues (R groups) esterified in the positions sn-1 and sn-3 are on the same side with respect to the glycerol plane and opposite to the fatty acid in position sn-2; (2) *chair* conformation where the residues in position sn-1 and sn-2 are on the same side and the sn-3 is opposite compared to the glycerol backbone forming the back of the chair. On nucleation, the chains of neighbour TAGs molecules assume an extended conformation and pack side by side to form a *lamella*. The thickness of the lamella layer or *long spacing* (or *d spacing*) depends on (i) chain length and degree of unsaturation of the hydrocarbon groups, (ii) the tilt angle between the R molecules axis and the basal plane formed by the methyl end groups, and (iii) the TAGs stacking modes (Timms, 1984). Furthermore, the fatty acid residues (R groups) are flexible molecules and can assume different orientations with respect to each other in the side-to-side stacking. The arrangement of TAG molecules in a solid fat crystal structure can be therefore characterised with respect to their longitudinal and lateral packing mode.

The type of *later packing* of TAGs within the unit cell lamella determines crystal polymorphism. The difference in the polymorphic forms relies on the difference in the so called *subcell structure*, where a *sub-unit* or *subcell* is identified by the ethylene groups within the aliphatic chains and visualised by taking a cross-section of the zig-zag hydrocarbon tails (Marangoni *et al.*, 2012; Sato, 2001). The ethylene group is also commonly called “zig-zag period” (Timms, 1984).

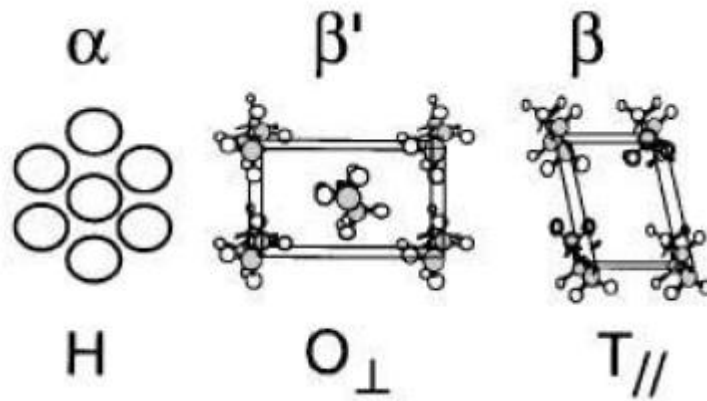


Figure 2.1: Schematic of the three basic polymorphs found in fats. Image taken from Sato (2001).

The subcell structure for α , β' , β forms are hexagonal (H), orthorhombic-perpendicular (O_{\perp}), and triclinic-parallel ($T_{//}$), respectively (Sato and Ueno, 2011). The main features of the three subcell structures are: the R groups within the *hexagonal subcell* are perpendicular to the methyl basal plane and have a high degree of freedom. The arrangement of α polymorph sub-unit is typically visualised using cylindrical rods representing the oscillating fatty acid residues (Timms, 1984) (Fig. 2.1). In the case of *orthorhombic-perpendicular sub-unit*, typical of the β' polymorph, the ethylene planes of the aliphatic chains are perpendicular to those of the neighbour chains and have limited freedom. In the *triclinic-parallel subcell*, the zig-zag periods are all parallel to each other and have least freedom of movements (Timms, 1984). This level of structural organisation is univocally determined by measuring the short spacing patterns of the crystals by Wide Angle X-ray Diffraction analysis (WAXRD) at $0.9 < q < 1.8 \text{ \AA}^{-1}$ (Lavigne *et al.*, 1993). Each polymorphic form is characterised by unique X-ray spectra (Tab. 2.1) (Chapman, 1962; Larsson, 1966).

Table 2.1: Nomenclature, subcell form, and characteristic short spacing lines for the three basic polymorphs in fats (Chapman, 1962; Larsson, 1966).

<i>Polymorph</i>	Subcell form	X-ray short spacing characteristic patterns
α	Hexagonal (H)	Single strong line at 4.2 Å
β'	Orthorombic Perpendicular (O _⊥)	Two strong lines at 3.8 and 4.2 Å Or three strong lines at 3.71, 3.91, and 4.27 Å
β	Triclinic Parallel (T _∥)	Strong line at 4.6 Å and none of the lines of the α and β' forms

Finally, it should be considered that if two or more polymorphs of the same types exist, these are distinguished using subscript numbers in order of decreasing melting point (Timms, 1984). This is particularly relevant in the case of cocoa butter where two β' and two β forms exist and distinguished using the subscript numbers “1” and “2”.

Along the dimension concerned with long-chain axis of a unit cell lamella, the characterising parameter is known as *long chain structure* and it describes the recurring ordered arrangement of hydrocarbon tails as determined by the stacking of TAG molecules (Sato, 2001). A *double chain length structure*, DCL (2L), is obtained when two TAGs pack in a “seat-to-seat” fashion as shown in Figure 2.2a; *triple chain length structure*, TCL (3L), occurs when two TAGs molecules pack in a “back-to-back” mode (Fig. 2.2b) (Marangoni *et al.*, 2012). It can easily be seen that a 3L structure is longer than a 2L one. This latter structure is formed when the R groups are very similar whereas a 3L structure occurs when at least one of the fatty acid group is different from the other

two (Sato, 2001). The type of chain length structure (-2 or -3) can be added to the symbol of the polymorph (Timms, 1984). The chain length structure determines the thickness of the lamella (or “long spacing”) of a fat crystal and is measured using Small Angle X-ray Diffraction analysis (SAXRD) at $0 < q < 0.9 \text{ \AA}^{-1}$ (Lavigne *et al.*, 1993).

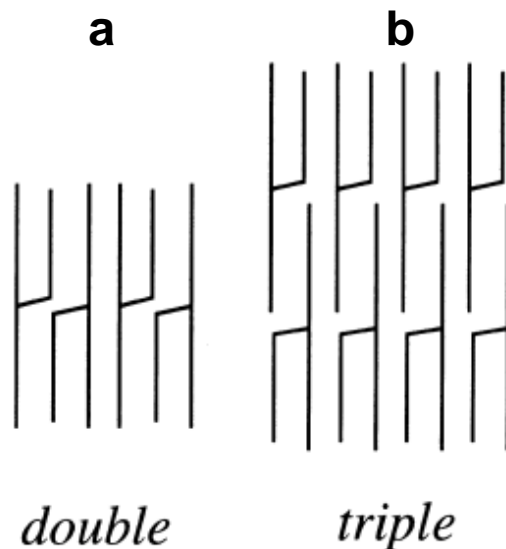


Figure 2.2: Double (a) and triple (b) chain length structure. Image taken from Sato *et al.*, (1999).

On crystallisation, the type of polymorph nucleated depends on both thermodynamic and kinetic aspects and is affected by several factors including fatty acid composition, cooling rate, temperature and medium of crystallisation, externally applied shear, and templating effect (Sato and Ueno, 2011). The three basic polymorphs can all be crystallised directly from the melt although differences exist with respect to the kinetics of formation due to their characteristic activation free energy of nucleation (ΔG^\ddagger) (Marangoni *et al.*, 2012; Sato *et al.*, 2013). In case of TAGs, the *Ostwald step rule* predicts that if crystallisation is promoted by kinetic factors, such as a decrease in temperature, the least stable transformation crystallises much faster (and, therefore, to a higher extent) than the stable ones (Sato *et al.*, 2013). This is due to the fact that metastable forms have considerably

lower activation energy of nucleation than the stable ones ($\alpha_{\Delta G^\ddagger} < \beta'_{\Delta G^\ddagger} < \beta_{\Delta G^\ddagger}$). Furthermore, the law predicts that over time (during and/or after crystallisation), the unstable forms evolve stepwise toward the stable polymorphs (Sato, 2001). Recalling that the polymorphism of fats described here refers to “monotropic polymorphism”, the driving force for transformation from α to (eventually) β form is the difference in the Gibbs free energy content (ΔG) between the crystalline phases: at any temperature where the fat exists in a solid state, α form has the highest free energy level followed by β' and β . To attain the maximum thermodynamic stability, the system will evolve toward the state characterised by the minimum ΔG content *via* monotropic phase transformations (Fig. 2.3). Polymorphic evolution can occur either *via* a melt-mediated or solid-mediated transformation (Fig. 2.4): Depending on the process conditions (temperature, pressure, cooling rate, application of shear), a lipid melt can crystallise in one or more polymorphic form (α , β' , β). Over time, the least stable form (α) will transform into β' and eventually in β . If the temperature of the system is below the melting point of the least stable polymorph, polymorphic evolution occurs *via* a *solid state transformation*. A *melt mediated transformation* occurs if the temperature is above the final melting point of the least stable polymorph. It should be finally considered that the validity of Ostwald step rule is limited. In fact, in crystallisation processes where external factors are involved (application of shear, cooling rate, templating, *etc*) the rule is not able to predict the occurring competitive nucleation of the different polymorphs (Sato *et al.*, 2013).

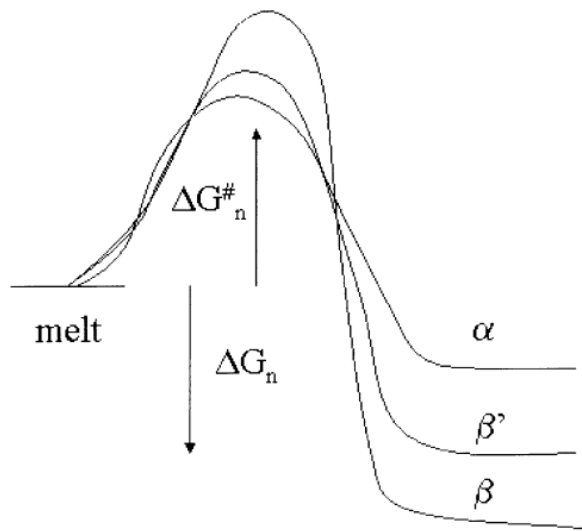


Figure 2.3: Free energy of activation ($\Delta G_n^\#$) and free energy of nucleation for the three basic polymorphs. Image taken from Marangoni (2002).

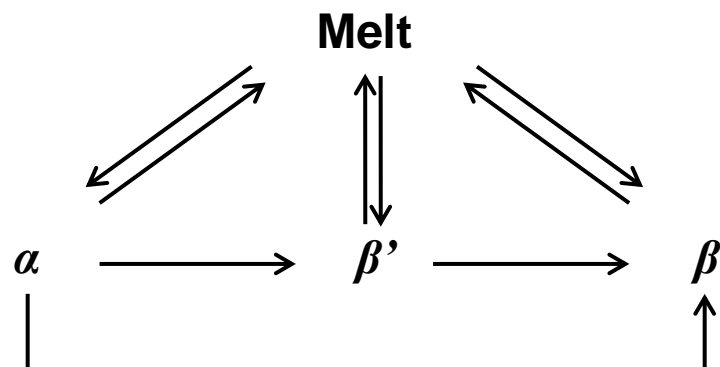


Figure 2.4: Schematic representation of polymorphic evolution in fats. Image modified from Sato *et al.* (1999).

2.1.3. Structure of fat crystal networks

Fat crystal networks can be defined as *soft colloidal crystal gels* characterised by a complex three dimensional hierarchical structure, which is fractal in nature (Tang and Marangoni, 2006b; Acevedo *et al.*, 2011). Different length-scale of organisation can be identified within a fat crystal network each of which contributes to the macroscopic physical behaviour. Figure 2.5 is a visualisation of the different levels of organisation as

proposed by Marangoni and co-workers in a series of publications (Narine and Marangoni, 1999a; Narine and Marangoni, 1999b; Tang and Marangoni, 2006b).

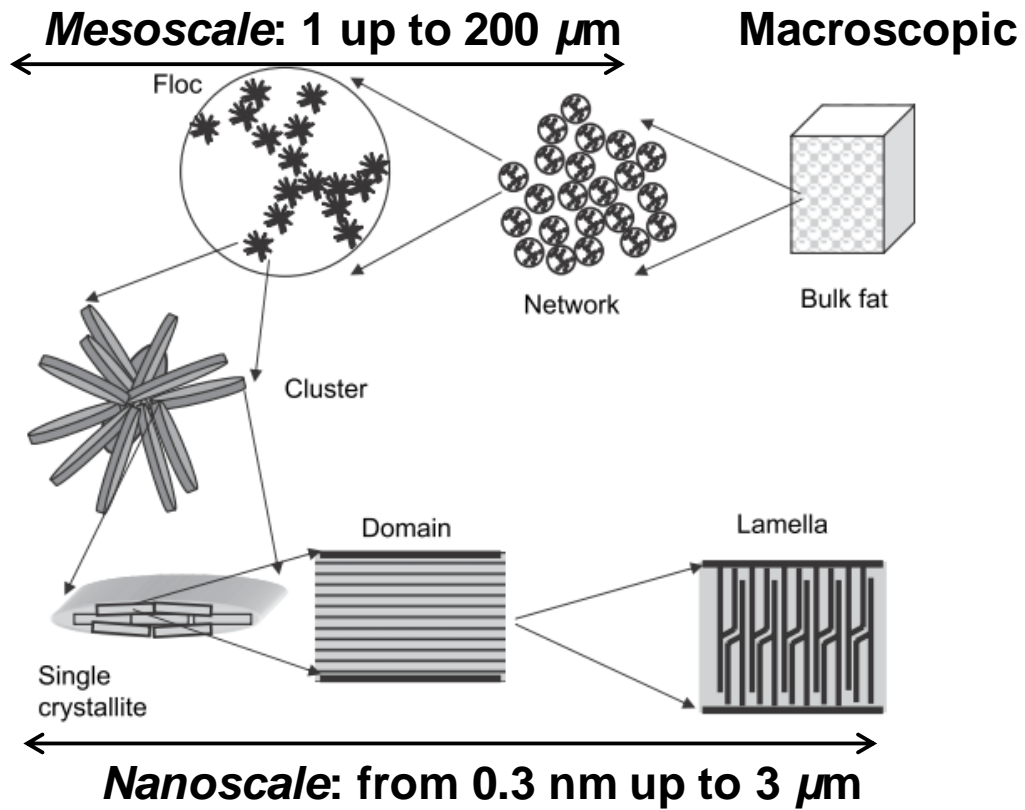


Figure 2.5: Hierarchical model for fat crystal networks. The characteristic length scales have been added to help the discussion. Image taken from Tang and Marangoni (2007).

The nanoscale level starts with the organisation of TAGs molecules to form lamellae as described in Section 2.1.2. These structures can stack epitaxially to form a *domain* or *nanoplatelet*. These *primary nano-crystals* can aggregate *via* momentum-, heat-, and mass- transfer limited processes to form *clusters* (or *primary particles*, of a size range of 1-3 μm) held together by van der Waals forces (Marangoni *et al.*, 2012). The *mesoscale* or *microstructural level* is characterised by structure ranging from 1 to 200 μm in size and results from the aggregation of the *clusters* in a fractal manner into larger clusters: the “microstructures” or “flocs” (~20 - 200 μm). The network growth process continues

until a continuous three-dimensional matrix is formed by the packing of microstructures (Narine and Marangoni, 1999b). Floccs aggregate in a Euclidean regular manner, therefore at the microstructural level the fat matrix is an orthodox amorphous material with the liquid oil filling the voids (Narine and Marangoni, 1999a; Marangoni, 2000). The forces holding fat crystals and crystal aggregates together are usually divided into two groups: primary and secondary bonds. *Primary bonds* are considered to be a result of mutual adhesion between crystals and are also referred as “sintered” bonds or solid bridges (Johansson and Bergenstål, 1995a). The mechanism of formation of these solid bridges is not fully understood as well as their nature. *Sintered bonds* can be formed between large crystals and/or small crystal nuclei flocculated together (Johansson and Bergenstål, 1995a). The *secondary bonds* are represented mainly by weak van der Waals interaction forces with Coulombic and steric forces also contributing to the network aggregation.

2.1.3.1. *Mechanical behaviour of fat crystal networks*

According to the model originally developed by Narine and Marangoni (1999a) for fat crystal networks, two regimes can be recognised according to the SFC level: strong and weak link regimes depending whether the SFC value is below or above 60%. In the case of the *strong link regime*, when the network is deformed, the microstructures forming the network are deformed. For fat networks in the *weak link regime* (as for those discussed in Chapter 5), the theory assumes that, if the colloidal matrix is deformed within its elastic strain region, the links between floccs forming the network are deformed with the microstructures remaining un-deformed. Therefore, the macroscopic measured stiffness of the system is the result of the addition of the stiffness of van der Waals inter-flocc bonds. Marangoni (2000) provided a thermodynamic basis for the explanation of the elastic behaviour and the increase in stiffness at higher SFC was explained with an

increase in the number of inter-flocs bonds. This model was later modified to take into consideration the heterogeneous stress distribution in fat networks under an applied stress due to the presence of structural defects and differences in the strength of the flocs (Tang and Marangoni, 2007). The authors concluded that number of stress-carrying flocs is an exponential function of the volume fraction of solids (i.e. the SFC). According to this model, the number of stress-carrying flocs (or load bearing solids, Φ_e) becomes approximately constant at high SFC, expressed as “volume fraction of solids”, Φ . The relationship between the “effective volume fraction of solids”, Φ_e , on “volume fraction of solids”, Φ , is given by:

$$\Phi_e = 1 - e^{-k\Phi^b} \quad (\text{Eq. 2.5}),$$

where k and b are constant (Tang and Marangoni, 2007).

Another explanation of the large deformation of fat network was provided by Kloek *et al.* (2005a, b). Even if the existence of a fractal structure occurs at the beginning of network formation, the authors concluded that the large deformation behaviour of fat networks cannot be explained in terms of fractal approach. In their view, a fat matrix appears to be a solid, where the stress carrying elements are the so called “rigid junctions”. These junctions consist of fat crystals and crystal aggregates, interconnected by the sintering of *solid bonds* while the fat matrix is developing. This is a considerable difference with the model proposed by Marangoni and co-workers who assume that only van der Waals interactions determine the mechanical behaviour of fat crystals networks. In the discussion in Chapter 5, data interpretations will be made in the light of one or the other approach.

2.1.4. Models describing fat isothermal crystallisation

This section discusses the main model (i.e. the Avrami model) reported in the literature to describe the kinetic aspects of the liquid-solid phase transition in TAGs. It is well known that experimental conditions significantly affect crystallisation behaviour and understanding when and to what extent crystallisation occurs is crucial in order to control operations to tailor fat properties (Herrera and Hartel, 2000). Mathematical models are a useful tool as they can be used to quantify TAGs crystallisation differences as a result of experimental factors (Foubert *et al.*, 2003a). When using a model, experimental data can be fitted to it and parameters extracted, thus allowing direct comparisons among different experimental conditions (Foubert *et al.*, 2006). Four mathematical models have been referred to in the literature to describe the kinetics of fat crystallisation and all assume isothermal conditions. The models are: (1) Avrami, (2) modified Avrami, (3) Gompertz, and (4) Foubert model (Avrami, 1939; Avrami 1940; Khanna and Taylor, 1988; Kloek *et al.*, 2000; Foubert *et al.*, 2006). Only the Avrami model is described in this thesis as it was used to quantify crystallisation kinetics of the produced systems. The main techniques used to model the kinetics of fat crystallisation are Differential Scanning Calorimetry (DSC) and pulsed Nuclear Magnetic Resonance (pNMR). In an isothermal experiment, the sample is cooled to the desired T_{Cr} at the maximum rate possible (to minimise crystallisation on cooling) and the relevant property measured over time.

2.1.4.1. Avrami model

This model takes the name from Avrami who described that the growth of a new phase starts with the formation of small nuclei within the liquid phase (Avrami 1939, 1940). It should be mentioned that mathematical formulation of the model was independently formulated in the same period by four researchers (Johnson, Mehl, Avrami, and

Kolmogorov, *JMAK model*) to describe the kinetics of crystallisation of low molecular weight materials (such as metals). This model was later extended to polymers and today is the mostly used approach to study isothermal phase transition, including fat crystallisation. A complete mathematical description of the model has been published by Foubert *et al.* (2003a). The final form of the model is known as “Avrami equation” and has form:

$$X = 1 - e^{-k t^n} \quad (\text{Eq. 2.6}),$$

where, X is the fraction of material transformed (also called “crystallinity”) at time t compared to the total at a given temperature, k is a *crystallisation rate constant* (or *Avrami constant*) having the dimension of “ t^{-n} ”. k is a complex rate constant in a process of n^{th} order. The “*Avrami exponent or index*”, n , is a dimensionless constant ranging between 1 and 4 depending on the mechanism of nucleation and crystal growth. The equation allows for the quantification of crystallisation kinetics and describes a phenomenon where the fraction of crystallised material increases slowly at the beginning (lag-period), followed by a steep increase in the fraction of crystal material, and terminates with a third region represented by a plateau where the entire supersaturated component has crystallised (Marangoni, 1998). Graphically a plot of the crystal fraction versus time has a sigmoid shape. It should be noted that the Avrami model does not distinguish between nucleation and crystal growth and considers the phenomenon as one overall process (Metin and Hartel, 1998).

The Avrami model is based on a few assumptions: constant temperature on crystallisation, random nucleation through the volume, dependency of the growth of the new phase only on temperature (and not on time), and the constant density of growing crystals. Avrami also made the assumption that growth ends if two growing nuclei

impinge on each other (Foubert *et al.*, 2003a). This assumption may not be valid in the case of fat crystal networks where sintering between fat crystals can occur.

From the Avrami parameters quantitative information on the kinetics of the crystallisation process can be obtained. The crystallisation rate constant (k) is a combination of nucleation and crystal growth and its temperature dependency is expressed by an Arrhenius-type equation (Metil and Hartel, 1998). It depends on the type of nucleation (see below) and on the value of n . The Avrami exponent (n) is found to be constant over a certain range of temperature and takes into account both time dependency of nucleation (sporadic vs instantaneous) and the main dimensions of crystal growth and morphology (linear, plate-like, and spherical) (Tab. 2.2). In the case of *sporadic nucleation* the number of nuclei increases linearly with the time, whereas for *instantaneous nucleation* the majority of the nuclei are formed at the beginning of the phase transition (Foubert *et al.*, 2003a). As it can be seen from Table 2.2, the Avrami exponent can assume the same value for the two types of nucleation. Therefore, care should be taken in defining a nucleation mechanism simply using the n value.

Table 2.2: Values of Avrami exponent (n) for different growth morphology and nucleation types.

Growth morphology	Instantaneous Nucleation	Sporadic Nucleation
Linear	1	2
Plate-like	2	3
Spherical	3	4

In theory n should always be an integer; however, fitting of the model to experimental data often produces non integer values. A number of reasons have been proposed to explain this result: co-occurrence of the two nucleation mechanisms, changes in the

nucleation and growth rate, development of different crystal morphologies, density change for the two phases (Foubert *et al.*, 2003a). As it will be shown in Chapter 3, the values of k and n can be obtained by linear regression of the linearized form of the Avrami equation.

2.1.5. Cocoa butter: composition and crystallisation behaviour

The aim of this section is to provide a brief, but comprehensive, review of the state of the art regarding cocoa butter (CB) static crystallisation. CB is the lipid phase of all the emulsions produced in this study; therefore, knowledge of its crystallisation properties is essential.

Among vegetable fats that have applications in food production, CB is one of the most important being widely used in the confectionery industry. CB crystallisation behaviour determines microstructural, thermal, and textural properties of many food products such as confections and chocolate. In the case of chocolate it determines the snap, glossiness, and melt-in-the-mouth behaviour. From a chemical composition point of view, it consists of a mixture of TAGs, the distribution of which depends on botanical and growing conditions and areas. However, the majority of TAGs (up to over 80%) is represented by mono unsaturated triglycerides, with the unsaturated fatty acid molecule (an oleic R group) esterified in position 2 (sn-2) of the glycerol molecule (Fessas *et al.*, 2005; Toro-Vazquez *et al.*, 2004; Loisel *et al.*, 1998a). The unique and complex CB polymorphism has to be attributed to this fraction of TAGs, so that CB behaves like a pseudo-single component system (Fessas *et al.*, 2005). In fact, although CB crystallisation has been extensively investigated using a wide range of techniques under different processing-formulation conditions, its phase transition and polymorphic behaviour is still debated. Wille and Lutton (1966) were the first to publish a complete study on CB polymorphism

using DSC and X-ray. The authors recognised six distinct solid forms, to each of which they assigned a single melting temperature and attributed increasing Roman numerals from I to VI in order of stability (Tab. 2.3). Despite the relevance of their work, it is accepted that the authors did not report the correct melting point for the least stable form (γ or sub- α). In the new approach used to describe CB thermal behaviour, each polymorphic form is characterised by a melting range rather than a single melting point (Marangoni and McGauley, 2003). Each polymorph is characterised by a unique sub-cell diffraction pattern which can be identified by measuring the short spacings (Tab. 2.4). Nevertheless, as reported by van Malssen *et al.* (1999) uncertainties still exist when dealing with CB polymorphism.

Table 2.3: Polymorphic forms and proposed corresponding melting ranges of cocoa butter (CB) solid phases according to literature.

Polymorphic form	Wille and Lutton (1966)	Lovegren <i>et al.</i>, (1976)	van Malssen <i>et al.</i>, (1999)	Fessas <i>et al.</i>, (2005)	Walstra (2003)
I or γ	17.3	13	-5 - + 8	19.0 ± 2.0	5-18
II or α	23.3	20	17 - 22	23.5 ± 2.0	16-24
III or β'_2	25.5	23	20 - 27	26.0 ± 0.5	20-27
IV or β'_1	27.5	25		29.0 ± 0.5	25-28
V or β_2	33.8	30	29 - 34	31.3 ± 0.5	26-33
VI or β_1	36.3	33.5		36.0 ± 1.5	32-36

Table 2.4: Long and short spacing values (Å) and chain length structure of CB polymorphic forms published in literature (for simplicity only strong lines are reported).

Polymorphic form	Unit cell and chain length structure	Wille and Lutton (1966)		Chapman <i>et al.</i> (1971)	
		Short spacing	Long spacing	Short spacing	Long spacing
I	γ	4.19; 3.70	-	4.17; 3.87	54.0
II	α	4.24	49; 16.3	4.20	51.0
III	β'_2 -L ₂	4.25; 3.86	49	4.20; 3.87	51.0
IV	β'_1 -L ₂	4.36; 4.15	45; 14.87	4.32; 4.13	49.0
V	β_2 -L ₃	4.58; 3.98	32.2; 63.1	4.58; 3.98; 3.65	66.0; 33.0
VI	β_1 -L ₃	4.59; 3.70	63.1; 12.76	4.53; 3.84; 3.67	12.7

Van Malssen *et al.* (1999) were the first to develop a complete phase transition diagram for CB under isothermal static conditions over a wide temperature range (from -20 to $+40$ °C) and time (up to 10 days) using standard and time-resolved WAXR measurements. They also established a clear melting range for each polymorph and confirmed the results of their previous work suggesting that CB consists of an aggregate of a large number of crystallites with specific TAGs composition and properties (van Malssen *et al.*, 1996). These authors showed that the initially created polymorphs and their evolution strongly depend on solidification temperature and resting time. The unstable forms (γ and α) could be observed for a long time only at temperatures below -10 and $+5$ °C, respectively. At temperatures above 5 °C, α form rapidly evolved to the β' . This solid state was recognised to be a “phase range” rather a group of two or more phases, which was attributed to the fact that CB is a mixture of TAGs. According to their scheme, the transition from β' to β is a slow process (requiring at least 10 hours) which can occur only at temperature above 14 °C. The authors also reported that direct formation of β' phase from the melt occurs at T_{Cr} between 20 and 27 °C. This result was later argued by Dewettink *et al.* (2004), who investigated CB isothermal crystallisation behaviour over a fairly narrow range of temperatures ($19 - 23$ °C). At all the investigated temperatures, these authors observed a two steps crystallisation process where the crystallisation equilibrium was reached within two hours. Using time-resolved X-ray measurements they showed that the melt always crystallises into α form (first step) and excluded the possibility of direct crystallisation into β' polymorph. In their view, such crystal polymorph develops as crystallisation progresses at the expense of α form *via* a solid state transition (second step). Marangoni and McGauley (2003) built their own time-temperature state diagram under static isothermal conditions from -20 to $+26$ °C up

to 45 days and recognised two possible mechanisms for β' formation depending on time-temperature combination: (1) evolution from α form; (2) direct CB crystallisation into β' polymorph, with the first mechanism being faster than the second. The authors also referred that the most stable form (β) was always formed starting from β' polymorph. Also in this study using DSC and WAXD techniques four polymorphic forms were identified, namely γ , α , β' , and β . The least stable form (γ , melting point of 1.6 °C) was never isolated alone whereas α form was always created at any T_{Cr} below 20 °C. The existence of two types of β' forms (β_2' and β_1') were mentioned, but details regarding differences in their thermal behaviour were not provided. Although the compiled state diagram showed the polymorphic evolution as a function of time-temperature combinations, melting ranges for the various forms were not clearly proposed. These could be partially deduced from data discussion: α form would melt completely in a range between approximately 19 to 21 °C, the β' from 22 to 28 °C, and β at temperature above 30 °C.

Despite the long lasting argument, the crystallisation of CB into six main distinctive polymorphs is generally accepted. The work by Loisel *et al.* (1998a) confirmed the existence of those forms and associated them to the crystallisation behaviour of monounsaturated TAGs. Interestingly, the authors showed that trisaturated TAGs crystallise as a separated phase and segregate from the major lipid fraction without affecting its polymorphism. Furthermore, it was shown that the overall CB polymorphism (which always includes the formation of least stable form prior to further evolution toward higher transformations), reflects the polymorphism of only the major fat fraction: the monounsaturated TAGs fraction of CB determines its crystallisation behaviour as the fat behaves as a pseudo-single component (Fessas *et al.*, 2005). DSC analysis has been

used to carry out a quantitative study of polymorphic evolution kinetics in CB at various cooling rates and temperature-time combinations (from 5 to 25 °C and from 5 minutes up to 20 h) (Fessas *et al.*, 2005). In their work, the authors defined unique “apparent” melting ranges for the six polymorphs (Tab. 2.3). The word “apparent” was used to highlight the dependency of the melting points on both heating rate and sample mass. The authors showed that under all thermal histories, the maximum achieved crystalline fraction of 0.9 (corresponding to the TAGs content) and that this value was attained faster at 20 °C. The polymorphism of the solid material changed according to the cooling rate and annealing temperature as well as the amount of amorphous material: at the slowest cooling rate (2 °C/min), the largest amount of forms V and VI was formed.

Toro-Vazquez *et al.* (2004) studied the crystallisation behaviour of CB under static conditions and under shear at five temperatures between 18 and 26.5 °C. Static isothermal crystallisation was investigated using DSC and oscillation rheology. As also reported by the authors, limitations to their work were both the used cooling rate (1 °C/min) and the selected crystallisation temperatures which did not prevent crystallisation occurring on cooling. Nevertheless, the authors claimed that their results were in agreement with the phase diagram produced by van Malssen *et al.* (1999): at T_{Cr} between 18 and 20 °C, α form was the first to nucleate and crystallise; this metastable form subsequently evolved into β' polymorph *via* a solid state transformation. Further nucleation and crystal growth occurred at a later stage as the solid material in the β' arrangement acted as templating element driving direct crystallisation into this more stable form. With increasing T_{Cr} smaller amounts of α form were created and the transition to β' polymorph required longer time until obtaining crystallisation directly into β' polymorph at 22 °C. These authors established that no crystallisation occurred at 26.5

°C, which is in disagreement with data published by Davis and Damick (1989) who had reported the formation of high melting point crystals ($T_m > 60$ °C) after 3h at 26.5 °C. In this thesis, the phase transition behaviour of CB systems has been investigated under static conditions (Chapter 6) as a function of microstructure and time-temperature combination. Therefore, the literature concerned with static crystallisation of CB will provide the main comparison elements to the experimentally obtained results. The effect of shear and chemical composition on crystallisation behaviour of CB has been investigated in a number of publications (Mazzanti *et al.*, 2003; Sonwai and Mackley, 2006, Dhonsi and Stapley, 2006; Perez-Martinez *et al.*, 2007; Campos *et al.*, 2010). Where appropriate, experimental results obtained in this thesis will be compared to findings shown in those works.

2.2. Emulsions and Emulsification

2.2.1. Emulsion definition and classification

An emulsion is usually defined as a mixture of two immiscible liquids (typically oil and water) with one (the internal phase) dispersed within the other (the external phase) in the form of small spherical droplets (Friberg *et al.*, 2003). The *internal phase* is also called *dispersed* or *inner phase*, while the *external phase* is often referred to as *continuous* or *outer phase*. Details regarding emulsion production are provided in Section 2.2.3. The physical boundary between a dispersed droplet and the continuous phase is called *interface* and the energy required to modify an interface is known as *interfacial tension*. The interfacial tension can be defined as “the force per unit length acting parallel to the interface [mN/m]” (Pichot, 2012). Emulsified systems are defined as water-in-oil (W/O) or oil-in-water (O/W), emulsions depending whether the continuous phase is oil or water,

respectively. Multiple emulsions can also be formed (for example, water-in-oil-in-water) but they will not be discussed here as they are outside the scope of this thesis.

Normal emulsions are two phase systems and belong to the category of *colloidal dispersions*, where the internal phase has none, or very little, affinity with the outer liquid phase and clear boundaries exist between phases (i.e. the *interface*). It should also be considered that the dispersed and/or the continuous phase may be partially crystallised. This type of emulsions will be discussed in Section 2.3.

Since emulsified droplets are generally spherical in shape, the mean diameter is used as primary characterising parameter. On the basis of the average diameter ($d_{3,2}$), single emulsions are classified into three groups (Pichot, 2012):

1. Macroemulsions: $d_{3,2} > 400$ nm
2. Mini- or nanoemulsions: $100 > d_{3,2} > 400$ nm
3. Microemulsions: $2 > d_{3,2} > 100$ nm.

It should be kept in mind that the size range of each emulsion type can slightly change from author to author. For example the formation of nanoemulsions with diameter below 50 nm has been reported (Wooster *et al.*, 2008).

Since the average $d_{3,2}$ of macroemulsions is comparable to the wavelength of the visible light (~300 – 800 nm), particles can scatter light and emulsions appear opaque. Given their characteristic size instead, nanoemulsions and microemulsions appear transparent as dispersed droplets can only weakly scatter the light (McClements, 2012b).

From a thermodynamic point of view macro- and nanoemulsions are unstable systems, which means droplets tend to merge with each other and eventually two separated phases are obtained. Their thermodynamic instability arises from the fact that the free energy content of the emulsion is positive and higher than the sum of the free energies of the two

separated phases (McClements and Rao, 2011). Therefore, the system will always eventually separate into the two bulk liquids (see Section 2.2.4.): nano- and macroemulsions can be, at most, kinetically stable (state known as *metastability*) (McClements, 2005). To promote emulsion formation and achieve kinetic stability, a third component, called *stabiliser*, is added to the mixture. Stabilisers are divided into two main categories: (i) *emulsifiers*: surface-active molecules with the ability of lowering the interfacial tension and forming a protective layer around newly formed droplets; (ii) *texture modifiers*: extend the metastability by decreasing droplets mobility, typically by increasing the viscosity of the continuous phase (McClements, 2005). In metastable systems, the shape of the dispersed particles tends to be spherical to minimise the interfacial area between phases, which in turns minimises the interfacial tension and Laplace pressure (McClements, 2010). Only microemulsions (sometimes called “swollen micelles”) are thermodynamically stable systems and form spontaneously. This phenomenon is due to the lower free energy content of the emulsified state compared to the bulk phases. However, microemulsions remain stable only under the existing conditions (temperature, pressure) (McClements, 2010). If these conditions change, microemulsions will become unstable (but could be further re-formed if the right conditions are met again). Due to the low interfacial tension characterising these systems, the droplets can assume various shapes (spherical, ellipsoidal, *etc*) depending on the type of emulsifier (McClements and Rao, 2011). The main drawback for the formation and use of these systems is the need of high amount of emulsifier ($\geq 20\%$, w/w) (Tadros *et al.*, 2004).

It is clear that the three types of emulsions need the addition of surface active species (i.e. *emulsifiers*) to be formed and that macro- and nanoemulsions differ for only their droplet

size as both systems need energy to be supplied to be produced (Section 2.2.3.). On describing the physical properties of an emulsion, two characterising parameters must always be mentioned: droplet concentration and their average size. Droplet concentration is usually described in terms of *disperse phase volume fraction* (Φ), often in percentage, defined as:

$$\Phi = \frac{V_D}{V_E} \quad (\text{Eq. 2.7}),$$

where, V_D and V_E are the volumes of the dispersed phase and emulsion, respectively (McClements, 2005). Droplet concentration can also be expressed as *disperse phase mass fraction* (Φ_m):

$$\Phi_m = \frac{m_D}{m_E} \quad (\text{Eq. 2.8}),$$

where, m_D and m_E are the masses of the disperse phase and emulsion, respectively. Disperse volume and mass fractions are related by Equation 2.8:

$$\Phi_m = \frac{\Phi \rho_D}{\Phi \rho_D + (1-\Phi) \rho_E} \quad (\text{Eq. 2.9}),$$

where, ρ_E and ρ_D are the densities of the continuous and internal phase, respectively.

When describing the size of the droplets, it is important to refer to the characterising parameter (usually the diameter). Different statistical definitions of diameter have been used in literature to describe the characteristic size of droplets. In this thesis, the *Sauter mean* or *surface weighted diameter* ($d_{3,2}$) has been used as parameter for the characterisation of droplet size. The $d_{3,2}$ is defined as the “third over the second frequency distribution of d ” (Walstra, 1993) and its mathematical expression is:

$$d_{3,2} = \frac{\sum_i n_i d_i^3}{\sum_i n_i d_i^2} \quad (\text{Eq. 2.10}),$$

where, i is a droplet size class and n and d are the number and diameter of the droplets in i , respectively, within a distribution. With respect to the number of size distribution classes, emulsions can be classified as monodisperse or polydisperse, depending whether all droplets are distributed around a single diameter value or in groups over a range of diameters, respectively.

2.2.2. Emulsifiers

The word “emulsifier” is generally used to indicate any surface-active species that adsorb at W/O interface promoting emulsion formation and stabilisation by lowering the interfacial tension and/or by forming a protective layer at the droplets interface (Friberg *et al.*, 2003). Emulsifiers are divided into two main groups:

- i. *Surfactants*
- ii. *Pickering Particles.*

The main features of each group are reported below.

2.2.2.1. *Surfactants*

The word “surfactant”, a short term for “surface-active molecule”, is used to identify small amphiphilic molecules that migrate and concentrate at the interface between two physically distinct phases (Stauffer, 2005). In this case “small” refers to their low molecular weight. Examples of surfactants are phospholipids, monoglycerides, and sorbitan esters. Sometimes the word *emulsifier* is used to identify high molecular weight molecules, such as proteins and surface active biopolymers. In this thesis, the words “surfactant” and “emulsifiers” will be used synonymously. Surfactants are amphiphilic molecules, which mean that their molecular structure contains hydrophilic and

hydrophobic (lipophilic) moieties. The molecular structure of surfactants can be schematically represented as in Figure 2.6 with a hydrophilic head group and a hydrophobic tail having affinity for the aqueous and lipid phase, respectively.

Hydrophilic Hydrophobic

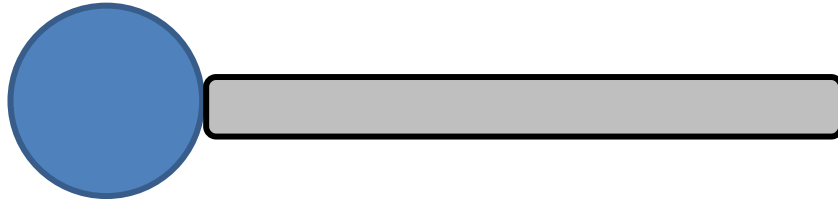


Figure 2.6: Highly schematic representation of a surfactant: the hydrophilic head is represented as a circle separated and the hydrophobic tail is depicted as a rod. More complex structures can be found in real systems.

Differences in the interfacial behaviour and the type of emulsion produced depend on surfactants structural properties. The head group can vary in terms of the size, chemical groups, and charge. With respect to the head charge, surfactants are identified as:

- *Non-ionic*: absence of net charge in the head group;
- *Ionic*: head bears net positive, *cationic*, or net negative charge, *anionic*;
- *Zwitterionic*: head contains both a positive and negative charge.

It is important to note that the environmental conditions (pH, ionic strength, blend of emulsifiers) can affect the hydrophilic behaviour. The hydrophobic portion can vary in terms of length and degree of unsaturation, presence of linear or aromatic chains, as well as in the number of the hydrophobic tails (Stauffer, 2005).

Prior to emulsification, surfactants are usually added to the phase in which they are most soluble in. When added in solution, surfactants exist as monomers at low concentration

and tend to self-assemble into thermodynamically stable structures at higher concentrations. These structures are generally referred to as *association colloids* and the type formed depends on surface-active species (geometry and inter-molecular interactions), temperature, and solvent (McClements, 2005). The self-association of surfactant molecules is due to the *hydrophobic effect*, a non-covalent force driving the system to minimise the number of unfavourable interactions between amphiphilic molecules and the bulk phase (McClements, 2005). In food emulsions the most common type of surfactant self-assembled structure is represented by *micelles* (McClements, 2005). Micelles are formed in aqueous media when surfactant concentration exceeds a certain level, defined as *Critical Micelle Concentration (CMC)* (Myers, 2002). Within a micelle, the hydrophobic surfactant tails will be packed close to each other to minimise contact with the aqueous phase and will expose the hydrophilic head. Below and above the CMC, molecules exist predominantly as monomers and organised in micelle, respectively.

As explained in Section 2.2.3., on emulsification the two immiscible liquids are mixed and the disperse phase is structured into droplets meanwhile surfactants move to the interface of the newly formed drops. The ability of emulsifiers to lower the interfacial tension between the two phases is associated with their ability of promoting emulsions formation. This property depends on concentration, kinetics of adsorption (time required to adsorb at the W/O interface), and the effectiveness of the interfacial tension reduction (McClements, 2005). Emulsion stabilisation is associated with the ability of surfactants to form a protective coating around the droplets, where steric interactions and/or surface charge prevent coalescence.

The ability of a surfactant to form a W/O or O/W emulsion is usually quantified by the so called *hydrophilic-lipophilic balance* (HLB). The HLB is a semiempirical method of classification and is calculated as the sum of the hydrophilic and hydrophobic groups on a molecule (Eq. 2.15) (Bergenståhl, 2008). This parameter provides an indication of surfactant's affinity for hydrophobic and hydrophilic phases which is quantified by doing an algebraic addition of the hydrophobic and hydrophilic groups:

$$\text{HLB} = 7 + \Sigma(\text{number hydrophilic groups}) - \Sigma(\text{number lipophilic groups}) \quad (\text{Eq. 2.11}).$$

Factor 7 in Equation 2.11 expresses equal affinity for lipid and aqueous and lipid phase. The counting of the hydrophilic and lipophilic groups is done starting from the chemical structure of the emulsifier.

Emulsifiers characterised by HLB values between 3 and 6 are mainly lipophilic and stabilise W/O emulsions. Surfactants with an HLB between 10 and 18 are hydrophilic and promote O/W emulsions. Emulsifiers with intermediate HLB values (6-8) are considered good wetting agents (McClements, 2005). The main advantage of this system is to provide a fast method to characterise the HLB of emulsifier blends. This classification system has also few drawbacks: (i) it does not take into account surfactant molecular weight; (ii) the influence of temperature is neglected; (iii) it does not provide any information for crystallising emulsifiers (monoglycerides) or zwitterionic molecules like phospholipids (Bergenståhl, 2008). Despite its limits, the HLB system is used to provide a prediction of type of emulsion formed.

2.2.2.2. *Pickering stabilisation*

The mechanism known as *Pickering stabilisation* refers to an emulsion where physical stability is achieved by colloidal solid particulate matter. Interfacially adsorbed particles

represent a *steric* barrier against destabilisation processes. The use of particles (in the nano- and micro- size range) to stabilise emulsions has significantly increased over the last decades due to the higher ability to provide stability against coalescence than surfactants (Binks and Clint, 2002).

The use of particles for the stabilisation of emulsions was first reported by Ramsden in 1903, but it was Pickering in 1907 who extensively studied their use as stabilising agents, hence the name of “Pickering stabilisation”. Today the expression “Pickering particles” is used to indicate any particulate material able to stabilise emulsions. With respect to the realm of food emulsions, the first example of Pickering particles is represented by tristearin fat crystals used to stabilise W/O emulsions (Lusassen-Reynders and van den Tempel, 1963). It is well known that to achieve stabilisation, particles have to adsorb at the liquid-liquid interface and form a dense protective layer (Pickering, 1907). The ability of particles to adsorb to liquid-liquid interfaces and provide stabilisation can occur if two conditions are met: (1) colloidal particles have to be much smaller than dispersed droplets, usually one order of magnitude (Dickinson, 2012); (2) particles have to be wetted by both phases (Levine *et al.*, 1989). This last concept is usually expressed in terms of *contact angle*. Assuming ideal spherical shape for the particles, *contact angle* (θ) is the angle formed by a particle at the interface as determined through the aqueous phase (Binks, 2002) (Fig. 2.7). The contact angle is a key parameter indicating the position of a particle at the oil-liquid interface and it is determined by its degree of hydrophobicity: values of $\theta < 90^\circ$ indicate it is predominantly hydrophilic and will promote O/W emulsions; hydrophobic particles have $\theta > 90^\circ$ and induce a curvature angle promoting W/O emulsions (Binks, 2002). The same concept is also expressed in terms of particles’ *wettability* mentioned above. Particles with a $\theta < 90^\circ$ and $> 90^\circ$ are preferably wetted by

the aqueous and lipid phase, respectively. Particles that are not wetted by one of the two phases (\ll or $\gg 90^\circ$) cannot be used to stabilise emulsions (Binks and Clint, 2002).

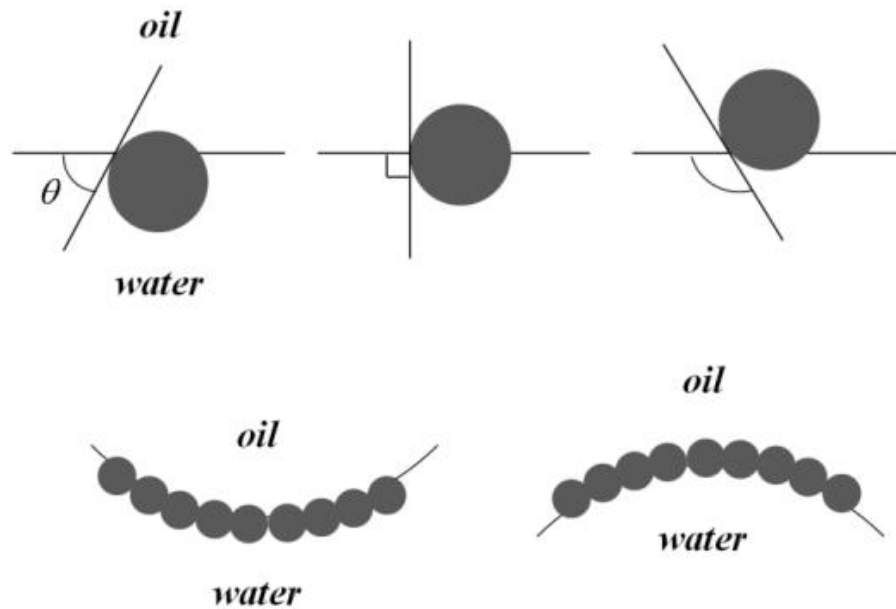


Figure 2.7: Schematic representation of the position of a particle at the interface according to its hydrophobicity. Image taken from Binks (2002).

The enhanced stability of Pickering stabilised emulsions results from the high energy required to displace particles from the interface. Assuming that the size of the particle is so small that we can neglect the effect of gravity, the energy (E) required to displace a spherical particle from the interface is quantitatively expressed by Equation 2.12 (Levine *et al.*, 1989):

$$E = \pi r^2 \gamma_{ow} (1 \pm \cos\theta)^2 \quad (\text{Eq. 2.12}),$$

where, r is the particle radius, γ_{ow} is the interfacial tension at the water-oil interface and θ is the contact angle. The maximum value of E is obtained for $\theta = 90^\circ$ (equal wetting by the two phases). The stability of Pickering emulsions also depends on packing density of

particles at the interface (Dickinson, 2012). For the objectives of this thesis, fat crystal stabilised emulsions are relevant and will be discussed in details in Section 2.3.

2.2.3. Emulsions formation

This section focuses on the main aspects regarding the production of a macroemulsion, which represent the system investigated within this study. The process of emulsion formation (*emulsification*) is generally called *homogenisation*, and *homogeniser* is the common term used to describe a mechanical emulsification device (McClements, 2005). Emulsion droplet size and size distribution depends on: (a) selected homogeniser; (b) surfactant (type and concentration); (c) volume fraction and type of the bulk phases (especially the viscosity ratio between the two) (Lee *et al.*, 2013). Emulsification is recognised to be a dynamic process; however, mechanistic models describing the overall phenomenon are often not available (Norton *et al.*, 2009). It is known that to produce a kinetically stable emulsion starting from two poorly miscible liquids, energy must be supplied to disrupt phases and the system must contain one (or more) emulsifiers, to lower the interfacial tension and prevent droplets merging, with the latter being the key role of a surfactant (Walstra, 1993). Emulsion formation can be schematically divided into a series of sub-processes occurring simultaneously: droplet deformation and break-up, surfactant adsorption to the newly formed interfaces, and droplets re-coalescence (Lee *et al.*, 2013). Mechanical homogenisers are conventionally divided into two broad categories: (i) systems where droplet formation starts from a coarse mixture (to increase efficiency); (ii) direct dispersion of droplets *via* micro-porous systems (Schubert and Engel, 2004). Here, the main features of the first type of emulsification devices (for simplicity “conventional homogenisers”) will be discussed as the mixers used in this study belong to that category. As reported by Walstra (1993), one key feature of

conventional homogenisers is that most of the supplied energy is dissipated into heat. High shear devices are example of conventional homogenisers and include rotor/stator mixer and high pressure valve homogenisers.

The flow profile occurring within a homogeniser affects the rate of droplet break-up and re-coalescence as well as surfactant adsorption to the naked interfaces, thus determining the final droplet size distribution of emulsions. Three main flow profiles that can be experienced within mixers are:

- 1) *Laminar flow*: it occurs at low rate and it is characterised by the parallel flow of the different layers of the fluid. Droplets are broken by shear and elongational forces (Stang *et al.*, 2001);
- 2) *Turbulent flow*: it occurs at medium-high flow rates and is characterised by an irregular flow pattern with the formation of vortexes (or eddies). Droplets break-up is determined by inertial forces (Stang *et al.*, 2001);
- 3) *Cavitation flow*: it is generated by the application of pressure variations which produces cavities. The implosion of the cavities produces shock waves responsible for droplets break-up.

It should be considered that within each category further classification exists. A more detailed explanation of the flow profiles together with the corresponding mechanisms of droplets formation can be found in the literature (Lee *et al.*, 2013; Windhab *et al.*, 2005; Lemenand *et al.*, 2013; Schubert and Engel, 2004).

It is clear now that energy must be supplied to the system to form an emulsion (microemulsions are an exception in this sense). The process of droplets deformation is opposed by the *Laplace pressure*. It has been already mentioned that droplets tend to assume a spherical shape to minimise the contact area (i.e. thermodynamically

unfavourable interactions) with the external phase. The interfacial force responsible for this behaviour is known as *Laplace pressure* (ΔP) (Eq. 2.13): it acts at the water-oil interface and is directed toward the centre of the droplet. For a spherical droplet, the Laplace pressure is mathematically expressed by:

$$\Delta P = \frac{2\gamma_{w/o}}{r}, \quad (\text{Eq. 2.13}),$$

where, $\gamma_{w/o}$ is the water-oil interfacial tension and r is the droplet radius. From Equation 2.11, the lower is $\gamma_{w/o}$, the smaller is the amount of energy needed to be supplied, which explains one of the role of surfactants. Furthermore, the smaller is r , the higher is the amount of energy necessary for droplet break-up to occur.

As mentioned above, the final emulsion droplet size results from the balance of two antagonistic processes occurring simultaneously: droplets formation and coalescence (Niknafs *et al.*, 2011). The main role of a surfactant is to limit as much as possible the back-reaction (i.e. re-coalescence) after emulsification (when an emulsion leaves the homogeniser, it is still in a high energetic state: droplets can collide with each other and potentially coalesce (Norton *et al.*, 2009)) and on storage. Therefore, type and concentration of emulsifier plays an important role on determining the final droplet size and droplets stability. Several mechanisms of emulsion destabilisations exist and are described in Section 2.2.4.

2.2.4. Emulsion physical instability

All emulsified systems (with the exception of microemulsions) will eventually breakdown into their bulk phases. The rate of emulsion destabilisation depends upon physical and chemical properties of both phases (viscosity, density, composition), interfacial characteristics (electric charge, thickness, surface load), and internal phase

properties (Φ and size distribution) (McClements, 2005). The mechanisms responsible for emulsion destabilisation are: flocculation, coalescence, gravitational separation, Ostwald ripening, and phase inversions. More than one mechanism can contribute to emulsion destabilisation at once. In Figure 2.8 a schematic of the instability mechanisms is shown and their main features are explained in the following sections.

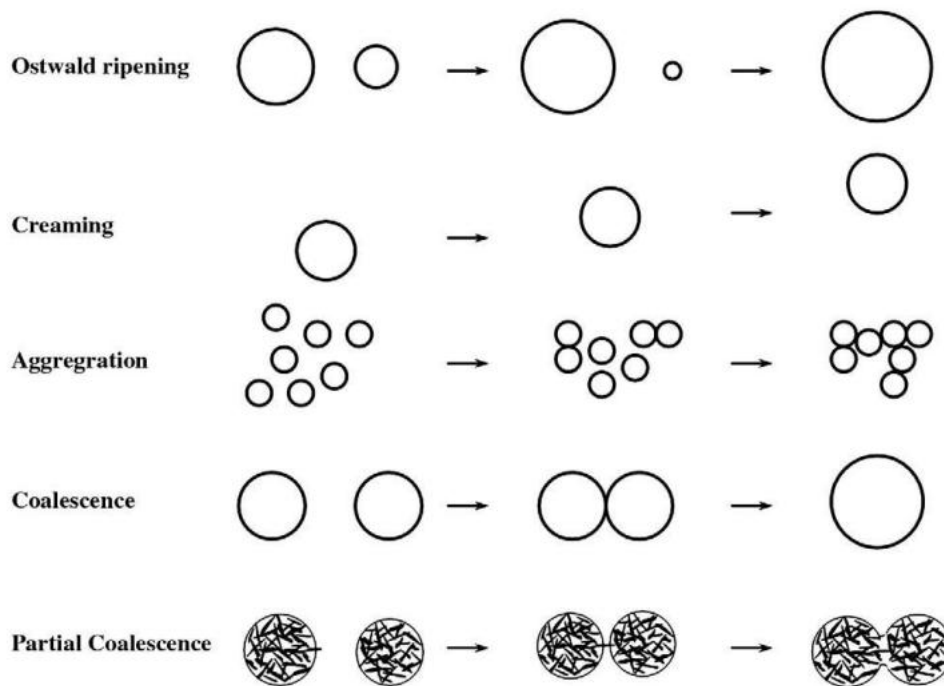


Figure 2.8: Representation of the destabilisation mechanisms occurring in emulsions. Image taken from Fredrick *et al.*, (2010).

2.2.4.1. Gravitational separation

Gravitational separation is a destabilising mechanism driven by the difference in densities between phases under gravitational force. Two types of droplet separation mechanisms exist: (i) *creaming*: is the movement upward of droplets having a lower density of the continuous phase; (ii) *sedimentation* droplets have higher density of the external phase (Robins, 2000). This mechanism is physically described by Stoke's law.

This law describes the constant velocity (v) of a rigid dispersed droplet moving vertically within a Newtonian medium (the force balance acting on the droplet is zero) (Hunter, 1986) and is given by:

$$v = \frac{2g r^2 (\rho_D - \rho_E)}{9\eta_E} \quad (\text{Eq. 2.14}),$$

where, g is the gravity acceleration (9.81 m/s^2), r is the radius, ρ_D and ρ_E is the density of dispersed and external phase, respectively, and η_E is the viscosity of the continuous phase. Since oils generally have lower densities than water, creaming and sedimentation occur in W/O and O/W emulsions, respectively. Gravitational separation is a reversible process causing a concentration of dispersed droplets, which retain their shape and size (McClements, 2005). If droplets are not adequately covered by emulsifier molecules, coalescence can occur more readily as droplets are in close proximity.

2.2.4.2. *Flocculation*

In absence of external forces, emulsified droplets move due to Brownian motion and density difference. They can collide with each other and aggregate to form flocs after a collision (McClements, 2005). Aggregation results from the combination of attractive (London and van der Waals) and repulsive (due to surfactant) forces and distance between particles (Rousseau, 2000). The aggregation mechanism and forces holding together the droplets have been examined in detail and shown to strongly depend on surfactant type and concentration, which in turn affects DLVO (Derjaguin, Landau, Verwey and Overbeek) and non-DLVO forces (Ivanov *et al.* 1998).

2.2.4.3. *Coalescence and partial coalescence*

Coalescence occurs when interfacial film rupture follows the collision of two droplets resulting in droplets merging and formation of a larger one (Ivanov *et al.*, 1998).

Coalescence is recognised to be the main mechanism of destabilisation in emulsions, as it leads to a decrease in contact area between phases, which is a thermodynamically favourable state (McClements, 2005). If the phenomenon continues, phase separation occurs. For this destabilisation phenomenon to occur a certain energy barrier must be overcome, which is represented by the repulsive forces between droplets, the resistance of the interface, and forces promoting droplet collisions (McClements, 2005; Robins, 2000). However, the physical mechanisms by which it occurs are not fully understood, and are rather case specific.

A special case of coalescence is the so called *partial coalescence*. This occurs in O/W emulsions where the internal phase contains fat crystals arranged to form a network within the *globule*. Partial coalescence, also known as *clumping*, is a complex phenomenon sharing some of the characteristics of coalescence and aggregation: globules mostly retain their original spherical shape (like in flocculation), but they share their internal material (like in coalescence). It can happen that some of the fat crystals protrude through the interface into the aqueous phase (Boode *et al.*, 1993). On globules collision, the fat crystals can pierce the interface of the other globule and become wetted by the oil. This is a favourable process and globule aggregation can continue until a network of partially coalesced droplets is formed (Fredrick *et al.*, 2010). If the solid crystalline networks within the droplets are able to counterbalance the capillary forces existing between partially coalesced globules, the system is said to be stable against coalescence (Boode and Walstra, 1993).

2.2.4.4. *Ostwald ripening*

The instability mechanism known as *Ostwald ripening* is characterised by the growth of large particles at the expense of small ones. This process involves the dissolution of small

particles, diffusive mass transport through the continuous medium toward large particles, and their growth (Kabalnov *et al.*, 1995). The same phenomenon can occur in emulsions where molecules within small droplets diffuse through the continuous phase toward the large droplets. It should be noted that Ostwald ripening can occur only if the material contained in the internal phase is partially soluble in the continuous phase. Given the low inter-solubility of water and medium-long chain triglycerides, Ostwald ripening is not of great relevance in most of food emulsions and will not be further discussed.

2.2.4.5. *Phase inversion*

The process named *phase inversion* (PI) is a phenomenon characterised by a change in the continuous phase, i.e. from W/O to O/W. It is recognised to be a very complex phenomenon sharing features of flocculation, partial and complete coalescence, and emulsification (Brooks and Richmond, 1998). PI is triggered by some processing and/or formulation conditions, such as variation in temperature, emulsifier type and concentration, and applied shear (McClements, 2005). *Surfactant* and *temperature* PI are the two main categories of PI processes described in the literature. Here only the *temperature induced PI* is considered as it can happen in O/W emulsions containing solid crystalline material within the droplets. This phenomenon starts with the partial-coalescence of globules (Section 2.2.4.3.). Under an externally applied shear, the globules can aggregate to form a continuous fat network entrapping the liquid water. This process is recognised to be fundamental in the manufacture of butter and margarine.

2.2.5. **Fat crystals stabilised emulsions**

The role of fat crystals on emulsion stability depends on the type of emulsion formed. For O/W emulsions the presence of fat crystals in the dispersed phase can be detrimental to the stability of the droplets (inducing ‘partial coalescence’ and/or PI). On the other hand,

fat crystals have been used for a long time as Pickering particles to stabilise W/O emulsions, with low-fat spreads being the most common examples. These emulsions are stable at temperatures below fat crystal melting point, but rapidly destabilise at temperatures above it. Destabilisation typically occurs on consumption in the mouth where the relatively high temperature induces crystals melting and the emulsion phase inverts to O/W releasing taste and flavour compounds (Norton *et al.*, 2006).

The remaining part of this section focuses on fat crystals stabilised W/O emulsion as this topic is relevant to the experimental results discussed in the thesis. It should be considered that emulsions characterised by the presence of fat crystals are three phase systems. Nevertheless, these are still classified as “emulsions” (i.e. liquid-liquid dispersions) since fat crystals are generally formed after the emulsion has been produced (van Boekel and Walstra, 1981).

Two mechanisms provide kinetic stability in W/O emulsions containing a partially crystalline continuous phase (Hodge and Rousseau, 2005; Gosh and Rousseau, 2011):

1. *Pickering stabilisation*: bulk formed fat crystals move to the interface, producing a layer of particulate matter encasing water droplets;
2. *Network stabilisation*: the development of a continuous fat network acts as a physical barrier limiting the mobility of dispersed water droplets.

Often the two mechanisms occur simultaneously, thus providing synergistic stability to emulsified systems. Although efforts have been made in elucidating the role played by each of them, there is still a lack of complete understanding.

The ability of fat crystals to provide effective Pickering stabilisation is determined by their interfacial behaviour and physical properties (Rousseau, 2000). The *interfacial*

behaviour refers to crystals wettability and the rheology of the formed interface (Section 2.2.2.2.). *Physical properties* refer to number, size, morphology, and polymorphism of fat crystals (Rousseau, 2000). The two aspects are strictly connected and often it is not possible to distinguish which factor has a major impact on stability. Nevertheless, the following discussion will try and examine some of these aspects separately.

Lucassen-Reynders and van den Tempel (1963) showed that it was possible to stabilise water-in-paraffin oil emulsions using glycerol tristearate crystals. However, it was shown that little amounts of water or oil soluble surfactant were necessary to reduce flocculation of the crystals. The decreased extent of flocculation allowed fat crystals to reach the interface and stabilise water droplets. Garti *et al.* (1998) also reported that a minimum concentration of emulsifier (PGPR) was necessary to improve Pickering stabilisation by tristearin crystals. The optimum PGPR to tristearin ratio in the lipid phase was 1 and this was attributed to the ability of PGPR to cover crystals and prevent aggregation. The effect of the polymorphic form on stability and the role of PGPR on polymorphic evolution were not clear from their study.

Fat crystals properties and ability to adhere to the interface are strongly affected by the presence, even at very low concentrations, of emulsifiers (Gosh and Rousseau, 2011). It has long been recognised that in absence of surfactant, fat crystals are non-polar particles and tend to attach to the water-oil interface from the lipid phase (Darling, 1982). The presence of polar surfactants added either to the aqueous or oil phase (lecithin, sorbitan esters, and sodium caseinate), increases the polarity of the crystals and, therefore, their interfacial activity. The effect of additives on the wetting of triglyceride crystals was investigated in detail using contact and interfacial tension measurements (Johansson and Bergensthåll, 1995a, b; Johansson *et al.*, 1995). β -form tristearin and β' -form palm

stearine were used to produce fat crystals (1%, wt%) in refined soybean oil. Contact angle measurements at the water-oil-fat crystal interface showed that β -form tristearin crystals were not surface-active (completely wetted by the oil) whereas β' palm stearine crystals had the tendency to adsorb to the W/O interface (i.e. more surface-active). Furthermore, α -form tristearin crystals were more surface-active than β type, whereas no difference was observed between α and β' form for palm stearine crystals. The authors hypothesised that the tighter packing of the β form may be responsible for the lower surface polarity of these crystals compared to the less dense α and β' crystals. It was also shown that hydrophobic emulsifiers (monoolein and lecithin) improved crystals wettability by the oil. This surface modification was expected to enhance stabilisation of W/O emulsions. Hydrophilic emulsifiers (saturated monoglycerides or phosphatidylcholine) decreased crystals wettability by the oil. Furthermore, emulsifiers adsorbed more tightly to the β' crystals than to the β ones, with the difference attributed again to a difference in the surface polarity.

With respect to *physical properties* of fat crystals, Lucassen-Reynders and van den Tempel (1963) showed that the number of glycerol tristearate crystals had to be 1000 times higher than the droplets. Garti *et al.* (1999) showed that to stabilise W/O emulsions with average diameter between 6 and 18 μm , α -crystals had to be submicron in size. Large crystals were unable to adsorb at the interface and flocculated in the bulk. The effect of *morphology* (shape and size) and *polymorphism* on fat crystals behaviour at the interface in real emulsified systems is still poorly understood (Rousseau, 2000). Sub-micron sized crystals are thought to provide a denser surface coverage than larger ones and improve stability (Rousseau, 2000). Processing conditions can be tailored to achieve

different morphologies. To the author's knowledge there is no work in the literature relating crystals shape and emulsions stability.

A scenario where crystallisation occurs directly at the interface following surfactant adsorption is also considered as Pickering stabilisation (Section 2.3.5.1.).

If fat crystals are at high concentration, they can aggregate to form a plastic dispersion within the continuous phase that prevents destabilisation. This mechanism is called *network stabilisation* and droplets are enclosed within a solid 3D structure. Hodge and Rousseau (2005) showed that if crystallisation had occurred following emulsification (*post-crystallisation regime*) surface-inactive crystals were small and able to form a network which was effective against destabilisation. On the contrary, if pre-formed fat crystals were added prior to emulsification (*pre-crystallisation regime*) they appeared large and unable to form such a network. The two mechanisms of stabilisation were directly compared by Gosh *et al.* (2011) in a model 20% (wt%) water-in-canola oil emulsions. Pickering and network stabilisation were achieved using glycerol monostearate (GMS) and hydrogenated canola oil (HCO), respectively. The authors showed that the minimum GMS concentration necessary to obtain stable Pickering emulsions was 4% (wt%). Using polarised light microscopy (PLM), droplets appeared to be surrounded by a bright ring, which was attributed to the presence of interfacial crystal shells. HCO was effective to provide network stabilisation only at concentrations above 10% (wt%). At this concentration of the network forming agent samples did not flow. Emulsions visualisation *via* PLM revealed the existence of spherulitic shaped crystals dispersed in the bulk phase and at the droplets interface. This result showed that non-polar crystals could also be adsorbed at the interface in presence of a liquid emulsifier as glycerol monooleate. Confirming the results obtained by Johansson and Bergensthå

(1995a, b), these authors showed that surfactant can adsorb onto the surface of the crystals and increase their surface activity. Pickering stabilised emulsions were more stable than network stabilised ones in term of sedimentation, but no difference in average droplet size were observed. The combination of the two stabilising approaches did not produce any significant improvement in stability.

2.2.5.1. *Pickering stabilisation via interfacial crystallisation*

The above explanation of Pickering stabilisation assumes that particles are formed in the bulk and brought to the interface during emulsification. Another possibility is represented by the formation of solid particles directly at the interface. Rousseau (2013) has recently attempted to establish a classification for mechanisms involved in fat crystals Pickering stabilised W/O emulsions. The author identified three categories:

1. *Type I*: direct interfacial crystallisation;
2. *Type II*: interfacial adsorption of nano or micro particles at the interface;
3. *Type III*: solid crystalline interface much thicker than droplet dimension.

Type II corresponds to a normal Pickering stabilisation as described above. Type III will not be discussed here as it was only observed by the author under specific conditions (Gosh and Rousseau, 2012). Type I is characterised by the formation of solid crystalline interfaces around water droplets, which appear as white bright rings if visualised using PLM (Gosh and Rousseau, 2011). Solid interfaces are the result of an *interfacial crystallisation* phenomenon. The development of a crystalline layer at the O/W interface was first observed by Krog and Larsson (1992). The authors investigated the effect of different types and concentrations of monoglycerides on the interfacial tension profile. In their model study, the decrease in the interfacial tension following a decrease in

temperature was associated with the formation of *surface-active crystals* directly at O/W interface visible to the naked eye.

It should be noted that the physical state of the interface represents a key difference between surfactant (and also particle) stabilised emulsions and systems where interfacial crystallisation has occurred: the former have a liquid interfacial layer, the latter are characterised by a solid interface. The interfacial thickness for these emulsions is believed to be in the range of nm or μm range for single or multilayered structures, respectively (Rousseau, 2013). Nevertheless, the interfacial thickness has never been measured.

The process of interfacial crystallisation must involve a nucleation and crystal growth step as for any other liquid-solid thermal phase transition. While for O/W emulsions *surface heterogeneous nucleation* has been proved to occur *via* solid-state *interfacial templating* (Ueno *et al.*, 2003; Arima *et al.*, 2007, 2009), in the case of W/O emulsions the mechanisms involved are not well understood although they must hold some similarities. The latest advancements regarding the phenomenon of crystallisation at the oil-water interfaces have been recently reviewed (Douaire *et al.*, 2014). Crystal nuclei (small solid molecular clusters) of the bulk lipid phase can be formed in the vicinity/at the interface as a result of the local ordering provided by the surfactants adsorbed at the interface (*templating effect*). The interfacial molecular arrangement (i.e. the *template*) lowers the nucleation activation energy (*interfacial heterogeneous nucleation*) increasing the rate of nucleation. For this phenomenon to occur, a certain structural similarity between surfactants and bulk TAGs must exist (Douaire *et al.*, 2014). As mentioned above, the impact of interfacial nucleation on the crystallisation behaviour in O/W emulsions has been investigated in several model systems. Ueno *et al.* (2003) reported the

formation of a pseudo-hexagonal crystal form resulting from the interaction between n-alkane and additive molecules solidified at the interface. This polymorphic form was not observed in bulk phase with and without the high melting point additives and in O/W emulsions without the additives. In those systems the triclinic form was predominant. Furthermore, it was observed that the nucleation rate of the pseudo-hexagonal form was faster than triclinic. The authors concluded that the solid *template film* formed by the additive molecules drives the nucleation into the new arrangement by a mechanism of *interfacial heterogeneous nucleation*. Arima *et al.* (2007) showed that the addition of hydrophobic and hydrophilic sucrose oligoesters delayed the destabilisation of semisolid O/W emulsions resulting from the formation of palm-mid-fraction crystals protruding through the interface. The authors showed that the hydrophobic additives enhanced interfacial crystallisation to form tiny crystals. In a later study, it was shown that the same hydrophobic sucrose palmitic oligoester promoted the formation of fat crystals with lamellar planes parallel to the O/W interface again *via an interfacial nucleation mechanism* (Arima *et al.*, 2009). A similar phenomenon was observed for palm-mid-fraction O/W emulsions using different polyglycerol fatty acid esters (Sakamoto *et al.*, 2004). The authors observed an increase in the crystallisation temperature with increasing emulsifier concentration, degree of esterification, and chain length of the fatty acid molecules. This result was attributed to interfacial freezing of fatty acid chains inducing heterogeneous nucleation. It appears clear that the process of interfacial nucleation has been investigated in detail for a range of emulsifier-oil-water combinations but much less is known for W/O emulsions. However, independently from the emulsion type, it is intuitive that the presence and type of emulsifier plays a critical role on the interfacial crystallisation process. For W/O emulsions, it is generally accepted that direct *interfacial*

crystallisation is promoted by oil soluble surfactants also considering that TAGs have very little surface-activity, therefore, their location at the interface is unlikely (Rousseau, 2013). The formation of solid sintered interfaces has been reported to occur when using surface active species with a high melting point such as saturated monoglycerides (Frash-Melnik *et al.*, 2010; Gosh *et al.*, 2011; Nadin *et al.*, 2014). The amphiphilic molecules can tightly pack at the interface and crystallise on cooling during and after emulsification. When using unsaturated monoglycerides (liquid at ~ 25 °C), interfacial crystallisation has also been observed (Gosh and Rousseau, 2012). Rousseau (2013) has proposed a four step mechanism to explain the interfacial crystallisation process for water-in-high melting oils emulsions stabilised by liquid monomeric surfactants (provided the existence of complementarity between monoglyceride and TAGs acyl moieties at the interface): (a) adsorption of surface active molecules at the W/O interface; (b) local alignment of bulk lipid and surfactant acyl chains; (c) occurrence of surface heterogeneous nucleation characterised by the development of crystal nuclei made up of TAGs bonded to the interface; (d) interfacial crystal growth until obtaining droplet surface coverage. For liquid polymeric emulsifiers such as PGPR, Rousseau (2013) predicted that interfacial crystallisation cannot occur due to the little compatibility between bulk lipid and emulsifier acyl chain. For these systems *heterogeneous nucleation* is believed to occur in the bulk fat phase. In absence of emulsifiers, no interfacial crystallisation is expected to occur given the molecular incompatibility between water and lipid molecules. Nevertheless, Johansson and Bergenståhl (1995b) using contact angle measurements concluded that fat crystals will always tend to adsorb to the W/O interface, even without emulsifiers. This result may imply that Pickering stabilisation (Type II) can still occur

provided that there are enough fat crystals of the correct size and shape to stabilise the droplets.

2.2.5.2. *Water-in-cocoa butter emulsions*

Water-in-cocoa butter emulsions are oil continuous systems where the external phase exhibits crystallising behaviour on cooling. These systems were initially developed by Norton *et al.* (2009). The authors showed that a bench scale margarine line (a device consisting of two mixers in series: a scraped surface heat exchanger and a pin stirrer; see Section 3.2.1.) could be used to produce emulsions containing up to 60% water. Furthermore, processing conditions could be manipulated to obtain different microstructural properties. In a later publication it was shown that at one processing temperature, the rotation speed of the units did not affect the melting behaviour of the emulsions whilst the $d_{3,2}$ decreased at increasing rotor rates of both mixers (Norton and Fryer, 2012). Results of microstructure visualisation using cryo-SEM were in agreement with previous findings (Norton *et al.*, 2009) and confirmed the existence of a crystalline “shell” around water droplets and a bulk network. Water-in-cocoa butter emulsions can therefore be ascribed to the group of fat-crystal stabilised emulsions where both Pickering and network stabilisation occur. Although crystal polymorphic form was shown to depend on the thermal profile within the SSHE, with the PS maintaining or melting the crystals depending on its jacket temperature, the possibility to temper CB on emulsification was mentioned but not investigated in detail. The authors concluded that throughput, applied shear, and PGPR concentration are the main parameters determining the final droplet size.

The role played by formulation on the microstructure and mechanical behaviour of water-in-cocoa butter emulsions was studied recently (Sullo *et al.*, 2014). The authors showed

that, for a given velocity gradient, the final droplet size and CB polymorphism depends on the gelation rate of the hydrocolloid in the aqueous phase, dispersed phase fraction as well as on the emulsifier blend. The authors described that at increasing *k*-carrageenan concentration, gelation occurs faster and even prior to starting emulsification. The viscosity increase of the dispersed phase affects the viscosity ratio between phases (viscosity dispersed phase η_D / viscosity continuous phase η_C) and results in reduced droplets break-up (at that velocity gradient). This effect was particularly evident at low dispersed phase volume fraction (Φ) while for Φ equal to 60% the increase in viscosity of the emulsion partially compensated for η_D increase. A PGPR at concentration of 1% was the most effective in droplets formation and stabilisation. Formulation was found to affect emulsions thermal behaviour. At *k*-carrageenan concentration $\geq 1.5\%$, the presence of rigid-gelled droplets within the SSHE was thought to be responsible for the inability to temper CB.

2.3. Conclusions and outlook

The objective of this chapter was to review the literature directly relevant to the work presented in this thesis and to identify areas of investigation. The obtained results aim to contribute to the current understanding in the field of water-in-oil emulsions.

It has been discussed above that various processing and formulation routes have been investigated for water-in-cocoa butter emulsions production. Nevertheless, the effect of each mixer of the margarine line on the droplet size of emulsions and CB polymorphism remains unclear. Furthermore, the role of CB fat crystals on emulsions formation and stabilisation has not been considered. These aspects have been investigated in this thesis and results are referred in Chapter 4. Water-in-cocoa butter emulsions are characterised by a solid-like structure due to cocoa butter crystallisation. The large deformation

behaviour of bulk CB and emulsions has been investigated to evaluate the impact of water droplets on the mechanical properties of the systems and gain an understanding of their structural properties. Results of this investigation are discussed in Chapter 5.

Finally, although CB phase transition has been widely studied in the literature, its crystallisation behaviour when existing as the continuous phase of a water-in-oil emulsion has not been investigated. The effect of the presence of water droplets on CB crystallisation has been studied in this thesis and results discussed in Chapter 6.

Chapter 3. Materials and Methods

3.1. Introduction

In this chapter the materials and the methods used to produce and characterise water-in-cocoa butter emulsions are presented. The chapter has been conveniently divided into two parts. In the first a description of the ingredients used to formulate emulsions is provided. The second part describes the methodology followed through the thesis for the characterisation of samples. The expression “CB systems” will be used where no further specification is required to indicate the samples produced (either bulk crystallised CB or emulsions). The technical description of the device used for emulsification-crystallisation is provided in Section 3.2.1. The analytical techniques, the instrumentations and the experimental settings used are also carefully described. Detailed information on the method developed for measure SFC in emulsions is included.

3.2. Materials

3.2.1. Lipid phase

The lipid phase used in this study was obtained by blending the appropriate amount of cocoa butter with polyglycerol polyricinoleate (PGPR). Both ingredients were of standard food grade and provided by Cargill (Vilvoorde, Belgium). No further purification was performed prior to use. In all the emulsions the lipid phase represents the external phase.

3.2.1.1. Cocoa butter

Cocoa butter (CB) from West Africa is the crystallising fat used in this thesis. Prior to any operation (mixing with emulsifiers, emulsification), CB was completely melted. Details on CB crystallisation and polymorphic behaviour can be found in Section 2.2.

3.2.1.2. *Polyglycerol Polyricinoleate*

Polyglycerol polyricinoleate (PGPR) is a synthetic emulsifier produced by an esterification reaction of condensed castor oil fatty acids with polyglycerols (polymerised glycerol molecules (Wilson *et al.*, 1998)). PGPR is a polymeric lipo-soluble non-ionic surfactant promoting the formation of stable oil continuous emulsions (HLB ~1.5 – 3.0) (Gunes *et al.*, 2010). Its molecular weight is represented by a broad distribution with a maximum at 500 g/mol (Gunes *et al.*, 2010). The ability of PGPR to sterically stabilise the interface in W/O emulsions is attributed to the water binding capacity of its chains (Garti *et al.*, 1998; Marquez *et al.*, 2010).

3.2.2. **Aqueous Phase**

In order to evaluate emulsion fat continuity using conductivity measurements, the aqueous phase was prepared by dissolving analytical grade sodium chloride (NaCl, Fisher Scientific, UK) in double distilled water (Aquatron, A4000D) to a final concentration of 0.02 M. After salt addition, the aqueous phase conductivity was approximately 1.0 mS/cm, i.e., a thousand times higher than the double distilled water. In all formulations referred in the thesis, dispersed phase concentration is expressed as mass percentage (Φ_m , %).

3.3. **Methods**

3.3.1. **Margarine line**

A bench scale margarine line was used to produce emulsions. It is a continuous emulsifying device consisting of two mixers in series: a scraped surface heat exchanger (SSHE) followed by a pin stirrer (PS). Both stainless steel mixers have a jacket in their stator within which a fluid can be circulated to control temperature on processing. In this

study water was used as fluid for heat exchange. The advantage of the margarine line is that it is a continuous emulsifying device and offers great flexibility in terms of processing combinations.

The SSHE consists of a rotating shaft with two blades mounted on and a stator with a processing volume of approximately 25 mL. On mixing the blades are forced by the centrifugal force to come into contact with the internal wall of the vessel and “scrape off” the surface any material that has crystallised on it. An image (a) and a schematic representation (b) of the SSHE are provided in Figure 3.1.

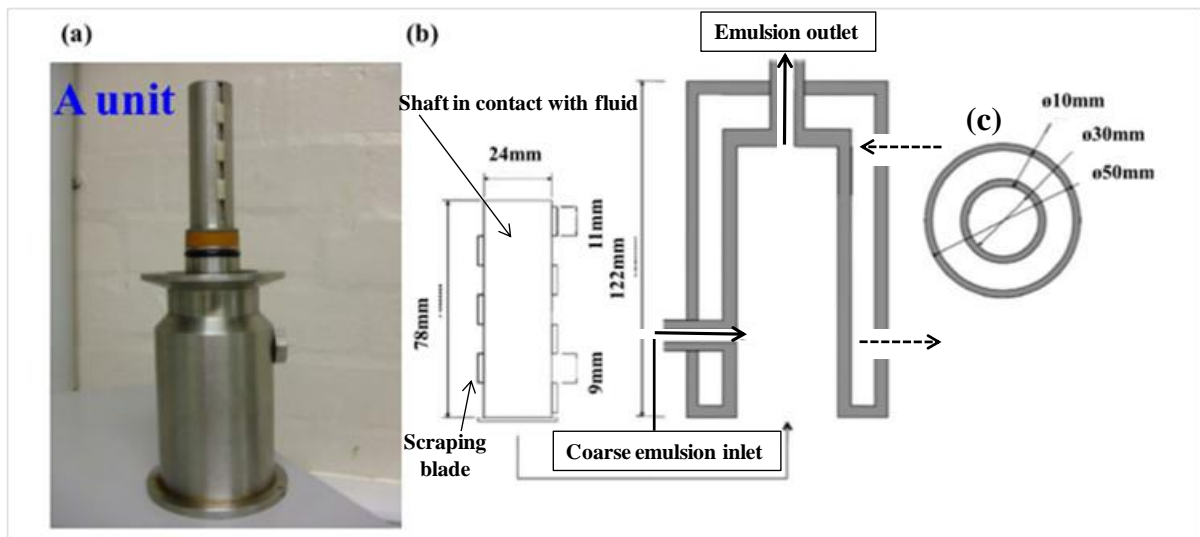


Figure 3.1: (a) Image of the SSHE shaft with the blades mounted on it. (b) Schematic design of the shaft, blades and jacket of the SSHE containing the dimensions of the elements. Full and dashed arrows represent flow of the emulsion and jacket water, respectively. (c) Dimensions of the SSHE in a cross section: $\phi 50\text{mm}$ is the cross section diameter; $\phi 30\text{mm}$ is the diameter of the inner cavity where emulsification occurs; $\phi 10\text{mm}$ is the gap distance between the internal and external jacket walls. Illustration modified from Norton and Fryer, 2012.

The PS also consists of a shaft with sixteen metal pins mounted on it and a stator with two series of 8 pins mounted on the internal wall of the stator. The processing volume is approximately 160 mL.

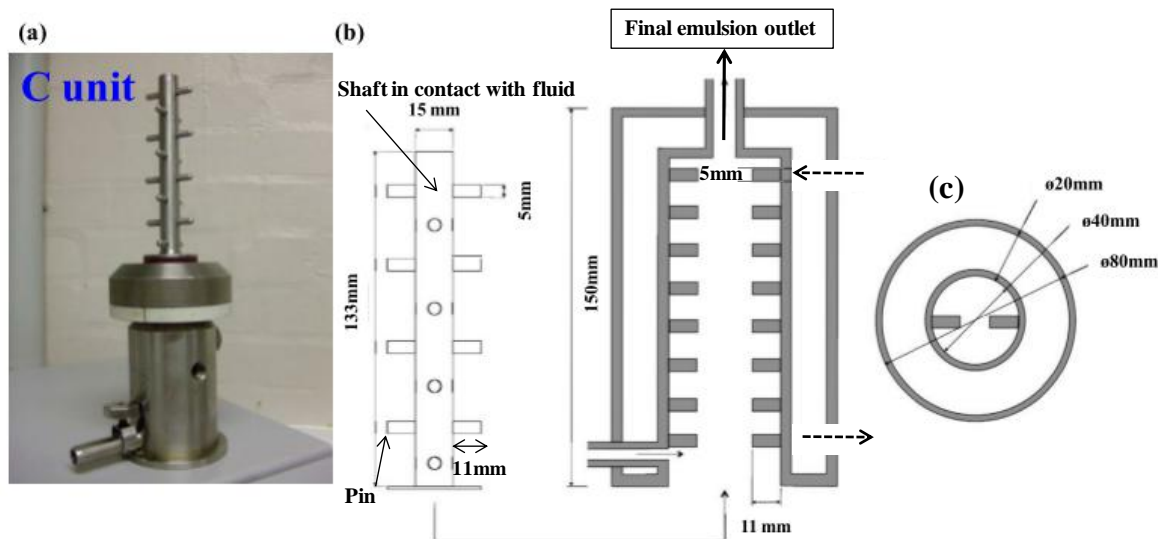


Figure 3.2: (a) Image of the PS shaft showing the pins. (b) Schematic design of the shaft, blades and jacket of the SSHE containing the dimensions of the elements. Full and dashed arrows represent flow of the emulsion and jacket water, respectively. (c) Dimensions of the PS in a cross section: $\phi 80\text{mm}$ is the cross section diameter; $\phi 40\text{mm}$ is the diameter of the inner cavity where emulsification occurs; $\phi 20\text{mm}$ is the gap distance between the internal and external jacket walls. Illustration modified from Norton and Fryer, 2012.

For the stirrers of both mixers nine levels of rotor rate could be selected. Rotational speed and corresponding tip speed values have been compiled in Table 3.1. In Figure 3.3 and 3.4 a schematic visualisation and a picture of the set up used are shown.

Table 3.1: Rotor level and corresponding rotor rate and tips speed for SSHE and PS. In bold there are the combinations used. Values of rotor rate have been measured using a rotation-speed laser sensor (Compact instrument, UK).

Rotor level	SSHE		PS	
	Rotor rate (rpm)	Tip Speed (m s ⁻¹)	Rotor rate (rpm)	Tip Speed (m s ⁻¹)
1	170	2.6	170	2.3
2	324	5.1	330	4.3
3	490	7.7	500	6.5
4	640	10.0	650	8.6
5	790	12.3	800	10.5
6	930	14.5	920	12.1
7	1090	17.0	1040	13.6
8	1250	19.5	1170	15.3
9	1315	20.5	1345	17.6

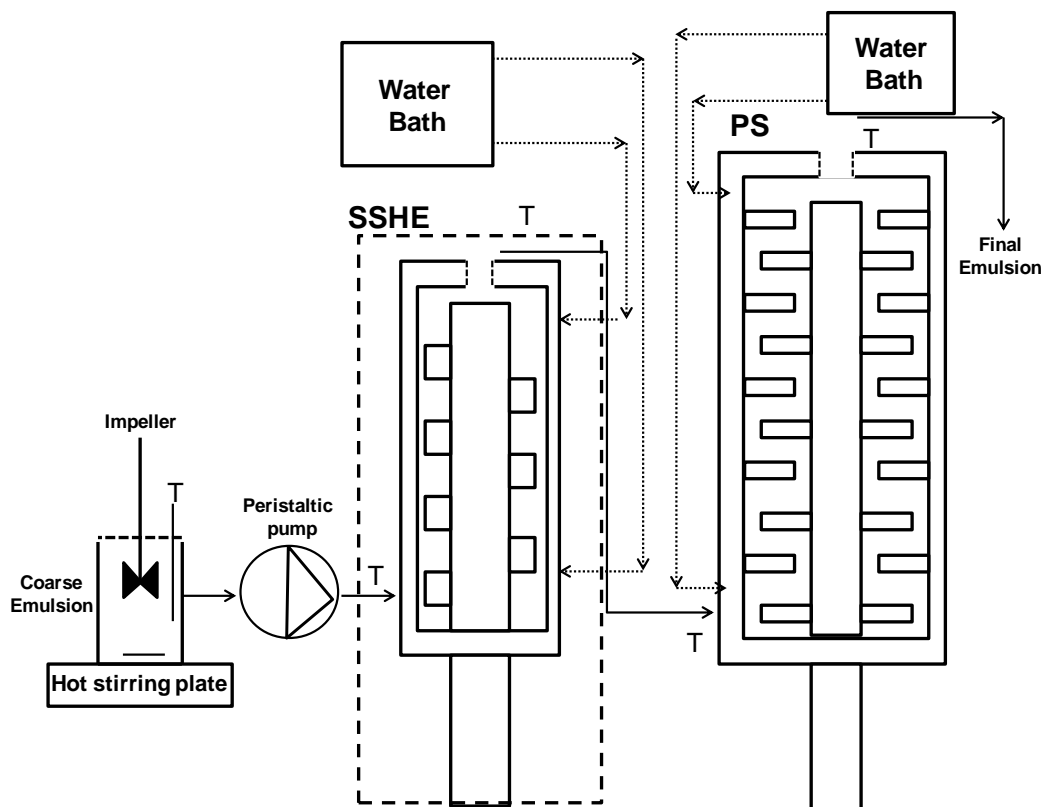


Figure 3.3: Schematic representation of the processing set up. The continuous arrows represent the flow of the emulsions, the dashed arrows the flow of the water into the jackets to control temperature and the “T” represents points where the temperature was monitored. The dashed box around the SSHE indicates a process based on the use of this mixer only. Schematic is not in scale.

3.3.1.1. Coarse emulsions preparation

For each formulation, a coarse emulsion batch of 400 g was prepared. To allow emulsification and evaluate the effect of processing on CB crystallisation, fat was completely melted prior to emulsification. Any form of nuclei remaining in a melting fat is usually considered as *crystal memory* as this would determine the behaviour on further crystallisation. The procedures referred in the literature to erase crystalline memory in CB vary greatly between authors. A 15 minutes isothermal step at 65 °C was found to be enough to erase crystal memory in CB (Foubert *at al.*, 2003). Here, CB was initially heated to 65 °C (± 5.0 °C) for two hours in a glass vessel using a hotplate stirrer (Hotplate Stirrers, Stuart, UK) and then added to PGPR (1%, wt% overall). The

temperature of the lipid phase was then lowered to 50 °C (± 1.0 °C) while continuously stirring with a magnetic bar ensuring temperature homogeneity through the volumes. The aqueous phase at 55 °C (± 1.0 °C) was slowly added to lipid phase and blended in using an overhead stirrer (IKA[®] RW 11, Sigma-Aldrich, UK). Emulsification was started when the coarse emulsions appeared homogeneous. To prevent water evaporation, the surface of the glass vessel was covered with aluminium foil lid. It is implied here that if emulsification was not carried out and mixing was stopped, the coarse emulsion would phase separate into the two bulk phases within few minutes.

3.3.1.2. *Tempering-emulsification process: theory and set-up*

To produce stable water-in-cocoa butter emulsions where the CB has also been tempered, the shear-temperature profile used has to mimic the chocolate tempering process. The term *tempering* is used in chocolate manufacture to indicate a shear-temperature profile by which the chocolate is crystallised in the desired form V (β_2 -3). Following typical tempering procedures referred in literature (Loisel *et al.*, 1997; Talbot, 2009), the adopted protocol consisted of four steps: (1) melting of the lipid phase for coarse emulsion preparation (~ 50 °C); (2) cooling of the coarse emulsion prior to emulsification to 40 °C; (3) emulsification and cooling to ~ 26 °C; (4) re-heating to ~ 33 °C to erase unstable fat crystals while mixing. The processing set-up described here was established after carrying out preliminary experiments and allowed to obtain the desired temperature profile. Each unit was connected to an external water bath (Julabo, UK) and for temperature control water was circulated in a counter current mode within the mixers jackets. The jacket temperature was set at 25 °C and 35 °C for the SSHE and PS, respectively. The distance between the feeding vessel and the SSHE inlet was approximately 1 m whereas the SSHE outlet and PS inlet were at approximately 20 cm.

All connections were made using silicon tubes with 3.2 mm inner diameter and thick wall. A peristaltic pump (Masterflex Pump, Cole-Parmer, UK) was used with the flow rate set at 30 mL/min, which resulted in a measured residence time of 56 s (± 2 s) and 320 s (± 5 s) within the SSHE and PS, respectively. The average residence time was determined visually (observing the fluid entering and leaving the mixers) and measured using a stopwatch. It represents the average time for the fluid to be pumped through each mixer. The temperature was monitored at the inlet and outlet of both mixers using a digital data logger (Omega, UK) fitted with K-type thermocouples ($\pm 0.1\%$ accuracy) positioned in the centre of the pipes using T-junctions. The described set-up ensured that coarse emulsion temperature at the SSHE inlet was above CB clear point (40.0 ± 0.5 °C). A rapid temperature decrease occurred in the SSHE under shear (from 40.0 to 26.0 °C ± 0.5 °C) followed by mixing and re-heating (from 26.0 to 33.0 °C ± 0.5 °C) within the pin stirrer (PS). It should be noted the temperature at the SSHE outlet and PS inlet was the same. On using this processing set-up the aqueous phase would be mechanically dispersed into droplets and CB crystallisation would occur simultaneously (more details in Section 4.2.1). Of nine levels of rotor rate available for both mixers, four values were selected (1, 3, 6, and 9, in bold in Table 3.1). Of the sixteen shearing combinations, twelve were investigated in detail (results in Chapter 4). Samples of the final emulsions were collected for droplet size analysis in 40 mL storage vessels and immediately transferred into a cooling unit at 5 °C.

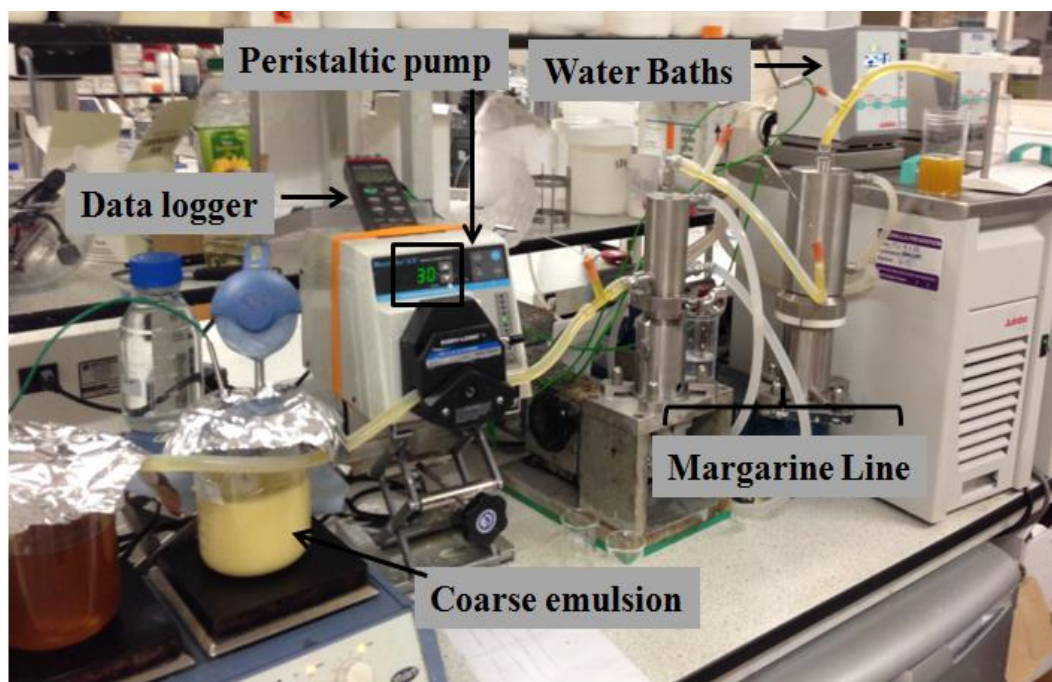


Figure 3.4: Processing set-up adopted on emulsification. See text for details.

3.3.2. Nuclear Magnetic Resonance

Nuclear Magnetic Resonance (NMR) belongs to the category of absorption spectroscopy techniques. It is a powerful, non-destructive technique where an oscillating radio-frequency is used to excite the nucleus of atoms of a sample immersed in a magnetic field and the relaxation monitored. In this thesis, low resolution NMR (magnetic field ~ 0.5 Tesla) was used to study cocoa butter systems, therefore, this technique will be discussed in detail.

3.3.2.1. Theory of low field pulsed NMR (pNMR)

The sensitive element in NMR studies is represented by nuclei characterised by a magnetic property called *spin* (I). I depends on the ratio between the number of protons and neutrons in a nucleus and can assume different values (Lens and Hemminga, 1998). The spin implies a rotation of the nucleus about its axis which produces a small *nuclear magnetic dipole moment* (μ) (Hemminga, 1992); μ produces a little magnetic field which

can interact with other magnetic fields (produced by other nuclei and/or an externally applied field). The NMR spectrometer used in this study is sensitive to the nucleus of hydrogen (^1H), which is characterised by a value of I of $1/2$. In absence of an external magnetic field, nuclei are oriented in all possible directions. However, in response to an externally applied magnetic field (B_0), they can assume only two different orientations: parallel (lower energy and favourable, $+0.5$) and anti-parallel (higher energy, -0.5). At a given temperature (thermal equilibrium), the number of nuclei aligned parallel is slightly larger than those aligned anti-parallel to the field and the phenomenon can be described by a Boltzmann distribution. The distribution depends on the strength of the magnetic field (B_0), therefore, the higher is B_0 the larger is the difference between the two states. The excess of nuclei aligned parallel to B_0 produces the so called *bulk magnetisation vector* (M_0). In Figure 3.5a the external magnetic field is depicted in the z direction and this component of *bulk magnetisation vector* is denoted as M_z . Here M_z is depicted for simplicity as static and parallel to it but in reality it is precessing (rotating) about z . The precession about the z axis occurs at a certain frequency known as *Larmor frequency* (ω_0) which depends on B_0 magnitude.

Being a spectroscopic technique, excitement occurs *via irradiation*. Here a sample is irradiated by a radio frequency (RF) electromagnetic wave. In most spectrometers irradiation is performed using pulses (or waves) of defined energy and time length (typically few μs) in the direction perpendicular to B_0 . To excite ^1H nuclei, the so called *resonance condition* must be fulfilled. This condition is expressed by:

$$\omega = \gamma H_{tot} \quad (\text{Eq. 3.1}),$$

where, ω is the angular momentum of the applied RF pulse, with $\omega = \omega_0$. γ is a constant characteristic for each nucleus known as the *gyromagnetic ratio*, and H_{tot} is total magnetic field felt by the nuclei, which has to be matched (van Putte and van den Ended, 1975).

The simplest experiment is known as *Free Induction Decay* (FID) where the applied RF pulse imposes phase coherence to the nuclei (they are forced to precess at the same frequency) and rotates the M_z in the x - y plane (this is also known as 90° pulse as M_z is rotated of 90°). In most spectrometers, the receiver coil (the element sensitive to the ^1H excitation) is situated in the x - y plane; therefore, the signal is maximum after the rotation has occurred. However, as the ^1H nuclei tend to lose phase coherence on the x - y plane and realign back to the original position, a signal decrease over time occurs (here the name FID). The low field NMR is also called *Time Domain NMR* which is due to the key feature of the technique: excitation of the sample and monitoring of the relaxation process over time. The signal decays over time in an exponential fashion and this phenomenon is defined as *relaxation*. Two types of relaxation mechanisms exist both of which with characteristic time constants. The first mechanism is called *spin-spin or transverse relaxation* and it characterises the loss of phase coherence in the x - y plane. This phenomenon results from inhomogeneities in the external magnetic field and by distance and mobility of nuclei (as these produce little magnetic fluctuations). The time constant characterising this relaxation process is indicated with the symbol T_2 and represents the time within which 63% of the phase coherence has been lost. T_2 value increase with increasing molecular mobility; therefore, liquids have a larger relaxation time than solids. This property is exploited to determine the SFC in crystallising fats (see below). The second relaxation mechanism is the *spin-lattice or longitudinal relaxation* characterised by the time constant T_1 which refers to time required for M_0 to return to the thermal

equilibrium position (parallel to z , i.e. M_z). Measurements performed using low-resolution NMR consist of sequences of pulses where the magnetisation vector is rotated of a defined angle and the signal produced on relaxation.

3.3.2.2. Bruker Minispec Spectrometer

A bench-top Bruker minispec spectrometer (mq series, Bruker, Germany) operating at B_0 of 0.47 T (Larmor frequency ~ 20 MHz) was used to perform the NMR experiments. The optimum magnet temperature is $40\text{ }^\circ\text{C}$ ($\pm 0.1\text{ }^\circ\text{C}$). The probe-head used was suitable for glass tubes having a 10 mm internal diameter, ~ 0.9 mm wall thickness, flat bottom, and height of 150 mm. The RF coil is 1 cm in length according to manufacturer's specifications and the temperature of the probe-head is controlled by water flowing within an externally built jacket. Prior to any experiment, digital thermometer (accuracy $\pm 0.1\text{ }^\circ\text{C}$) was used to ensure the temperature inside the measuring cell was at the desired value. The pulsed field gradients used for droplet size measurements (as explained below) had strength of 2 T/m.

In any pulsed experiment three parts can be identified: (1) *pulse width* (PW); (2) *acquisition time* (AQ); (3) *recycle delay* (RD). In the minispec software the whole sequence is termed *Relaxation time* (or *delay*) (RT) defined by Equation 3.2:

$$\text{RT} = \text{PW} + \text{AQ} + \text{RD} \quad (\text{Eq. 3.2}).$$

The *pulse width* refers to the length of time the RF irradiation is switched on for the excitement and the time length is expressed in ' μs '. The *acquisition time* (AQ) is the time within which the relaxation of the excited nuclei is recorded for quantitative analysis. It is usually a few milliseconds long. The *recycle delay* (RD) is the time prior to the next pulse sequence; it is necessary to allow that all nuclei have relaxed back to the original state. This last step is usually the longest (seconds).

In this thesis, the Bruker “water droplet size” application was used to characterise emulsion droplet size while for SFC measurements the original pulse sequence was modified (details in Section 3.2.2.4.).

3.3.2.3. *Droplet size measurement*

The determination of the droplet size is based on the principle of restricted diffusion of the proton carrying molecules within an enclosed volume, i.e. the droplet. In its simplest explanation, the size of the droplets is determined by tracking the protons movement within the boundary of the droplets (van Duynhoven *et al.*, 2007). The pulse sequence is generally known as “Pulsed Field Gradient (PFG) Spin-Echo Experiment” (Packer and Rees, 1972). This is a modification of the sequence called “Hahn Spin-Echo Experiment”.

A *Hahn Spin-Echo Experiment* is performed by applying two consecutive pulses spaced by a defined time τ and by measuring the relaxation (*spin-echo*) of the hydrogen nuclei as they return to the original position (Fig. 3.4). The first pulse is a 90° pulse which rotates the bulk magnetisation vector from the z axis (M_z) in the x - y plane (to simplify it will be considered that M is on the y -axis, M_y , Fig. 3.5a). The first RF-pulse is identical to a FID experiment as explained above: proton will tend to de-phase and this is denoted as “fan-out” (Fig. 3.5b). After a time τ , a second RF-pulse (180°) is applied which reverses the “fan” (simply the “group” of nuclei is rotated with respect to the x -axis) (Fig. 3.5c). With time the nuclei continue moving and to re-phase (movement called “fan-in”) in the y -axis (Fig. 3.5d). The maximum echo-signal is recorded by the RF coil after 2τ (Fig. 3.5e). Nuclei continue to move and fan-out again (Fig. 3.5f).

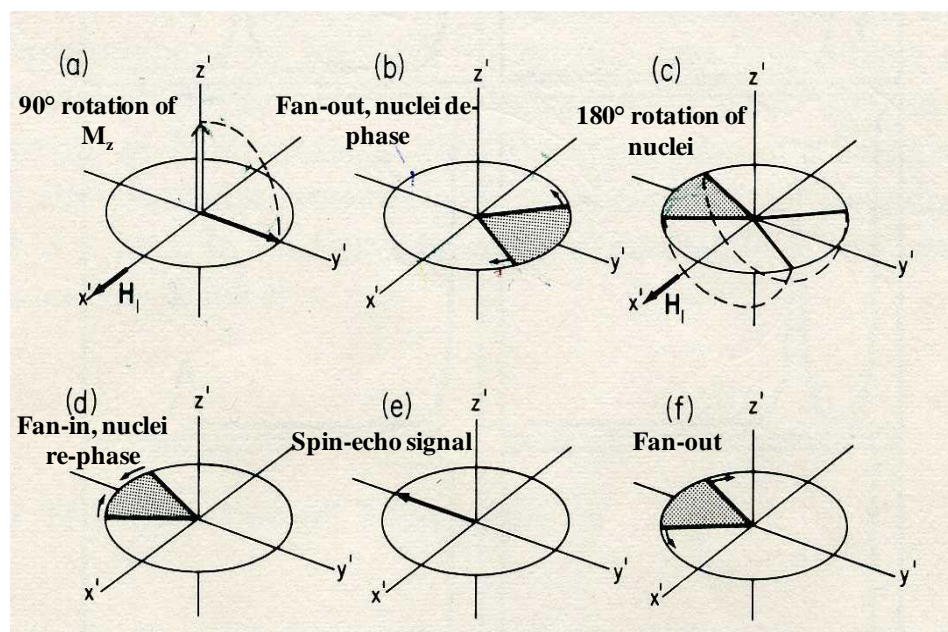


Figure 3.5: Visualisation of a Hahn Spin-Echo sequence. Each step of the experiment is indicated by a letter, for explanation see text. Image taken from Bruker minispec manuals.

To improve the sensitivity to diffuse, pulsed field gradient pulses are inserted between the 90° and 180° pulse, and the 180° pulse and echo signal (Tanner and Stejskal, 1965). The sequence mostly used today is known as *PFG-stimulated echo sequence* which includes the two pulsed gradients and the substitution of the 180° with two 90° pulses. The name “pulsed field gradients, PFG”, as opposed to “steady state field gradients” in a normal Hahn-spin echo experiment, has been given as the magnetic fields are turned on only for a short period of time (hence *pulses*). The pulses (or *gradients*) are produced by strong capacitors (*gradient coils*). The main result of applying pulses is an increase in the amplitude of the echo signal (the shape remains the same) (Tanner and Stejskal, 1965). The sequence is schematically illustrated in Figure 3.6. The length and the intensity of the gradients are represented by δ and G , respectively. The *balance*, a variation in the amplitude G of one pulse, is applied to compensate for any heterogeneity in the magnetic field and ensure the echo signal is in the right position for detection. τ represents the time

between the pulses (as depicted in the figure) and Δ is the time distance between the two gradients and is generally 210 ms.

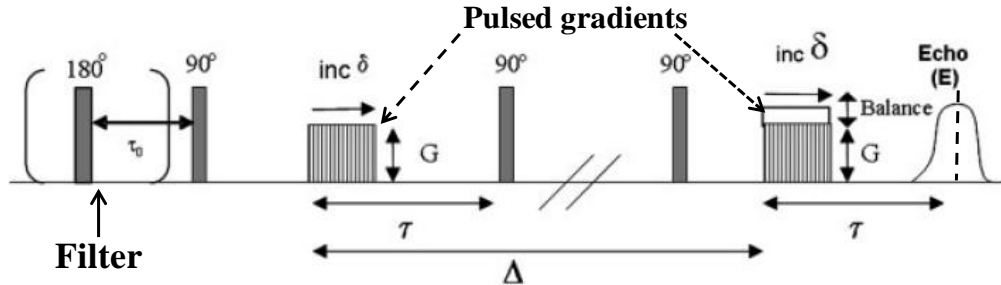


Figure 3.6: Schematic representation of the stimulated echo sequence. The first 90° pulse and the second two pulses are depicted as grey rectangles and the field gradient pulses are indicated by the dotted arrows. The spin-echo signal is depicted at right-hand side of the sequence. For “filter” and symbols explanations see text. Image taken from van Duynhoven *et al.* (2007).

To remove the signal contribution produced by the ^1H of the continuous phase, a *time-domain filter* is applied exploiting the difference in the T_1 of aqueous and lipid phase (indicated as “filter” in Fig. 3.6). For W/O emulsions the filter consists of an inverse 180° pulse which suppresses the contribution from the oil at the start of the PFG sequence (van Duynhoven *et al.*, 2002) and the oil suppression delay was set at 85 ms as also referred by Gosh *et al.* (2011). In a typical droplet size measurement, the time length of the gradients is progressively increased and the change in the signal intensity measured. In this thesis eight values of δ were used (automatically changed by the software). The algorithm for the calculation of droplet size distribution is complex and dependent on several parameters. Its full explanation is beyond the objective of this thesis and can be found in the literature (Tanner and Stejskal, 1965). It should be considered that the algorithm assumes droplets are all spherical, not aggregated, and with a lognormal probability distribution of sizes, which has been demonstrated to be a good approximation for W/O emulsions (van Duynhoven *et al.*, 2002). Droplet size measurements were performed using a “water droplet size application”. The application was calibrated prior to the

experiments using a standard containing copper sulphate ($\text{CuSO}_4 \cdot 5\text{H}_2\text{O}$) *via* an automatic procedure. Another calibration called *daily check* had to be performed every 24h to ensure all parameters were set at the corrected value. In this thesis, all droplet size measurements were performed at 5 °C as this temperature allows following water molecule diffusion while minimising the diffusion of the entire droplets. Emulsions samples (~10 mm in height) were obtained by using a metal plunger provided by the manufacturer and inserted into glass tubes. Samples (equilibrated at 5 °C) were transferred into the measuring unit of the NMR and the analysis started.

On completing the measurement the characterising parameters ($d_{3,3}$ and σ) were automatically reported. The *Sauter mean diameter*, $d_{3,2}$ was calculated using Equation 3.3 (van Duynhoven *et al.*, 2002; 2007):

$$d_{3,2} = d_{3,3} \times e^{-0.5\sigma^2} \quad (\text{Eq. 3.3}),$$

where, $d_{3,3}$ is the *volume weighted average droplet size* (in μm), and σ is the *width* of the distribution. Droplets with a $d_{3,3}$ value exceeding 50 μm were not included in the calculation, automatically classified as “free water”, and expressed as percentage of the total aqueous phase. Values of free water equal or below 5% were considered negligible. For all systems droplet size characterisation was performed 24h after production and for each sample at least three replicates were taken and average values and standard deviation reported.

3.3.2.1. *Solid Fat Content measurement: direct and indirect method*

The solid fat content (SFC) quantifies the physical property of crystallising fats to exist as mixtures of liquid and solid components. It represents the mass fraction of a lipid system existing in a solid state compared to the total. SFC is usually expressed in percentage.

NMR is the official technique for the determination of SFC and generally the pulse sequence used is a simple “free induction decay” experiment as explained above. The physical property allowing differentiating between liquid and solid is the T_2 value. As shown in Figure 3.6, after having applied a 90° pulse (for $3 \mu\text{s}$), the signal intensity in solid fats decreases much faster (usually relaxation occurs within $10 \mu\text{s}$) than in liquid oils (relaxation over $1000 \mu\text{s}$) (van Putte and van den Enden, 1974). Two official methods exist to determine the SFC, direct and indirect method, which exploit different points of the FID curve (Fig. 3.7). Here, only the indirect method is explained as this is the used method.

SFC determination via indirect method

The determination of the SFC using the indirect method relies on the determination of only the point at $70 \mu\text{s}$ of the FID curve, where the signal decay of the liquid component can be considered negligible and the signal of the solid is less than 0.1% of the original value (van Putte and van den Enden, 1974). A measurement is then performed at a temperature where all fat is completely melted and the SFC can be calculated using Equation 3.4:

$$SFC(\%) = \frac{c \times S_m - S_L}{c \times S_m} \times 100\% \quad (\text{Eq. 3.4}),$$

where, S_m is the signal produced by the molten fat, S_L is the signal produced by the liquid fraction at the measuring temperature, and c is a correction factor taking into account the signal loss due to the temperature increase to the melting point of the fat. The factor c is calculated by measuring the signal intensity of a known amount of reference oil at working (c_T) and melting temperature (c_m) and by taking the ratio of the two values: $c = c_T/c_m$.

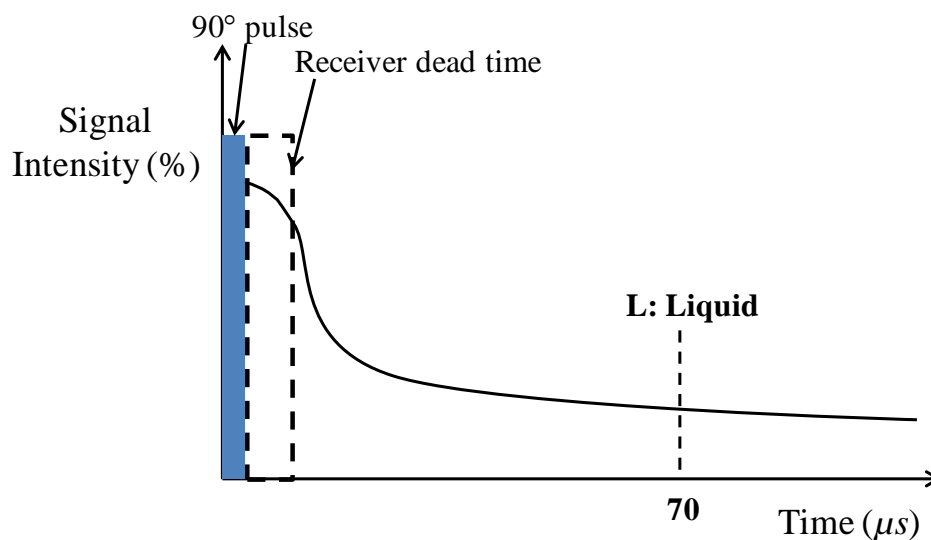


Figure 3.7: Schematic of a relaxation curve after a 90° pulse. L is the signal produced by the liquid components. The characteristic time point of signal detection (70 μs) is also shown.

As mentioned above, solids are characterised by shorter T_2 values than liquids, and water has a longer T_2 than oils. In order to measure the SFC in emulsions these differences in the physical behaviour had to be taken into account in developing the method. Also for SFC measurements the NMR jacketed probe-head was used as it allows good temperature control.

3.3.2.2. Method development for SFC measurements

The SFC measurements were performed using the “*data_oil*” application provided by Bruker. This application is defined by the manufacturer as an “absolute application” meaning that it requires a calibration prior to use. However, standards are not available

and “customer standards” need to be used. As described below, laboratory standards were prepared to calibrate the application. On completing a calibration procedure, the application automatically returns a linear equation having form:

$$y = mx + y_0 \quad (\text{Eq. 3.5}),$$

where, y is the signal intensity (in %) measured by the NMR and expressed in percentage, m is the slope (g^{-1}) and x is the oil mass (g). The intercept y_0 is also expressed in percentage and represents the signal measured in absence of oil. The “*data_oil*” application is a quality control application designed to measure oil content in seeds. On measuring, the result is not expressed as ‘signal intensity’ value but directly as ‘oil content’, expressed in grams. The signal intensity can be calculated re-arranging Eq. 3.5, knowing the calibration parameters.

The following sections refer the main results obtained in adapting and validating the “*data_oil*” application to measure oil content in emulsions. It should be noted that to determine the SFC content in emulsions using the indirect method, the aqueous phase contribute to the NMR signal has to be removed.

Technical note: The Bruker minispec uses the *Spin Echo pulse sequence* to determine the oil content as this is a more precise method to determine the NMR signal intensity. The advantage of the spin echo is that it is possible to signal average the intensity of the peak echo thereby increasing the precision of the measurement (Ablett, personal communication, 2013).

Filling of the RF coil

A preliminary experiment was performed to evaluate the amount of oil necessary to fill the RF coil thus optimising the oil signal. Twelve standards of commercially purchased sunflower oil (SFO) were prepared by weighing the oil directly into the glass tubes and

masses were measured with a laboratory scale. In this experiment performed at 5 °C, a RD of 2 seconds was used and 4 scans were taken. The *number of scans* is the number of experiments executed and averaged by the NMR (one scan is equivalent to a relaxation time sequence (Eq. 3.2)). A linear relationship between the NMR signal intensity (%) and the SFO mass was shown to exist until a SFO mass of approximately 0.4 g, which corresponded to approximately 1 cm in height (Fig. 3.8). For SFO standards with masses above 0.5 g, the relationship was longer linear and could not be used to quantitatively determine the oil content.

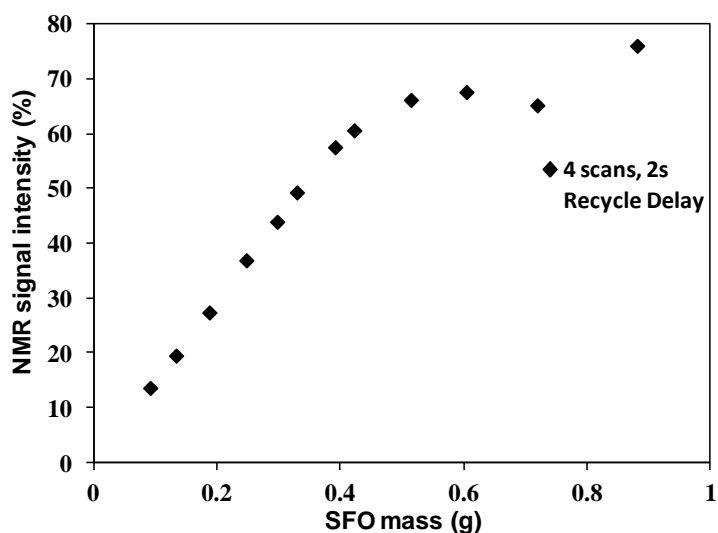


Figure 3.8: NMR signal intensity as function of SFO mass. A linear response occurs for a mass up to ~0.5 g.

Effect of number of scans

The number of scans (ns) is one of the parameters to control in performing NMR measurements. It represents the number of experiments performed in a measurement and averaged by the application. In this experiment ten SFO standards were prepared with mass ranging between 0.05 and 0.5 g and the application calibrated using four values of ns : 4, 8, 12, and 16 (2 s of RD). No difference in the calibration curves were shown on increasing ns . In Figure 3.9 the calibration points obtained for ns of 4 and 16 are shown to perfectly overlap. Therefore, it was decided to work with 4 scans to decrease the amount of time for analysis.

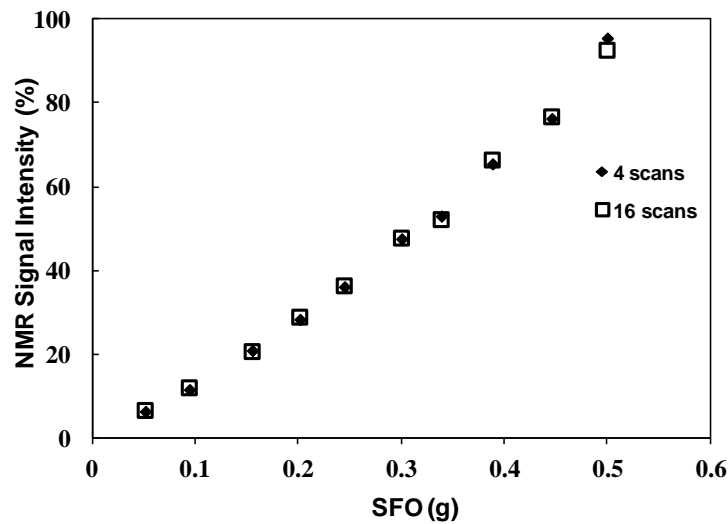


Figure 3.9: NMR signal intensity as function of SFO standards at two values of ns : 4 (diamonds) and 16 (squares).

Effect of Recycle Delay (RD) length on oil content measurements

An experiment was performed to evaluate the effect of the length of the recycle delay (RD) on oil content measurements. This time is necessary to allow full relaxation of sample protons prior to the next scan. RD is usually set to a value equal to $5T_1$ of the sample having the slowest relaxing protons (water in this study). The RD is the longest

part of a pulse-sequence and it should be optimised to avoid signal loss (resulting in a decrease in accuracy) and reduce the length of analysis.

The minispec software does not allow for directly changing the RD, whereas the relaxation time (RT) can be varied. The pulses width (PW) and acquisition time (AQ) were left unchanged and three values of RT were evaluated: 2, 8, and 10 s. Considering that the sum of the length of the PW and AQ is smaller than 1 ms, an increase in RT effectively corresponds to an increase in RD. Other measuring parameters, namely the τ spacing and the “sampling window” (the time range where AQ occurs) were not modified (Table 3.2).

Ten standard of SFO with a mass ranging from 0.091 to 0.422 g were prepared as described above. Samples were left to equilibrate at 5 °C for at least 10 minutes prior running the calibration and in all experiments 4 scans were used. Calibration points obtained for 2 and 10 s of RD are shown in Figure 3.10 (points obtained for 8 s RD show the same trend and have been excluded for clarity).

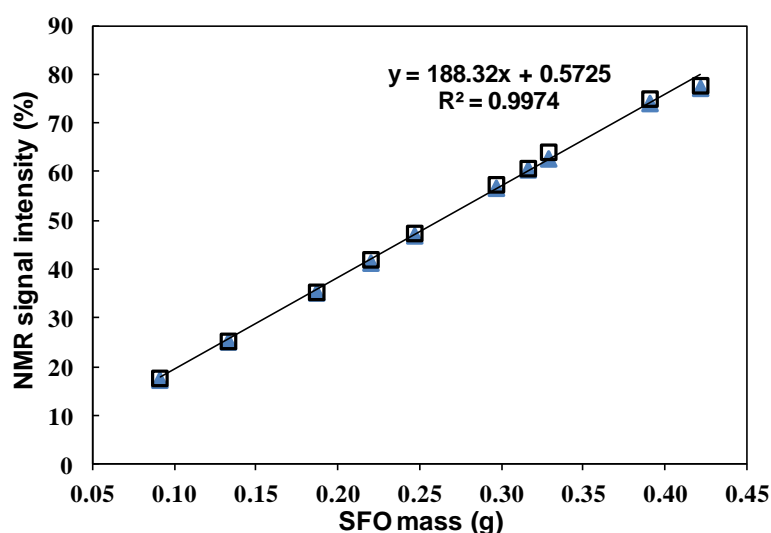


Figure 3.10: Calibration points for 2 (triangle) and 10 s (square) RD. The R^2 and equation refer to the 10 s RD calibration.

Three samples containing a known amount of SFO were prepared to evaluate the accuracy in measuring the oil content. The average measured oil contents and standard deviation have been compiled in Table 3.2. Results demonstrate that SFO can be accurately determined. For the last sample some discrepancies in the weighed and NMR measured oil mass were observed. This result was shown to be a consequence of small amount of water condensation around the tubes within the NMR probe-head.

Table 3.2: Bulk SFO weighed masses and corresponding amounts measured by the NMR at different recycle delay (RD) values.

SFO mass (weighed, g)	Oil mass (g) at 2 s R.d.	Oil mass (g) at 8 s R.d.	Oil mass (g) at 10 s R.d.
0.297	0.300	0.300	0.300 ± 0.006
0.316	0.320	0.320	0.320
0.211 ¹	0.219 ± 0.003	0.222 ± 0.001	0.218 ± 0.001

Another experiment was carried out to evaluate the possibility of measuring water and water-SFO mixtures. At this stage the NMR was unable to correctly quantify water mass (data not shown). This result was attributed to the relatively large default value for the τ spacing (time between 90° and 180° pulses).

Reducing the tau (τ) spacing

To take into account the contribution of the water to the NMR signal, a further calibration was performed using the same SFO standards and measuring parameters referred above and a τ spacing value of 100 μ s. The sampling window (SW) was automatically recalculated by the application (Tab. 3.3). Also in this case no difference in the calibration curve was obtained using a RD of 2 or 10 s (data not shown). Equation 3.6 was obtained on calibration:

$$y = 183.1x + 0.36 \quad (\text{Eq. 3.6}),$$

where, y is the signal intensity measured by the NMR, 183.1 is the slope (g^{-1}) and x is the oil mass. The intercept is also expressed as a percentage. The results shown below were obtained using a RD of 10 s as this delay time allows full relaxation of water protons.

Table 3.3: Values of tau spacing (τ) and corresponding sampling window used on calibration.

τ spacing (μs)	Sampling window length (ms)	Sampling window range (ms)
200 ¹	0.100	6.95 – 7.05
100	0.034	0.206 – 0.240

1: default value of τ spacing and sampling window.

A preliminary test was performed to validate its use on measuring oil content in pure oil systems. Data compiled in Table 3.4 show that the NMR could correctly quantify the weighed oil (standard deviation was below 0.001, showing high measurement accuracy).

Table 3.4: Values of weighted and measured SFO. The NMR signal intensity is also reported.

Weighted SFO (g)	NMR signal Intensity (%)	NMR Measured SFO (g)
0.175	33.25	0.176
0.231	43.75	0.233
0.314	59.25	0.318

SFO-water mixture were produced as described above (i.e. water added to oil) and the total liquid content measured. Double distilled water was used for this experiment. Data of the measured liquid content have been compiled in Table 3.5 together with the weighed mass of the SFO-water mixture and the SFO/water ratio. It was concluded that

the calibrated NMR application could accurately measure the liquid content of the samples.

Table 3.5: Samples masses of SFO-water mixtures measured by NMR. The SFO/water ratios have been also compiled.

SFO-water mixture mass (weighed, g)	SFO-water ratio (%)	NMR liquid content (g)
0.230	24	0.231
0.256	32	0.255
0.283	38	0.286
0.372	16	0.372
0.401	22	0.396
0.288	20	0.289
0.394	42	0.392

A final validation test was performed using a double distilled water sample to which known amounts of SFO were progressively added. Results have been compiled in Table 3.6 and confirm that “data_oil” calibration with the selected settings (10 s RD, τ 100 μ s, 4 ns) can be used to accurately quantify the liquid content in water-oil systems.

Table 3.6: Total liquid content measured by NMR for water-SFO mixtures.

Water mass (g)	Added SFO (g)	Total mass (g)	SFO-water Ratio	NMR measured oil (g)
0.173	0	0.173	0	0.171
	0.044	0.217	20.3	0.220
	0.043	0.260	33.5	0.260
	0.042	0.302	42.7	0.303
	0.043	0.345	49.9	0.349

3.3.2.3. Solid fat content (SFC) determination

SFC measurements were performed using the Minispect software following the calibration described above and according to the indirect method. On performing the analysis, approximately 0.3 g of material for each sample was weighed directly into NMR glass tubes and heated to 50 °C for 20 minutes using a dry hot plate to erase crystal memory. The selected sample mass was below the maximum amount necessary to fill the RF coil to prevent any signal loss following thermal expansion on heating. After melting, samples were transferred into the NMR probe-head (set at the desired temperature, T_{Cr}) and readings started immediately. Data points were acquired every forty seconds. It should be considered that often the frequency of data acquisition is missing in published works as it is replaced with the expression “appropriate time intervals” which does not provide enough information for reproducing the experiment. Here, measurements were performed until SFC curves had achieved a plateau region. SFC values determined within this region of the crystallisation curves were regarded as maximum (SFC_{max}) (Perez-Martinez *et al.*, 2007). At least two replicates were determined for each CB system as a

function of T_{Cr} – time combination and average values reported. Furthermore, the SFC evolution described in this thesis differs from those referred to in the literature for two aspects: (1) the cooling to the T_{Cr} was performed directly into the RF-NMR probe. This step is usually performed using external water baths. However, even if great care is taken, a significant temperature variation can be introduced in the sample while transferring the test tubes from the water bath to the NMR probe which subsequently affects the SFC readings. In this work, the error associated with the sample transfer was completely eliminated; (2) often the time required to reach the desired isothermal temperature is not clearly expressed. For each sample type and temperature combination, the cooling profile to the T_{Cr} was recorded using a data logger (Omega, UK) fitted with type-K thermocouple. Since the temperature sensor could introduce signal interference and contamination, temperature cooling profile was recorded separately using a comparable sample mass for all the systems-temperature combinations. In Figure 3.11a an example of a sample and temperature sensor is shown. In Figures 3.11b and c, the set-up used to record real-time the temperature profile is shown. The measured cooling profile will be shown for each isothermal crystallisation temperature investigated in Chapter 6.

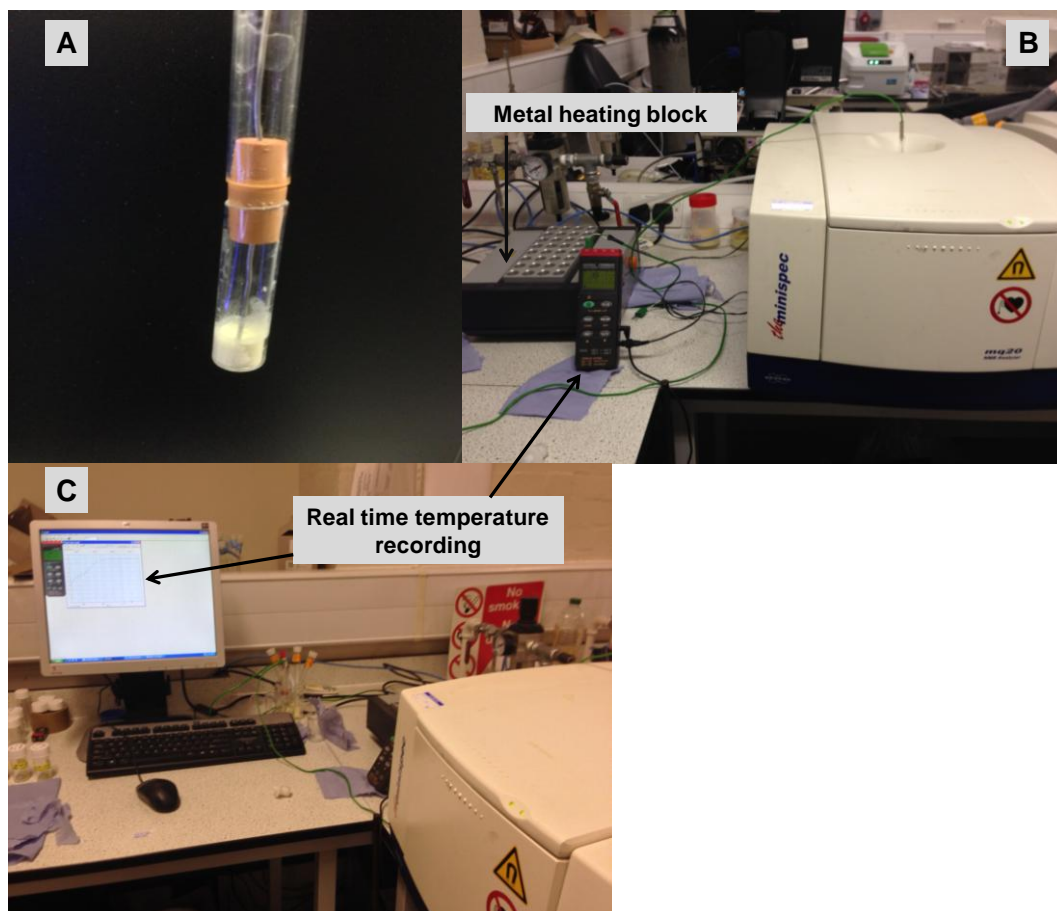


Figure 3.11: Example of sample used to measure the temperature profile (A); general set-up for real-time temperature recording (B, C).

At any temperature, the total signal produced by an emulsion sample is given by Equation 3.7:

$$S_{Tot} = (1 - x_{Aq}) S_{Lip} + x_{Aq} S_{Aq} \quad (\text{Eq. 3.7}),$$

where, S_{Tot} , S_{Lip} , S_{Aq} is the total signal, the signal of the lipid phase, and of the aqueous phase, respectively, and x_{Aq} is the aqueous phase mass fraction. The equation used in the thesis to calculate the SFC content was obtained substituting Eq. 3.7 into Eq. 3.4 to obtain:

$$SFC (\%) = \frac{c[(1-x_{Aq}) S_{Lip} + x_{Aq} S_{Aq}]_m - [(1-x_{Aq}) S_{Lip} + x_{Aq} S_{Aq}]_L}{c[(1-x_{Aq}) S_{Lip} + x_{Aq} S_{Aq}]_m} \quad (\text{Eq. 3.8}),$$

where, the subscript m and L indicate “molten” and “liquid” signal, respectively. The amount of CB solidified at any time point was calculated rearranging Equation 3.8 considering that the mass fraction of PGPR was known.

3.3.2.4. Crystallisation kinetics

To evaluate of the effect of sample-time-temperature combination on kinetics of crystallisation, data were fitted to the Avrami model (Section 2.1.3.1.). This model describes the change in the fraction of solids over the time and its mathematical expression is given by:

$$(1 - X) = \exp(-k t^n) \quad (\text{Eq. 3.9}),$$

where, X is the fraction of crystallised material during the crystallisation time t , and k and n are the *Avrami rate constant* and *exponent*, respectively. The crystal fraction X was expressed here as $\text{SFC}_t/\text{SFC}_{\text{max}}$ with SFC_t and SFC_{max} being the SFC at any time point and at equilibrium, respectively. The parameters k and n were calculated by fitting of data to the linearised form of Equation 3.9. The linearisation was obtained by a double logarithmic transformation:

$$\ln(-\ln(1 - X)) = \ln(k) + n \ln(t) \quad (\text{Eq. 3.10}).$$

In Figure 3.12 and example of a crystallisation curve (a) and the corresponding double logarithmic transformation (b) is shown; the linear part of the curve (white squares in Fig. 3.12b) was used to determine the Avrami parameters by linear fitting ($R^2 = 0.96$). From the double logarithmic plot $\ln(-\ln(1 - X))$ vs. $\ln(t)$, n and k were calculated as the slope and the y-intercept of the linear fitting, respectively. A detailed description of the physical meaning of the kinetic parameters can be found in Section 2.1.3.1. The time interval in

which the fitting was performed corresponded to a linear region in the double logarithmic plot and it will be specified case-by-case in Chapter 6.

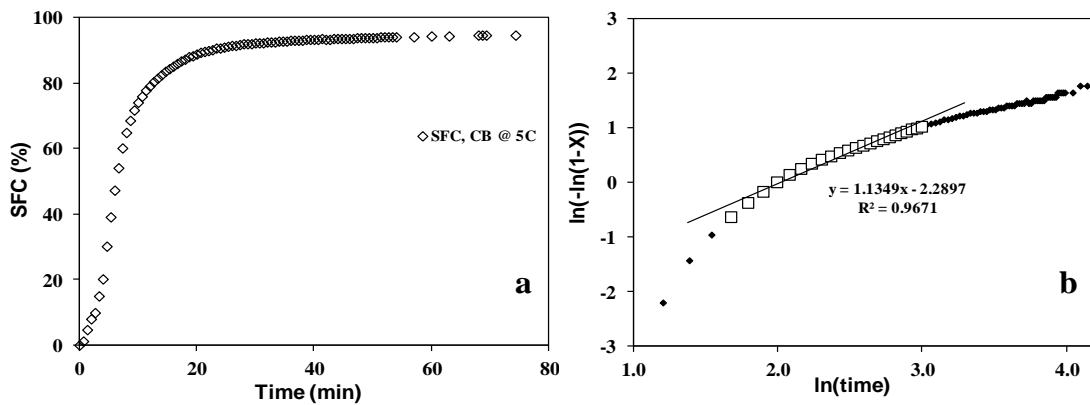


Figure 3.12: (a) Solid fat content (SFC) evolution curve over time for bulk cocoa butter crystallised at 5°C; (b) corresponding double logarithmic transformation (Section 3.3.2.4.). In 3.12b the full diamond represents the whole transformed curve while the white square represent the portion of the curve used to calculate the Avrami parameters using linear fitting (a detailed explanation for the chosen interval is provided in Section 6.2.3.).

For all systems the half time of crystallisation ($t_{1/2}$) was calculated according to Metin and Hartel (1998):

$$(t_{1/2})^n = \frac{\ln(2)}{k} \quad (\text{Eq. 3.11}).$$

3.3.3. Differential Scanning Calorimetry (DSC)

Differential scanning calorimetry (DSC) is a technique widely used to characterise the thermal behaviour of food and non-food materials. It is generally defined as a thermal analytical technique which measures the energy change, i.e. the *enthalpy*, associated with the phase transition occurring on heating, cooling, or isothermal hold, as compared to a reference material. DSC also measures the temperature at which the phase transition occurs (Gabbot, 2008). When analysing a sample using the DSC, the main measured property is *heat flow*: heat flow represents the amount of energy that flows in or out of a

sample over the experimental temperature or time range (the heat flow dimension is “mW”, which corresponds to “mJ/s”, i.e. energy per unit time). The word “differential” indicates that heat flow measured depends on the sample and reference material (composition and mass of both), while “scanning” implies a dynamic mode of operation (in general a linear change of temperature over time is implied). Two main categories of DSC exist. For both the signal is proportional to the heat flow, but they differ in their design and measuring principle:

- Power compensated;
- Heat flux.

Power compensated DSCs were used in this study to investigate the thermal behaviour of CB systems. Therefore, only this category will be explained in more detail.

A *power compensated DSC* contains two small identical furnaces with their own heating block and temperature sensor(s): by convention, the left furnace is for the sample and the right for the reference (usually an inert material). Both furnaces follow the pre-established thermal (linear) profile, and power compensation in the form of electrical heat is supplied to either furnace to attain the desired rate of temperature change while keeping sample and reference at the same temperature. The output of the measurement is contained in a plot known as *thermograph* and reflects the difference in the power supplied to the sample furnace compared to the reference one over the time-temperature range. The fundamental equation for power compensated DSC is (Foubert *et al.*, 2008):

$$\frac{dQ}{dt} = C_p \times \frac{dT}{dt} + f(T, t) \quad (\text{Eq. 3.12}),$$

where, dQ/dt is the heat flow signal measured by the DSC normalised by the sample mass ($J/\text{min g}$), C_p is the heat capacity at constant pressure (P as subscript), defined as the amount of heat to be supplied (or removed) to change of one Kelvin degree the

temperature of a unit mass of material ($J/g\ K$), dT/dt is the imposed rate of temperature variation (K/min), and $f(T,t)$ is the heat flow due to the phase transition. When the sample undergoes a phase transition, the temperature of the sample remains constant until the phase transition terminates and the DSC tries to compensate the temperature difference (ΔT) by supplying heat *via* electrical resistance (the reference is heated in case of crystallisation). By convention in a typical thermograph obtained by power compensated DSC, an endothermic (melting) and exothermic (crystallisation) event is represented by an upward and downward curve, respectively. A plot of the temperature as function of time should provide a line, with the slope being the scan rate (a zero slope is obtained for isothermal analysis). In the sections below the two types of DSC analysis used to characterise the samples are described in detail.

3.3.3.1. *Melting behaviour of processed CB systems*

Melting analysis *via* DSC was used to gain an insight into the effect of processing and formulation on the formed polymorphs in CB systems. Measurements were performed using a power-compensated DSC (DSC-7, Perkin-Elmer, UK) equipped with a dry box. Prior to the analysis, the device had been calibrated with indium and zinc for temperature and indium for enthalpy. Nitrogen (20 mL/min) was used as purge gas and an empty pan was used as reference (Toro-Vazquez *et al.*, 2004). To obtain information only about the CB polymorphs formed on processing little volumes of samples (less than 5 mL) were collected using pre-chilled weighing boats and quickly transferred to a cooling unit set at $-10\ ^\circ C$. All the tests were performed within two hours of emulsification. This procedure aimed at minimising the effect of phase transition occurring on slow cooling and storage. For each sample, a mass of 5 mg (± 2 mg) was weighed using directly in the centre of pre-chilled 40 μL aluminium pans. Pre-chilled aluminium covers were used for hermetic pans

sealing with a crimper press. “Pyris thermal analysisTM” software was used to run the device. A one minute isothermal step at 5 °C was used to thermally equilibrate the samples before melting (although this did not allow obtaining a straight baseline, a longer isothermal time may have induced some polymorphic transition). Samples were then heated from +5 to +45 °C at 10 °C/min. For each samples at least two measurements were performed. Endotherms were analysed using the Pyris software to determine the melting peak(s). The results of this analysis have been referred in Chapters 4. The melting behaviour of CB systems produced in Chapter 5 was investigated using the same device and conditions. In this case the investigated temperature range was from –10 to +45 °C at 10 °C/min.

3.3.3.2. *Stop-and-return thermal analysis*

The thermal method known as “stop-and-return method” has been described by Foubert in a series of publications (Foubert *et al.*, 2003; 2008). It is also referred to as “indirect” DSC method (Fredrick *et al.*, 2011). This analysis is similar to any isothermal crystallisation experiment where a molten sample is cooled to the desired annealing temperature (T_{Cr}) and left to rest; the only difference is that the isothermal hold is interrupted prior to completion of crystallisation (indicated by the return to the baseline of the heat flow signal) by a re-heating step to gain an insight of the formed polymorphs during the annealing period (and on cooling). Therefore, the method can be seen as a “sequence” containing four steps: (1) isothermal holding at high temperature above the final melting point of the material (T_m) to erase crystal memory; (2) cooling to T_{Cr} at a rate selected to minimise crystallisation on cooling; (3) isothermal annealing at T_{Cr} for an established length of time; (4) re-heating to T_m . By repeating this sequence several times while increasing the length of the annealing step, an understanding of the polymorphic

evolution over time at a T_{Cr} can be gained. This method was preferred to standard isothermal calorimetry (IC) in the light of results by Fessas *et al.* (2005), who concluded that the former technique is more suitable than IC for the study of CB TAGs polymorphism. Results from this analysis will be shown in Chapter 6 and details on both samples and method used are referred below.

Samples and method technical specifications

Samples analysed using this technique were bulk CB, and emulsions containing 20% and 40% aqueous phase (wt%), respectively. Emulsified systems were produced according to the optimised process set-up described in Chapter 4. To normalise the content of emulsifier between emulsions, the ratio emulsifier/dispersed phase was kept constant and at 5% (wt%). For crystallisation experiments at 5 and 20 °C (see below), the effect of the emulsifier only on CB crystallisation was evaluated producing a CB system containing a PGPR amount equivalent to the one used for a 20% aqueous phase emulsion.

DSC experiments were performed with a DSC 8000 (PerkinElmer, UK) equipped with an intracooler 2 and controlled *via* “PyrisTM software”. For each sample type, a mass corresponding to approximately 4 mg (± 1 mg) of CB was weighed directly in an open 40 μ L aluminium pan. Thereafter, pans were hermetically sealed using an aluminium lid and immediately transferred in the DSC furnace. An empty pan was used as reference and dry nitrogen was used to purge the system (20 mL/min). The applied thermal program consisted of four steps (Fig. 3.13): (1) isothermal at 50 °C for five minutes; (2) cooling to the desired T_{Cr} (5, 10, 15, 20 °C) at 10 °C/min; (3) annealing (5, 10, 15, 20, 30, 45, 60, 120, 180 minutes); (4) re-melting to 50 °C at a heating rate of 5 °C/min. This scan rate was selected as it allows minimising polymorphic evolution and thermal lag on re-heating (Dewettinck *et al.*, 2004).

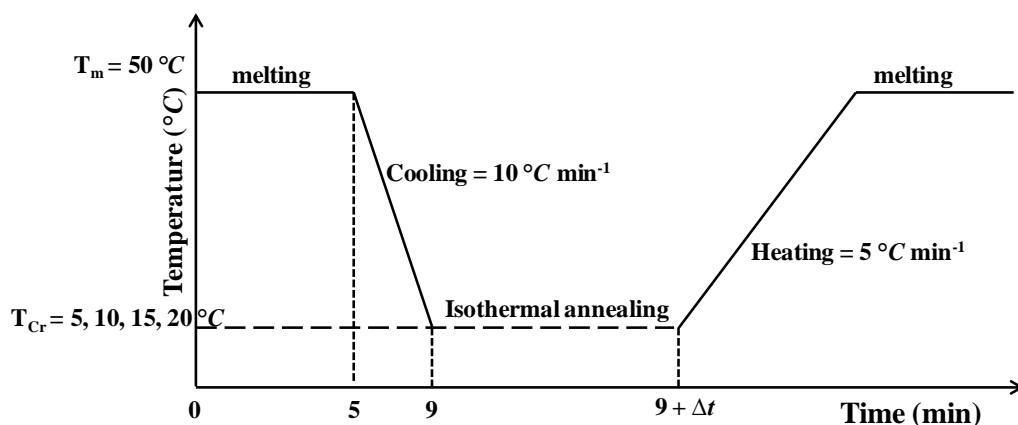


Figure 3.13: Schematic illustration of the time-temperature profile applied for the “stop-and-return” method. Sample is initially melted at 50 °C for 5 minutes, followed by cooling to the desired T_{Cr} and isothermal hold for a defined time (Δt). Finally the sample is re-melted. The cycle was be repeated several times.

The initial isothermal step was applied to erase crystal memory according to literature (Fessas *et al.*, 2005). As discussed by Foubert *et al.* (2003a), important differences exist in literature regarding the minimum temperature necessary to erase crystalline memory in CB. For example Metin and Hartel (1998) used a cooling of 100 °C/min from 80 to 50 °C, followed by a three minutes isothermal step and final cooling to T_{Cr} at 100 °C/min. Foubert *et al.* (2003) investigated three melting protocols and concluded that an isothermal of 15 minutes at 65 °C is enough to erase crystal memory. However, a temperature of 50 °C is over 15 °C above form V melting point which is the most stable polymorph observed for processed CB (form VI is only formed over time periods longer than the observation time referred in this thesis). According to Fessas *et al.* (2005) a five minute holding step at 50 °C allows erasing completely crystal memory as long as the repeated melting curves completely overlap. Melting traces overlapping was experimentally observed indicating complete melting at 50 °C (see Appendix 2). With respect to the cooling step, it has been referred by Dewettick *et al.* (2004) that when studying the isothermal crystallisation of materials, ideally the melt should be brought to

the T_{Cr} instantaneously and measurements start immediately. However, this is often not possible given instrumental limitations, with the problem usually partially solved by applying the fastest achievable cooling rate. In this study, a cooling rate of $10\text{ }^{\circ}\text{C}/\text{min}$ was chosen as it is generally considered comparable to industrially applied cooling rates (Fessas *et al.*, 2005) and suitable for minimising crystallisation before achieving the T_{Cr} . With respects to the isothermal steps, after preliminary experiments, the minimum isothermal time was set at 5 minutes. This is in agreement with results by Marangoni and McGauley (2003), which referred the necessity of a minimum isothermal time of 3-4 minutes for obtaining DSC signal stabilisation.

The heat flow signal (mW) was normalised by sample mass and heating rate obtaining the *apparent heat capacity*, which was scaled with respect to the molten state (providing the baseline of the trace) to produce the *excess of heat capacity* expressed in $\text{J}/\text{g }^{\circ}\text{C}$.

One limit of “stop and return” method is that the melting of the sample starts together with the re-heating step, therefore, no stable baseline can be obtained at the lower end of the endotherm (Foubert *et al.*, 2005). This limitation was partially overcome by using a linear baseline overlapping the straight line provided by the experimental curve after melting had been completed. The higher extreme of integration for the calculation of melting enthalpy was taken after the signal had returned to the baseline and the lower extreme was taken at the interception of the baseline and theoretical curve (arrows in Figure 3.14). It should be noted that the two extremes have approximately the same y value. However, with this technique only an estimate of the crystallisation enthalpy is obtained.

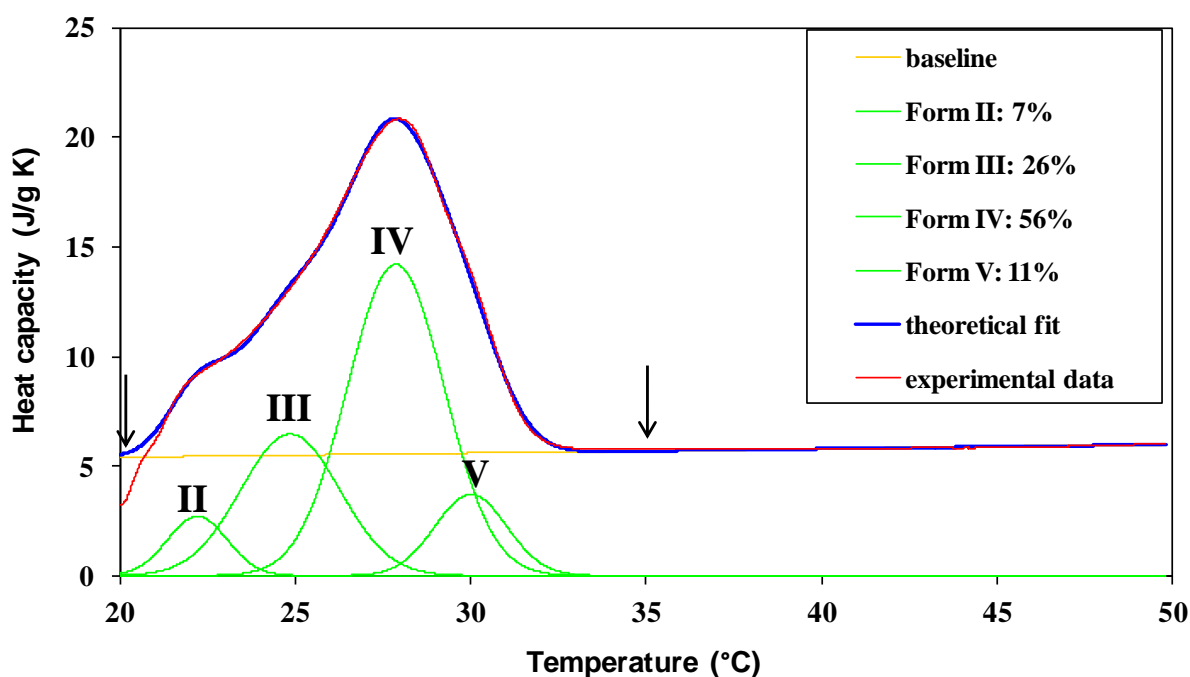


Figure 3.14: Example of deconvolution analysis of a melting curve of a CB sample obtained following a 120 minutes isothermal holding at 20 °C. The red, blue, and yellow line represents the experimental, theoretical, and baseline curve, respectively. Each green line represents the polymorph referred by the Roman numeral; the “relative mass fraction” of each polymorph is referred in the legend. Arrows indicate the extremes of integration for total enthalpy calculation.

Another limit of this technique is that only an estimate of the formed polymorphs can be gained from the melting peak, provided that no polymorphic transition occurs on heating (Foubert *et al.*, 2008). To obtain quantitative polymorphic information a scan rate of 5 °C/min was used, as this heating rate was shown to prevent polymorphic transitions (Foubert *et al.*, 2005), and endotherms were deconvoluted. The deconvolution analysis carried out in this thesis was similar to the method described by Fessas *et al.* (2005): each melting curve was divided into a number of Gaussian curves corresponding to one of the six CB polymorphs. The deconvolution of the endotherms was carried out using the “Solver” tool available in Excel (Microsoft Office, version 2010). This program tool allows the optimum fitting to the experimental curves, provided that the right constraints are defined. A Gaussian curve is represented by an equation having the form:

$$y = a \exp\left(-\frac{(x-b)^2}{2c^2}\right) \quad (\text{Eq. 3.13}),$$

where, a , b , and c are three constants representing *height*, *position*, and *width* of the curve, respectively. The parameter b is given here by the melting temperature of a polymorph. The value of all parameters has been optimised using the Solver tool by minimising the sum of the square difference (point-by-point) between the experimental and the theoretical curves. The theoretical curve was judged to have converged to a solution when the difference between the successive estimates of the sum of the square differences fell below a value specified in the Solver algorithm, typically 0.0001. It should be noted that for the position (b) and width (c) of the curves constraints were applied. This was done in order to restrict the relevant curve to a particular temperature range corresponding to the literature values (Chapter 2, Table 2.3) and preserve the physical difference among polymorphs. The values of melting point and range have been selected according to this procedure and compiled in Table 3.7. An example of deconvolution analysis is shown in Figure 3.11: the experimental curve (red line) and the theoretical fit (blue line) have the same shape. The Gaussian curves, representing the polymorph indicated by the Roman numeral, are in green. The *relative mass fraction* of each polymorph was calculated by using the ratio between the area of one Gaussian and the area of total theoretical curve.

Table 3.7: Polymorph and corresponding melting peak and range used for the deconvolution analysis. Melting peak and range correspond to parameters b and c in equation 3.13.

Polymorphic form	Melting peak temperature ($^{\circ}\text{C}$)	Melting range ($^{\circ}\text{C}$)
	(b)	(c)
I or γ	≤ 4	-
II or α	18 ± 2.0	4.0 ± 1
III or β'_2	23 ± 1.5	2.0 ± 1
IV or β'_1	26 ± 1.5	2.0 ± 1
V or β_2	30 ± 1.0	1.5 ± 1
VI or β_1	≥ 35	-

Note: as also referred by Fredrick *et al.* (2011), a requisite for the use of this method is that the sample remains stable over the cycles. Emulsion stability was evaluated measuring droplet size prior and after the crystallisation experiment. In all cases emulsions remained stable (results shown in Chapter 6). Furthermore, curves on cooling and re-melting perfectly overlaps confirming systems remained stable (Appendix 2).

3.3.4. Wilhelmy plate interfacial tension measurements

The *Wilhelmy plate* is a static method to measure the interfacial tension between two liquids. The principle is to measure the normal force (F) acting on a solid body (the plate) located at the liquid-liquid interface when this latter is being removed from the interface (Pichot, 2012). Here it was used to study the interfacial tension between a CB lipid phase and the aqueous phase. The instrument used in this thesis was a K-100 Tensiometer (Kruss, Germany) and measurements were carried out at 40°C (Chapter 4).

The set up consisted of a vertical static sandblasted Platinum plate (characterised by a small thickness, < 0.2 mm) and a movable vessel containing the liquid (> 20 mL), with

the plate perpendicular to the surface of the liquid. The system was first calibrated by immersing the plate into the lipid phase only (the lower density liquid). This oil was thereafter discarded. On measuring, the vessel containing the aqueous phase (the higher density liquid) was moved close to the plate until its lower edge came into contact with the liquid. Finally, the lipid phase was carefully added until obtaining complete coverage of the plate. Interfacial tension measurements were performed for 4000 seconds, which allowed reaching equilibrium and data points were collected every ten seconds. The interfacial tension was calculated using Equation 3.14 which describes the total force (F) acting on the plate (Pichot, 2012):

$$F = mg + 2(l + L)\gamma\cos\theta \quad (\text{Eq. 3.14}),$$

where, g is the gravity acceleration, m , l and L are the mass, length and thickness of the plate, respectively, and θ is the contact angle (usually assumed to be 0, i.e. complete wetting). The value of mg is calculated on calibration. The surface tension γ is, therefore, the only unknown parameter and is easily calculated considering that F is measured by the microbalance installed in the device.

3.3.5. Uniaxial compression analysis

3.3.5.1. Casting of the samples for mechanical analysis

Five molds were designed and built to allow the preparation of cylindrical test specimens with standardised dimensions (25 mm height, 16 mm diameter). In compression testing it is advisable to have a ratio of sample height to diameter above 1 to reduce frictional effects at the interfaces between sample and plates (Nielsen, 2009).

Mold design included two main parts: a bottom-lateral section made up of stainless steel and a polyvinyl chloride (PVC) core. The PVC part was shaped so to obtain four 25 mm high elements. Ten casting cavities were formed by aligning the PVC elements within the metal section. The mold was finally fastened. On samples preparation, the crystallising fluid was carefully poured into molds to fill the casting cavities. Care was taken to minimise the formation of air bubbles. The molds had been pre-equilibrated to the laboratory ambient temperature (20 °C). Samples were left to cure for approximately 24 h, after which the specimen showed contraction, indicating the presence of CB form V (Fig. 3.15). Preliminary experiments had shown that it was not possible perform samples setting at 5 °C as samples would show macroscopic in-homogeneities. This was thought to be due to strong temperature gradients through the specimens. Therefore, no further experiment was carried out at 5 °C. Before de-molding, the excess of poured sample was removed by carefully trimming the upper end with a razor blade and samples were left to rest for 24h more to allow sintering of bonds which had been broken on cutting. Samples were then de-molded showing a very smooth bottom and lateral surface.



Figure 3.15: Example of specimens of 20% emulsion after 24h at 20 °C. The arrows indicated portions where sample contraction is well visible.

3.3.5.2. Compression analysis

The compression tests were performed using a TA.XT.plus texture analyser (Stable Micro-system Ltd., Surrey, UK) universal testing machine interfaced with a desktop computer. A 30 kg loading cell fitted with a 40 mm diameter cylindrical aluminium probe was used and the trigger force was set at 0.05 N. It should be noted that sample diameter was always smaller than the probe diameter by a factor of approximately 2.5; therefore, this experiment can be treated as a compression test between two parallel infinite plates accounting for specimen's lateral expansion. Before measuring, the load cell was calibrated with a 5 kg weight. According to Kloek *et al.* (2005a), both the static and the mobile plate were covered with parafilm, thus ensuring a clean surface and further reducing frictional effects between the plates and the surface of the specimens (Section 3.2.5.1.). The upper plate was lowered to determine its zero position (*height calibration*). A 'measure force in compression' mode and a 'return to start' test type were selected.

Test specimens were loaded on the static plate and carefully aligned with the cylindrical probe axis. The target compression distance was set to 2.5 mm, corresponding to 10% of engineering strain (see below) within which *fracture* occurred. The maximum sampling rate of 500 data point/s was used for data collection and the force-deformation data were converted into a stress-strain data using a Matlab script written to the purpose (Appendix 1). The engineering strain (ε_E) was calculated by:

$$\varepsilon_E = \frac{\Delta h}{h_0} \quad (\text{Eq. 3.15}),$$

where, Δh is the sample length change and h_0 is the sample initial height (25 mm). The engineering stress (σ_E) was calculated using Equation 3.16:

$$\sigma_E = \frac{F_t}{A_0} \quad (\text{Eq. 3.16}),$$

where, F_t is the force measured and A_0 is the initial cross sectional area.

When a test piece was compressed, the initial part of the curve (ε_E up to approximately 0.001) reflected the mechanical stress needed for the creation of good contact area between sample and upper plate (tau region). This was then followed by a fairly small linear region from which the apparent Young's modulus (E_{app}) accounting for the *stiffness* of the material was calculated by linear regression not passing through the origin in the true strain range between 0.003 and 0.005. The portion of the curve between $0.005 \leq \varepsilon_E \leq 0.01$ showed a continuous change in slope and was followed by a second linear region before yielding and final failure. The bulk modulus (BM) was calculated as the slope to the curve in the true strain region between 0.01 and 0.03. This region was chosen as it accounts for a large deformation but is below the structure yielding for all of the CB systems investigated in this thesis. BM accounts for the overall *deformability* of the

systems before yielding. The coordinates of the point of fracture are the stress (σ_{Fr}) and strain to fracture (ε_{Fr}). The σ_{Fr} represents the material resistance to deformation and will be used as indicator of material hardness. The work to fracture (J/m^3) is given by the area under the σ_E versus ε_E curve up to the point of fracture and represents the *toughness* of the materials. The work to fracture per unit volume was calculated according to Equation 3.17:

$$W_{Fr} = \int_0^{\varepsilon_{E,fr}} \sigma_{Fr} d\varepsilon \quad (\text{Eq. 3.17}).$$

In Figure 3.15a an example of the true-stress/true-strain curve up to the point of failure is depicted together with the parameters used to characterise the materials:

- *Stress of fracture* (σ_{Fr})
- *Strain to fracture* (ε_{Fr})
- *Work to fracture* (W_{Fr})
- *Bulk modulus* (BM , slope in the strain region 0.01 - 0.03 (in green in Fig. 3.16A))
- *Apparent Young's modulus* (E_{App} , slope in the strain region 0.003 - 0.005 in red in Fig. 3.16B).

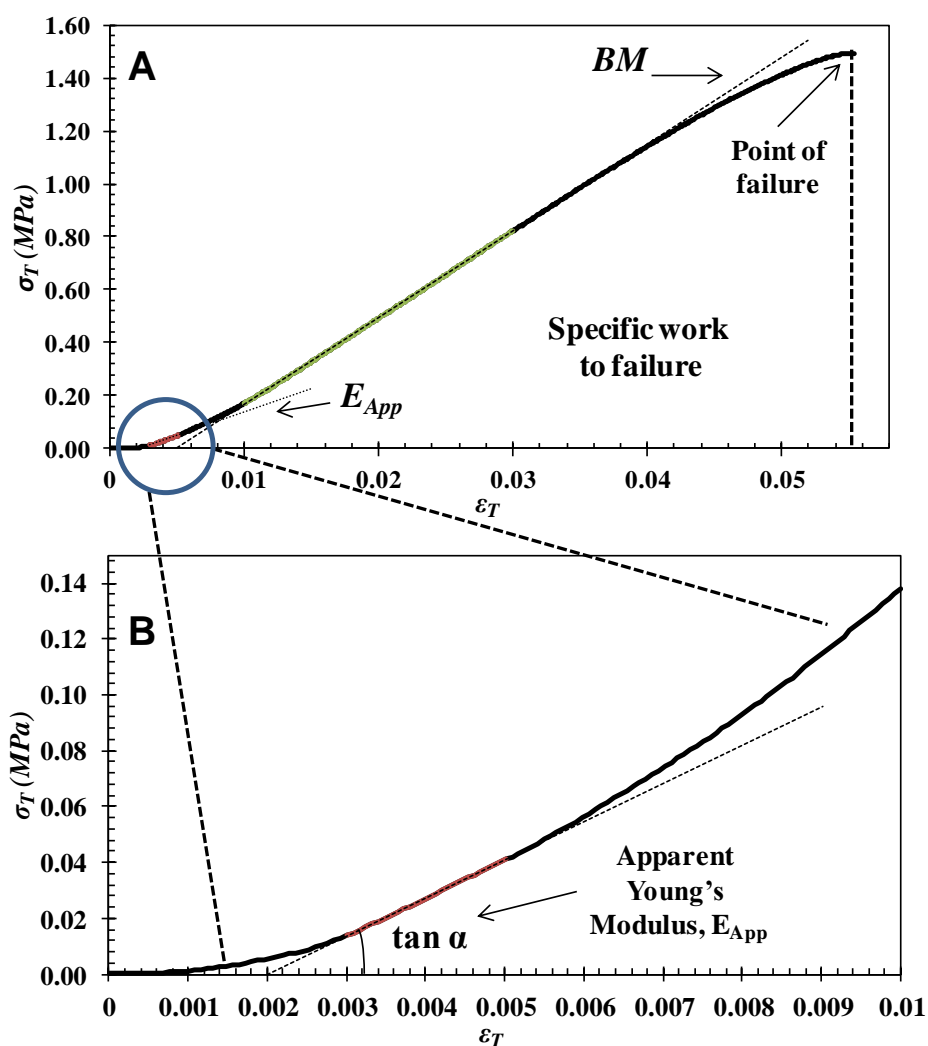


Figure 3.16: Representation of the characterising parameters used in uniaxial compression analysis. (B) Magnification of the portion of the curve used for E_{app} calculation.

3.3.6. Microstructure visualisation

3.3.6.1. Bright-field and Polarised light microscopy

Emulsion microstructure was visualised using an optical microscope (Brunel Microscopes Ltd, SP 300F, UK) fitted with a digital camera (Canon 100D) operating at 20 or 40x. Bright field micrographs served as confirmation of NMR data. Polarised images were taken to gain an insight of fat crystal network structure in the bulk CB and emulsions. In both modes, all the images were taken at ambient temperature (~ 20 °C).

For all of the systems, a small drop of material was transferred with a glass pipette on a glass slide at ambient temperature (20 °C) and covered with a glass cover slip aiming for a low sample thickness. Samples were left to crystallise for 24h at 20 °C. Polarised light micrographs were converted into grey-scale images using ImageJ free-software.

3.3.6.2. *Cryogenic-Scanning Electron Microscopy*

Cryogenic-Scanning Electron Microscopy (Cryo-SEM) was used to gain an insight of droplets structure using a Phillips XL30 microscope equipped with a Gatan low temperature stage. A small sample amount was inserted into the holes of a brass stage attached to a steel support and quench cooled using liquid nitrogen (-198 °C). Thereafter, the sample was introduced in the preparation chamber (-180 °C) of the instrument where it was cut with a knife and was etched for 5 minutes at -90 °C to reduce the formation of ice crystals. The sample surface was then covered with gold and imaged in the measurement chamber (-180 °C) with a 5 keV beam.

3.3.7. **Conductivity measurement**

Conductivity measurements were used as a fast test on-line with the emulsification process to evaluate the production of oil-continuous emulsions: any detected conductivity would indicate the presence of water not structured into droplets. Tests were performed by using a conductivity meter (Mettler Toledo, UK) before crystallisation occurred.

**Chapter 4. Effect of processing and
formulation on the microstructural
properties of water-in-cocoa butter
emulsions**

4.1. Introduction

The aim of this chapter was to further advance the understanding of the effect of processing and formulation on the microstructural properties of water-in-cocoa butter emulsions initially discussed in Section 2.3.2.1. The emulsifying device used was a bench scale margarine line, consisting of a scraped surface heat exchanger (SSHE) in series with a pin stirrer (PS) (see Section 3.2.1.).

The first part of the chapter develops around two exemplifying concentrations of disperse phase and investigates the effect of a wide range of processing conditions on emulsion microstructural properties. Particular attention is given to the role played by the rotational speed of each unit on emulsion droplet size and CB polymorphic form. It should be noted that the role of the second mixer on droplet size had not been described prior to this study in addition to the possibility of using the SSHE alone on emulsification. Flow rate and emulsification temperature are engineering parameters also investigated for their effect on emulsion droplet size. Furthermore, although Norton and Fryer (2012) studied the effect of several processing combinations on emulsion microstructural properties, they did not investigate in detail the effect of processing on CB polymorphism. The role played by the shear-temperature combination on CB polymorphism will be therefore discussed in this chapter. It has been demonstrated that the application of shear increases the rate of polymorphic transition toward more stable polymorphs in crystallising fats (toward form V for CB) (Mazzanti *et al.*, 2003; MacMillan *et al.*, 2002). Therefore, it was hypothesised that an increase in the applied shear applied would promote the development of more stable polymorphs.

In the second part of this chapter the role of formulation parameters, i.e. disperse phase percentage and emulsifier concentration, on emulsion microstructure will be considered.

It is argued that the surface active molecules naturally contained in CB and fat crystals can promote emulsion formation and stabilisation. However, the addition of PGPR allows smaller droplets to be obtained by reducing the interfacial tension and quickly covering the newly formed interfaces.

In the final part of the chapter, evidence of the formation of a solid crystalline interface, referred to as *shell*, encasing the dispersed water droplets, is provided. These results are in good agreement with literature data (Norton *et al.*, 2009). It is shown that crystalline *shells* can be formed for different formulations and in absence of PGPR. The chapter ends with an indication of the thickness of the *shell* which represents a key novelty of the work discussed in this chapter.

The ultimate goal of this work is the development of a continuous process for the production of stable tempered water-in-cocoa butter emulsions to use as a novel ingredient for the reduction of fat content in chocolate.

It should be noted that in this chapter, results published by di Bari *et al.* (2014) are discussed in more detail and unpublished results have been added to gain a better understanding of the role played by engineering parameters on water-in-cocoa butter emulsion production, stabilisation, and tempering.

4.2. Results and discussion

At all the processing-formulation combinations used, emulsions were always fat continuous, i.e. the electrical conductivity of the systems was 0 $\mu\text{S}/\text{cm}$. This result suggests that it was always possible to emulsify. The differences in the microstructural properties as a result of the parameters investigated will be discussed in the following sections.

4.2.1. Effect of processing condition on emulsion droplet size

The aim of the work presented in this section was to investigate the role played by each mixer of the margarine line on the final droplet size of 10 and 20% (wt%) water-in-cocoa butter emulsions. To this purpose, twelve combinations of rotation speed were studied in detail. To facilitate the discussion, results have been divided into sections which consider the effect of increasing the rotational speed of one mixer while setting the other at a constant value. Results of emulsions produced using the SSHE alone are reported in Section 4.2.1.3. The jacket temperatures of the SSHE and of the PS were set to 25 °C and 35 °C, respectively and, unless differently specified, the throughput was set to 30 mL/min which resulted in a measured residence time of 56 s (± 2 s) and 320 s (± 5 s), in the SSHE and PS, respectively. In all formulations the polymeric emulsifier PGPR was used at 1% (wt%) of the total emulsion mass. PGPR is a W/O emulsifier known for its ability to quickly cover the interface and provide steric stabilisation to water droplets (Gülseren and Corredig, 2012; Pawlik *et al.*, 2010; Le Révérend *et al.*, 2011).

Prior to the discussion of results, the phenomena occurring on processing are briefly described according to author's view. Within the SSHE the events which occur are: (I) cooling of the water-oil mixture at approximately 15 °C/min from 40 °C to 26 °C; (II)

mechanical breaking of the aqueous phase into dispersed droplets, coalescence and further breaking of droplets; (III) coverage of the droplets “naked” interfaces by PGPR molecules and other surface active species contained in CB; (IV) rapid shear-promoted undercooling of the CB and crystallisation at the SSHE internal surface; (V) scraping of CB crystals from the internal surface and mixing through the bulk: the large quantity of small scraped crystals, act as secondary heterogeneous nuclei and accelerate the crystallisation process; (VI) increase in viscosity. Although the mechanical action of the blades does not allow the development of a continuous fat network (van Aken and Visser, 2000), the crystallised material is expected to contribute to emulsion stabilisation in two synergistic ways: (1) some of the fat crystals could be brought to the interface by the mechanical agitation where they would act as Pickering particles and drive the sintering of a fat crystalline shell; (2) the ongoing bulk crystallisation increases the viscosity of the system and reduces the frequency of droplet collisions thus decreasing coalescence. All of these physical changes occur simultaneously and affect the microstructural properties of the emulsions.

Emulsions produced in the SSHE enter the PS. Within this mixer the following events occur: (I) re-heating of the system to 33 °C; (II) melting of the unstable crystal polymorphs while preserving and distributing, throughout the volume, the more stable, higher-melting ones; (III) shear induced coalescence and droplet break-up.

After processing, emulsions appeared as highly viscous suspensions which rapidly crystallised. The final emulsions are characterised by an average $d_{3,2}$ and polymorphic form dependant on the shear-temperature profile experienced within the mixers. Although the effect of processing conditions on polymorphism will be discussed in Section 4.2.2., it should be considered here that the SSHE jacket temperature was set at 25 °C (following

preliminary experiments) to obtain an outlet temperature comparable to that used in chocolate manufacture (~ 27 °C) (Afoakwa *et al.*, 2009). It is hypothesised that the imposed shear-temperature profile within the SSHE would promote the formation of fat crystals in the desired form, V. The PS should then allow preservation of form V crystals and melt the unstable forms. As mentioned above, it is also reasonable to hypothesise that emulsification occurs in the PS but no clear results showing its effect on droplet size of water-in-cocoa butter emulsions are available.

4.2.1.1. *Use of Margarine line: Effect of SSHE rotational speed on droplet size*

The objective of the work presented in this section was to evaluate the effect of SSHE rotational speed (N_{SSHE}) on water-in-cocoa butter emulsion droplet size when using the margarine line. To this purpose, four N_{SSHE} values were considered: 170, 490, 930, and 1315 rpm. In order to also consider the impact of the PS on the final $d_{3,2}$, the minimum and maximum rotational speed for this mixer were selected (N_{PS} : 170 and 1345 rpm).

Analysis of the droplet size data for emulsions containing 10 and 20% (wt%) aqueous phase shows the same trend: $d_{3,2}$ decrease at increasing N_{SSHE} (Fig. 4.1A and B). With respect to the average $d_{3,2}$ (μm), when the PS was set at its minimum rotor rate (170 rpm), if the SSHE was also rotating at its minimum rate ($N_{SSHE} = 170$ rpm), the final $d_{3,2}$ was large (approximately 25 μm). With increasing N_{SSHE} , $d_{3,2}$ values decreased linearly until reaching approximately 6 μm for both emulsified systems (10 and 20% aqueous phase). The observed linear trends ($R^2 \geq 0.98$) indicate that with low N_{PS} , the N_{SSHE} dominates the droplet break-up process as it has a greater effect on the particle size. Free water content data shows a similar trend (Figure 4.1C and D): when the rotor rate of the SSHE and PS were set at their minimum values, free water content was over 20%. Nevertheless,

for all systems, the content of free water decreased significantly with increasing N_{SSHE} reaching approximately 5% at N_{SSHE} of 1315 rpm.

Conversely, when the N_{PS} was set at its maximum rotor rate (1345 rpm, Figure 4.1A and B), an increase in the N_{SSHE} produced only a small reduction in the $d_{3,2}$ values (from ~6 to 4 μm , with $R^2 \leq 0.68$) suggesting that, in this case, the droplet break up process is not dominated by the SSHE. For both emulsified systems the reduction in the free water content followed the same trend as the $d_{3,2}$ with the average value being below 5%. It is important to observe that for a N_{SSHE} of 170 rpm, the increase of PS rotor rate from 170 to 1345 rpm, produced a decrease in $d_{3,2}$; this trend similarly occurred for a N_{SSHE} of 490 rpm. Nevertheless, for N_{SSHE} above 900 rpm an increase in N_{PS} seems to have a smaller impact on $d_{3,2}$ reduction, with a negligible reduction at a N_{SSHE} of 1315 rpm. These results are in agreement with those published by Norton *et al.* (2012) where it was shown that the PS has an effect on droplet size reduction (from 13.3 to 5.7 μm) only when the SSHE unit is set at its minimum rotor rate. These results also indicate that when the SSHE is set at its top rotor rate, the shear applied by this mixer produces the smallest droplets.

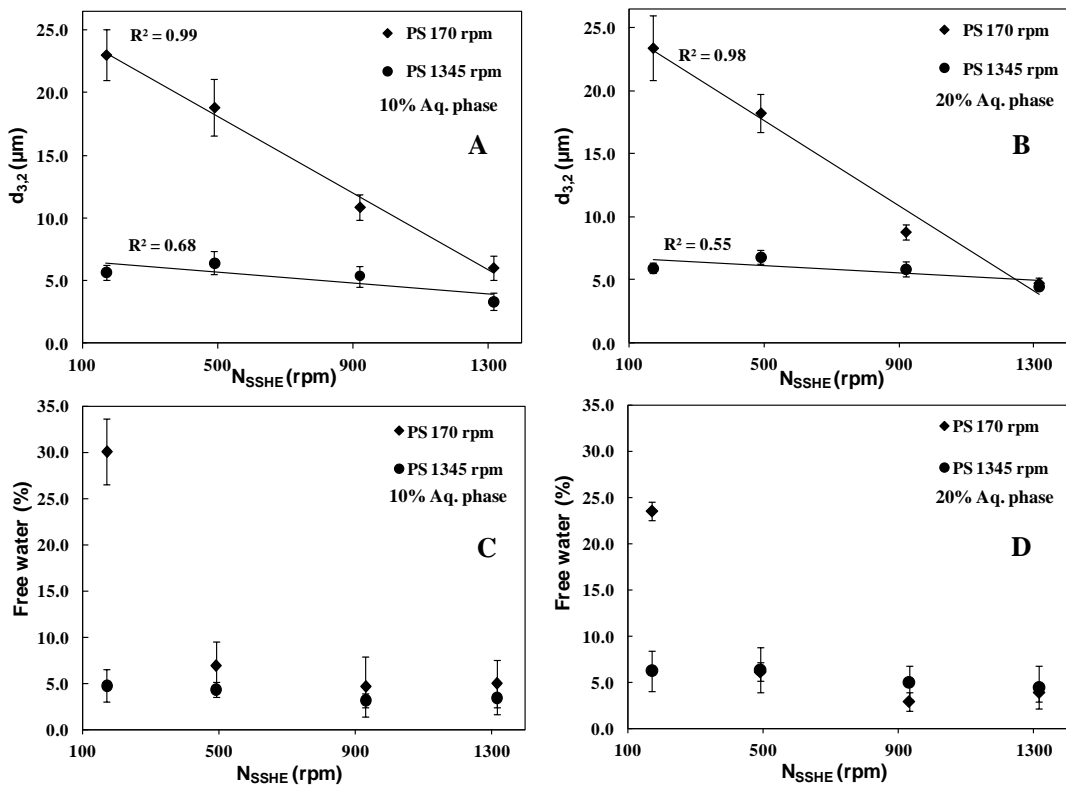


Figure 4.1: Average $d_{3,2}$ of emulsions containing (A) 10% and (B) 20% (wt%) aqueous phase; average free water content (%) of emulsions containing (C) 10% and (D) 20% aqueous phase. All emulsions contain 1% PGPR (wt%) overall. Diamonds and circles represent emulsions produced using a N_{PS} of 170 and 1345 rpm, respectively. Error bars are one standard deviation of triplicates (where no visible, error bars are smaller than symbols).

4.2.1.2. Use of Margarine line: Effect of PS rotational speed on droplet size

To elucidate the role played by the PS on emulsion formation and final droplet size, 10 and 20% aqueous phase emulsions were produced using two N_{SSHE} speeds (490 or 930 rpm) at increasing N_{PS} (170, 500, 920, 1345 rpm).

When the N_{SSHE} was set at 490 rpm (Figure 4.2A and B), an increase in the N_{PS} produced a considerable reduction in the final $d_{3,2}$ values (from approximately 19 to 7 μm): the decrease in $d_{3,2}$ was linear with increasing N_{PS} ($R^2 \geq 0.98$) suggesting a predominant PS role on emulsion formation. The trend was similar when N_{SSHE} was set to 930 rpm. Nevertheless, increasing N_{PS} at this higher N_{SSHE} had a smaller effect on droplet size reduction (from approximately 11 to 6 μm) than observed with N_{SSHE} at 490 rpm. This

result suggests that when small droplets are formed within the SSHE (at higher N_{SSHE}), the PS can effectively only reduce the size of droplets at high rotor rates (maximum N_{PS}). The results also indicate that $6 \mu\text{m}$ is the smallest achievable droplet size (within the experimental conditions). Nevertheless, the good linear correlation between $d_{3,2}$ data and N_{PS} ($R^2 \geq 0.91$) suggests that the final droplet size is determined by the PS.

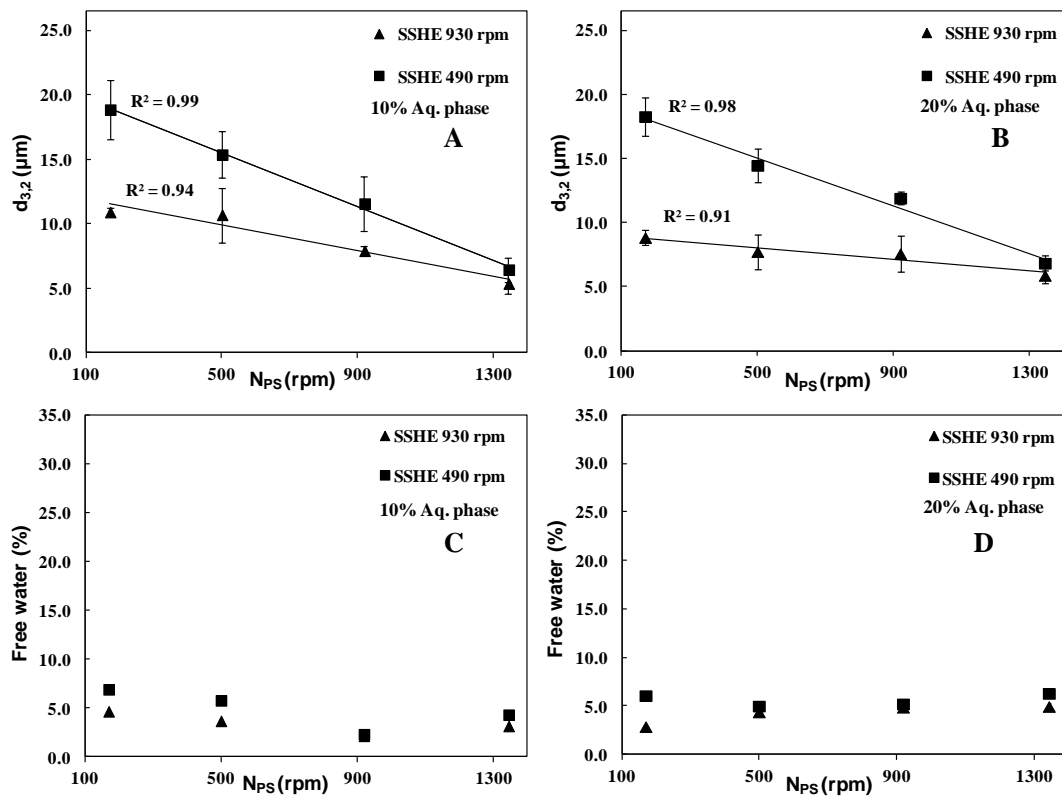


Figure 4.2: Average droplet size ($d_{3,2}$) of emulsions containing (A) 10% and (B) 20% (wt%) aqueous phase; average free water content (%) of emulsions containing (C) 10% and (D) 20% aqueous phase. All emulsions contain 1% PGPR (wt%) overall. Squares and triangles represent emulsions produced using a N_{SSHE} of 490 and 930 rpm, respectively. Error bars are one standard deviation of triplicates (where no visible, error bars are smaller than symbols).

For all systems, the dispersed phase was mostly structured into small droplets with free water values of approximately 6% (Figure 4.2C and D).

Although the results shown suggest that emulsion droplet size is determined by the mixer of the margarine line set at the highest rotational speeds, it remains unclear whether it is

necessary to use both the SSHE and PS to obtain emulsions with an average droplet size below 10 μm (which would ensure higher microbial stability), as to obtain this data neither mixer was used in isolation.

4.2.1.3. Effect of SSHE alone on emulsion droplet size

Results discussed in previous sections refer to emulsions produced with the margarine line using different combinations of the rotational speeds of both mixers. To gain a better understanding of the role played by each mixer on water-in-cocoa butter emulsion droplet size, an emulsifying process based on the use of the SSHE alone was investigated. To allow comparisons, the four SSHE rotational speeds (N_{SSHE}) described in Section 4.2.1.1. were again used here. The SSHE jacket temperature was kept at 25 °C and the flow rate at 30 mL/min. Average $d_{3,2}$ and free water content values for 10 and 20% water emulsions are shown in Figure 4.3A and B, respectively, as a function of N_{SSHE} .

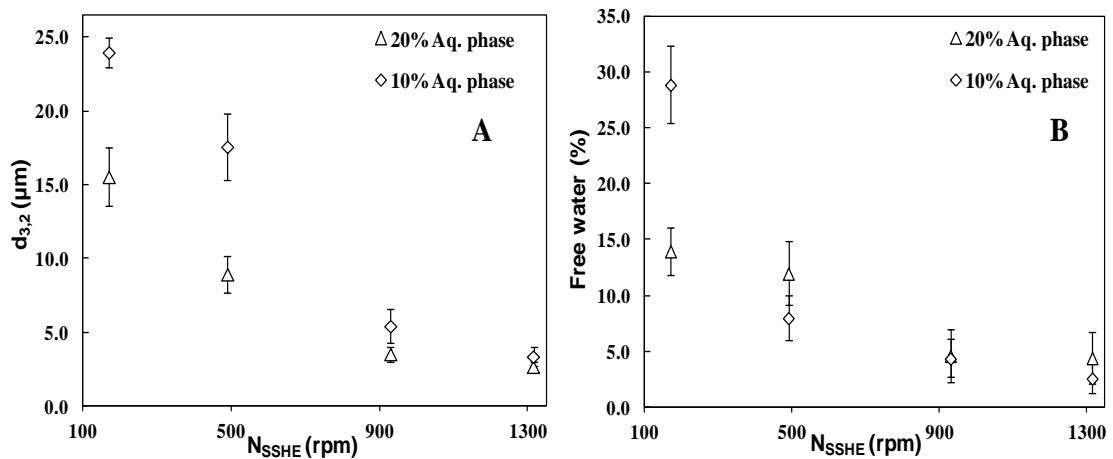


Figure 4.3: (A) average $d_{3,2}$ and (B) free water (%) of emulsions containing 10 and 20% (wt%) aqueous phase as function of N_{SSHE} . All emulsions contain 1% PGPR (wt%) overall. Error bars represent plus and minus one standard deviation of triplicates (where no visible, error bars are smaller than symbols).

It can be observed that for both emulsified systems the $d_{3,2}$ and free water content decreased at increasing N_{SSHE} ; reaching the minimum values ($d_{3,2} \sim 3 \mu\text{m}$ and free water $\sim 3.5 \%$) at maximum N_{SSHE} . This $d_{3,2}$ is smaller than those reported in the previous sections. The decrease in droplet size with increasing N_{SSHE} can be explained considering that at higher rotational speed, more energy is put into the systems and, therefore, a higher number of droplet break-up events is expected to occur. Furthermore, the increase in the N_{SSHE} enhances heat exchange and cooling-crystallisation of CB. This would result in an increase in the viscosity of the continuous phase which in turn would promote droplet deformation and break-up. At low N_{SSHE} (≤ 500 rpm), emulsions containing 10% aqueous phase have a larger droplet size than the 20% systems. This difference may be due to differences in the viscosity ratio between dispersed and continuous phase. At low rotational speed (≤ 500 rpm) this may have a larger impact than at higher rate (≥ 900 rpm), hence the observed discrepancy in droplet size.

Emulsion samples for microstructure visualisation were collected immediately after emulsification and prior to the completion of crystallisation. The microstructures of 20% aqueous phase emulsions produced with the SSHE at four shaft speeds are shown in Figure 4.4.

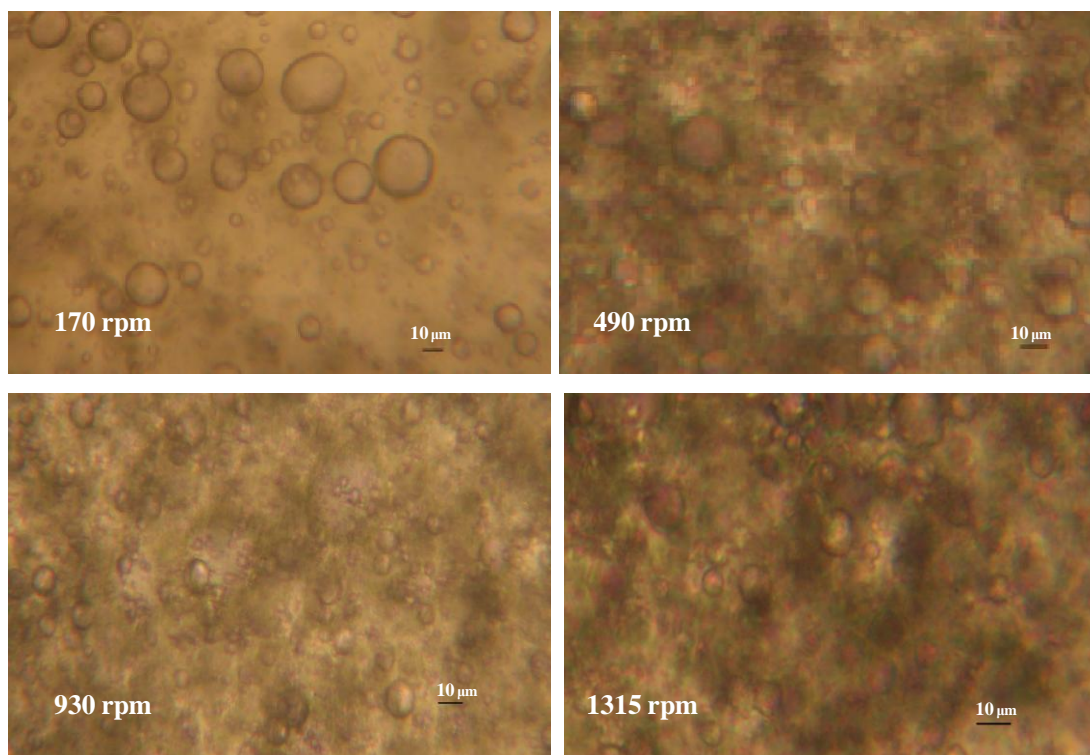


Figure 4.4: Micrographs of 20% aqueous phase emulsions produced using the SSHE at four rotational speeds (indicated in the image).

The emulsions appear to be characterised by spherical droplets with a size range in agreement with NMR data shown in Figure 4.3A. Systems produced with the lowest N_{SSHE} (170 rpm) were mainly characterised by large droplets ($> 20 \mu\text{m}$), whereas emulsions produced at N_{SSHE} of 490 rpm represents an intermediate situation where both small and large droplets are visible. For emulsions produced with a N_{SSHE} of 930 or 1315 rpm, most water droplets appear to have a diameter below $10 \mu\text{m}$. The dark background visible in the micrographs is due to the presence of crystalline fat material. After processing, the emulsions appeared as a viscous material due to the ongoing crystallisation process and then completely solidified within a few minutes, which imposed some limitations to microstructure visualisation using bright field microscopy.

Stability over time represents a requisite for the application of water-in-cocoa butter emulsions and it is defined here as the ability of the systems to retain their original droplet size. Emulsion stability was evaluated at 20 °C using emulsions containing 20% aqueous phase. Values of $d_{3,2}$ and free water content were measured at 1, 7, and 30 days after production and have been compiled in Table 4.1.

Table 4.1: $d_{3,2}$ and free water (%) values (standard deviation given in brackets) as a function of SSHE and PS rotational speed for emulsions containing 20% water at three time points.

Shear Combination	$d_{3,2}$ (μm)			Free water (%)		
	1 day	7 days	30 days	1 day	7 days	30 days
N_{SSHE} 170 rpm,	5.9	5.1	5.3	5.0	4.0	4.4
N_{PS} 1345 rpm	(± 0.4)	(± 0.5)	(± 0.2)	(± 2.0)	(± 1.0)	(± 1.0)
N_{SSHE} 500 rpm,	6.8	6.2	6.4	5.2	6.0	5.4
N_{PS} 1345 rpm	(± 0.6)	(± 0.5)	(± 0.3)	(± 1.5)	(± 0.8)	(± 1.0)
N_{SSHE} 930 rpm,	5.9	4.3	4.5	5.0	5.0	4.8
N_{PS} 1345 rpm	(± 0.6)	(± 0.8)	(± 0.6)	(± 2.0)	(± 2.0)	(± 1.7)
N_{SSHE} 1315 rpm,	4.5	4.4	4.6	4.4	6.0	5.0
N_{PS} 1345 rpm	(± 0.3)	(± 0.5)	(± 0.3)	(± 2.2)	(± 1.0)	(± 1.0)
N_{SSHE} 170 rpm	15.5	17.0	16.5	15.1	13.3	11.0
	(± 2.0)	(± 1.5)	(± 1.3)	(± 2.2)	(± 1.0)	(± 0.8)
N_{SSHE} 1315 rpm	2.7	3.0	3.1	4.4	5.0	4.7
	(± 0.3)	(± 0.4)	(± 0.3)	(± 0.6)	(± 1.0)	(± 1.0)

Over the investigated storage time, all systems remained stable. These results indicate that bulk and/or interfacial fat stabilisation of water droplets is effective against destabilisation mechanisms below the melting temperature (≥ 35 °C). The small changes

observed for emulsions produced using a N_{SSHE} of 170 rpm (characterised by a large initial $d_{3,2}$ and free water content) could be explained due to sampling variation (indicated by the larger error bars).

These results indicate that stable water-in-cocoa butter emulsions with similar droplet sizes can be produced using either the full margarine line or the SSHE alone. To quantify the contribution of each mixer on final droplet size, the difference ($\Delta d_{3,2}$) in the average $d_{3,2}$ for emulsions produced using the two processing conditions were calculated using Equation 4.1, where, $\Delta d_{3,2}$ (expressed in μm) is the change in the average droplet size and $d_{3,2[SSHE\&PS]}$ and $d_{3,2[SSHE]}$ are the average $d_{3,2}$ values of water-in-cocoa butter emulsions produced using the SSHE and PS (i.e., the margarine line) and SSHE alone, respectively:

$$\Delta d_{3,2} = d_{3,2[SSHE\&PS]} - d_{3,2[SSHE]} \quad (\text{Eq. 4.1}),$$

The data used for the calculation are those shown in Figures 4.1A and B and 4.3A for both 10 and 20% aqueous phase emulsions. From Eq. 4.1 it can be easily understood that a positive $\Delta d_{3,2}$ indicates that the emulsion produced by the margarine line has a larger size than the corresponding one produced using the SSHE only. The opposite is, therefore, true in the case of a negative $\Delta d_{3,2}$. Values of $\Delta d_{3,2}$ have been compiled in Table 4.2 with the four corresponding values of SSHE rotational rate displayed in the first column.

Table 4.2: Values of $\Delta d_{3,2}$ (in μm) for emulsions containing 10 and 20% aqueous phase and produced using either the SSHE alone (at four rotor speeds) or in series with the PS working at two rotor speeds (N_{PS}). According to equation 4.1, positive and negative values denote an increase and decrease in $d_{3,2}$, respectively, as a result of using the PS.

N_{SSHE} (rpm)	<i>10% Aqueous Phase</i>		<i>20% Aqueous Phase</i>	
	N_{PS} 170 rpm	N_{PS} 1315 rpm	N_{PS} 170 rpm	N_{PS} 1315 rpm
170	-0.9	-18.3	+6.4	-11.1
490	+1.3	-11.1	+9.4	-2.1
930	+5.5	-0.1	+5.3	+2.4
1315	+2.7	0.0	+2.1	+1.8

Data shown in Table 4.2 suggest that the use of the PS produces an increase in water droplet size. In detail, water-in-cocoa butter emulsions produced using the SSHE at any N_{SSHE} appear to be characterised by $d_{3,2}$ values smaller than those of emulsions produced using the full margarine line with the PS set at 170 rpm. This result suggests that when the PS is set at low rotational rate, the shear provided by this mixer produces an increase in the average droplet size probably induced by droplet coalescence. For N_{SSHE} below 500 rpm, 10 and 20% emulsions produced using the margarine line with the PS set at its top rotor rate (1345 rpm) were characterised by significant lower $d_{3,2}$ values ($\sim 10 \mu\text{m}$) than the emulsions with the same formulation produced using the SSHE alone. Nevertheless, for N_{SSHE} above 900 rpm, emulsions produced using the SSHE alone had the smallest droplet size.

To summarise, these results clearly suggest that the effect of PS on final droplet size depends upon the rate at which the SSHE and PS are rotating with respect to each other.

When low rotational speed is applied in the SSHE ($N_{SSHE} < 500$ rpm), the droplets produced are large and can be either coalesced and further broken in the PS: if the PS is set at low rotor rate ($N_{PS} < 500$ rpm), the increase in $d_{3,2}$ is a result of increased coalescence and limited droplet break-up; however, for N_{PS} above 900 rpm, the shear applied in the PS promotes the formation of smaller droplets, with a $d_{3,2}$ value of approximately $6 \mu\text{m}$ being the minimum achievable size (at $N_{PS} = 1345$ rpm). These results are in agreement with those published by Norton and Fryer (2012): the authors concluded that the shear rates within the PS could further reduce the $d_{3,2}$ if droplets produced in the SSHE were larger than the smallest achievable size in the PS. However, the authors did not consider the possibility that the use of PS could also promote an increase in the final $d_{3,2}$. In fact, the results reported in this work show that for N_{SSHE} higher than 900 rpm, a process based on the SSHE alone allowed for the production of emulsions with the smallest diameter ($d_{3,2} \sim 3 \mu\text{m}$) whilst utilising the whole margarine line produced emulsions characterised by larger droplets at any N_{PS} . Although the observed differences in $d_{3,2}$ are small and may be within experimental error, these results clearly suggest that the use of the PS is not necessary to obtain emulsions with small droplets, with a $d_{3,2}$ of $3 \mu\text{m}$ being the minimum achievable droplet size, when N_{SSHE} is above 900 rpm. A similar effect on water droplet size has been observed for margarine, where the shear applied within PS also promoted an increase in size (Heertje *et al.*, 1988).

4.2.1.4. *Effect of residence time on average droplet size*

It has been shown above that stable water-in-cocoa butter emulsions with small average droplet sizes can be produced using the SSHE alone. It is reasonable to think that the total shear experienced, as governed by number and type of mixers used, residence time, and processing temperature, would play a key role on determining emulsion droplet size. The work presented in this section evaluates the effect of residence time on the $d_{3,2}$ and free water content of 20% aqueous phase emulsions. A flow rate of 60 mL/min was selected which resulted in a measured residence time of 28 s (± 2 s) and 165 s (± 3 s) in the SSHE and PS, respectively. In order to maintain a SSHE inlet temperature of 40 °C (± 0.8 °C), the temperature in the feeding vessel was decreased to approximately 46 °C while all the other settings were left unchanged. The average outlet temperature was 28 (± 0.7 °C) and 33.9 °C (± 0.1 °C) for the SSHE and PS, respectively. In order to be able to compare these results with those obtained for emulsions produced at 30 mL/min, some of the rotational speed combinations discussed in the previous sections were assessed again here and are listed in Table 4.3.

Table 4.3: $d_{3,2}$ and free water values, (standard deviation given in brackets) as a function of SSHE and PS rotational speed, for emulsions containing 20% water experiencing different time lengths and combinations of shearing.

Shearing conditions	$d_{3,2}$ (μm)		Free water (%)	
	30 mL/min	60 mL/min	30 mL/min	60 mL/min
N_{SSHE} 170 rpm, N_{PS} 1345 rpm	5.9 (± 0.4)	5.1 (± 0.5)	5.0 (± 1.2)	4.7 (± 1.7)
N_{SSHE} 1315 rpm, N_{PS} 170 rpm	4.8 (± 0.3)	5.6 (± 0.4)	3.9 (± 0.7)	5.9 (± 1.5)
N_{SSHE} 1315 rpm, N_{PS} 1345 rpm	5.4 (± 0.4)	5.1 (± 0.4)	4.4 (± 1.2)	4.1 (± 2.3)
N_{SSHE} 170 rpm	15.5 (± 1.5)	17.0 (± 2.0)	15.1 (± 2.2)	13.5 (± 3.5)
N_{SSHE} 1315 rpm	2.7 (± 0.5)	5.1 (± 0.6)	4.4 (± 0.6)	4.7 (± 2.1)

Results compiled in Table 4.3 show that no difference was observed in the $d_{3,2}$ and free water content values for emulsions produced using the full margarine line. This result indicates that the overall applied shear allows for the production of emulsions with small droplets even at low residence times. For emulsions produced using the SSHE alone a larger droplet size was observed, although only for the emulsion produced at the maximum N_{SSHE} the size increase is significant. However, the average $d_{3,2}$ and free water content value of the emulsion produced using the SSHE alone at its maximum rotor rate and 60 mL/min as flow rate were comparable to that obtained using the full margarine line. This result suggests that an emulsification process based on the use of this mixer alone is still preferable. These results are in good agreement with those reported by

Norton and Fryer (2012). It can be predicted that a flow rate above 60 mL/min would result in larger droplets; therefore, no experiments were done to further investigate the effect of this processing parameter.

4.2.1.5. *Effect of the SSHE outlet Temperature on the final droplet size*

Processing temperature is expected to play a critical role on emulsion droplet size as it determines the temperature gradients experienced by the sample and the physical state of CB. It should be noted that the level of CB crystallisation affects the rheological properties of the system, the subsequent droplet break-up, and the total amount of crystallised material stabilising the emulsions. Due to the complexity of the system and the number of phenomena occurring simultaneously, an empirical approach was adopted to evaluate the effect of temperature on final droplet size.

Emulsions containing 20% aqueous phase and 1% PGPR were produced using the SSHE alone ($N_{SSHE} = 1315$ rpm), at 30 mL/min. During emulsification, the SSHE jacket temperature was varied to obtain five outlet temperatures (T_{out}): 23, 26, 28, 34, and 50 °C. Values of T_{out} below 30 °C, aimed to initiate crystallisation while shearing. A T_{out} of 34 °C was selected as it is very close to CB form V final melting point (~35 °C) and, therefore, no, or very little, crystallisation was expected to occur within the mixer. For these emulsions the start of crystallisation was visually observed soon after leaving the SSHE. Finally, for a T_{out} of 50 °C no crystallisation occurred within the mixer and the system remained mostly liquid for over 15 minutes after leaving the SSHE. In Figure 4.4 data showing the effect of processing temperature on the droplet characteristics are shown.

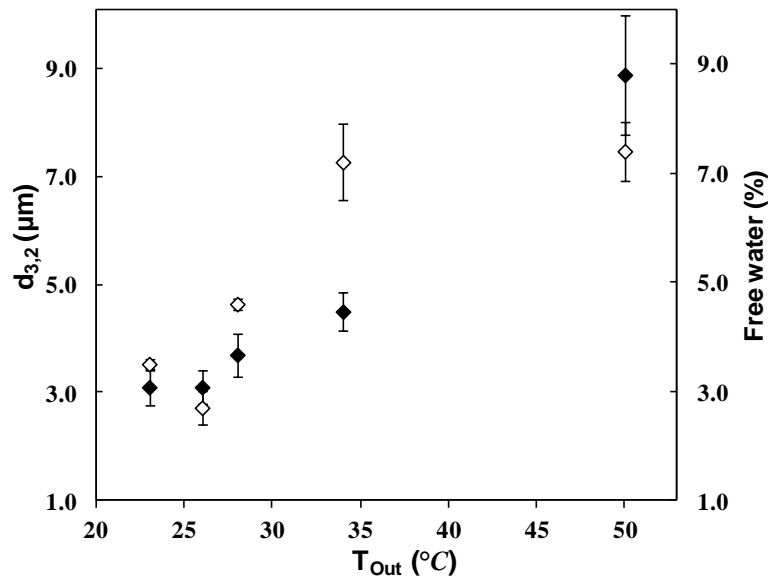


Figure 4.5: Average $d_{3,2}$ (◆) and free water % (◇) of 20% (wt%) aqueous phase emulsions as function of the SSHE T_{out} . All emulsions contain 1% PGPR (wt%) overall. Error bars represent one standard deviation of triplicates.

For emulsions produced with a T_{out} below 30 °C, no difference in droplet size was observed, suggesting the systems must overall behave similarly within this temperature range. This can be explained considering that at the selected temperatures the extent of CB crystallisation is comparable. The presence of crystalline fat would then promote droplet formation, by increasing the shear transmitted by the blades (see below), and stabilisation.

A small increase in the $d_{3,2}$ value was observed for emulsions produced with an outlet temperature of 34 °C together with a more pronounced increase in free water content. To explain this result it could be hypothesised that, at this temperature, only a small amount of TAGs can crystallise under shear and then contribute to emulsion stabilisation. This implies that only a small amount of fat crystals would be available for Pickering stabilisation of the newly formed droplets and bulk crystallisation would occur over a longer time scale. The reduced contribution of crystallised fat to droplet stabilisation

would result in increased coalescence and, in turn, a higher $d_{3,2}$ and free water content. The average $d_{3,2}$ and free water obtained for emulsions produced with a T_{out} of 50 °C were characterised by larger values (by approximately threefold) than those obtained for systems produced when crystallisation occurred on emulsification. Also, in this latter case, the absence of fat crystals providing stability could explain the larger droplet size. Another explanation for this result may be gained considering that when crystallisation occurs during emulsification, the presence of fat crystals produces a viscosity increase of the continuous phase and a decrease in the viscosity ratio between phases (viscosity dispersed phase η_D / viscosity continuous phase η_C), which would result in a greater droplet break-up at a given shear rate (Walstra, 1993).

To evaluate droplet stability in the absence of crystalline material, emulsions produced at 25 °C were heated to 50 °C for over 60 minutes. As will be shown in more detail in Chapter 6, no increase in droplet size occurred following this re-heating step, suggesting that the interfacial layer created by the PGPR was able to prevent coalescence.

In the light of what has been discussed above, it is reasonable to think that the smaller droplet size obtained at processing temperatures below 30 °C arises mainly from a more efficient droplet break-up process.

4.2.1.6. *Data model fitting*

It has been shown, in Section 4.2.1.5., that emulsions characterised by a $d_{3,2}$ of approximately 3 μm can be produced when the temperature of the emulsion at the exit of the SSHE is below or equal to 28 °C. In order to be able to predict emulsion characteristics when using different devices and/or attempting to scale-up processes, it is useful to have models relating droplet size to key processing parameters. Despite SSHEs

being widely used in the food industry to produce complex emulsions, such as ice cream and margarines (Rao and Hartel, 2006), no models are available which express the final $d_{3,2}$ as a function of process parameters such as “energy dissipation rate”. This is probably due to the highly complex hydrodynamic conditions occurring on emulsification, which result from the combination of a Couette and Poiseuille flow, where the action of the scraping blades creates perturbations (Dumont *et al.*, 2000).

The aim of the work presented in this section was to evaluate whether the empirical model used in the literature for other high shear mixers could provide a good fitting of droplet size data for emulsions produced using a SSHE. Emulsions containing 20% aqueous phase and 1% PGPR were produced using the same rotational speeds as in Section 4.2.1.3., and at three outlet temperatures (T_{Out} , 23, 26, 28 °C), to ensure crystallisation occurred on emulsification.

It should be considered that, for high shear mixers, only a few empirical models are available in the literature, which provide good predictions of droplet size data and useful indications for scaling-up, and therefore much research is needed in this field (Hall *et al.*, 2011a, b). For continued stirred tanks, empirical approaches have been used, expressing the $d_{3,2}$ as a function of the energy density (Schubert and Engel, 2004) or tip speed (EL-Hamouz *et al.*, 2009), both using a power law model. A power law equation has the general form shown in Equation 4.3, where, a , the pre-exponential factor, and b , the exponent, are two constants:

$$y = ax^b \quad (\text{Eq. 4.3}).$$

Considering that some similarities exist between a continuous stirrer tank and a SSHE, and that it was not possible to measure the power draw of the SSHE, it was decided to

adopt the model proposed by EL-Hamouz *et al.* (2009); therefore, in Figure 4.6 the average Sauter mean diameter ($d_{3,2}$) of emulsions has been expressed as a function of the tip speed.

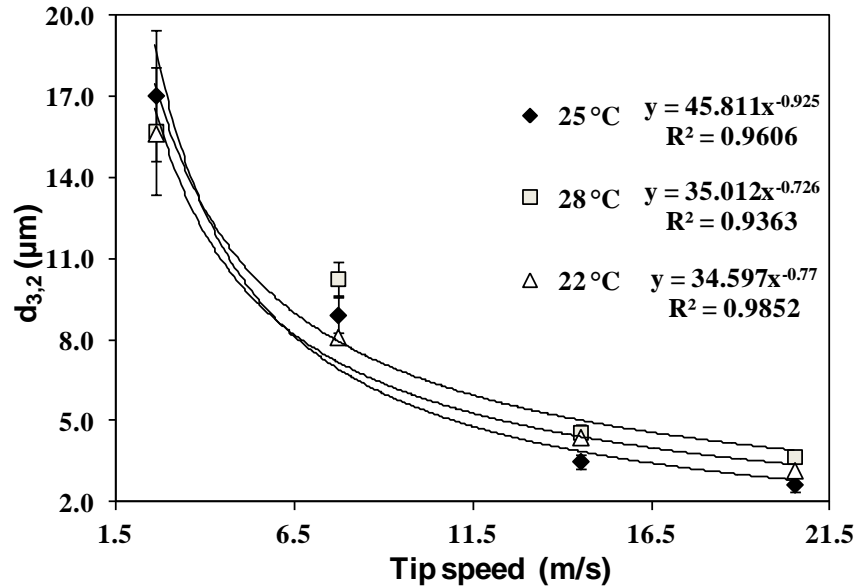


Figure 4.6: $d_{3,2}$ values as function of tip speed for emulsion containing 20% (wt%) dispersed phase and produced at different T_{out} . All emulsions contain 1% PGPR (wt%) overall. Results are average of triplicates and error bars represent one standard deviation (where no visible, error bars are smaller than symbols).

Results suggest that data fitting to the model was good with an R^2 of 0.986, 0.960, and 0.936, for a T_{out} of 23, 26, 28 °C, respectively. It should be noted that the droplet size is comparable among systems at Tip speed- T_{out} combinations, suggesting that the overall emulsifying process must be the same when CB crystallisation occurs on emulsification. However, from the data available here, it is not possible to define the type of flow which determines the droplet break-up process. In the case of in-line rotor-stator mixers, Schubert and Engel (2004) showed that an exponent value of approximately -0.75 indicates that the $d_{3,2}$ is determined by turbulent shear flow. Although here the exponent (b) had a value < -0.73 for all systems, it cannot be concluded that the same type of flow determined the droplet break-up for the investigated systems. Although it is not clear, at

this stage, why droplet size data expressed as a function of the tip speed, are well fitted by a power law model, results suggest that this model may be used to obtain an approximate prediction of the final $d_{3,2}$ when using a different SSHE under similar processing conditions. The development of a more accurate model would need to consider other parameters such as dispersed phase fraction, effect of temperature on the viscosity changes of continuous and dispersed phases, and CB phase transition. These aspects were not the focus of this thesis and, therefore, were not further investigated.

4.2.2. Effect of processing conditions on CB polymorphic form

The polymorphism of CB is significantly affected by processing conditions, with applied shear and cooling profile playing a critical role. As referred to in the introduction of this chapter, the goal of this work is the production of stable tempered emulsions. In this section, the melting behaviour of the systems was characterised in order to assess the effect of processing on continuous fat phase crystallisation. The systems investigated contained both 10 and 20% aqueous phase and were produced using the full margarine line. The polymorphism of emulsions prepared using the SSHE alone was also investigated.

A temperature profile similar to that applied in chocolate manufacture was applied here, as it was hypothesised this would allow tempering of the emulsions (see Section 3.2.1.2.). Accordingly, CB should be initially crystallised in the SSHE (first mixer) in a mixture of polymorphic forms (unstable (II, III, and IV) and stable (V) polymorphs) and then partially re-melted in the PS (second mixer) to erase unstable forms while preserving the stable ones. These crystals would then act as “secondary heterogeneous nuclei”, driving

the crystallisation, upon cooling, into the desired form. The result of such process would be a tempered CB showing a major melting peak at around 32 °C.

In Table 4.4 the rotational speed combinations studied have been compiled together with the melting properties of the emulsions: number of peaks, melting peak temperatures, and corresponding polymorphic forms according to literature data (Wille and Lutton, 1966; Loisel *et al.*, 1998a). The melting temperature was determined as the maximum point of the endothermic curves, rather than at the onset, because of polymorph peak overlapping (Loisel *et al.*, 1998a; Maleky and Marangoni, 2008). Results clearly indicate that emulsion melting behaviour was directly influenced by the shear experienced, and the majority of systems were characterised by a mixture of polymorphic forms. The measured melting points are in agreement with those published by Wille and Lutton (1966), although higher as theirs referred to the onset temperature. A similar shift to higher temperatures of melting was also reported for CB in chocolate systems (Loisel *et al.*, 1998b).

Table 4.4: Melting properties of water-in-cocoa butter emulsions.

<i>Shearing combination</i>	<i>Number of peaks</i>	<i>Peak values (°C)</i>	<i>Polymorphic form</i>
N_{SSHE} 170 rpm, N_{PS} 1345 rpm	3	23; 29; 33	III, IV, V
N_{SSHE} 490 rpm, N_{PS} 170 rpm	3	22; 29; 32	III, IV, V
N_{SSHE} 930 rpm, N_{PS} 1345 rpm	3	22; 27; 32	II, IV, V
N_{SSHE} 1315 rpm, N_{PS} 1345 rpm	3	22; 28; 33	III, IV, V
N_{SSHE} 170 rpm	3	23; 28; 32	III, IV, V
N_{SSHE} 490 rpm	3	23; 28; 32	III, IV, V
N_{SSHE} 930 rpm	1	33	V
N_{SSHE} 1315 rpm	1	32	V

The melting curves of samples produced using the full margarine line showed a complex profile (Fig. 4.7) indicating that the experienced shear-temperature profile did not provide effective tempering. Inspection of the endothermic curves for all the emulsions revealed the presence of a peak at around 32 °C, indicating the presence of form V; although in some samples this peak was only small peak.

In detail, when both mixers were set at a low rotational speed (170 and 500 rpm; Fig. 4.7A, B, C, D), CB crystallised mostly in the unstable polymorphic forms (II and III) with a main melting peak at temperatures between 20 and 25 °C. The presence of small amounts of the desired form V was revealed by a small peak in the corresponding temperature range (above 30 °C).

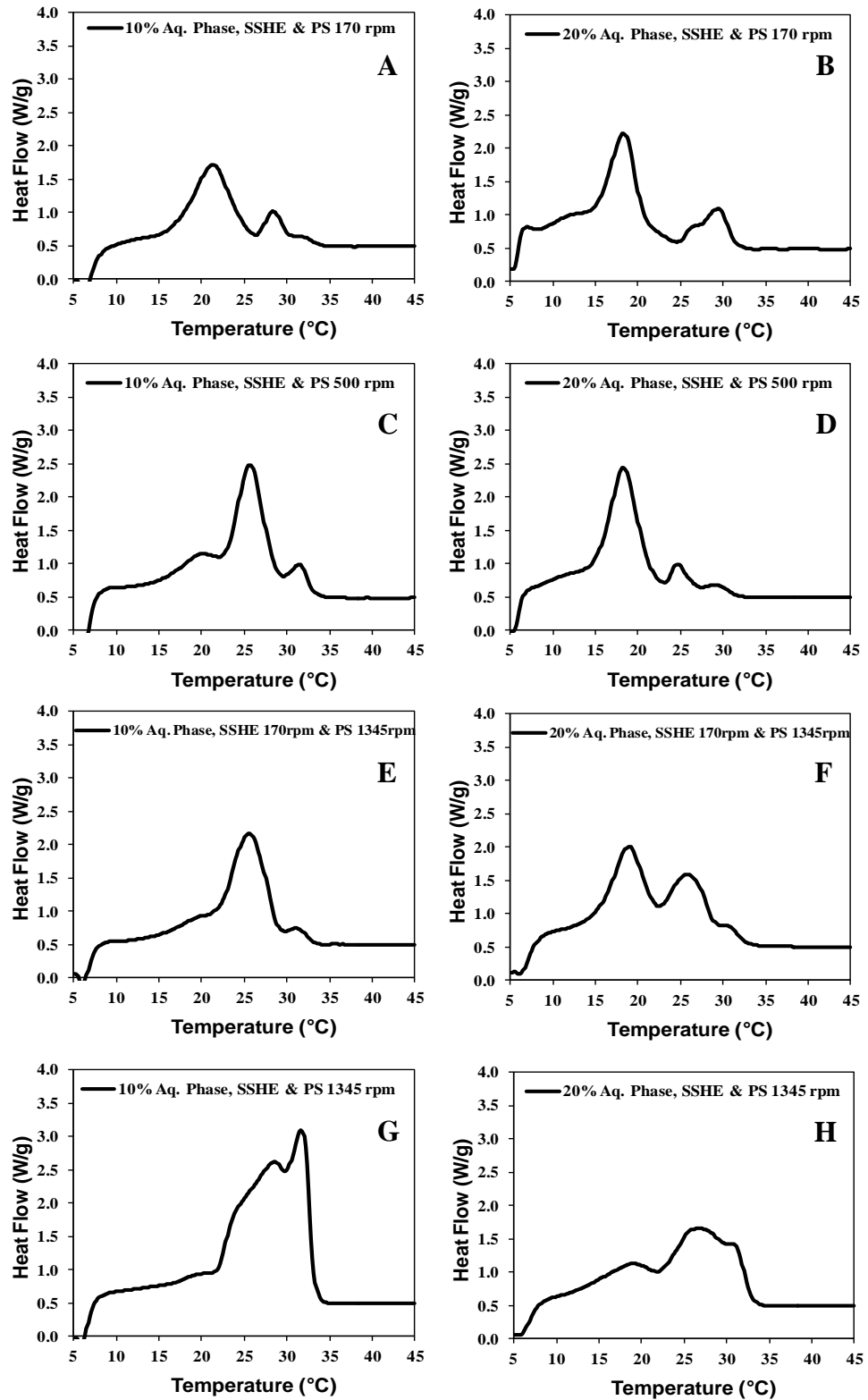


Figure 4.7: Melting curves of 10 (left) and 20% (right) aqueous phase emulsions produced using various combinations of SSHE and PS rotor rates: A – B, C – D, and G - H correspond to a set up where both units are at 170, 500, and 1345 rpm, respectively. E – F have been obtained with SSHE at 1315 rpm and PS at 170 rpm. For clarity the used shear combinations are referred for each curve together with the percentage of dispersed phase.

When the SSHE was providing minimum shear (N_{SSHE} of 170 rpm, Fig. 4.7E and F), so that a lower extent of crystallisation would be expected to occur, and when PS was set at the maximum rotor rate, emulsions crystallised mostly into unstable forms. In a scenario where the SSHE was providing maximum shear (N_{SSHE} of 1315 rpm, Fig. 4.7G and H), the presence of a larger fraction of form V could be deduced from the endotherms, suggesting that this mixer on its own may be effective at tempering emulsions. According to the initial hypothesis, a process based on the margarine line, should have mimicked the tempering procedure used in chocolate manufacture, thus producing an emulsion crystallised predominantly in form V. However, results show that with the selected set-up it is not possible to achieve tempering. Norton and Fryer (2012) have also shown the impossibility of tempering water-in-cocoa butter emulsions using the same margarine line but whilst adopting a different set-up. Two explanations could be found for this result: (1) CB crystals in form V produced in the SSHE were re-melted in the PS; (2) if form V crystals endured the re-melting stage, they were below the 1-3 (volume%) thought to be necessary to temper CB (Svanberg *et al.*, 2011). All systems showed to be in form V within 48 hours. This result was to be expected as the presence of fat crystals in form V, within all samples, would act as a template promoting the monotropic evolution toward the more stable form.

In Figure 4.8 the thermographs of 20% water-in-cocoa butter emulsions produced using the SSHE only are shown. These results strongly suggest that if the SSHE is working at high rotational speed, it can temper the CB.

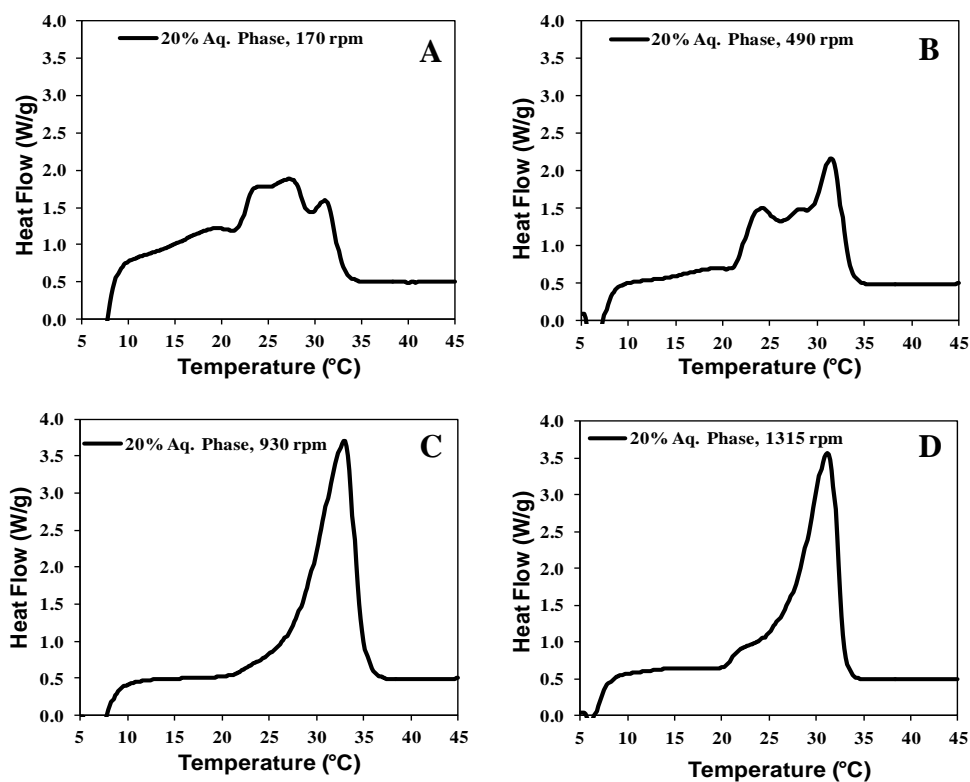


Figure 4.8: Melting curves of 20% aqueous phase emulsions produced using the SSHE only at four rotational speed: 170 rpm (A), 490 rpm (B), 930 rpm (C), and 1315 rpm (D).

For systems processed using a N_{SSHE} of 170 and 490 rpm, the presence of several peaks revealed the co-existence of different polymorphs: the broad peak at the lower temperatures is due to form II (α), whereas the large peak at temperatures between ~ 20 and 32 °C is due to the coexistence of forms III, IV, and V. It can be noted that for a N_{SSHE} value of 490 rpm the peak at 32 °C is the main one. Furthermore, for N_{SSHE} values of 930 and 1315 rpm CB was crystallised predominantly into the desired polymorph V as clearly indicated by a predominant sharp melting peak at around $32-33$ °C. The observed transition toward more stable polymorphs at increased applied rotor rates is in line with results published in literature for different crystallising fats, including CB (MacMillan *et al.*, 2002; Mazzanti *et al.*, 2003; Maleky *et al.*, 2008). It was shown in these works that the structure, in addition to the rate of transformation toward more stable, higher melting,

polymorphs, is due to the applied mechanical force, in particular shear stresses. In line with the findings of Mazzanti *et al.* (2003), it can be postulated that an increase in rotational speed promotes the formation of a larger number of smaller crystals and the application of shear forces on crystal surfaces would promote a faster transition toward the desired polymorphic form. These results strongly suggest that the SSHE can be used as a continuous direct emulsifying-tempering device as an alternative to the full margarine line.

Finally, over a thirty day period of observation at 5 °C, no transition to the highest polymorph (form VI) was observed in any of the systems, suggesting the systems remained stable.

4.2.3. Effect of process and formulation on emulsion droplet size

4.2.3.1. Production of emulsions with higher dispersed phase percentage

It has been shown in previous sections that stable water-in-cocoa butter emulsions can be produced using the margarine line. Furthermore, the SSHE alone is a suitable device for the production of stable tempered water-in-cocoa butter emulsions with an aqueous phase percentage up to 20%. However, to be able to effectively reduce the fat content of chocolate, the dispersed phase fraction should be increased. Therefore, the aim of the work presented in this section is to investigate the production of emulsions containing higher aqueous phase percentage using either the margarine line (with both mixers at maximum rotational speed) or the SSHE alone (at the maximum shaft speed; for other settings see Section 3.2.1.2.). Findings of this work will allow us to establish whether a process based on the SSHE alone is suitable for the production of emulsions with a

higher aqueous phase percentage. For this set of experiments the concentration of PGPR was kept at 1% (wt%) of the total emulsion mass.

In Figure 4.9A and B the average $d_{3,2}$ and free water content of emulsions produced using the SSHE alone or the margarine line at increasing aqueous phase fraction percentage is shown.

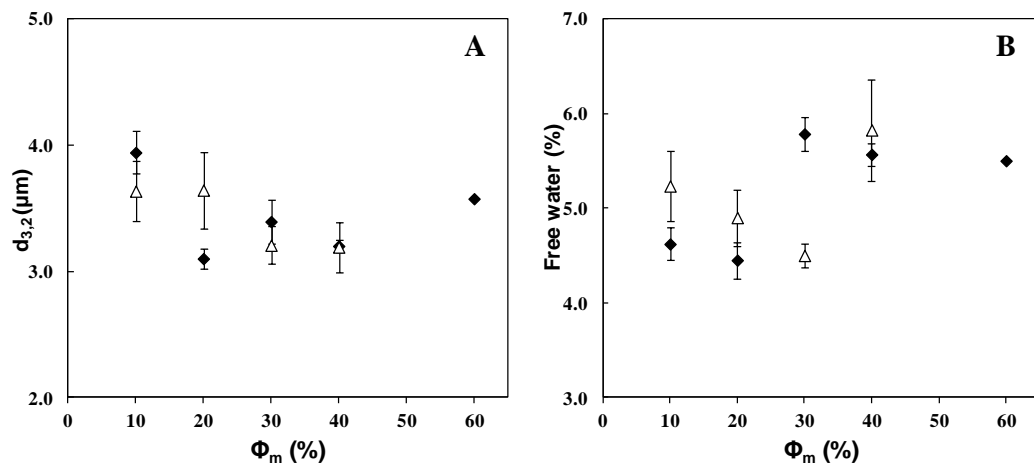


Figure 4.9: Effect of dispersed phase percentage (Φ_m , %) on (A) droplet size ($d_{3,2}$) and (B) free water content for emulsions produced using the SSHE alone (diamonds) or the full margarine line (white triangles). All emulsions contain 1% PGPR (wt%) overall. Error bars represent one standard deviation of triplicates (where no visible, error bars are smaller than symbols).

Results shown in Figure 4.9 demonstrate that when using the full margarine line, water-in-cocoa butter emulsions containing up to 40% dispersed phase can be produced, with the average $d_{3,2}$ and free water content being approximately 4 μm and 5%, respectively. These results are in agreement with those stated by Norton *et al.* (2012), where the droplet size and free water content remained constant at increasing water mass fractions (up to 50%).

Emulsions produced using the SSHE alone (Fig. 4.9) were characterised by the same droplet size as emulsions produced using the full margarine line. This result strongly

suggests that a SSHE alone can also be used to produce emulsions containing up to 40% aqueous phase. Furthermore, all emulsions remained stable over a month of observation. Results also suggest that only a small amount of PGPR is necessary to obtain stable water-in-cocoa butter emulsions. In fact, all formulations contained 1% PGPR (wt%); therefore at increasing aqueous phase percentages, less emulsifier was available to promote emulsification. Considering that the final droplet size was comparable across all systems, the number of droplets (and subsequently the total interfacial area) contained in the 40% aqueous phase was approximately four times larger than in the 10% aqueous phase emulsion. It is logical to think that low PGPR concentrations are needed to effectively lower the water-molten CB interfacial tension and provide full surface coverage. The formulation aspect concerned with the concentration of emulsifier will be discussed in more detail in Section 4.2.3.2.

It is important to highlight that the production of emulsions containing 60% aqueous phase was not reproducible, i.e. out of three experiments, only on one occasion could a fully emulsified system be obtained which was characterised by a small droplet size. In the other cases, a bi-continuous system was produced consisting of a layer of water at the bottom, containing suspended fat crystals, and a coarse mixture on the top. Also when using the full margarine line, it was not possible obtaining stable emulsions with 60% dispersed phase. This inability to emulsify may be due to multiple reasons: (1) PGPR concentration too low to effectively reduce water-cocoa butter interfacial tension and provide droplet coverage; (2) fat crystals number too small to obtain bulk crystallisation and effective Pickering stabilisation of the droplets; (3) low energy input; (4) low residence time to obtain effective water breakage into small droplets.

The higher dispersed phase emulsions were also crystallised into the desired form V when the SSHE alone was used as tempering-emulsifying device (this will be shown in Chapter 5).

To conclude, the same droplet size was obtained when using the full margarine line or the SSHE alone, to produce water-in-cocoa butter emulsions containing up to 40% aqueous phase. A phase inversion approach may provide a suitable route for the production of emulsions containing a dispersed phase fraction above 40%, but this approach was not attempted here.

4.2.3.2. Effect of emulsifier concentration on emulsion production and stabilisation

Water-in-cocoa butter emulsions can be considered as mixed emulsifier systems, where both PGPR and fat crystals contribute to emulsion stabilisation. Nevertheless, the role played by each of them, in the production and stabilisation of water-in-cocoa butter emulsions, remains unclear. The aim of the work presented in this section is to evaluate the effect of PGPR concentration on emulsion formation and stability over time. Interfacial tension between the lipid and aqueous phase, droplet break-up, as well as surface coverage of newly formed interfaces, are all phenomena affected by the type and concentration of surface active species.

In order to reduce the number of variables, and to allow comparisons with previous results, the aqueous phase percentage was kept constant (20%, wt%) and processing conditions as described in Section 4.2.1.3. were used. PGPR concentration ([PGPR]), expressed as a percentage fraction (wt%) of the total emulsion mass, was manipulated to obtain five levels: 0.0, 0.1, 0.5, 1.0, and 2.0%. The results are shown in Figure 4.10.

The $d_{3,2}$ and free water content values decrease at increasing PGPR concentration, remaining fairly constant ($d_{3,2} = 3 - 4 \mu\text{m}$) at PGPR concentrations above 0.5%. For all formulations, emulsions remained stable for one month at 20 °C. Water-in-cocoa butter emulsions could be produced without the addition of PGPR, but they were characterised by large $d_{3,2}$ and free water values, of 13 μm and 14% respectively. This result indicates that naturally contained surface active molecules (free fatty acids, phospholipids, mono and diglycerides) and CB fat crystals contribute to emulsion formation and stabilisation. Emulsions containing 0.1% PGPR were characterised by a high free water content (12% \pm 0.5%) but a small $d_{3,2}$ (6 $\mu\text{m} \pm$ 0.7 μm). For PGPR concentrations equal to, or above, 0.5%, emulsions had all the same droplet size. These results are partially in disagreement with those published by Norton and Fryer (2012) where no difference in the $d_{3,2}$ and free water content values was observed between systems containing 0.1, 0.5, 1.0, and 2.0% (wt/wt) PGPR. A possible explanation for this difference may be attributed to the different process set-up used by those authors; specifically their lower processing temperature (promoting a higher extent of fat crystallisation) and the use of both SSHE and PS allowing a longer time for the PGPR to adsorb to the interface.

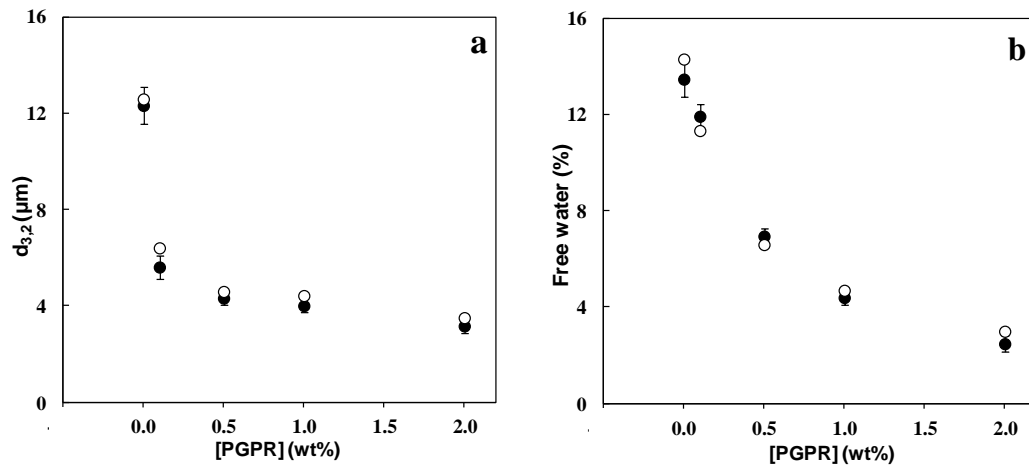


Figure 4.10: Effect of PGPR concentration ([PGPR]) on (a) droplet size ($d_{3,2}$) and (b) free water content at one day (full circles) and at one month after production (empty circles). Error bars represent one standard deviation of triplicates (where no visible, error bars are smaller than symbols).

In order to gain a better understanding of the dependency of droplet characteristics on PGPR concentration, the interfacial tension at the aqueous-lipid interface ($\gamma_{w/CB}$) was measured for all formulations. Measurements were performed using the static Wilhelmy plate method at 40 °C (± 1 °C). This temperature was selected as it is above CB final melting point and corresponds to the temperature at the inlet of the SSHE. Therefore, the measured interfacial tension ($\gamma_{w/CB}$) provided a good indication of the interfacial tension between phases prior to the start of emulsification. The $\gamma_{w/CB}$ profiles are shown in Figure 4.11 as a function of measuring time and PGPR concentration. Each curve is the average of at least three replicates. For clarity reasons error bars are shown only for the systems containing 0 and 0.1% PGPR.

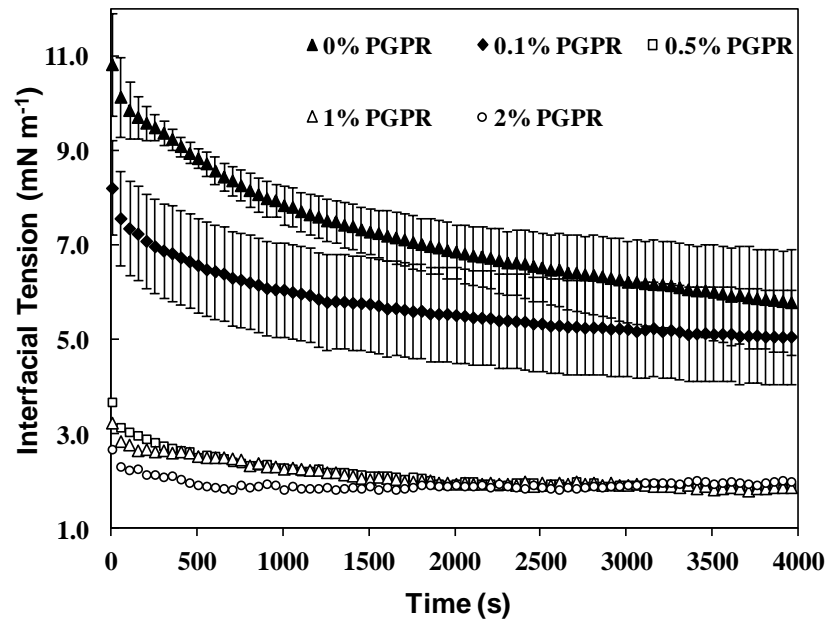


Figure 4.11: Water-cocoa butter oil interfacial tension as function of time at different PGPR concentration (symbols are explained in the legend).

It can be observed that the initial interfacial tension value decreases with increasing PGPR concentration, with the highest value of $\gamma_{w/CB}$ measured in the absence of added emulsifier (0% PGPR). For this sample, the interfacial tension decreases steeply over the first 1000 seconds and then levels off after approximately 3000 seconds, although a plateau value is not achieved. The inability to attain a plateau value is attributed to the presence of surface active impurities in the oil phase (Gaonkar, 1989; Pichot *et al.*, 2010): impurities progressively adsorb to the water-oil interface over time, thus resulting in a decrease in interfacial tension. Considering the results reported by Gaonkar (1992) for soybean oil-water interfaces where an increase in the interfacial activity of the impurities was observed in the presence of different salts (including NaCl), it could be hypothesised that the adsorption of naturally contained surface active molecules may be enhanced by the presence of NaCl in the aqueous phase. Future studies may consider this effect in

more detail, using different salts at varying concentrations. The presence of naturally contained surface active molecules would explain a water-CB interfacial tension lower than that measured for other edible rapeseed oil (O'Sullivan *et al.*, 2014). For the system containing 0.1% PGPR, the initial interfacial tension is lower than that observed for 0% PGPR although, at the end of the observation period the values are the same. Finally, no difference in $\gamma_{w/CB}$ was observed for systems containing 0.5, 1.0, and 2.0% PGPR, and for all these systems the $\gamma_{w/CB}$ remained constant over time. For these formulations it seems reasonable to think that PGPR is the predominant molecule at the interface, as that would justify the constant $\gamma_{w/CB}$ profiles. Although the presence of surface active molecules, naturally contained in CB, at the interface, cannot be completely ruled out, their effect seems to be smaller.

Data of droplet size reduction shown earlier in Figure 4.10 can be better explained in the light of the interfacial tension results: on emulsification, a more efficient droplet break-up is likely to occur as $\gamma_{w/CB}$ decreases with increasing emulsifier concentration. At a PGPR concentration $\geq 0.5\%$, there is no difference in the interfacial tension value, and droplet characteristics also remained constant. Two explanations for this result can be provided: (1) at these levels of PGPR there are enough molecules to quickly provide complete coverage of the newly formed water-CB droplets so as to reduce the interfacial tension and allow further droplet break-up; (2) PGPR molecules prevent droplet re-coalescence *via* interfacial steric stabilisation, before the fat crystals can effectively contribute to stabilisation *via* Pickering and network mechanisms. In the absence, or at low concentrations, of PGPR ($\leq 0.1\%$), the naturally contained emulsifiers reduce the interfacial tension to a lower extent than PGPR. Furthermore, these natural emulsifiers may be less effective at delaying droplet re-coalescence prior to the occurrence of fat

stabilisation. These factors determine the larger droplet size observed for PGPR $\leq 0.1\%$ final result.

A similar stabilisation mechanism was described for emulsions containing mixed emulsified systems; namely, monoolein and silica particles (Pichot *et al.*, 2009). The authors concluded that monoolein molecules rapidly cover the newly formed interfaces lowering the interfacial tension and providing short term stability. After emulsification, silica Pickering particles can migrate to the interface and provide long term stability.

4.2.3.3. *Cryo-SEM visualisation of emulsions*

Cryo-SEM investigation of emulsions containing different PGPR concentrations showed that water droplets are embedded within a continuous fat crystal network (Fig. 4.12).

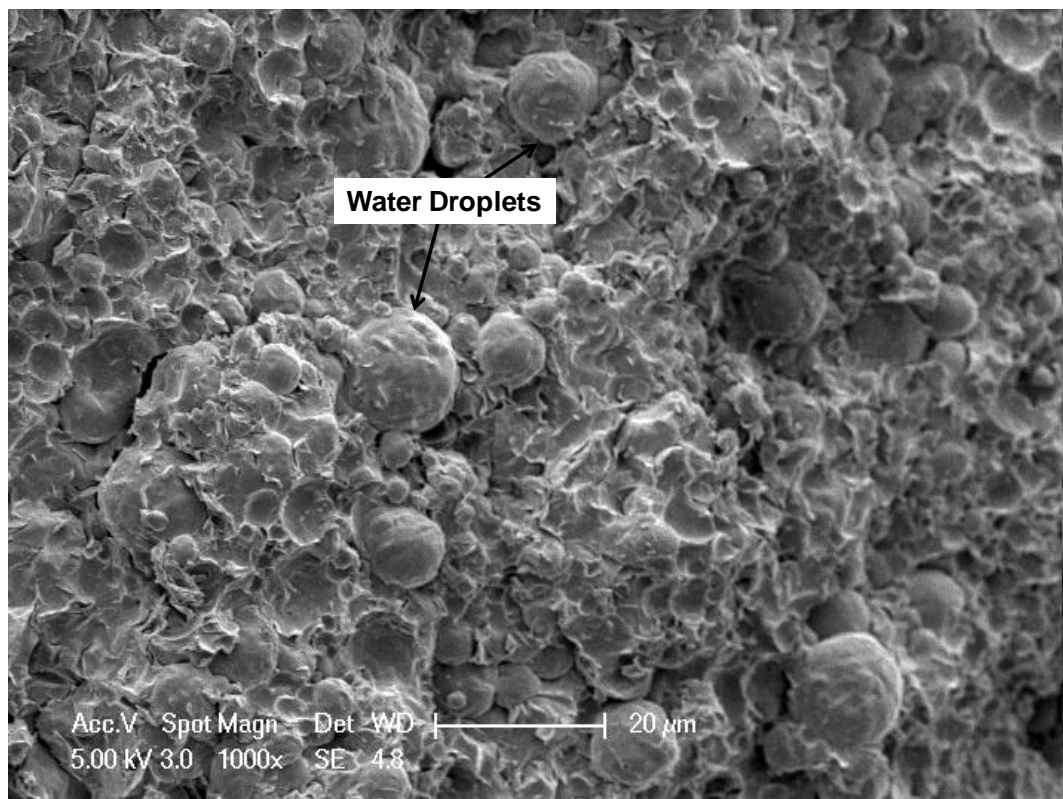


Figure 4.12: Cryo-SEM visualisation of 20% aqueous phase emulsions with 0% PGPR. Water droplets appear encased within the fat crystal network.

A closer look at the droplets also revealed that they were surrounded by a crystalline layer (Fig. 4.13): the droplet surfaces appear as a continuous (smooth) crystalline “shell” physically trapping the water.

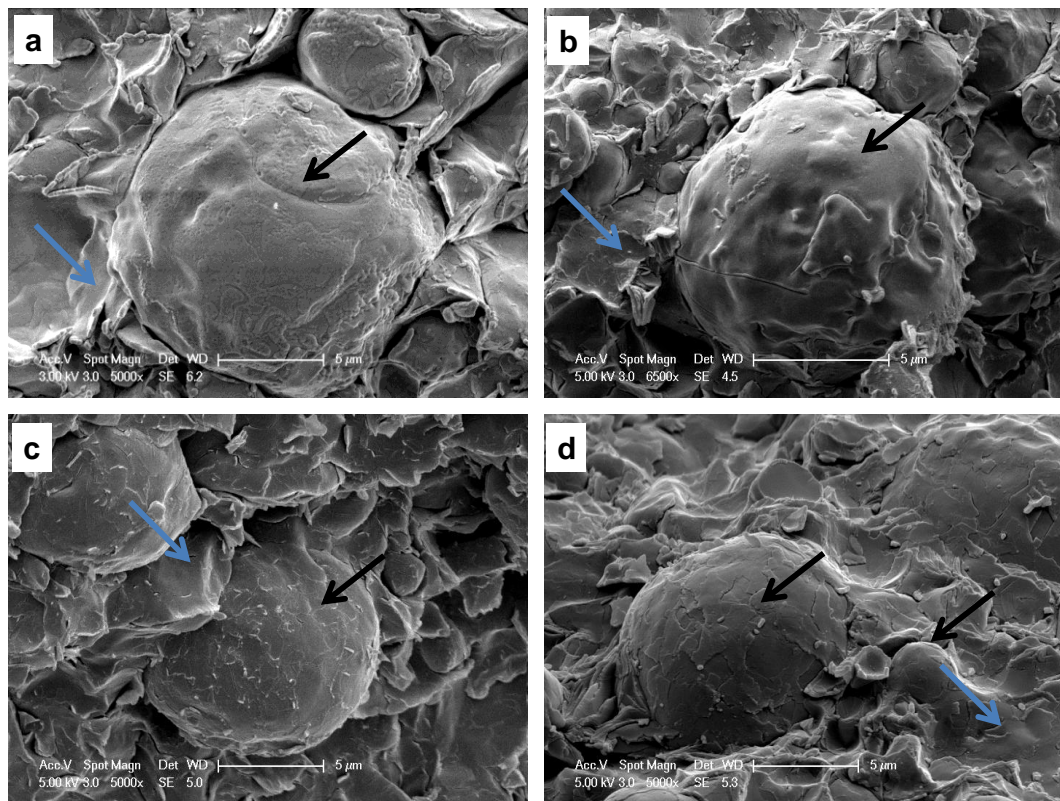


Figure 4.13: Micrographs of emulsions containing 0% (a), 0.1% (b), 1% (c), and 2% (d) PGPR. Droplets are surrounded by a crystalline shell (black arrows) within a fat network (blue arrows).

This result is in agreement with previous results (Norton *et al.*, 2009; Norton and Fryer, 2012) and confirms that fat crystal Pickering stabilisation occurs in water-in-cocoa butter emulsions similarly to what is observed in fat spreads (Heertje, 2014). It should be pointed out that, although some differences in the appearance of droplet interfaces were observed for different PGPR concentrations, it was not possible to establish a correlation between emulsifier concentration and surface morphology.

As discussed in Section 2.2.5.1., the mechanism of development of this type of interface has not been fully elucidated. Similarly to what was referred to by Frash-Melnik *et al.* (2010), it is reasonable to hypothesise that in water-in-cocoa butter emulsions fat shells result from the sintering of small individual crystals directly at the interface. These fat crystals are formed on processing by the rapid cooling at the internal wall of the SSHE and mechanical scraping of the blades. Fat crystals are then brought to the interface on mixing where they grow together (“sinter”) forming a continuous solid interface, i.e., the *shell*. It is logical to raise a question about the thickness of this type of interface. Micrographs shown in Figure 4.14 represent droplets which have been broken following sample preparation for cryo-SEM visualisation. These evidences suggest that crystalline shells may be approximately 250 nm thick, which would indicate they result from the stacking of several layers of TAGs lamellae.

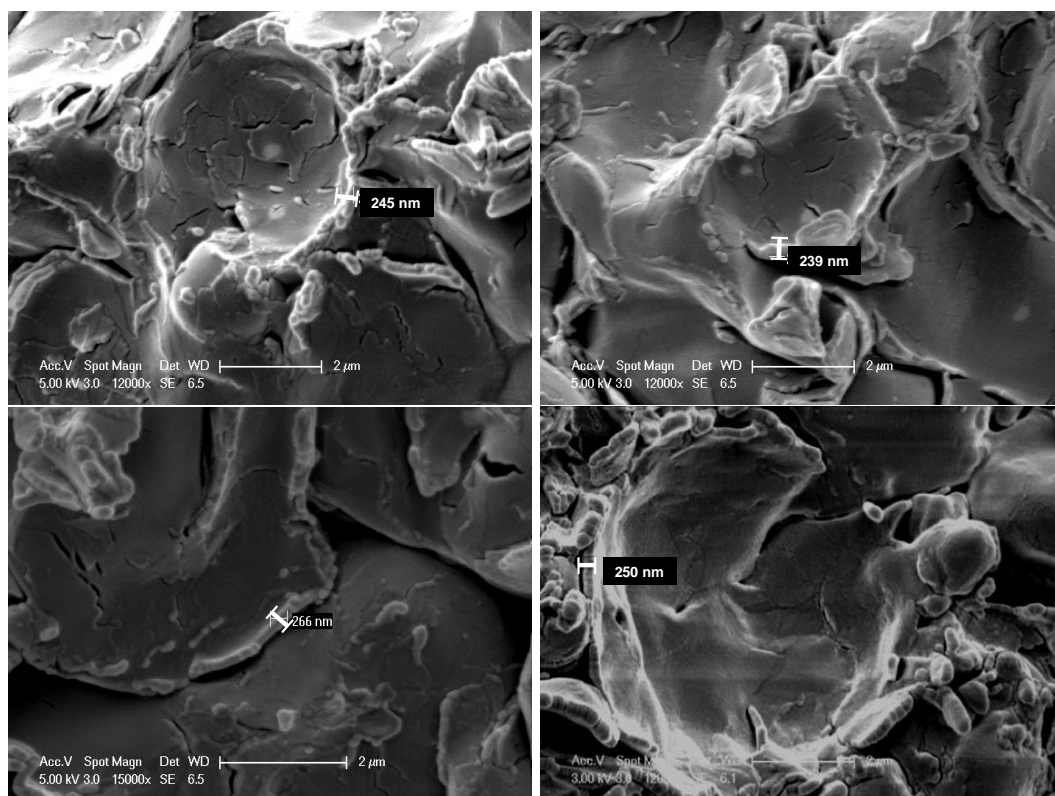


Figure 4.14: Micrographs of broken water droplets as a result of sample preparation providing an evidence for interfacial “shell” thickness. The thickness values have been estimated using the Cryo-SEM microscope software.

4.3. Conclusions

This chapter has focused on gaining a better understanding of the effect of processing and formulation on water-in-cocoa butter emulsion formation and microstructure. Experimental results clearly suggest that the PS can reduce the final droplet size only if the rotational speed (N_{SSHE}) in the SSHE is below 500 rpm and the N_{PS} is above 900 rpm. In any other case the PS produces an increase in $d_{3,2}$. Considering that emulsions containing up to 40% aqueous phase produced using the SSHE alone have a $d_{3,2}$ comparable to those produced using the full margarine line, and that the average residence time in the PS is approximately six times longer than within the SSHE, it can be concluded that this latter mixer is a more efficient emulsifying device.

With respect to the crystallisation process, it has been shown that when high shear is applied in the SSHE, CB is crystallised in the desired polymorph (form V). The shear-temperature profile in the PS erases the desired fat crystals, thus preventing tempering from occurring. Although the effect of the PS on CB polymorphism may be investigated at lower jacket temperatures, in the light of the obtained results it can be concluded that the SSHE provides a suitable route for the production of stable tempered water-in-cocoa butter emulsions. Therefore, its use should be preferred to the full margarine line.

A better understanding of the mechanism of emulsion formation and stabilisation was gained from results obtained at different temperatures and PGPR concentrations. It was revealed that both engineering parameters play a key role on emulsion droplets characteristics. Processing temperature seems to determine an increased droplet size only if the T_{out} of the SSHE is close to, or above, CB melting point: as when a smaller amount of solid material is crystallised, larger droplets are formed. This is due to a less efficient

droplet break-up process and the fact that no fat crystals are available for droplet stabilisation. Therefore, both Pickering and network stabilisation provided by the crystals appear important in delaying the back reaction, i.e. coalescence, when emulsions leave the SSHE and are still in a high energy state. With respect to surfactant effect, small water droplets can be produced only if PGPR concentration is enough to achieve full surface coverage and reduce the interfacial tension for further droplet break-up. Combination of results obtained at different aqueous phase percentages and PGPR concentrations suggest that a minimum of 0.5% PGPR (wt%) is necessary to achieve a $d_{3,2}$ of $\sim 3 \mu\text{m}$. Nevertheless, an excess of PGPR may still be preferred to ensure full interfacial coverage on processing and higher stability.

Emulsion visualisation using cryo-SEM revealed the presence of a continuous crystalline shell around water droplets. No differences in *shell* appearance were observed for different PGPR concentrations, which may suggest that the used emulsifier does not affect the sintering of the interface. Finally, some evidences of shell thickness of approximately 250 nm were provided suggesting a structure made up of several layers of TAGs *lamellae*. However, it should be pointed out that fractured droplets were rarely observed, suggesting that they were able to resist the fractural stresses experienced on sample preparation. The effect of droplets on the large deformation behaviour of water-in-cocoa butter emulsions will be studied in detail in Chapter 5.

**Chapter 5. Effect of microstructure on
the large deformation behaviour of
cocoa butter systems**

5.1. Introduction

In Chapter 4 the process for the production of water-in-cocoa butter emulsion was optimised. These emulsions are characterised by a solid-like structure, which results from cocoa butter (CB) crystallisation. It is reasonable to think that the addition of water would yield a softer product. In order to use water-in-cocoa butter emulsions as a novel ingredient for chocolate manufacture (Chapter 1), it is important to develop a fundamental understanding of their mechanical behaviour so as to design structures with the desired properties. From a structural-mechanical point of view, water-in-cocoa butter emulsions can be classified as composite materials; where the filling phase, i.e., the water droplets, are embedded within the continuous CB matrix and represent structural defects. In order to gain a better understanding of the relationship between microstructure and mechanical behaviour, the aim of the study presented in this chapter was to characterise the large deformation properties of CB systems. This type of study implies a deformation above the linear viscoelastic region, which for fat dispersions has been found to correspond to a strain value of approximately 0.001 (Kloek *et al.*, 2005b).

Large deformation and fracture properties were studied as they can yield structural information while providing an indication of material functional properties, i.e. handling, behaviour on consumption (van Vliet, 1996).

All samples were analysed using parallel plate uniaxial compression test until material fracture. It should be pointed out here that, although a universal definition of “fracture” does not exist, it is a phenomenon characterised by several events occurring simultaneously within the experimental time-scale: (1) breaking of the bonds between the structural elements which form the material; (2) structure degradation (i.e. development of macroscopic cracks) at a scale larger than the structural elements; (3) breakdown of the

material into smaller pieces (Kloek *et al.*, 2005a; van Vliet, 2002). According to theories on fracture mechanics, all materials contain defects (small cracks) or structural inhomogeneities, which determine weakening of the structure: when a solid-like material is deformed, stress-strain concentration occurs in the vicinity of defects (Luyten and van Vliet, 1995). Fracture occurs if defects can grow enough to determine material breakdown and is the result of two processes: (i) initiation; (ii) propagation. *Fracture initiation* corresponds to the initial growth of a crack, which occurs only if the stress at the tip of the crack is higher than adhesion or cohesion stresses between building units of the material. *Fracture propagation* represents the growth of a crack, which occurs only if the energy required for the growth is lower than the strain energy released (van Vliet and Walstra, 1995).

To study the mechanical behaviour of water-in-cocoa butter emulsions and evaluate the role of structural defects, different microstructures were designed and their large deformation behaviour characterised. As explained in Section 3.3.5., the large deformation properties considered were: (I) *apparent Young's modulus* (E_{app}) and (II) *bulk modulus* (BM) calculated as the slope of stress-strain the curve in a strain region between 0.003 and 0.005 and between 0.01 and 0.03, respectively; (III) *stress* (σ_{Fr}) and (IV) *strain* (ε_{Fr}) *to fracture* as the coordinates of the point of fracture; (V) *work to fracture* (W_{Fr}) as the area under the stress-strain curve up to failure.

This chapter begins with a discussion on the large deformation properties of bulk CB. In order to evaluate the effect of processing, CB was crystallised either statically or using the same process as for emulsification.

The second part of the chapter focuses on understanding the role of water droplets on the large deformation behaviour of emulsions. Since it was hypothesised that droplets behave

as “defects” (causing a reduction in the mechanical strength of emulsions compared to bulk CB), their effect was assessed by engineering the microstructure to evaluate two main variables:

- Disperse phase fraction (wt%)
- Disperse phase average droplet size (for 20%, wt%, emulsions)

In the final part of the chapter, the dependency of the mechanical response on the compression rate is discussed.

It should be considered that the mechanical properties of fats are difficult to interpret and predict using the models available (Section 2.1.3.) as they depend on several microstructural parameters, which include: number, morphology, and size of crystals, solid fat content (SFC), polymorphism, and type of bonds formed (Section 5.2.1.) (Campos *et al.*, 2002). In this study an attempt to correlate mechanical and microstructural properties has been made for a novel class of soft-solid materials. Interpretation of the experimental results with respect to the structural models proposed in the literature for fat crystal networks will also be attempted.

5.2. Results and discussion

5.2.1. Large deformation behaviour of bulk cocoa butter

The aim of the work presented in this section was to investigate the large deformation behaviour of bulk CB as a function of crystallisation conditions. CB was crystallised either statically or using the emulsification-crystallisation process optimised in Chapter 4 (scraped surface heat exchanger, SSHE, at a rotational speed of 1315 rpm, 25 °C jacket temperature, 30 mL/min). In this case CB is cooled rapidly and under the action of shear,

which promotes the development of small crystals arranged in polymorph V (see Fig. 5.1). CB crystallised using the SSHE will be called for simplicity “sheared CB”. Statically crystallised specimens were prepared by cooling of molten CB from 50 to 30 °C in a 50 mL glass beaker while gently mixing with a magnetic bar to ensure homogeneity. Once at 30 °C (within approximately 30 minutes), CB was poured into the molds and left to crystallise at room temperature (~25 °C). These samples will be called “static CB”. Ten specimens (height (h) 25 mm; diameter (d) 16 mm; $h/d = 1.56$) for both materials were analysed at 48h after production using uniaxial compression test with a cross-head speed of 1 mm/s.

As expected, the different crystallisation profiles determined the development of different polymorphs in the two samples. Differential scanning calorimetry (DSC, scan rate of 5 °C/min) was used to determine the polymorphic form of the systems.

Static and sheared CB were characterised by a main melting peak at 29 and 32 °C, respectively (Fig. 5.1). According to literature data (Loisel *et al.*, 1998a), these melting temperatures indicate that static and sheared CB had crystallised mainly in form IV and V, respectively. In agreement with results discussed in Chapter 4, the applied shear-temperature profile promotes faster polymorphic transition, thus explaining the presence of form V. Statically crystallised CB does not follow any specific shear-temperature profile and it crystallises in a less stable, faster nucleating polymorph.

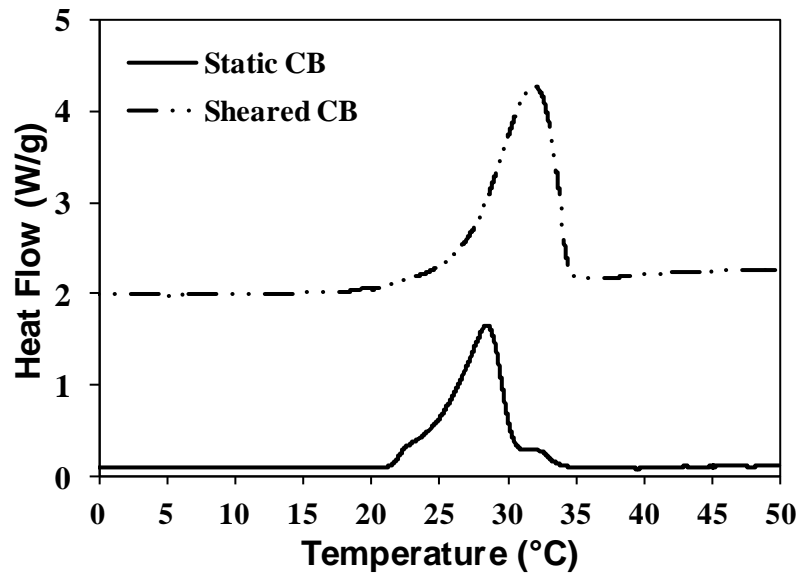


Figure 5.1: Melting profile of statically and sheared crystallised CB.

Figure 5.2 shows an example of engineering stress-strain curve measured for both types of samples.

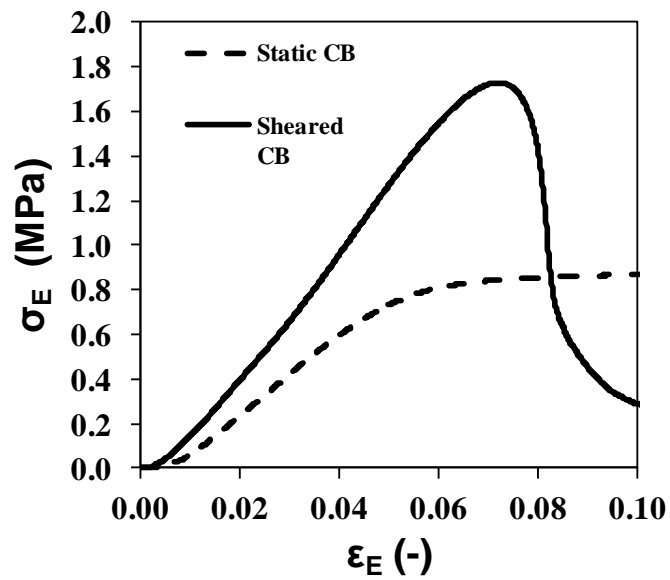


Figure 5.2: Example of stress (σ_E)-strain curve (ϵ_E) for statically and sheared crystallised CB.

The mechanical behaviour of statically crystallised CB is similar to that described for a plastic dispersion (Chronakis and Kasapis, 1995): while increasing the strain (ε_E), the stress (σ_E) increases until achieving a maximum. In correspondence of this point, the formation of visible cracks was observed suggesting that on a microscopic scale some of the bonds within the fat network had been broken. However, specimens did not fracture within the experimental time scale. In the view of the classification proposed by Kloek *et al.* (2005a), for these samples *yield* occurred. At larger ε_E , the σ_E remains constant indicating the material behaves as a highly viscous dispersion of fat crystals in liquid oil.

The large deformation response of sheared crystallised CB is very similar to that reported for other food materials showing brittle fracture (Baltsavias *et al.*, 1997): at increasing ε_E , the σ_E increases until achieving a maximum (i.e., fracture stress), where the samples fractured. This event was characterised by the formation of many small pieces and by a dramatic decrease in the resistance of the material, which was related to the degradation of the crystal network (Fig. 5.3 and 5.4). The most common breaking pattern observed for sheared CB specimens was characterised by a fracture along the central longitudinal axis with the formation of two cones corresponding with the flat ends and several lateral pieces. It has been reported that this fracture mode accounts for brittle fracture (Peleg, 2006). In Figure 5.3 a specimen before and after fracturing is shown, with the cone formed in the bottom part also shown. An example of sample during fracturing is shown in Figure 5.4; here the cone formed at the upper part of the specimen is visible.

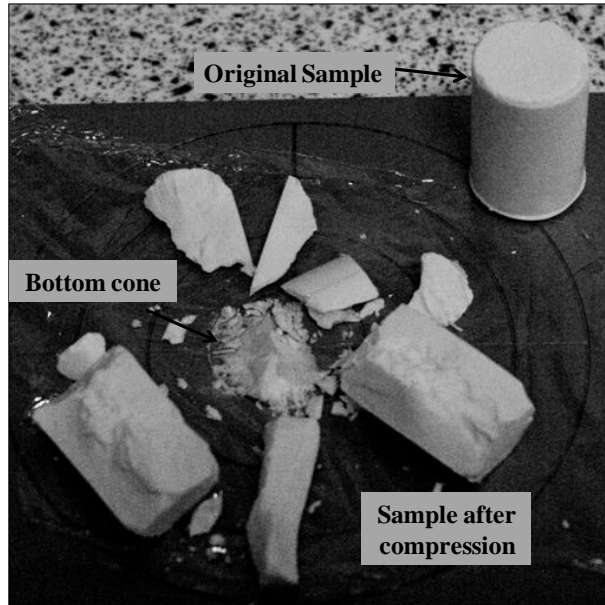


Figure 5.3: Image of a test specimen before and after compression.

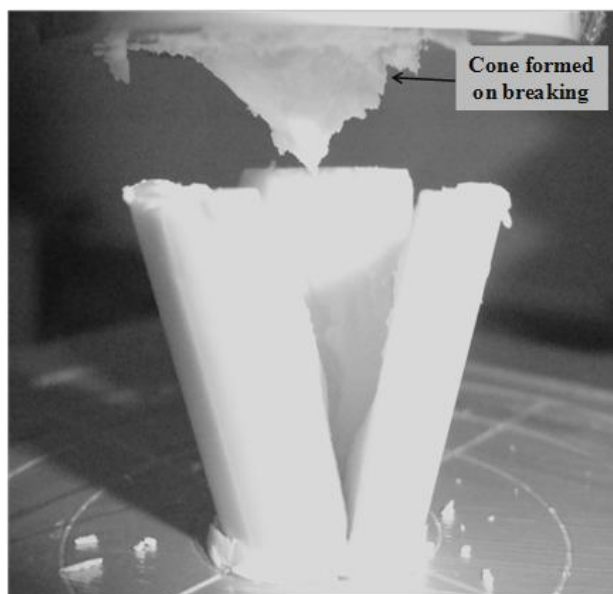


Figure 5.4: Micrograph of a test specimen while failure is occurring.

Figures 5.5a and b show the apparent Young's (E_{app}) and bulk modulus (BM) for the static and sheared CB.

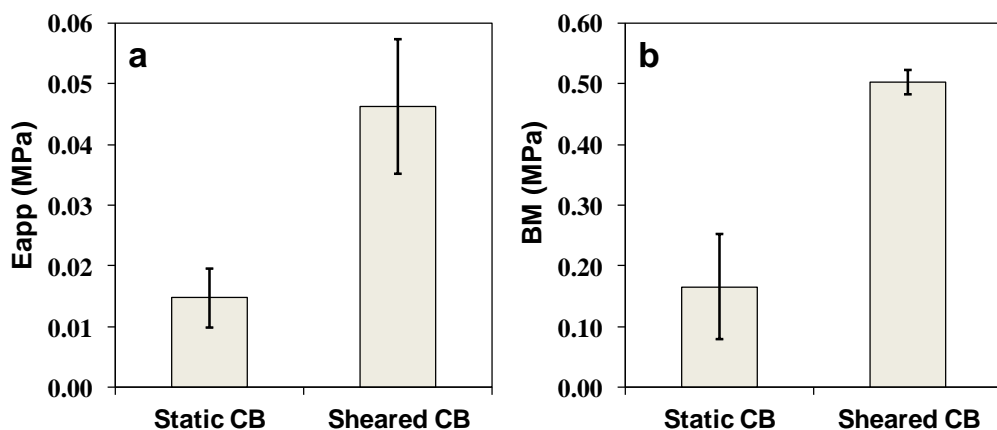


Figure 5.5: (a) Apparent Young's (E_{app}) and (b) bulk modulus (BM) for statically and sheared crystallised CB. Error bars are plus/minus one standard error of the mean.

The values of both parameters measured for sheared CB are more than a factor of two larger than those measured for static CB. It should be mentioned here that it is not possible to determine the true Young's modulus with the adopted experimental set up. This limitation is due to the fact that the strain required to measure the real Young's modulus (~ 0.001) is below the detection limit of the experimental set-up. Therefore, only an apparent Young's modulus (E_{app} ; $0.003 \leq \epsilon_E \leq 0.005$) could be determined, with E_{app} being smaller than the true Young's modulus. Kloek *et al.* (2005a) reported a similar limitation in their work.

The E_{app} provides an indication of the stiffness of the material and can be associated with the elastic deformation of bonds formed within the network (Deman and Beers, 1987). As explained in Section 2.1.3., fat crystal networks are *polycrystalline materials*, i.e. they are formed by small particles (*fat crystals*) aggregating *via* two types of bonds: primary and secondary bonds.

Primary (or *sintered*) *bonds* result from a process of fat crystals growing together (*sintering*) during crystallisation and/or melt-mediated polymorphic transition. These

bonds are irreversible: once broken they cannot be reformed. It is possible that the strength of primary bonds may change with composition, polymorph, and crystallisation conditions of a fat but there is currently no study which investigates these aspects in detail.

Secondary bonds are represented by weak and reversible van der Waals forces. Sintered bonds are characterised by a higher energy content (i.e. energy to break) than secondary bonds and contribute more to network stiffness (Deman and Beers, 1987).

Although sheared CB was characterised by a higher E_{app} than static CB (Fig. 5.5), the two samples were characterised by a comparable value of solid fat content, which was 79.0% ($\pm 0.8\%$) and 74.0% ($\pm 1.1\%$) for sheared and static CB, respectively). The SFC value quantifies the amount of crystalline material but does not provide any indication on the type of bonds characterising a system. As discussed in Chapter 4, the rapid shear-cooling profile applied within the SSHE and the mechanical scraping of the blades promotes the formation of a large number of small crystals *via* secondary nucleation, which, on post-processing, sinter together to determine network formation. The presence of many small crystals in sheared CB promotes the development of a larger number of primary bonds than in static CB, thus determining a higher E_{app} . In statically crystallised CB, given the imposed slow-static cooling, sintering of crystals was still under development when the mechanical test was performed. As shown earlier in Figure 5.1, static and sheared CB had crystallised mainly in form IV and V, respectively. Although it is reasonable to think that a more stable and tightly packed crystalline arrangement (form V) would be characterised by a higher E_{app} , the effect of polymorphism on the elastic properties (as well as on the overall mechanical behaviour) of fats is not considered by any of the models available in literature (Marangoni *et al.* 2012; Kloek *et al.* 2005a). Therefore, for simplicity the

difference in E_{app} will be considered to reflect only the difference on the types and number of bonds (in agreement with the models).

The difference in the values of BM for sheared and static CB closely follows the trend observed for E_{app} (Fig. 5.5b). A physical interpretation of this parameter has been reported for hydrocolloid gels (Norton *et al.*, 2011). The authors suggested that the BM , calculated as the slope in the second linear region of a stress-strain curve, accounts for matrix deformability and stiffness.

To gain a better understanding of the physical meaning of the BM it should be considered that while a sample is compressed toward final failure its structure evolves, passing from elastic to visco-elastic through a transition zone ($0.005 \leq \varepsilon_E \leq 0.01$). This latter zone corresponds to a strain region of rapid microstructure evolution (as suggested by the continuous change in slope), where some of the initially stress-deformed sintered bonds are probably broken and replaced by weak van der Waals interactions. The following strain region ($0.01 \leq \varepsilon_E \leq 0.03$) also denotes continuous microstructure evolution. The phenomena hypothesised to occur are: bending and breaking of solid bonds, development of local permanent fractures, breaking and re-forming of van der Waals bonds, deformation of structural elements (i.e., crystals and crystals clusters), friction between structural elements, and viscous flow of the liquid oil. The observed linear dependency of the stress on the strain suggests that the rate of structure breakdown is somehow balanced by the rate of structure re-arrangement. In this study the strain region used to calculate the BM ($0.01 \leq \varepsilon_E \leq 0.03$) was selected as yielding did not occur within this range for any of the samples (see Section 3.3.5.2.).

The larger BM measured for sheared CB suggests that its microstructure is more stiff and able to resist a larger applied stress than static CB. As with the E_{app} this result can be

associated with a higher extent of sintering (more bonds and a higher degree of connectivity between crystals), with these solid bonds bearing the applied mechanical load.

Figures 5.6a and b show the average stress (σ_{failure}) and strain ($\epsilon_{\text{failure}}$) to failure for static and sheared CB. The word “failure” is used here to indicate the breaking of the fat network in terms of both yielding and fracture. The σ_{failure} was used in this study to indicate the *hardness* of materials, i.e. the resistance opposed by the material to final breakdown.

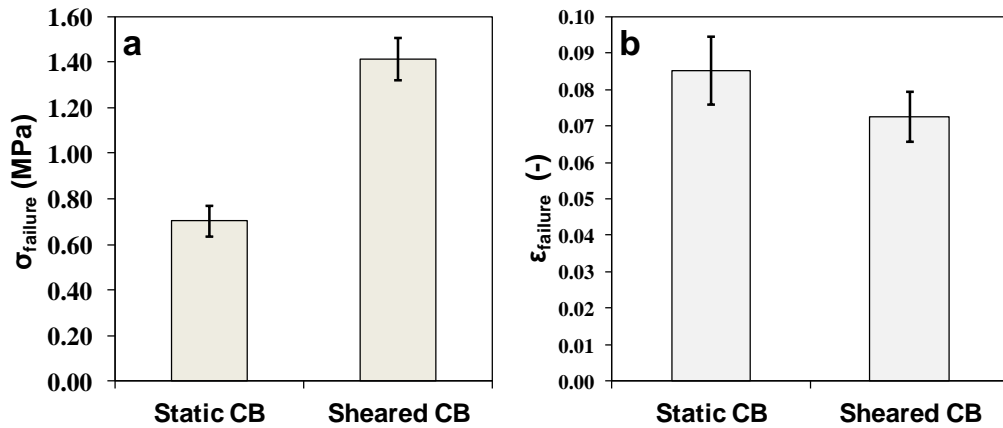


Figure 5.6: Average (a) stress (σ_{failure}) and (b) strain ($\epsilon_{\text{failure}}$) to failure for statically and sheared crystallised CB. Error bars are plus/minus one standard error of the mean.

Results shown in Figure 5.6a clearly indicate that the hardness of sheared CB is higher than that measured for static CB. However, this latter material can deform more at failure than sheared CB (Fig. 5.6b). This result can be explained considering that the sintered bonds behave like rigid junctions and exhibit low deformability at failure ($\epsilon_{\text{failure}}$).

Polarised light microscopy was used to gain an insight of the microstructure of both CB systems (Fig. 5.7). Statically and sheared crystallised CB (Fig. 5.7a and b, respectively)

are characterised by a granular microstructure with fat crystals (bright elements in the micrographs) suspended in the liquid oil (dark zones). This microstructural arrangement is in agreement with the one shown by Narine and Marangoni (1999a). In the case of sheared CB, crystal clustering (represented by large bright elements in Fig. 5.7B) seems to be more common than in static CB. Furthermore, only for sheared CB could large microstructures with a complex internal arrangement be observed (Fig. 5.7c-d). These structures are similar to those shown by Marangoni and McGauley (2003) where, for CB in form V, granular crystals were shown to coexist with large microstructures. Although a larger number of images would be necessary to establish quantitative differences in the microstructure of the two CB systems, it seems reasonable to think that the large structural elements contribute to the brittle behaviour observed for sheared CB.

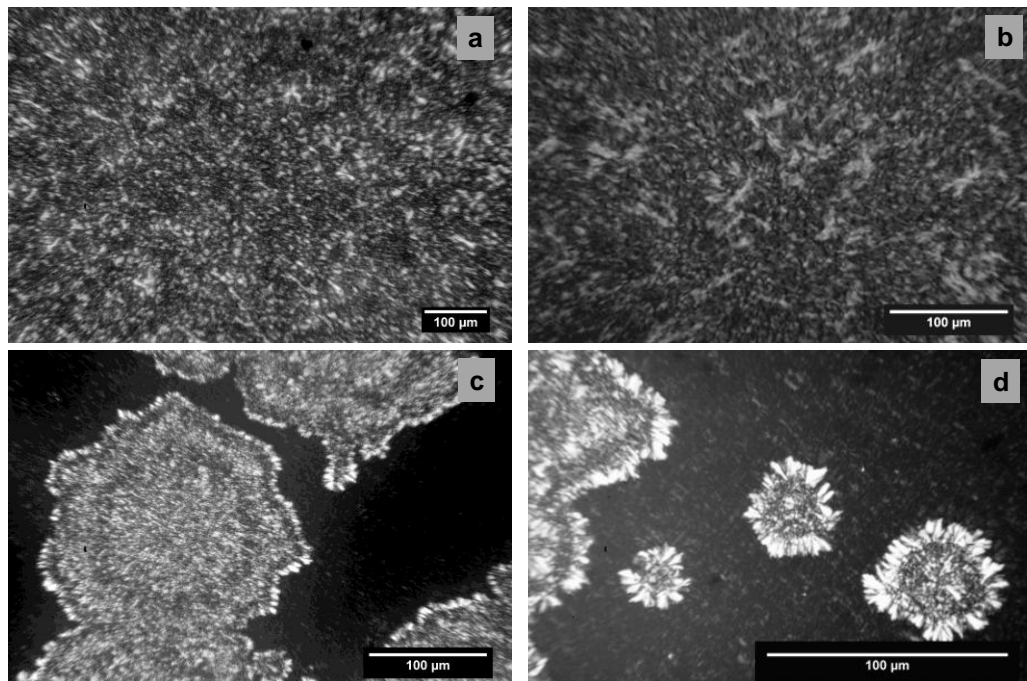


Figure 5.7: Microstructural visualisation of CB (a) statically and (b, c, d) sheared crystallised. A granular microstructure was common to both systems. For sheared CB microstructures with a granular centre and surrounded by a featherlike arrangement were also observed (C, D).

In agreement with the model proposed by Kloek *et al* (2005a), the higher E_{app} , BM , and σ_F measured for sheared CB can be considered to result from the higher number of solid bonds formed between crystals and crystal aggregates and a complex microstructure. This is in agreement with results reported for other fat systems (Campos *et al.*, 2002): the development of a large number of small crystals determines a higher number of connections, which results in a harder but less deformable structure. Furthermore, results do not depend on the SFC. This is in agreement with findings from Brunello *et al* (2003), who showed that the hardness of statically crystallised CB sample was a function of microstructure and polymorphism, with SFC having a smaller impact.

5.2.2. Effect of water percentage on the large deformation behaviour of water-in-cocoa butter emulsions

As mentioned in Section 5.1., water-in-cocoa butter emulsions can be considered composite materials, where water droplets are structural defects dispersed within the CB matrix. Although emulsions are expected to have lower strength than bulk CB, a more quantitative understanding of the role of water droplets on the mechanical properties of emulsions needs to be developed. Furthermore, with respect to their colloidal properties, similarly to margarine, water-in-cocoa butter emulsions can be classified as particle gels formed by the aggregation of fat crystals to produce a continuous three dimensional network trapping the liquid oil and water (this latter phase dispersed in the form of droplets). As shown in Chapter 4, droplets are also surrounded by a crystalline fat shell. However, no work is available in the literature investigating the interaction forces between the interfacial crystalline layer and network. In his review, Heertje (1993) reported that fracture occurred mostly around and through water droplets when saturated and unsaturated monoglycerides, respectively, were used to stabilise droplets in

margarine. This result was attributed to differences in the structure of the shell formed: a multi-layered and particulate interface for saturated and unsaturated monoglycerides, respectively. However, the author did not discuss the type of bonds connecting the shell and the bulk network. Two hypotheses concerning this aspect will be formulated later in this section.

The aim of the work discussed in this section was to understand the effect of disperse phase mass fraction on the large deformation behaviour of water-in-cocoa butter emulsions. In order to reduce the number of variables, emulsions microstructures were designed on the basis of the results shown in Chapter 4.

Emulsification was performed using the SSHE alone at its maximum rotational speed (1315 rpm) and 25 °C jacket temperature (30 mL/min flow rate). Samples of bulk CB (reference material) were prepared using the same process. The use of this set-up allowed to control two key microstructural parameters: (1) *droplet size*: at increasing water mass percentages (from 10% to 40%, wt%), the same droplet size for all emulsions was obtained (Tab. 5.1); therefore, only the number of structural defects will increase at increasing aqueous phase; (2) *polymorphic form*: the selected processing conditions allowed to control the main polymorphic form in which the CB had crystallised. As shown in Figure 5.8, all samples were in form V.

For each formulation, uniaxial compression test until final fracture was performed on at least 10 specimens using a compression speed of 1 mm/s.

The average values of $d_{3,2}$ (μm), free water (%), and SFC (%) of emulsions have been compiled in Table 5.1. For all parameters no difference was observed between systems.

Table 5.1: Average droplet size $d_{3,2}$ (μm), free water (%), and SFC (%) for bulk CB and emulsions containing 10, 20, 30, and 40% (wt%) aqueous phase (plus/minus one standard error of the mean of triplicates). All emulsions contained 1% PGPR overall.

Aqueous phase (%)	$d_{3,2}$ (μm)	Free water (%)	SFC (%) ¹
CB ²	-	-	79.0 \pm 0.8
10	3.9 \pm 0.2	4.6 \pm 0.2	79.7 \pm 1.6
20	3.1 \pm 0.1	4.4 \pm 0.2	78.3 \pm 0.8
30	3.4 \pm 0.2	6.2 \pm 0.2	78.4 \pm 1.0
40	3.2 \pm 0.1	5.6 \pm 0.1	78.0 \pm 2.5

¹ Percentage expressed as gram of solid fat per gram of total fat.

² Reference material (i.e. 0% aqueous phase)

To gain an insight on the polymorphism of samples investigated using uniaxial compression test, analysis of the melting behaviour was carried out using fragments of the samples after fracture. In Figure 5.8 the melting thermographs of the systems (normalised per gram of CB) are shown. All endotherms exhibited a single peak at 33 °C indicating that CB had crystallised in form V. This result is in agreement with those reported in Chapter 4: the shear-cooling profile applied in the SSHE promotes crystallisation in the desired form V.

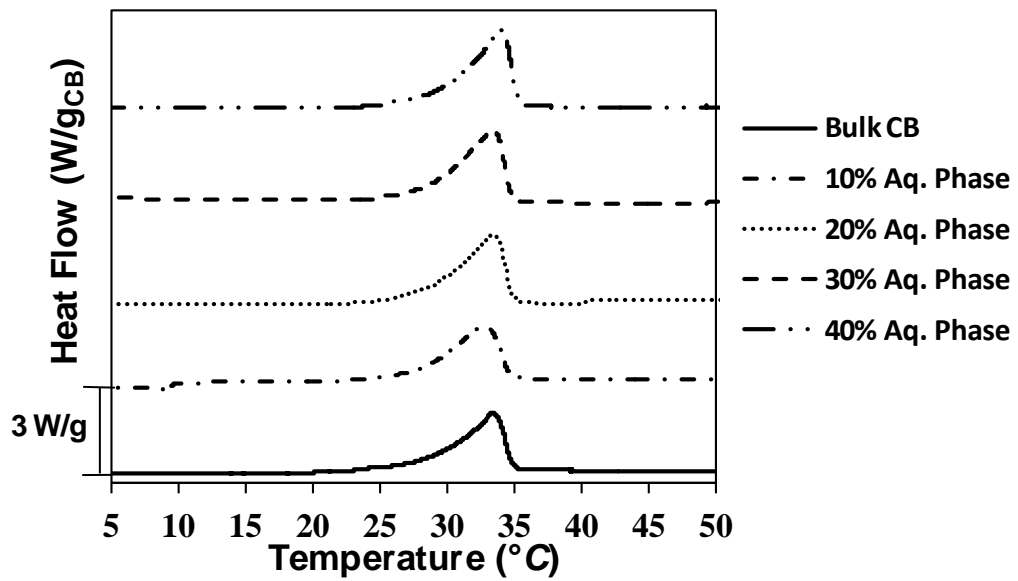


Figure 5.8: Melting profile of CB systems (at 5 °C/min). Each endotherm corresponds to the sample indicated in the legend and have all been normalised per gram of CB.

Figure 5.9 shows PLM images of 20% (a) and 30% (b) emulsions: water droplets appear as spherical inclusion within the network. To simplify the discussion, the following assumptions have been made: (1) water droplets are spherical defects; (2) the fraction of defects over 50 μm (represented by *free water* values) is comparable among systems; (3) water droplets behave as rigid particles (given the solid interface).

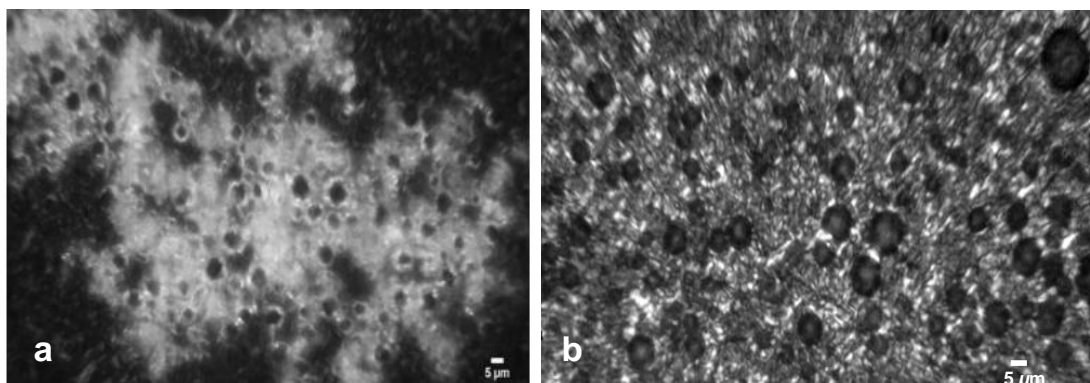


Figure 5.9: PLM visualisation of a 20% and 30% water-in-cocoa butter emulsion.

It should be pointed out here that a quantitative relationship between mechanical properties and number of droplets could not be established as fat crystals promoted droplet clustering (Fig 5.9a and b).

Figure 5.10 shows the average values of the apparent Young's modulus (E_{app}) as a function of water percentage.

The E_{app} measured for bulk CB was comparable to that of emulsions containing up to 30% water.

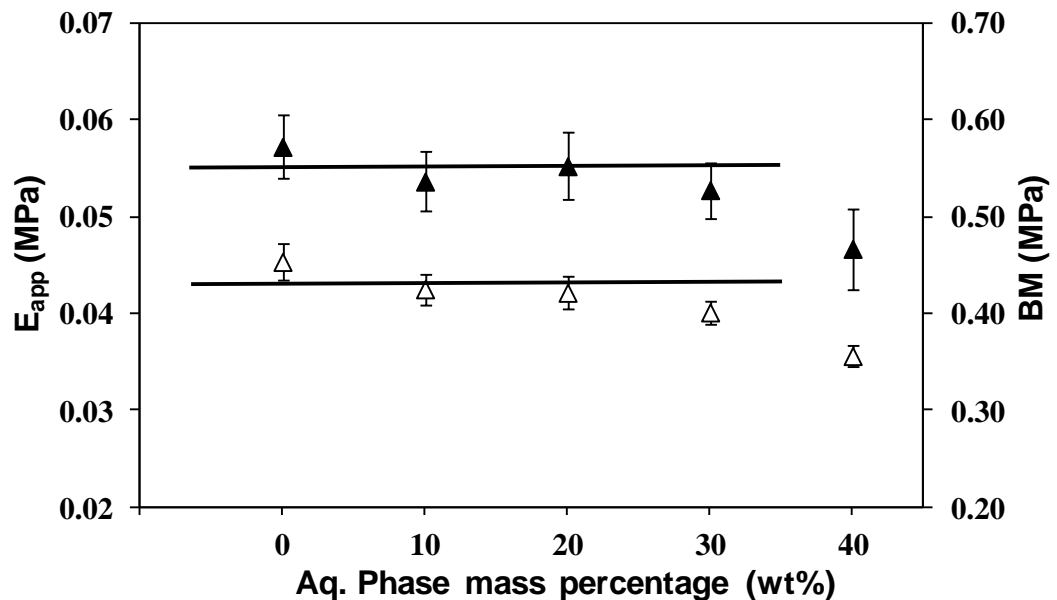


Figure 5.10: Apparent Young's modulus (E_{app} , ▲) and Bulk modulus (BM , △) for CB systems with increasing water mass fraction. Error bars are plus/minus one standard error of the mean. Solid lines serve only to guide reader's eye.

Elastic properties of fat networks are known to depend on the connectivity between structural elements (i.e. crystal aggregates or flocs) and on the stiffness of the stress concentrators (i.e. the weakest aggregates) (Tang and Marangoni, 2007). In bulk CB the E_{app} results from the large number of solid bonds between crystals and crystal aggregates (see Section 5.2.1.). In the case of emulsions, although solid bonds are probably still

formed between CB crystals which form the network, the interaction forces between droplets and CB matrix are unknown. On describing the uniaxial compressive behaviour of water-in-cocoa butter emulsions Sullo *et al.* (2014) discussed two possible scenarios: droplets were (1) bound or (2) un-bound from the matrix, although no information on the type of bonds was provided as well as of the impact of either scenarios on the E_{app} .

To explain the comparable values of E_{app} measured for bulk CB and emulsions (up to 30% water) two hypotheses can be formulated: (1) solid bonds are developed between crystals which form the interface and the bulk network. Therefore, the decrease in E_{app} observed for emulsions containing 40% water may be due to droplet aggregation leading to a weaker interaction with the fat phase. The stiffness of these aggregates would be expected to be lower than that of clusters connected by solid bonds; (2) if the development of solid bonds between matrix and droplets is excluded (due to a geometrical restriction caused by the curved droplet surface), it may be hypothesised that at low aqueous phase percentages (~30%), the total number of solid bonds is only partially reduced. Furthermore, the decrease in the number of solid bonds may be counterbalanced (at very small strain) by droplet-matrix van der Waals attractive forces and droplet-droplet interactions. The latter includes interfacial tension and hydrodynamic forces between droplets (Cisneros Estevez *et al.*, 2013).

With respect to the overall elastic behaviour, it is known that when compressing an elastic element, with k being its stiffness (given by Hooke's law), the elastic energy per unit volume of material (W_e , N/m³) stored into the body is given by Equation 5.1:

$$W_e = \frac{1}{2} E \varepsilon^2 \quad (\text{Eq. 5.1}),$$

where, ε is the engineering strain and E the Young's or elastic modulus (N/m²).

Considering that the values of E_{app} are comparable among systems (Fig. 5.10), the elastically stored energy, which is available for fracture, is also comparable. This consideration will be recalled later together with two hypotheses to interpret results at fracture.

Values of BM also remain comparable between systems for water content up to 30% (Fig. 5.10). This result indicates that the inclusion of water in the form of small rigid droplets does not decrease the overall matrix deformability in a strain range below yielding. If the hypothesis of a lower number of solid bonds is followed, this result may be interpreted considering that the presence of droplets increases the viscosity of the systems and the friction between the structural elements, thus determining a comparable BM to bulk CB (see Eq. 5.2).

The results of stress (σ_{Fr}) and strain (ε_{Fr}) to fracture as a function of aqueous phase percentage are shown in Figure 5.11a.

Bulk CB is characterised by highest hardness (σ_{Fr}), and σ_{Fr} values decrease with increasing aqueous phase. These results are in agreement with those of Sullo *et al.* (2014). In their study the authors showed that σ_{Fr} values decreased with increasing water fraction emulsions independently of the concentration of gelling agent (*k*-carrageenan) in the aqueous phase.

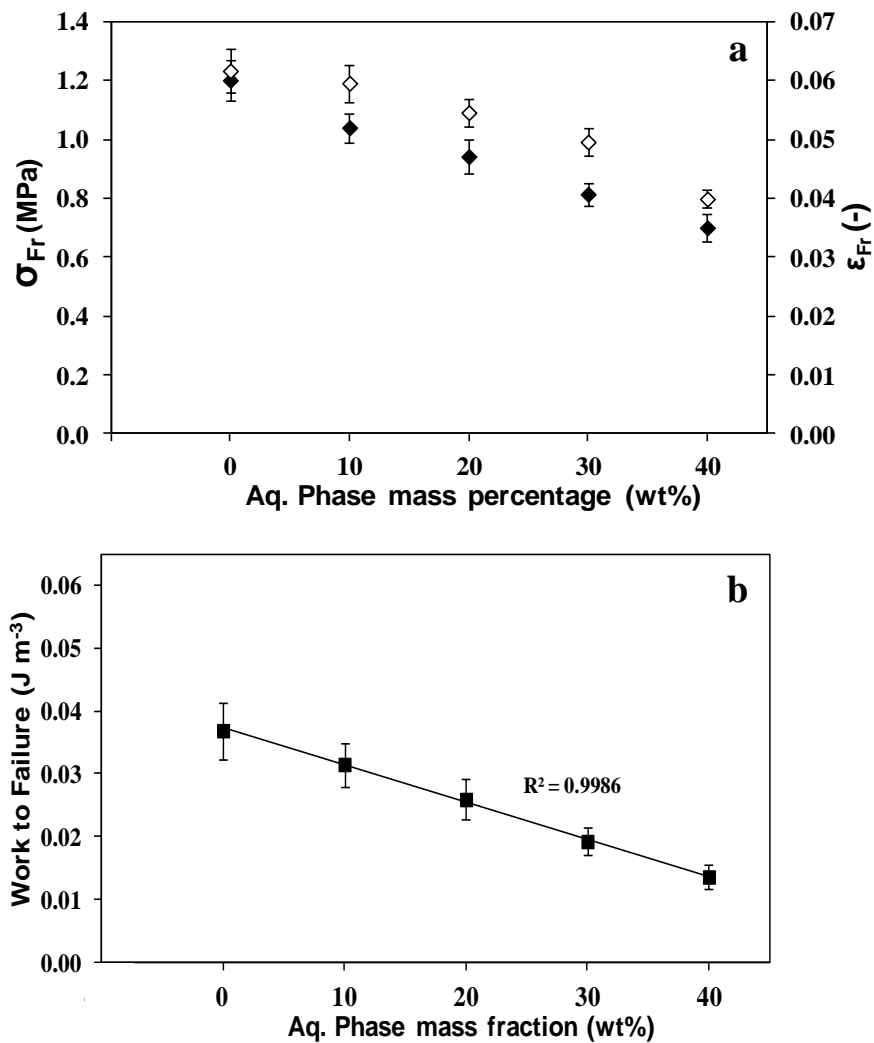


Figure 5.11: (a) Stress (♦) and strain (◇) to fracture and (b) work to fracture (■) expressed as function of aqueous phase percentage. Error bars are plus/minus one standard error of the mean.

The deformation at fracture (ϵ_{Fr}) (Fig. 5.11a) follows a similar trend: CB is able to deform the most before fracture occurs and then the systems become more brittle at increasing dispersed phase percentages. Furthermore, all the ϵ_{Fr} values are below 0.1, in agreement with what was observed by Kloek *et al.* (2005a) for fat crystal networks.

Figure 5.11b shows values of work to fracture of CB systems at increasing aqueous phase percentages. It can be seen that for water percentages above 10%, the energy required to fracture emulsions is considerably lower than that for bulk CB. It should be considered

that when compressing a system, only part of the mechanical energy supplied is used for fracture. The total supplied energy (W_{Tot}) is given by (Van Vliet, 1996):

$$W_{Tot} = W_e + W_{d,v} + W_{d,c} + W_F \quad (\text{Eq. 5.2}),$$

where, W_e is the elastically stored energy, $W_{d,v}$ is the energy dissipated due to the viscoelasticity of the system, $W_{d,c}$ is the energy dissipated due to frictions processes at large deformation, and W_F is the total work to fracture. Here, being the amount of elastically stored energy among systems overall comparable, differences in fracture energy reflect differences in the energy dissipating mechanisms, the number of the structural defects, and crack propagation. It is usually difficult to quantify the values of $W_{d,v}$ and $W_{d,c}$ and this problem is usually overcome performing test at different compressive rates. This aspect is investigated in Section 5.2.4.

With respect to the role played by the structural defects (i.e., cracks), a better understanding of the interaction between the droplets and the CB matrix was gained *via* cryo-SEM visualisation of emulsions. In Figure 5.12 and 5.13 the structure of a 20% aqueous phase emulsion at two magnifications is shown.

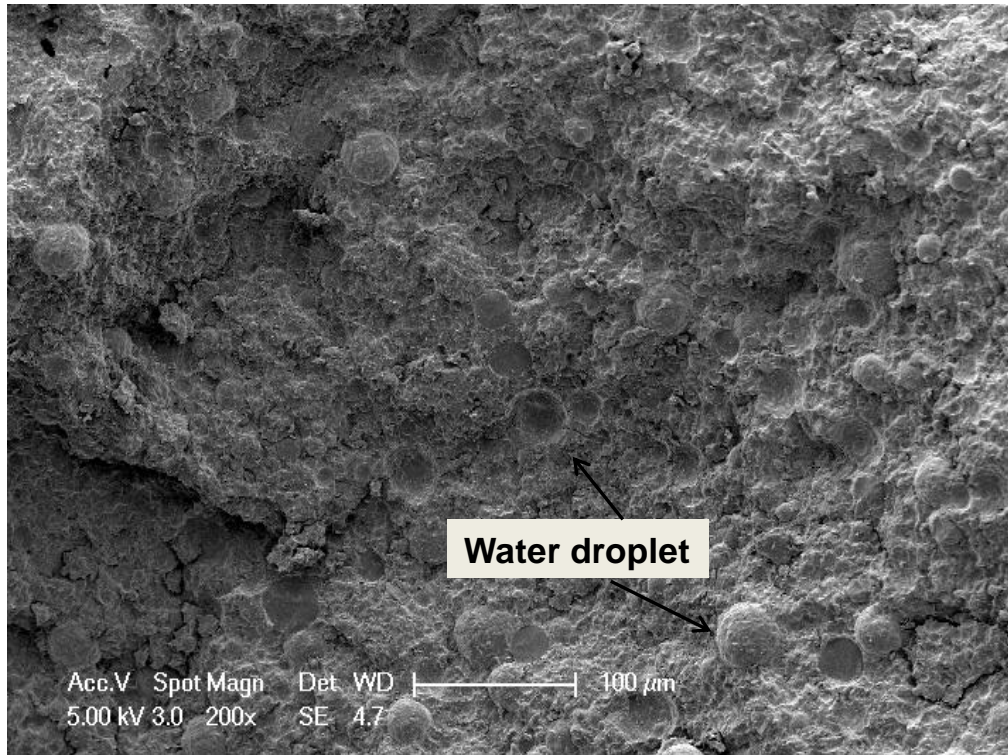


Figure 5.12: Cryo-SEM of a 20% (wt%) water-in-cocoa butter emulsion (scale bar = 100 μm).

In both cases, water droplets appear surrounded by a crystalline interfacial layer and embedded in the CB matrix. As mentioned in Chapter 4, the majority of droplets appear intact. A similar result was referred by Heertje (1993) who suggested that this behaviour accounts for *surface fracture*: the fracture pattern occurring on sample preparation is characterised by cracks propagating around the droplets.

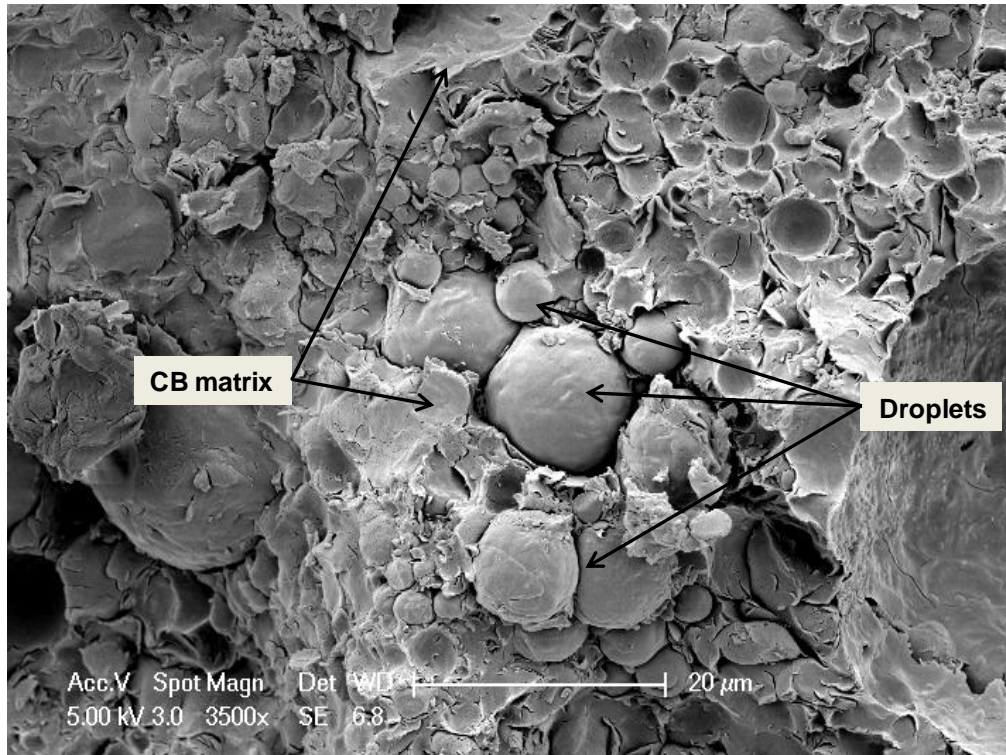


Figure 5.13: Cryo-SEM image of a 20% (wt%) water-in-cocoa butter emulsion (scale bar = 20 μm). Water droplets (covered by a continuous crystalline shell) and the cocoa butter (CB) matrix are indicated in the figure.

In Figure 5.13 it can also be seen that water droplets appear to be only partially sintered with the fat matrix. This phenomenon was also observed at higher magnification in various systems (Fig 5.14A, B, C correspond to 20, 30, and 40% aqueous phase respectively).

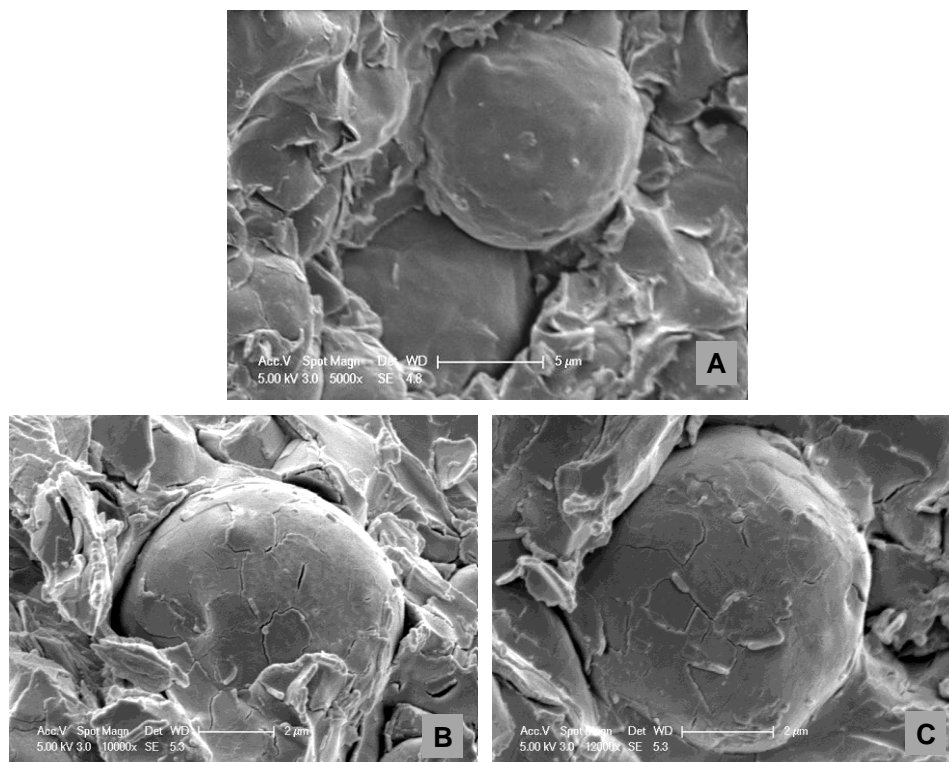


Figure 5.14: Detail of a water droplet for a (A) 20%, (B) 30%, and (C) 40% aqueous phase emulsion (w/w basis).

Droplets visualised in Figure 5.14 all appear to be partially sintered to the CB network. Although on sample preparation some of the droplet-matrix solid bonds may have been broken, a non-complete droplet-matrix bonding appears to be a common pattern. This evidence also suggests that in emulsions weak van der Waals forces may contribute to the interactions between fat crystals at the interface and in the bulk.

In the light of the results discussed above, the most intuitive explanation for the lower mechanical strength of emulsions compared to bulk CB can be gained considering that network density decreases with increasing water amounts. Fat matrix density can be simply thought of in terms of number of load-bearing elements (the rigid junctions and crystal aggregates) per unit volume of material: at increasing aqueous phase percentages, the number of load-bearing elements supporting the structure decreases. This view, however, does not consider the role of water droplets. In this sense, a more

comprehensive explanation can be gained considering the mechanical behaviour of particle filled polymer composites. When a composite material is subjected to a load, the stress will concentrate around the particles. The stress can be transmitted to the particles if they are connected (bonded) to the matrix. If the matrix is a continuous brittle polymer, the addition of a filling phase, usually represented by un-deformable inorganic particles, decreases the brittleness (Lauke and Fu, 2012). The damage process following stress-concentration events starts with particle-matrix interfacial de-bonding and continues with the crack propagating through the material. With good approximation, this structure is comparable to the one formed in CB emulsions where the continuous brittle fat matrix is filled with “rigid water particles”. When the CB systems are subjected to a load, stress-concentration will occur in the area neighbouring the droplets and can be transmitted to the droplets (*via* solid bonds). If the stress reaches a critical value, de-bonding of a particle from the matrix occurs, causing the formation of a fracture zone (*fracture initiation*). This view implies that the droplet-matrix bond is broken while the crystalline interface is able to resist the applied stress. The evidence of limited fractured droplets (as observed by cryo-SEM visualisation) supports the hypothesis of particles resisting the stress. The crack developed following fracture initiation (i.e. breaking of a solid bond) is scattered by the crystalline shell and can grow in all directions determining a stress-concentration increase in the volume of network close to the droplets. Since only weak van der Waals forces are left to support the structure in the vicinity of the droplets, the crack can easily propagate around the droplet (*fracture propagation*) and through the material leading to the development of larger local fractures. The process continues until macroscopic fracture occurs.

Finally, a more speculative consideration about the microstructural changes produced by the introduction of water droplets could be gained by the adoption of the model proposed by Marangoni and co-workers. The majority of the water is structured in small droplets (average $d_{3,2}$ approximately $5 \mu\text{m}$) having a size comparable to that of the spherical primary particles as described in the fractal model in a weak-link regime (Section 2.1.3.). This allows thinking that those droplets introduce defects at the intra-floc level. Large droplets ($d_{3,2} > 50 \mu\text{m}$) have a size comparable to that of microstructures, therefore introducing defects at the inter-floc level. As such, in the small deformation region, the elastic behaviour is determined by the inter-floc interactions, the same E_{app} for different systems could be considered to be a result of an overall small number of defects introduced at the floc-structural level. The significant decrease of the fracture parameters, where deformations at the intra-floc level are involved, would be justified by the presence of a large number of in-homogeneities. This proposed explanation is in line with the other approach described above: stress concentration would occur in the vicinity of an intra-floc droplet and, after local fracture has occurred, the stress will quickly concentrate on the neighbouring primary particles inducing fast crack propagation until structure breakdown.

5.2.3. Effect of dispersed phase droplet size on the large deformation behaviour of water-in-cocoa butter emulsions

Having investigated the role of increasing aqueous phase at constant droplet size (Section 5.2.2.), the aim of the work presented in this section was to understand the effect of droplet size on the large deformation behaviour of water-in-cocoa butter emulsions at a single water content (20%, wt%). On the basis of the knowledge developed in Chapter 4, this was achieved by manipulating the processing conditions: emulsions were prepared using the SSHE at four rotational rates (N_{SSHE}) to obtain different values of $d_{3,2}$ and free water content. Both the average $d_{3,2}$ value and free water content decrease at increasing N_{SSHE} , whereas the SFC content remained constant (Table 5.2).

Table 5.2: rotor rate and microstructural parameters of emulsions produced at different rotor rate.

SSHE Rotational rate (N_{SSHE})	$d_{3,2}$ (μm)	Free water (%)	SFC (%)
170 rpm	14.0	15.7	78.7 ± 1.7
500 rpm	8.1	7.6	79.7 ± 1.6
930 rpm	3.8	5.4	76.3 ± 2.0
1315 rpm	3.5	5.1	78.3 ± 0.8

To better understand the approach used in this section, it should be recalled that the $d_{3,2}$ is the average droplet diameter, while *free water* (%) represents the fraction of droplets with a $d_{3,2}$ above 50 μm . Considering the emulsions produced with a N_{SSHE} of 170 and 1315 rpm, respectively, the difference in the designed defect size can be easily appreciated: the $d_{3,2}$ for $N_{SSHE} = 170$ rpm is four times bigger than that obtained with a N_{SSHE} of 1315 rpm

and the free water is three times larger. It should be pointed out that it was not possible to produce emulsions having larger/smaller droplets than those reported here.

For each emulsion type, ten cylindrical specimens were produced and analysed using uniaxial compression test at 1 mm/s. Fragments of broken material for all samples were collected after compression and analysed *via* DSC to determine the main polymorphic form (Fig. 5.15). At least two melting DCS curves for each sample type were recorded. All of the samples had a melting peak at 32-34 °C suggesting they were all in form V.

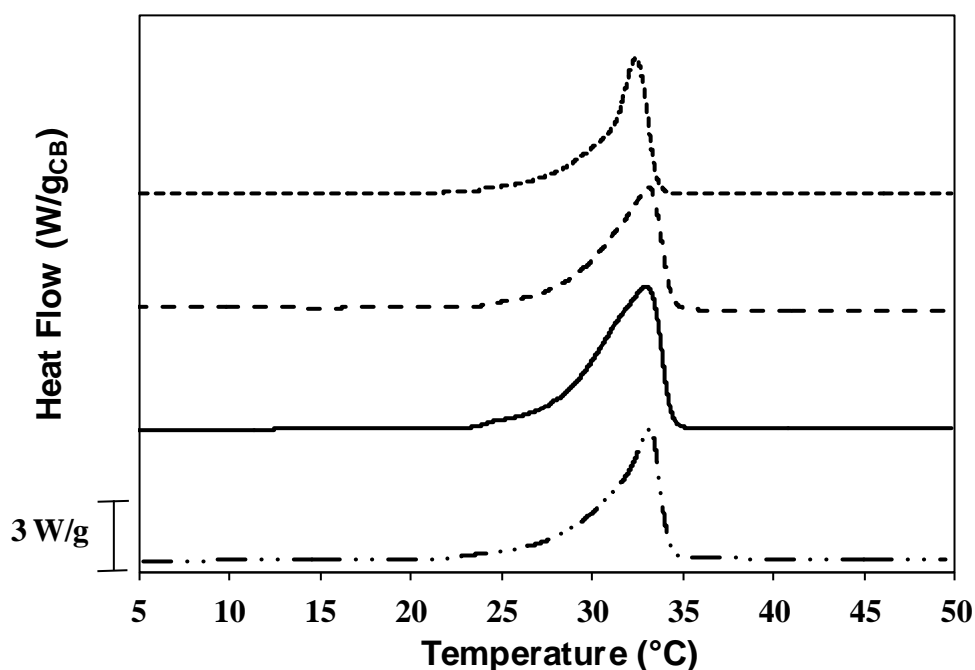


Figure 5.15: melting behaviour of emulsions produced at four SSHE rotational speeds. Endotherms correspond to samples with an average $d_{3,2}$ of (from top to bottom) 14, 8.1, 4, and 3.5 μm , respectively. Endotherms have been normalised per gram of CB.

In Figure 5.16 the values of E_{app} and BM measured for the four emulsions are shown. Although a higher E_{app} was measured for emulsions with a smaller $d_{3,2}$, differences are within the experimental error. This result suggests that the sintering of rigid junctions is not affected by increasing droplet size.

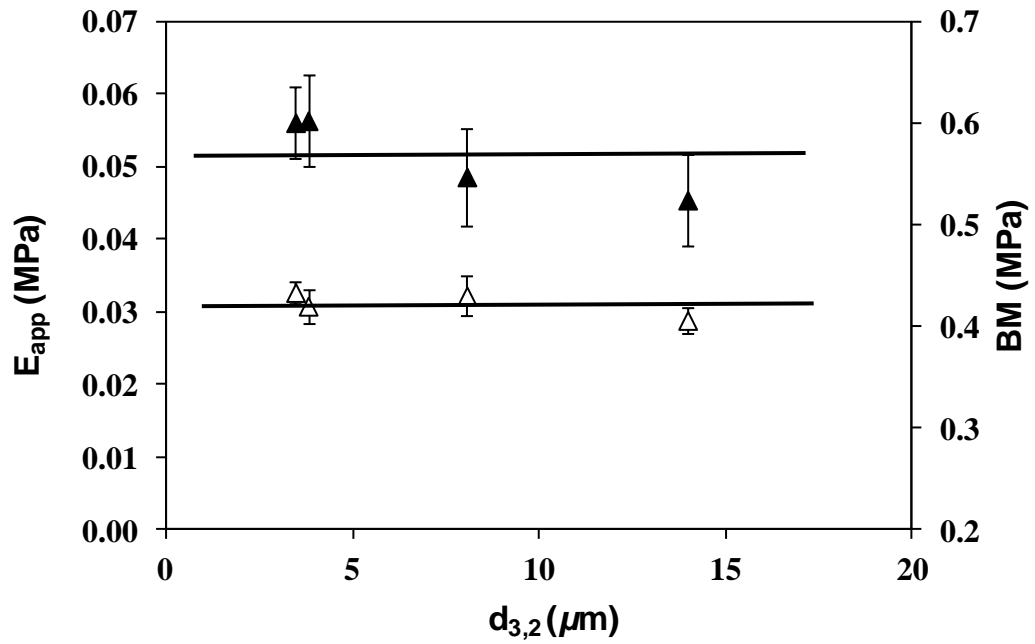


Figure 5.16: Apparent Young's modulus (E_{app} , ▲) and bulk modulus (BM, Δ) as function of the average droplet size ($d_{3,2}$, μm). Error bars represent one standard error of the mean. Solid lines serve only to guide reader's eye.

Also values of BM are the same among systems indicating that the overall matrix deformability is not affected by the size of in-homogeneities.

Figure 5.17a shows the fracture stress (σ_{Fr}) and strain (ε_{Fr}) as a function of the average $d_{3,2}$. The σ_{Fr} remains constant with increasing droplet size (and free water content). This finding indicates that, in the investigated range of defect size, the material hardness is not affected by in-homogeneities.

The ε_{Fr} decreases at increasing $d_{3,2}$ values. This result indicates that the material deformability at fracture is affected by the addition of larger defects. It should be kept in mind that the same dependency of the parameters at failure could also be expressed as a function of free water content.

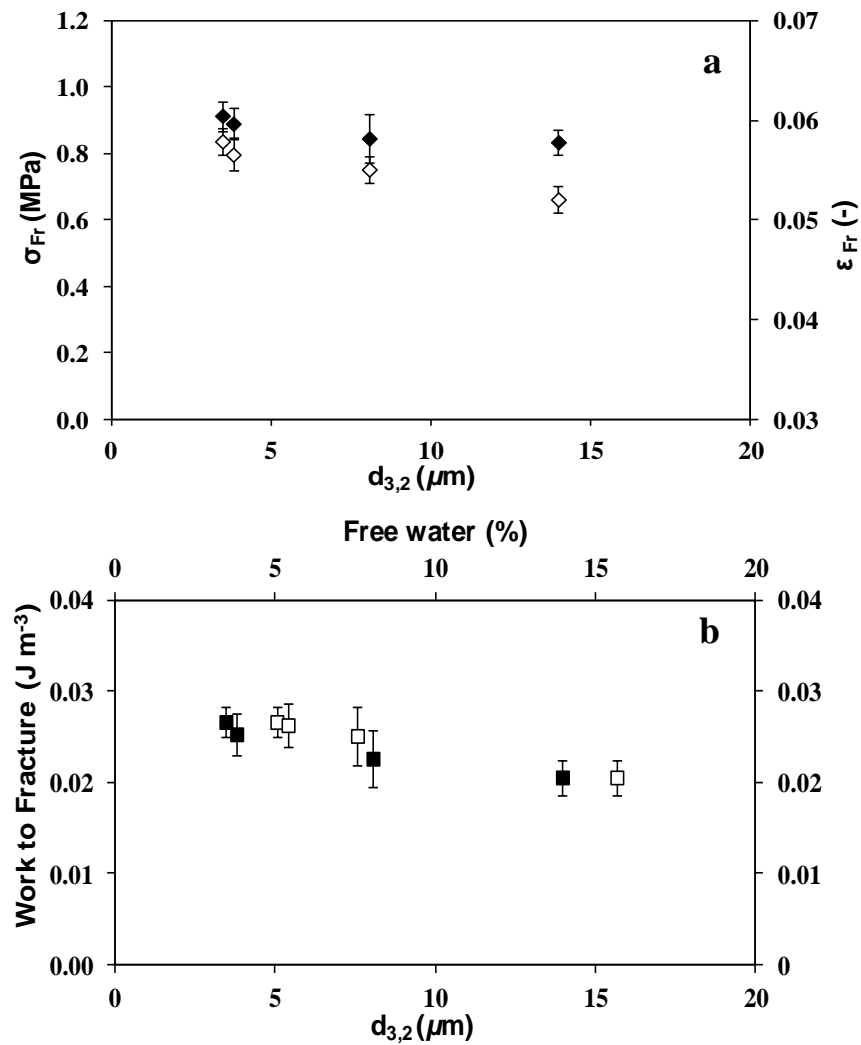


Figure 5.17: (a) True stress (\blacklozenge) and strain (\diamond) to failure expressed as function of average droplet size $d_{3,2}$ (μm). (b) Specific work to failure as function of $d_{3,2}$ (μm) (\blacksquare) and free water (\square). Error bars represent plus/minus one standard error of the mean.

Figure 5.17b shows the data of work to failure expressed as function of average $d_{3,2}$ (bottom x axis) and free water content (upper x axis). It can be seen that the profile of the data is the same: at increasing defect size, the mechanical energy needed for fracturing the material decreases.

Since all systems contained 20% (wt%) aqueous phase, two aspects must be considered to explain the reduction in the mechanical energy required to achieve material failure: (1) the size of each introduced structural defect is larger at higher $d_{3,2}$ and free water values;

(2) when larger in-homogeneities are dispersed within the fat matrix, the total number of defects decreases.

As mentioned above, the defect size in emulsions produced with a N_{SSHE} at 170 rpm is approximately three times larger than the one obtained for N_{SSHE} at 1315 rpm. However, the values of work to fracture do not differ by a factor of three between the two systems. This result suggests that the mechanism of failure does not depend linearly on the average size of in-homogeneities.

By using compression and wire cutting experiments Kloek *et al.* (2005a) calculated that the critical average defect length responsible for stress concentration in a fat crystal network is approximately 20 μm (size range 8 – 130 μm). This value corresponds to a fat crystal aggregate at the gel point (the point at which the network is formed). Such a value is very close to the defect size calculated for the weakest system in this study. This evidence may support the hypothesis that larger in-homogeneities are responsible for a more pronounced stress concentration effect as they may hinder the network aggregation process as they allow the development of less solid bonds. Furthermore, for a given percentage of aqueous phase, by decreasing the size of particles, a larger number of droplets is formed and, therefore, a larger number of solid bonds between the interface and the bulk network is expected to be formed, which determines higher material strength and allow more deformation prior to fracture.

5.2.4. Large deformation behaviour as function of compressive rate

CB systems can be considered visco-elastic materials, which means that their behaviour incorporates aspects of liquid (viscous) and solid (elastic) components. Therefore, their mechanical response is expected to be test speed dependent. The study of the uniaxial load response over a wide range of test speeds would provide an understanding of how network relaxation and fracture propagation influence failure behaviour of those materials (Zhang *et al*, 2005). Network stress relaxation is associated with energy dissipating mechanisms occurring on deformation, i.e. viscous flow and friction between structural elements (terms $W_{d,v}$ and $W_{d,c}$ in Eq. 5.2, respectively).

The aim of this experimental section was to determine how the large deformation behaviour of CB systems is affected by the compressive rate. To gain an understanding over a wide range of rates, test speeds were evaluated from 0.01 to 10 mm s⁻¹. Test specimens of bulk and emulsified CB were produced using a SSHE (Section 5.2.2.). Emulsions contained 20% and 40% (wt%) of dispersed phase, respectively. The average $d_{3,2}$ (μm), free water (%), and SFC (%) have been compiled in Table 5.1. The two emulsified systems are characterised by the same droplet size and the SFC is the same for the three systems. For each compression rate and formulation, at least ten specimens were analysed and the average and standard error of the mean reported.

On compression, independently from the compressive speed, samples always fractured after a small deformation. The most commonly observed failure pattern was characterised by a fracture along the central longitudinal axis with the formation of two cones in correspondence to the flat ends and several lateral pieces (as also shown earlier in Fig. 5.2 and 5.3). So for these systems, brittle fracture was also thought to occur.

The measured E_{app} values (Fig. 5.18) are independent of the compressive rate and formulation. This behaviour can be explained recalling that the behaviour of an ideal (Hookean) solid material is not deformation rate dependent: when a purely elastic element experiences a load (higher than its stiffness), it deforms instantaneously. Since the E_{app} of the CB systems is independent from the formulation within the investigated deformation time scale, it can be concluded that this property is strictly due to the deformability of solid bonds formed within the matrix (before introducing any permanent mechanical damage).

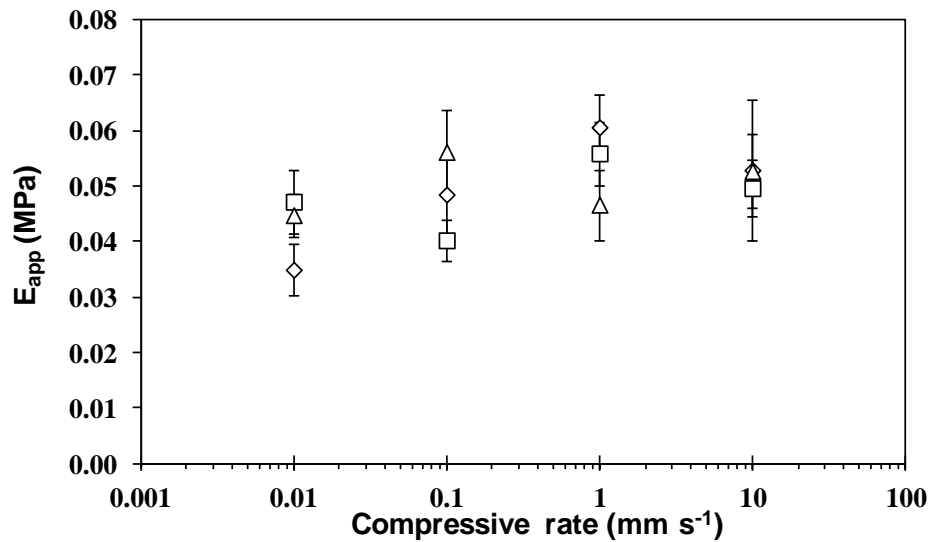


Figure 5.18: Apparent Young's modulus (E_{app}) as function of compressive rate. Bulk cocoa butter (\diamond), 20% aqueous phase (\square) and 40% aqueous phase (Δ). Error bars are plus/minus one standard error of the mean.

As the E_{app} is the same among systems, it could be hypothesised that the same elastic energy ($\sim \frac{1}{2} E_{app} \cdot \epsilon^2$) is stored in all the systems and can be used for fracture propagation. Differences in the failure behaviour will therefore arise from discrepancy in the number of microstructural defects (*fracture initiation*) and energy dissipation (*fracture propagation*).

Also the values of BM (Fig. 5.19) are the same at all compressive rates and no differences among systems were observed. A general trend showing an increase in the BM values at increasing compressive rate can be noticed, suggesting materials display higher resistance to deformation at increasing compressive rate. This result can be explained considering that energy dissipation processes has a larger impact at increasing test speed (see Fig. 5.20 and text).

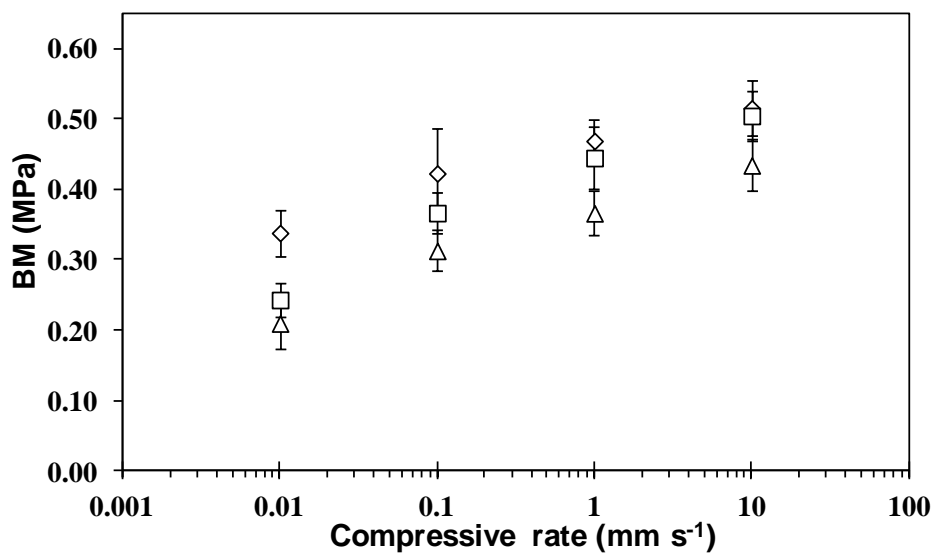


Figure 5.19: Bulk modulus (BM) as function of compressive rate. Bulk cocoa butter (\diamond), 20% (wt%) aqueous phase (\square) and 40% (wt%) aqueous phase (Δ). Error bars are plus/minus one standard error of the mean.

Figure 5.20a, b, and c show results of fracture stress (σ_F), fracture strain (ε_F), and work to fracture, respectively.

Bulk CB had a higher value for all of the fracture parameters at any compressive rate. Furthermore, for a cross-head speed up to 0.1 mm/s, no significant difference was observed between 20% and 40% emulsified systems. For all samples, the measured mechanical parameters at failure increased with increasing compressive rate. This result suggests that the fracture behaviour of CB systems is rate dependent, which is expected

for viscoelastic materials. It should be pointed out that the behaviour observed here for the three CB systems at a compressive rate of 1 mm/s is in agreement with the data shown previously (Fig. 5.11a and b). This indicates that the results are reproducible.

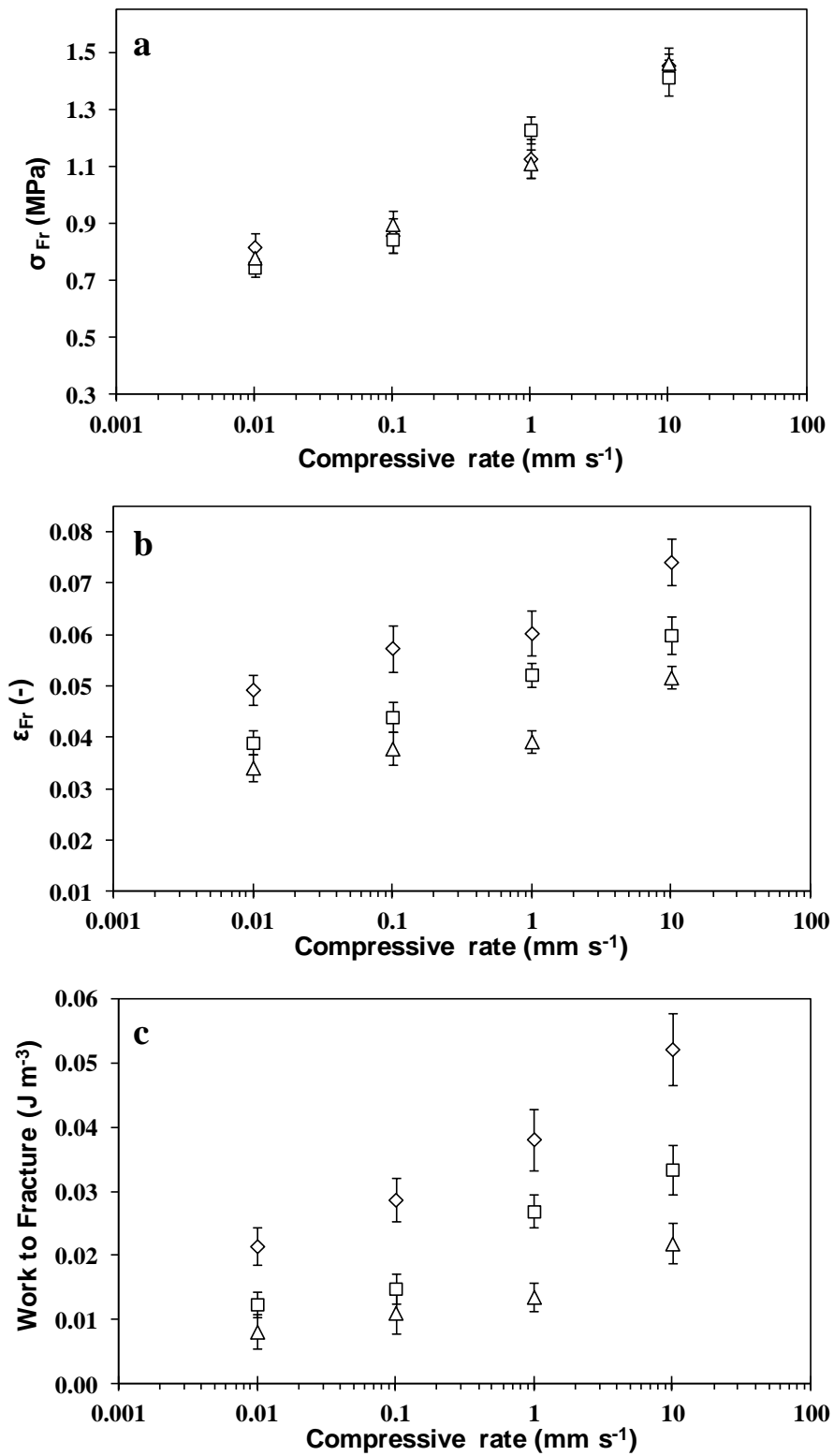


Figure 5.20: (a) fracture stress, (b) fracture strain, (c) work to fracture as function of compressive rate for bulk cocoa butter (\diamond), 20% (wt%) aqueous phase (\square) and 40% (wt%) aqueous phase (\triangle). Error bars are plus/minus one standard error of the mean.

Fracture stress represents the hardness of materials, and values measured for CB systems are shown in Figure 5.20a. Two regions can be observed: for each CB system at a low cross head speed (≤ 0.1 mm/s) there is no significant difference between measured values, whereas at higher test speed, the σ_{Fr} for all materials increases with increasing compressive rate. This result may have important implications from a product design perspective: considering that the perceived hardness on biting is affected by both material properties and bite rate (usually above 10 mm/s), it is reasonable to think that the development of a product having a lower fat content may be achieved by tuning the material properties to deliver the expected mechanical behaviour in the mouth.

Data referring to fracture strain (ε_{Fr}) are shown in Figure 5.20b. Although values increase with increasing test rate, up to 1 mm/s there is no difference among ε_{Fr} values for each of the three CB systems. For all sample types an increase of ε_{Fr} occurs at 10 mm/s. Within the range of used compressive rates, results suggest that ε_{Fr} is less influenced than σ_{Fr} by the test speed.

Work-to-fracture data are shown in Figure 5.20c. The results suggest a strain rate hardening behaviour for all of the CB systems: the mechanical energy required to fracture a material increases with increasing test speed. The small error bars suggest that test reproducibility was high overall. However, the error increases at higher compressive rates. A similar trend both in terms of strain hardening behaviour and increasing error with test rate was described on compressive analysis of butter (Rohm, 1993). To explain the observed strain hardening behaviour, it should be recalled that water-in-cocoa butter emulsions are viscoelastic (food) materials, where some of the mechanical energy supplied on deformation is stored in the elastic elements (solid bonds) and some is dissipated *via* viscous flow and friction between structural elements. While the

mechanical behaviour of the elastic components does not depend on deformation rate, energy dissipating mechanisms are deformation rate dependent (Calzada and Peleg, 1978). As mentioned above, two main energy dissipating mechanisms occurring in the systems studied here are viscous flow and frictional effects between structural elements. However, it is very difficult (if at all possible) to determine the effect of each of these mechanisms on mechanical properties. The difficulty arises from the fact that each dissipating mechanism correlates differently with the strain rate, leading to results difficult to interpret (van Vliet and Walstra, 1995; van Vliet, 2002).

In this study, at low compression rates, network stress relaxation occurs over a broader time-scale, but the time available for fracture propagation is also longer. The lower values of the failure parameters indicate that fracture propagation occurs faster than network relaxation. However, at higher uniaxial load rates, the deformation rate is faster than fracture propagation; and stress relaxation mechanisms dominate. This behaviour results in a higher deformation at fracture (ε_{Fr}). Furthermore, it is likely that if a given deformation is applied faster, the sliding of structural elements against each other and viscous effects of the liquid oil trapped within the fat crystalline matrix are more pronounced. Therefore, more energy is dissipated and, as a result, the material appears to be harder and requires more energy to fracture.

5.3. Conclusions

The results presented and discussed in this chapter show that cocoa butter (CB) systems produced using a scraped surface heat exchanger (SSHE) behave as brittle materials at large deformation. The bulk fat phase, displayed a considerably different mechanical behaviour according to the crystallisation process: plastic, if crystallised statically, or brittle fracture, if crystallised under shear. Differences were attributed to the development of more solid bonds in sheared CB than in static CB.

In the case of emulsions, the presence of water droplets provides zones in the structure where stress concentration occurs. On the basis of these results, it can be concluded that by increasing the amount of water (hence the number of in-homogeneities) or the size of the defects, the system becomes more prone to collapse under large deformation and less mechanical energy has to be supplied to obtain fracture (initiation and propagation). Experimental evidences support the hypothesis that on compression the crack may initiate in the vicinity of the droplets and propagate around them by overcoming the adhesion stresses between fat crystals forming the network and the interface. This hypothesis suggests that fracture may be occurring according to a preferred growth pattern in emulsions.

The visco-elastic nature of CB systems was confirmed by their strain hardening behaviour. Bulk CB showed higher hardness than emulsions at any compressive rate. However, the elastic properties of the systems were not influenced by either compression rate or formulation, suggesting that the fat crystal network dominates the small deformation region.

With respect to the performance of these novel food materials on consumption, the lower mechanical strength observed for emulsions compared to the bulk fat phase suggests that these systems will be perceived as different, mainly on first bite. A potential route to increase their mechanical strength may be the use of an emulsifier to increase the interfacial crystallisation and the development of more solid bonds between interfacial and network crystals.

Chapter 6. Crystallisation in water-in-cocoa butter emulsions

6.1. Introduction

It has been discussed in Chapter 4 that water-in-cocoa butter emulsions kinetic stability is provided by both PGPR molecules and fat crystallisation. CB solidification contributes to droplets stability by both network formation and Pickering stabilisation. The interfacially adsorbed crystals eventually sinter together to form a solid *shell*. This latter phenomenon implies a process of interfacial crystallisation at the water droplets interface. It should be pointed out here that the process of crystallisation in W/O emulsions has been studied in less detail than in O/W systems and has gained attention only in recent years as it may provide an novel route for texture modification and bioactives incorporation.

For O/W emulsions it has been shown that TAGs crystallisation behaviour is affected by interfacial layer composition. When high melting point surface active additives are at the interface, *interfacial heterogeneous nucleation* occurs if structural similarities with oil TAGs exist. The presence of a layer of crystalline molecules induces the ordering of the TAGs located in the vicinity of the droplet interface, which results in the formation of different polymorphs compared to bulk fat crystallisation (see Section 2.2.5.1.). This process may also induce an increase in nucleation rate (Ueno *et al.*, 2003, Arima *et al.*, 2009).

Fewer evidences of interfacial local ordering and its effect on fat phase polymorphism are available for W/O emulsions. Saturated monoglycerides have been shown to solidify directly at the interface, which in turn might induce continuous fat phase TAGs nucleation *via interfacial heterogeneous templating* (Gosh *et al.*, 2011). The same phenomenon may occur in monomeric liquid surfactants stabilised droplets in presence of crystallising bulk TAGs (Rousseau, 2013). For PGPR, the liquid polymeric emulsifier used in this study, Rousseau (2013) has hypothesised that interfacial crystallisation

cannot occur. This was postulated to be due to its physical state (liquid) and complex interfacial arrangement (not fully elucidated), which would not allow the necessary TAGs-emulsifier interaction and local ordering.

The aim of the work presented in this chapter was to investigate the crystallisation behaviour of water-in-cocoa butter emulsions produced using PGPR as emulsifier. To the best of author's knowledge, no study on kinetics of crystallisation of water-in-oil emulsions exists. This is probably due to the fact that emulsions quickly destabilise when fat is melted as discussed in literature Rousseau *et al.* (2003; 2009). As mentioned in Chapter 4, emulsions remained stable even when CB was molten, which was attributed to the ability of PGPR to sterically stabilise the droplets.

It was hypothesised that water droplets would act seeds-impurities promoting CB crystallisation *via interfacial heterogeneous nucleation* similarly to that observed in O/W emulsions. This hypothesis implies that PGPR molecules organised at the interface would interact with CB TAGs increasing the rate of crystallisation compared to bulk CB.

The effect of the interface on the polymorphism of water-in-cocoa butter emulsions is more difficult to predict. This is due to the lack of studies investigating the role played by oil soluble surfactants on the polymorphism of crystallising TAGs in water-in-oil emulsions. Nevertheless, considering that some structural similarities exist between acyl chains of the emulsifier and CB TAGs and that the interface is expected to behave as viscous liquid, the interfacial layer may enhance polymorphic evolution by promoting molecular re-arrangement.

To test the hypothesis, two emulsions were formulated containing 20 and 40% (wt%) aqueous phase, respectively, and the same droplet size. Since the 40% emulsion contains the highest number of seeds-impurities (i.e. droplets), it is expected to be the fastest to

crystallise. To evaluate the effect of CB systems microstructure, samples were melted to erase the crystal memory and crystallised at four temperatures (5, 10, 15, 20 °C). This allowed investigating the combined effect of microstructure and degree of supercooling on CB crystallisation.

6.2. Results

6.2.1. Overview of the crystallisation study

To facilitate data discussion, the chapter has been divided in sections corresponding to each crystallisation temperature investigated ($T_{Cr} = 5, 10, 15, 20$ °C). Here 35 °C is taken as CB final melting point (T_m), therefore, the degree of supercooling can be calculated as: $T_m - T_{Cr}$.

Section 6.3 contains a general discussion of the effect of temperature and microstructure on CB crystallisation.

The solidification was followed using pNMR and data fitted to the Avrami model to evaluate kinetics of phase transition. Polymorphic evolution was investigated *via* DSC using the “stop-and-return” method (Section 3.2.3.2.). On the basis of the results by van Malssen *et al.* (1999) and Marangoni and McGauley (2003), at any isothermal T_{Cr} between 5 and 20 °C, CB is expected to initially crystallise in α form. The time required for the subsequent monotropic transition to higher polymorphs depends on T_{Cr} and, in the view of the formulated hypothesis, on the microstructure of CB systems. Polymorphic evolution is discussed here both in qualitative and quantitative terms. Qualitative information was gained from the average endotherms and the corresponding main melting peaks (i.e. curve maxima). The relative mass fraction of polymorphs for all

temperatures-samples combinations was calculated using the deconvolution analysis (Section 3.2.3.2.).

Prior to discussing results, two more considerations with respect to polymorphism are needed: (1) given the temperature range investigated here, γ polymorph crystallisation (Form I, melting range: from -8 to +5 °C) can be excluded; (2) the presence of form VI can be ruled out as it is generally produced over periods much longer than those used in this study. Furthermore, the expressions “form II and α form”, “form III and β'_2 form”, and “form IV and β'_1 form” will be used synonymously throughout this chapter.

Finally, it should be pointed out here that an attempt to evaluate the kinetics of polymorphic transformation was made but it was not successful. The expression “faster polymorphic transformation” will be used here to indicate a higher amount of more stable form in one sample compared to another at the same time point.

6.2.2. Emulsions: formulation and droplet size

Although it is not possible to calculate PGPR surface coverage, the same ratio PGPR/aqueous phase was used (5% wt% of the aqueous phase) in order to minimise any difference in the interfacial composition between emulsions. Furthermore, processing conditions were tuned to obtain the same average $d_{3,2}$ (i.e., same size of impurities) among systems. Data of droplets characteristics have been compiled in Table 6.1 for emulsions prior and after the crystallisation experiments. Therefore, at increasing dispersed phase percentage, the number of heterogeneous nuclei within the fat matrix increased. Data in Table 6.1 demonstrate that systems were stable on re-melting. Although a small increase in the $d_{3,2}$ and free water content value occurred, differences were negligible. Furthermore, the decrease in the sigma value suggests that only the largest droplets were affected by the re-heating step with the others remaining stable.

Table 6.1: Droplet characteristics of emulsions prior to crystallisation and after re-crystallisation experiment.

Emulsion system	After production			After re-crystallisation		
	$d_{3,2}$ (μm)	Σ (σ)	Free water (%)	$d_{3,2}$ (μm)	Σ (σ)	Free water (%)
20% Aq. phase	2.0 ± 0.11	0.61	0.00	2.8 ± 0.26	0.38	3.4
40% Aq. phase	2.8 ± 0.20	0.44	2.64	3.7 ± 0.37	0.41	3.1

6.2.3. Crystallisation at 5 °C

In Figure 6.1a the SFC evolution over time for CB systems crystallised at 5 °C is shown. The dotted line represents the cooling profile experienced by the samples within the probe. The initial cooling rate was approximately 15 °C/min and samples reached the T_{Cr} within 10 minutes after the start of the experiment. No differences in the cooling profiles were observed between samples. Although it may seem that crystallisation has mostly occurred before attaining the T_{Cr} , it should be considered that the thermocouple recorded the temperature evolution at the centre of the sample, i.e., the “warmest” point of the material. It is reasonable to assume that at the wall and in the outer portions of the tubes, samples had reached the desired T_{Cr} much faster (within 2-3 minutes), thus allowing to consider the occurrence of isothermal crystallisation. Furthermore, the overall cooling time scale was comparable to that obtained by DSC. Therefore, despite the difference in masses and equipment used, it is reasonable to think that a qualitative correlation between kinetic evolution of crystalline material and its polymorphism can be made.

For none of the crystallisation curves the presence of induction time was observed (Fig 6.1a). This result was attributed to the high level of imposed supercooling ($= 30\text{ }^{\circ}\text{C}$). For all samples, the SFC profile increased steeply within the first 20 minutes of crystallisation reaching a plateau value above 90% after approximately 30 minutes. No difference in the SFC content was observed among systems. The SFC value obtained for CB is in agreement with that of 90.9% ($\pm 1.2\%$) reported by Oliver *et al.* (2015) (at $5\text{ }^{\circ}\text{C}$).

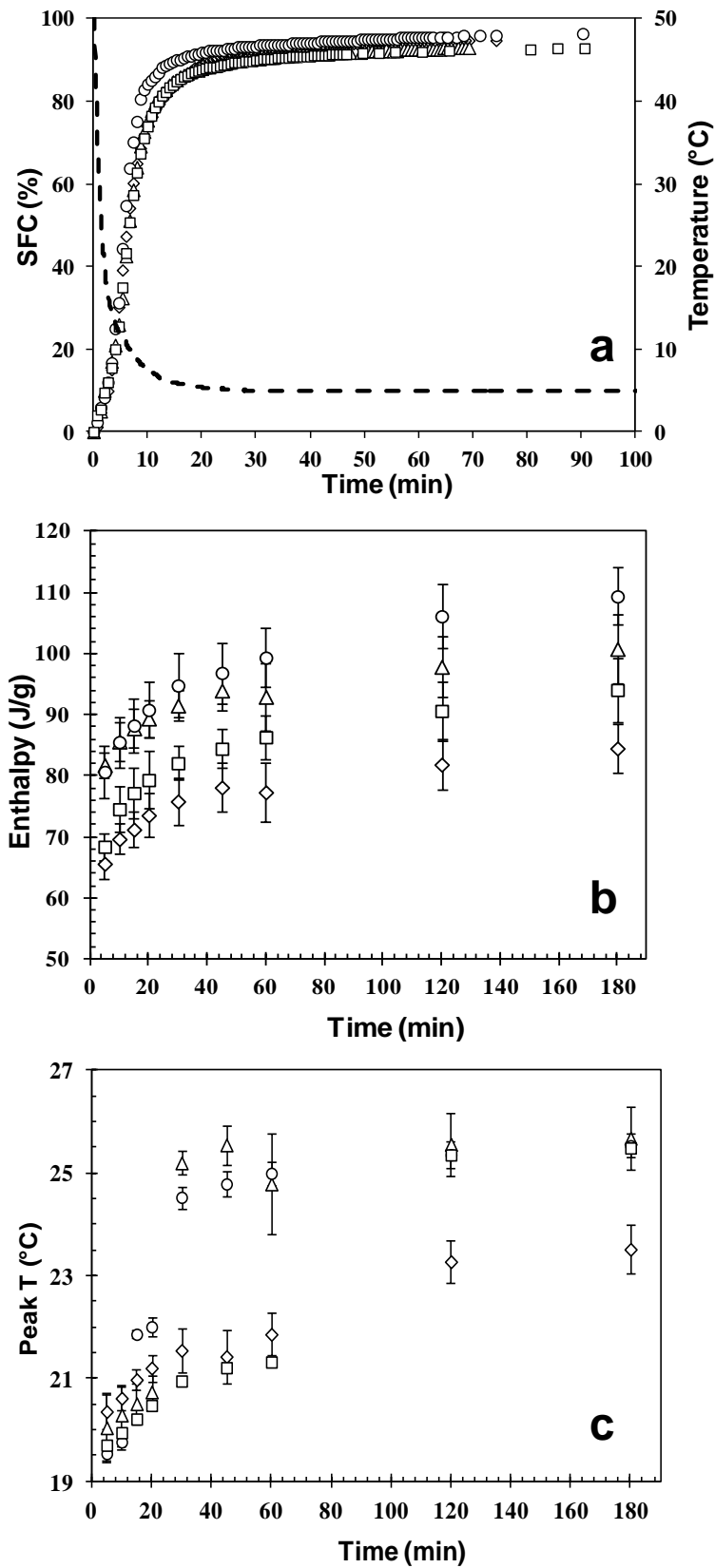


Figure 6.1: (a) SFC curves, (b) enthalpy of fusion per gram of CB, and (c) main melting peak temperatures for bulk CB (\diamond), 20% (Δ) and 40% (\circ) aqueous phase emulsions, and CB containing 1% PGPR (\square) at 5 °C. Error bars represent one standard deviation of triplicates and where not shown is within symbol size.

To compare the kinetics of crystallisation among systems, only the SFC data recorded between 5 and 20 minutes after the start of the experiment were used for the Avrami fitting. This was done to compare the kinetics of α polymorph formation. As it will be discussed in detail below, α polymorph is the main form in the early stage of the crystallisation process. Fitting of SFC data for longer isothermal holding times was not considered as it would have been a function of both further crystallisation and polymorphic evolution. Parameters obtained from the Avrami fitting have been compiled in Table 6.2. In all cases, fitting of the data to the model gave good results ($R^2 \geq 0.89$).

The calculated exponent n had a value of approximately 1 for all systems suggesting an instantaneous nucleation mechanism, i.e. nuclei appear at all at once after reaching the T_{Cr} (Yang *et al.*, 2013). This result is expected considering the high level of imposed supercooling. The obtained n value is in agreement with the one reported by Marangoni and McGauley (2003). The crystallisation rate constant (k) is also comparable among systems, and, therefore, the half time of crystallisation ($t_{1/2}$) is the same for all samples (Tab. 6.2).

Table 6.2: Avrami parameters (n and k) and R^2 of the fitting for SFC data obtained on isothermal crystallisation at 5 °C of CB systems.

Sample	n	k (t^{-n})	$t_{1/2}$ (minutes)	R^2
CB	1.13	0.10	6.0	0.967
20% Aq. Phase	1.29	0.07	7.4	0.929
40% Aq. Phase	1.03	0.16	4.2	0.892
1% PGPR in CB	1.27	0.07	7.3	0.951

Values of melting enthalpy are shown in Figure 6.1b. As expected, for all systems the measured enthalpy increased over time indicating increasing extent of crystallisation.

Emulsions were characterised by higher melting enthalpies than those recorded for bulk CB at all time points, whereas CB containing 1% PGPR was characterised by intermediate values. It should be noted that the enthalpy of melting for the dispersed system containing 40% aqueous phase was always the highest. Considering that the SFC values were comparable among systems, the difference in the enthalpies may result from differences in the polymorphism as suggested by melting temperature values shown in Figure 6.1c. Melting peak temperatures indicate that in the first twenty minutes of crystallisation all CB systems solidified mainly in α form (melting point ≤ 21 °C). This result is in agreement with the results of Marangoni and McGauley (2003) who reported that α polymorph existed after 2 minutes at 5 °C. Fessas *et al.* (2005) also reported that at T_{Cr} of 5 °C, CB would crystallise in form II. At holding times above 30 minutes (Fig. 6.1c), melting peak temperature for emulsions remained considerably higher than that recorded for bulk CB, while the system containing 1% PGPR reached the same melting temperature of the emulsions only after two hours of crystallisation.

Analysis of the endotherms (Fig. 6.2) revealed some differences concerning the polymorphic evolution between bulk CB and emulsions. Although all samples had a main peak at around 20 °C in the first 20 minutes of crystallisation, suggesting the presence of α form, a shoulder at approximately 25 °C was observed at an early stage for emulsions. Furthermore, in the case of emulsions, melting curves were centred at 25 °C after 30 minutes of annealing with the peak corresponding to α form decreasing over time. This was particularly evident for the 40% emulsion where α form peak appeared as a small bump at the end of the experiment. For bulk CB the main peak was at around 23 °C suggesting that it remained mostly in form III. Nevertheless, the development of a second peak at approximately 26 °C was visible toward the end of the experiment revealing the

presence of form IV. CB containing 1% PGPR showed the presence of two distinct peaks: the lower temperature peak was broader and smaller, the higher temperature peak was sharp and high, indicating form II and III and form IV, respectively.

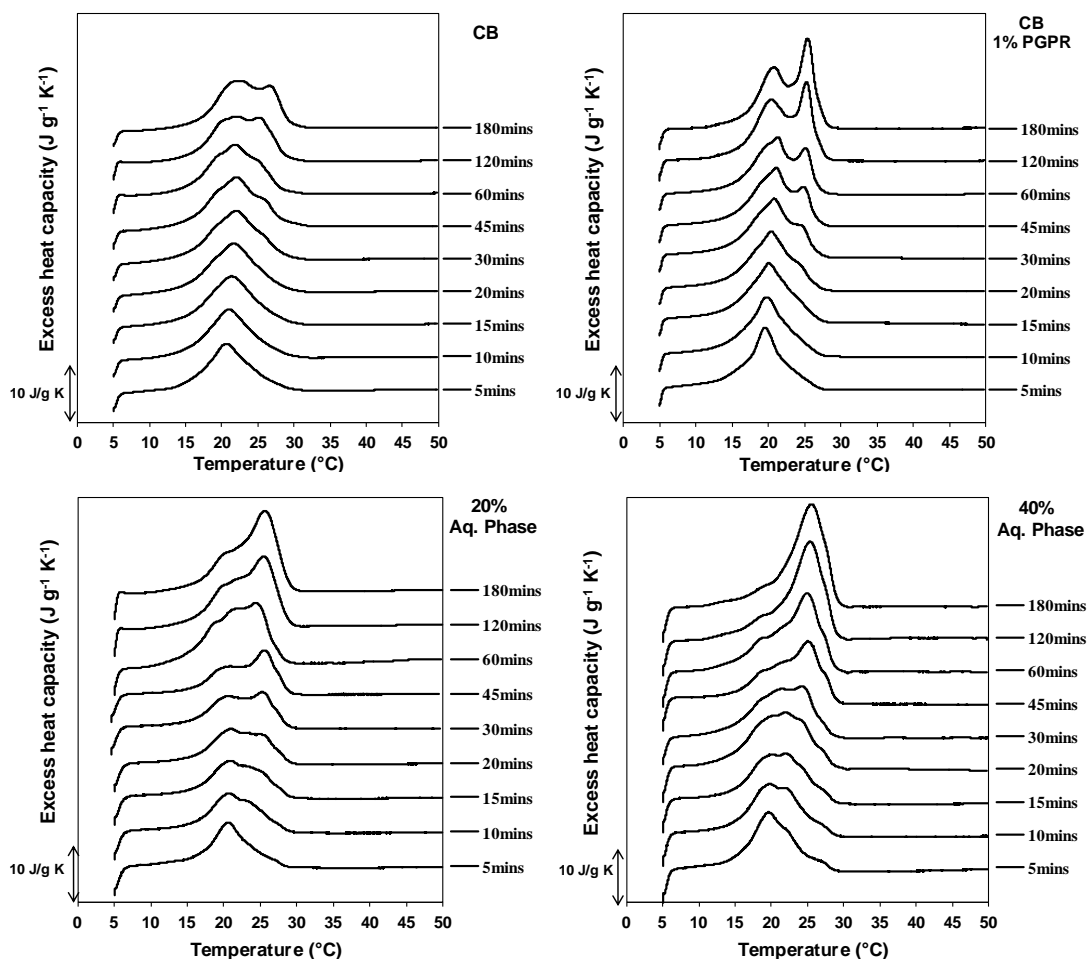


Figure 6.2: Average melting curves for CB systems crystallised at 5 °C at all holding times. The time point corresponding to each melting curve and the CB system are referred in the figure.

Results obtained from deconvolution analysis are shown in Figure 6.3. In each graph, the relative fraction (expressed in percentage) of each polymorph is shown as a function of the annealing time. After 5 minutes of crystallisation, all systems were mainly in form II (α polymorph). This result is expected as α polymorph is the fastest form to crystallise according to the *Ostwald step rule*. This rule predicts that the least stable form (α) is the

fastest to crystallise when crystallisation is induced by a temperature decrease. α polymorph remained the predominant form for the first 20 minutes for bulk CB and CB containing 1% PGPR. In the case of emulsions, form III remained predominant until 30 minutes of crystallisation being thereafter replaced by form IV. As general trend, form IV grows at the expense of form III, with the latter evolving from form II. It should be considered that while in all systems the least stable α form represented approximately 20% of the solid phase after 60 minutes of crystallisation, form IV became predominant ($\geq 50\%$) only in the emulsions. Bulk CB and CB with 1% PGPR remained mostly in form III, with form IV being approximately 40%. It is important to consider that as the equilibrium in the SFC value was reached after about 45 minutes of crystallisation (crystal fraction of ~ 0.9), the increase in the enthalpy values at longer annealing time (Fig. 6.1b) can be attributed to the polymorphic transition. This latter result is in agreement with Fessas *et al.* (2005) who reported that after the crystallisation was completed, the DSC signal was produced by the polymorphic transitions.

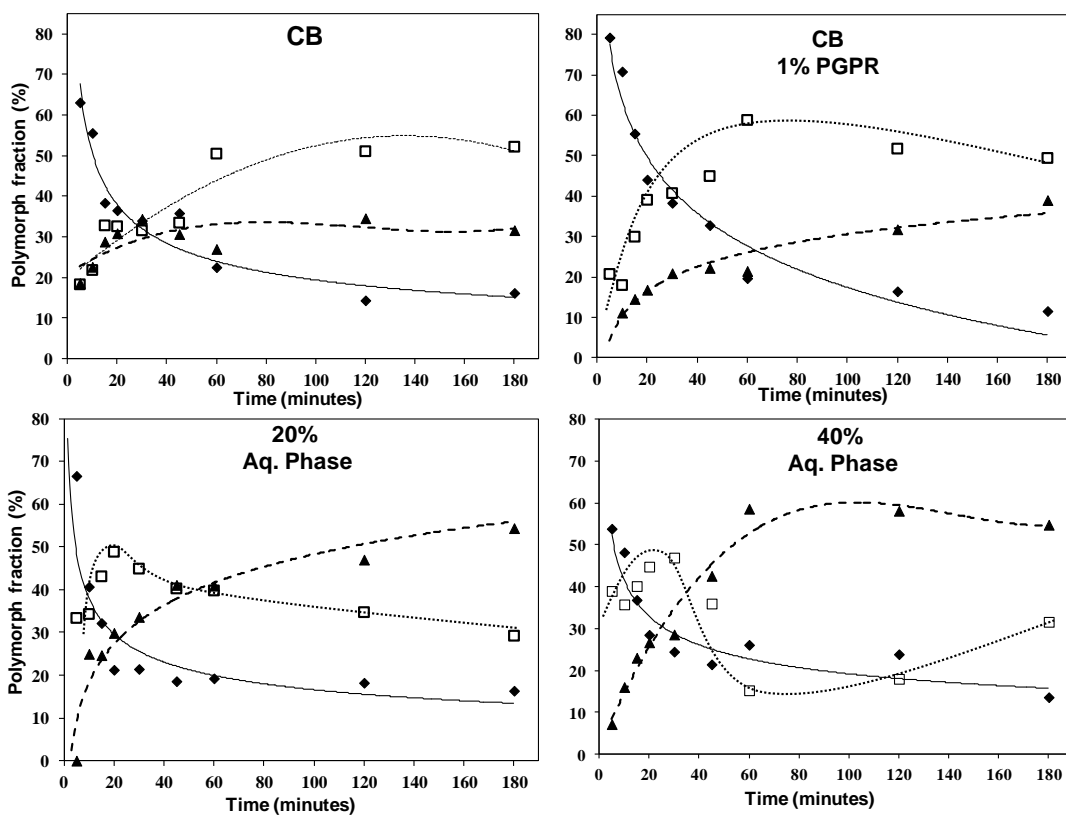


Figure 6.3: Polymorphic evolution of CB systems crystallised at 5 °C. Form II, III, and IV are represented by diamond, square, and triangles, respectively. Lines serve only to guide the reader's eye: solid, dotted, and dashed lines correspond to Form II, III, and IV, respectively.

6.2.4. Crystallisation at 10 °C

SFC curves are shown in Figure 6.4a together with the measured cooling profile. As seen for crystallisation at 5 °C in Section 6.2.3., the annealing temperature was reached within 2-3 minutes after the start. Crystallisation started immediately after reaching T_{Cr} (no induction time due to high supercooling = 25 °C). The absence of induction time was also reported for CB at the same T_{Cr} by Marangoni and McGauley (2003). Furthermore, both curve shape and SFC_{max} (~88% after 45 minutes) reported by those authors are very similar to the ones reported here for bulk CB with a SFC_{max} of 90% \pm 0.2%. This latter value is also in agreement with that of 88.8% (\pm 0.8%) reported by Oliver *et al.* (2015). The differences in the SFC_{max} (94% \pm 0.7% for emulsions vs 90% for CB) were considered to be within the experimental error. To compare the kinetics of crystallisation among systems, the same approach as described in Section 6.2.3. was used. The calculated Avrami parameters have been compiled in Table 6.3 and they quantify the kinetics of α polymorph formation. In all cases, data showed very good fitting to the model ($R^2 \geq 0.995$).

The value of the Avrami exponent ($n = 1.09$) suggests that bulk CB crystallisation occurs *via* an instantaneous nucleation mechanism, as also discussed for crystallisation at 5 °C. This value is comparable to that reported by Marangoni and McGauley (2003). Differences in the values of n across systems are too small to hypothesise a difference in the crystallisation process. Furthermore, k and $t_{1/2}$ were comparable for all systems, suggesting that microstructural differences did not produce an increase in the rate of crystallisation.

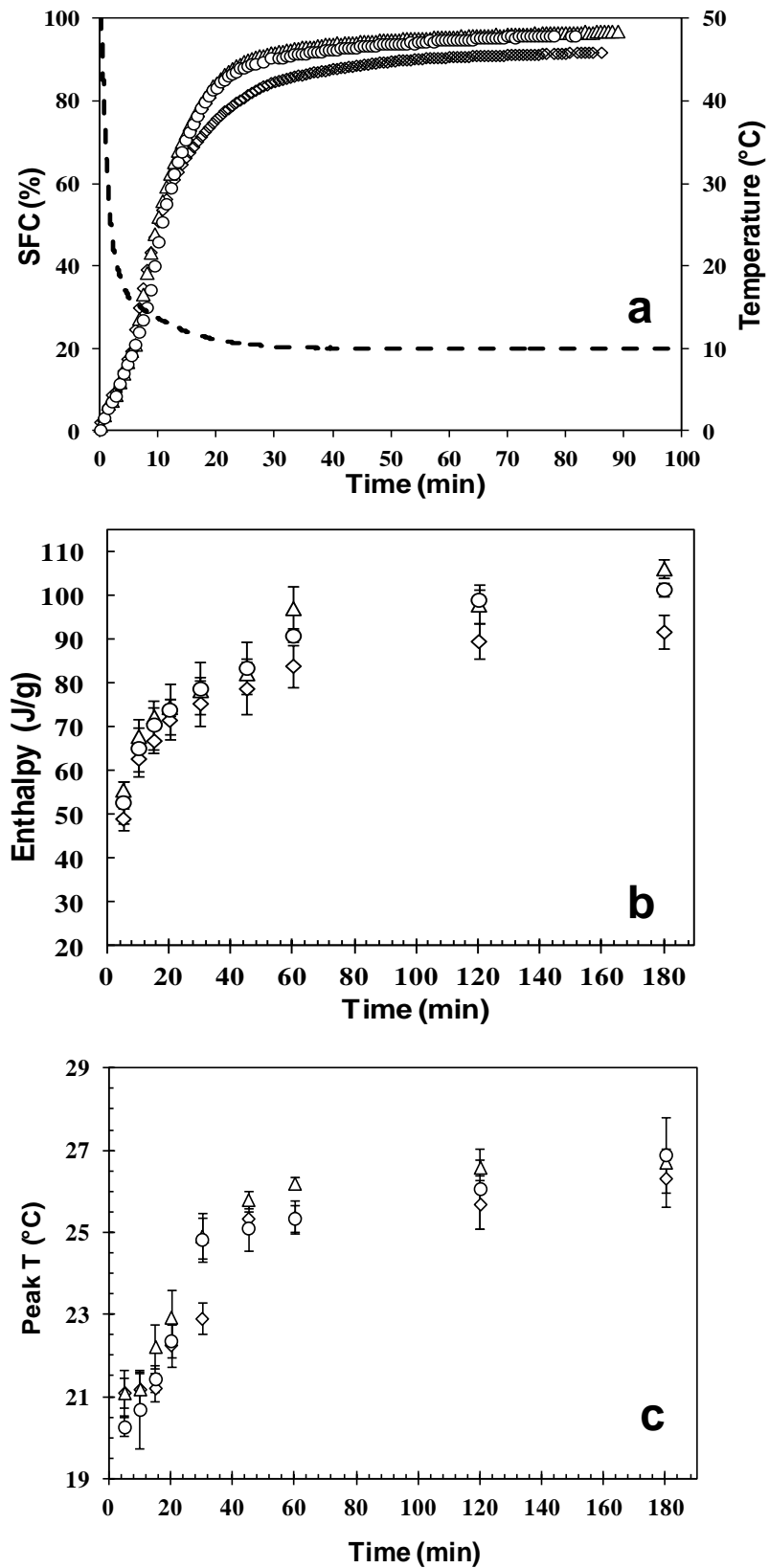


Figure 6.4: (a) SFC curves, (b) enthalpy of fusion, and (c) melting peak temperatures for CB (\diamond), 20% (Δ) and 40% (\circ) aqueous phase emulsions, respectively, at 10 °C as isothermal crystallisation temperature. Error bars represent the standard deviation and where not shown are smaller than symbols.

Table 6.3: Avrami parameters (n and k) and R^2 of the fitting for SFC data obtained on isothermal crystallisation at 10 °C of CB systems.

Sample	n	k (t^{-n})	$t_{1/2}$ (minutes)	R^2
CB	1.09	0.05	8.9	0.995
20% Aq. Phase	1.40	0.03	9.1	0.998
40% Aq. Phase	1.36	0.06	8.4	0.997

Values of enthalpy of melting (Fig. 6.4b) recorded in the first 30 minutes of crystallisation were the same for the three systems. At annealing time above 45 minutes, emulsions were characterised by a higher melting enthalpy. Differences in the enthalpy values were significant only toward the end of the annealing process. This result suggests that CB in emulsions was arranged in a more stable crystalline form than in the bulk fat.

With respect to the polymorphic behaviour, all systems were characterised by comparable values of the main melting temperature (~21 °C, Fig. 6.4c) up to 20 minutes of annealing time. For the three samples, the corresponding average melting curves (Fig. 6.5) exhibit the above mentioned maximum and after 15 minutes of crystallisation, a shoulder peak at 25 °C was also visible, indicating the growth of more stable polymorphs. In the case of emulsions, a significant change in the melting behaviour was observed after 30 minutes of resting time (Fig. 6.5), which resulted in a rapid increase in the main fusion point to 25 °C (Fig. 6.4c). A similar polymorphic evolution occurred for bulk CB at 45 minutes of annealing time (Fig. 6.4c and 6.5). For all systems, melting peaks became narrow and centred around 26 °C after 60 minutes. A better understanding of polymorphic evolution can be gained from results of deconvolution analysis (Fig. 6.6).

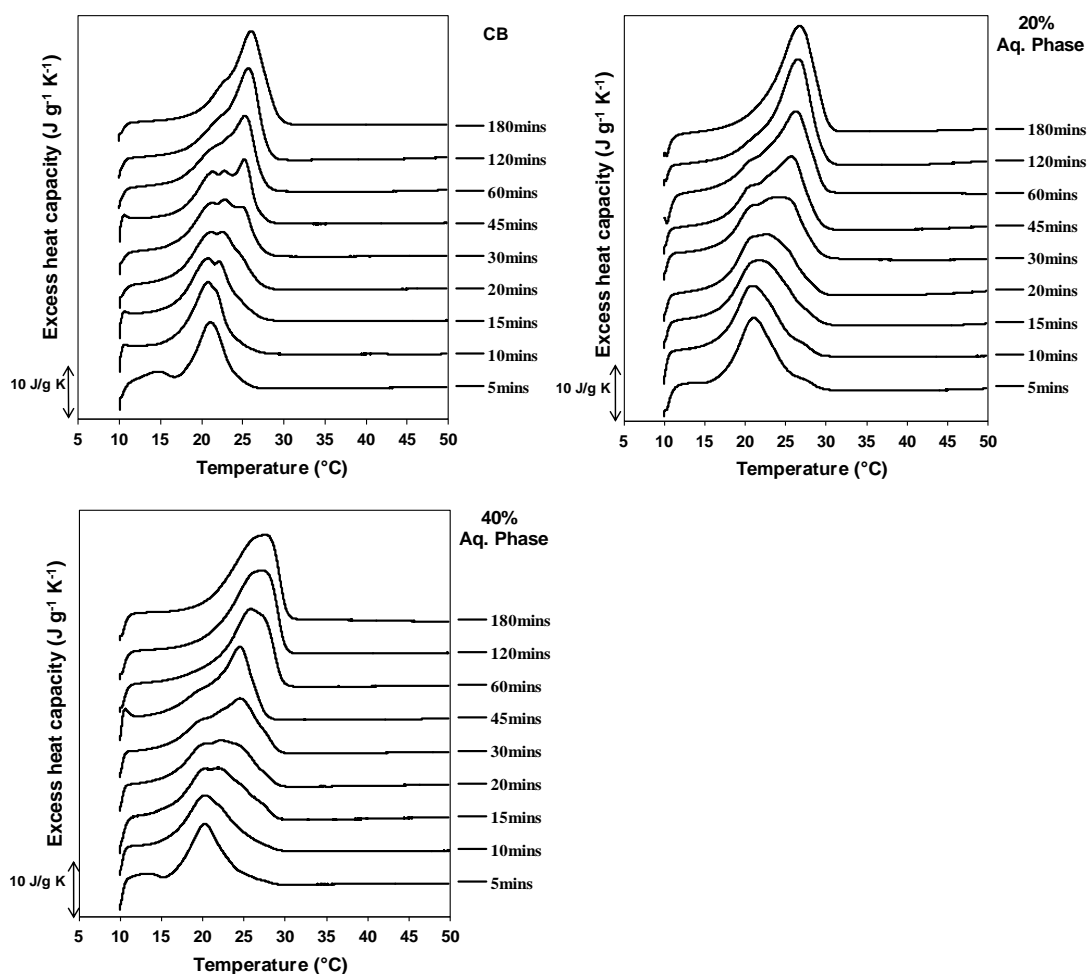


Figure 6.5: Average melting curves for CB systems crystallised at 10 °C at nine holding times. The time point corresponding to each melting curve and the CB system are referred in the figure.

Results of deconvolution analysis (Figure 6.6) confirm that in all systems CB initially crystallised in α polymorph, although in bulk CB it represented a higher fraction ($\geq 70\%$) than in emulsions ($\leq 55\%$). This solid phase progressively decreased to reach a final fraction of 10% accompanied by an increase in the other forms.

In the case of bulk CB, α polymorph remained the predominant form within the first 20 minutes, while the content of form III decreased together with an increase in form IV, suggesting a direct form III to IV conversion. A significant change in the relative proportion among polymorphs was observed after 20 minutes, thus quantitatively

explaining the appearance of the second peak in the corresponding endotherms shown in Figure 6.5. The significant increase in the content of form III is probably due to a fast transformation of α modification as a direct crystallisation from the melt into form III seems unlikely given the high degree of supercooling. Furthermore, almost the same amount (approximately 35%) of form II and III existed until 45 minutes of annealing time, after which a second fast polymorphic transformation occurred. Namely, the content in form II decreased significantly due to transformation to form III, whose growth was somehow limited by the development of form IV. This latter polymorph progressively increases throughout the annealing period becoming the main one at the end. The described polymorphic evolution is in agreement with that reported by Fessas *et al.* (2005).

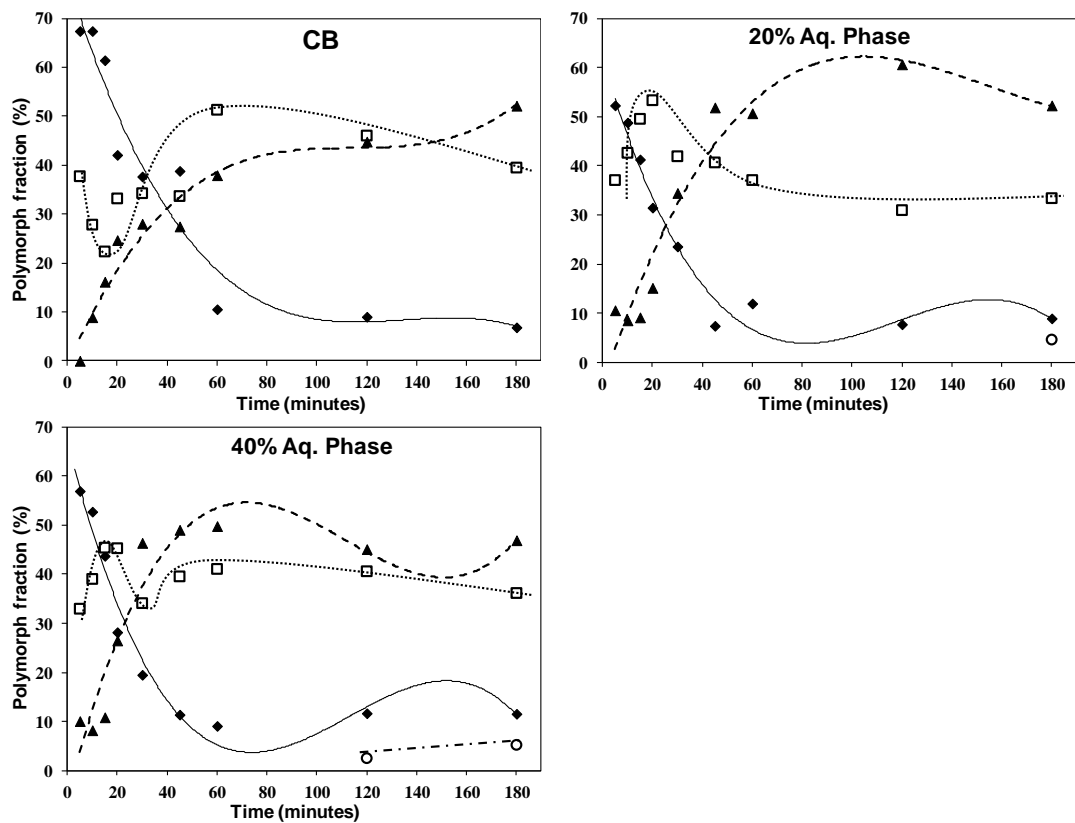


Figure 6.6: Polymorphic evolution of CB systems crystallised at 10 °C. Form II, III, IV, and V are represented by diamond, square, triangles, and circles, respectively. Lines serve only to guide the reader's eye: solid, dotted, dashed, and dashed-dotted line is for Form II, III, IV, and V, respectively.

Also the emulsified CB initially crystallised mainly in form II, which remained the predominant form at the beginning of the annealing process. However, similarly to what discussed for the experiment at 5 °C, emulsions evolved faster than bulk CB towards higher polymorphs. In particular, the decrease in form II was accompanied by a significant increase in form III after 15 minutes of annealing time. This remained the main modification until approximately 30 minutes of resting time, being then replaced by form IV. Furthermore, for both emulsified systems approximately 5% of form V was detected towards the end of the experiment. The observed faster polymorphic evolution may justify the higher value of Avrami exponent estimated for the emulsions than for bulk CB (Table 6.3).

6.2.5. Crystallisation at 15 °C

SFC evolution over time for CB systems crystallised at 15 °C is shown in Figure 6.7a. The experienced cooling profile is given by the dotted line and the target T_{Cr} was reached approximately 5 minutes after the start of the experiment. Although the shape of the SFC curves is similar among systems, a small induction time was observed only for bulk CB. Furthermore, the increase in the SFC value for this system is less steep and the plateau attains at a lower SFC_{max} (88.1% \pm 0.4%) than that recorded for emulsions (92.7% \pm 0.2% and 94.2% \pm 0.4% for 20 and 40% aqueous phase emulsions, respectively). However, as for results with T_{Cr} set at 5 and 10 °C, also in this case, differences in the SFC values seem too small to hypothesise an effect of emulsion droplets on the extent of crystallisation. In their study on CB isothermal crystallisation, Metin and Hartel (1998) reported that complete crystallisation would occur within 35 minutes (SFC ~95%) at 15 °C. In this study, the SFC curve entered the plateau region after approximately 45 minutes of isothermal holding, with the difference being most likely due to the TAGs profile of the fats and the experimental set-up. Furthermore, the SFC_{max} measured here is comparable to that reported by Oliver *et al.* (2015) (85.9 \pm 0.6%) but is considerably above that of 75% reported by Marangoni and McGauley (2003). Nevertheless, the general curve shape and the time to reach the plateau region reported by the latter authors are in agreement with those described here. Results from isothermal crystallisation suggest that emulsified CB crystallises faster than a bulk fat phase: in the first 20 minutes, emulsions were characterised by a SFC value approximately twice than that of bulk CB. Although differences are smaller than those observed for the SFC, also values of melting enthalpy (Fig. 6.7b) measured at the early stages of the annealing process suggest the presence of a higher solid fraction for emulsions compared to bulk CB. To

compare kinetics of crystallisation, SFC data between 5 and 20 minutes and between 10 and 25 minutes for emulsions and bulk CB, respectively, were fit to the Avrami model (Tab. 6.4).

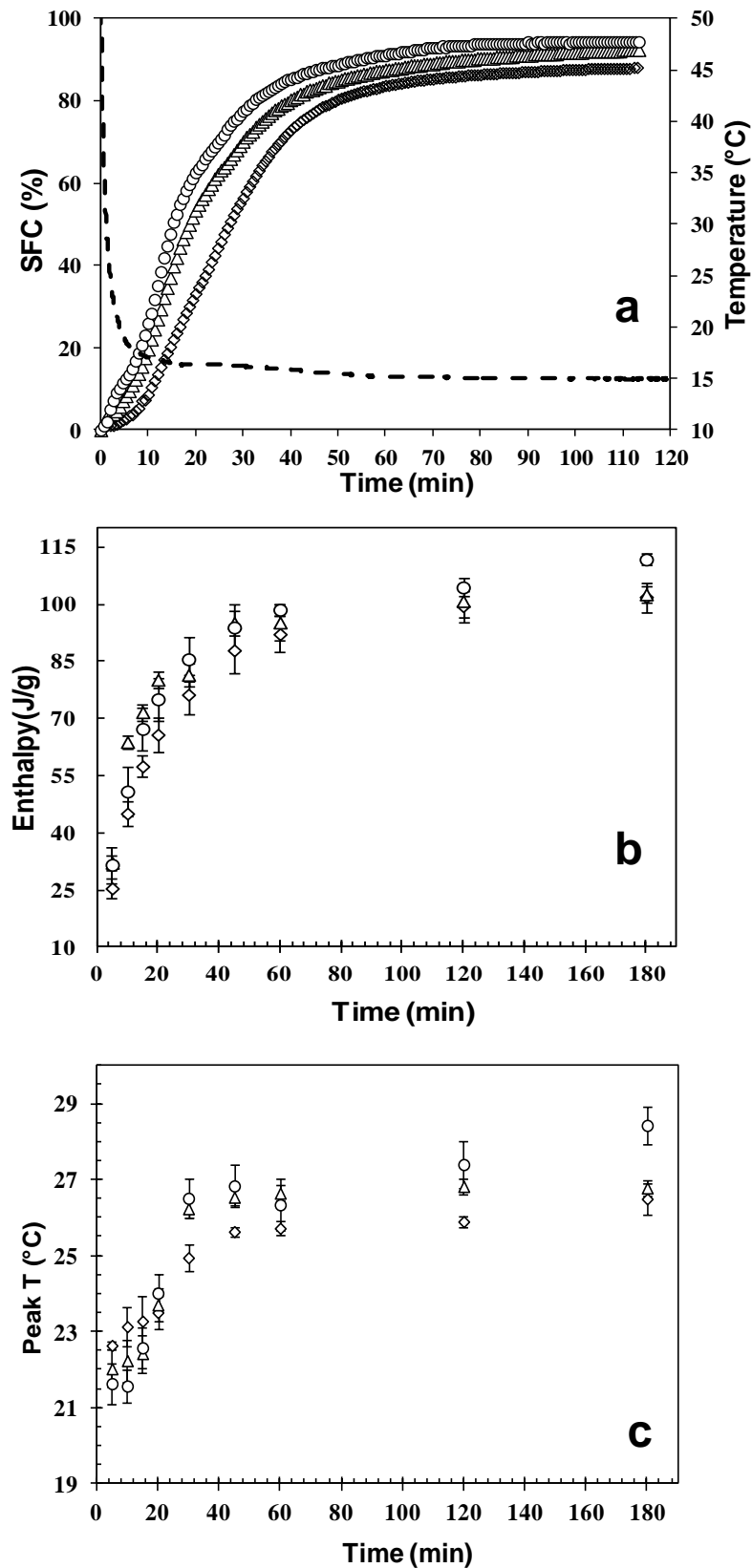


Figure 6.7: (a) SFC curves, (b) enthalpy of fusion, and (c) melting peak temperatures for CB (\diamond), 20% (Δ) and 40% (\circ) aqueous phase emulsions, respectively, at 15 °C as isothermal crystallisation temperature. Error bars represent the standard deviation and where not shown are smaller than symbols.

For all systems, the Avrami exponent had value of approximately 2 (Tab. 6.4) suggesting that crystallisation had occurred *via* an instantaneous nucleation process (this result is discussed in more detail in Section 6.3). The Avrami kinetic constant (k) (Tab. 6.4) was larger for emulsions than for CB (with $t_{1/2}$ values lower for emulsions than for bulk CB). The values obtained for kinetics parameters together with SFC curves shape indicate that CB in emulsions crystallises faster than in bulk. While microstructural differences did not affect the kinetics of solidification at 5 and 10 °C, results obtained at 15 °C suggest that droplets act as seeds increasing the rate of crystallisation.

Table 6.4: Avrami parameters (n and k) and R^2 of the fitting for SFC data obtained on isothermal crystallisation at 15 °C of CB systems.

Sample	n	k (t^{-n})	$t_{1/2}$ (minutes)	R^2
CB	2.1	8.0×10^{-4}	25.0	0.995
20% Aq. Phase	1.9	3.3×10^{-3}	12.8	0.997
40% Aq. Phase	1.9	4.6×10^{-3}	10.9	0.992

Examination of the main melting points (Fig. 6.7c) suggests that within the first 20 minutes of annealing CB existed mainly in form III in all systems. The melting curve recorded for bulk CB after 5 minutes of crystallisation (Fig. 6.8) was characterised by the presence of a second peak centred at 17 °C, thus suggesting the presence of a large fraction of α form. The average melting curves for the three samples up to 20 minutes of resting time exhibit the peak at 23 °C as well as a shoulder peak at approximately 25 °C after 15 minutes of crystallisation. Thereafter, simultaneously with an increase in the total amount of crystallised material (Fig. 6.7a and 6.7b), a polymorphic evolution from form III to IV occurred as indicated by the significant increase in the melting temperature (Fig.

6.7c). Bulk CB was characterised by a lower peak temperature than emulsions throughout the whole resting period, suggesting that emulsions had transformed to a more stable polymorph.

The average melting curves are shown in Figure 6.8 and results of the deconvolution analysis in Figure 6.9.

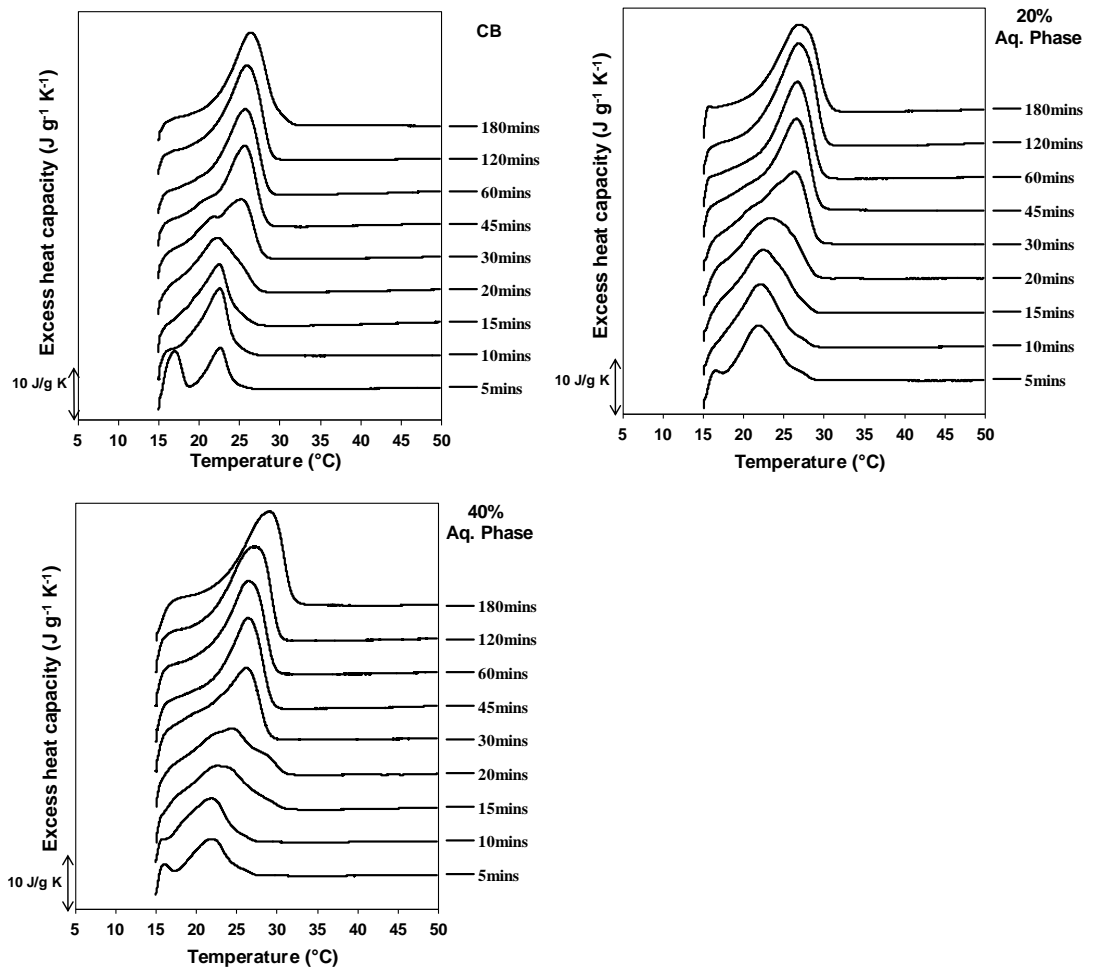


Figure 6.8: Average endothermic curves for CB systems crystallised at 15 °C at all the selected holding times. The time point corresponding to each melting curve and the investigated system are referred in the figure.

An initial arrangement of CB mainly in form III for all systems was confirmed and the presence of a considerable amount of α form ($\geq 35\%$) was also revealed. Considering the *Ostwald step rule* and in the light of results by van Malsen *et al.* (1999) and van Langevelde *et al.* (2001), it is likely that this latter polymorph was the first to crystallise. However, some evolution to form III may have occurred prior and on re-heating. For all samples the content of α polymorph started to decrease considerably after 15 minutes of crystallisation reaching a final fraction of 10%, while form IV became the main polymorphic transformation. It is important to note that evolution to form IV seems to occur at the expense of form III in agreement with Fessas *et al.* (2005). This phenomenon is particularly clear in the case of bulk CB: in the first 15 minutes of the annealing process, while the content of α form remains constant, form III progressively decreases accompanied by an increase of form IV. Between 20 and 30 minutes of resting periods, α form decreases significantly due to conversion to form III, whose fraction remained constant due to a co-occurring transformation to form IV. The same amounts of the two β' polymorphs were reached after approximately 45 minutes of isothermal holding (which is within the time range where the SFC had reached the equilibrium) and form IV became the main polymorphic modification only toward the end of the crystallisation experiment.

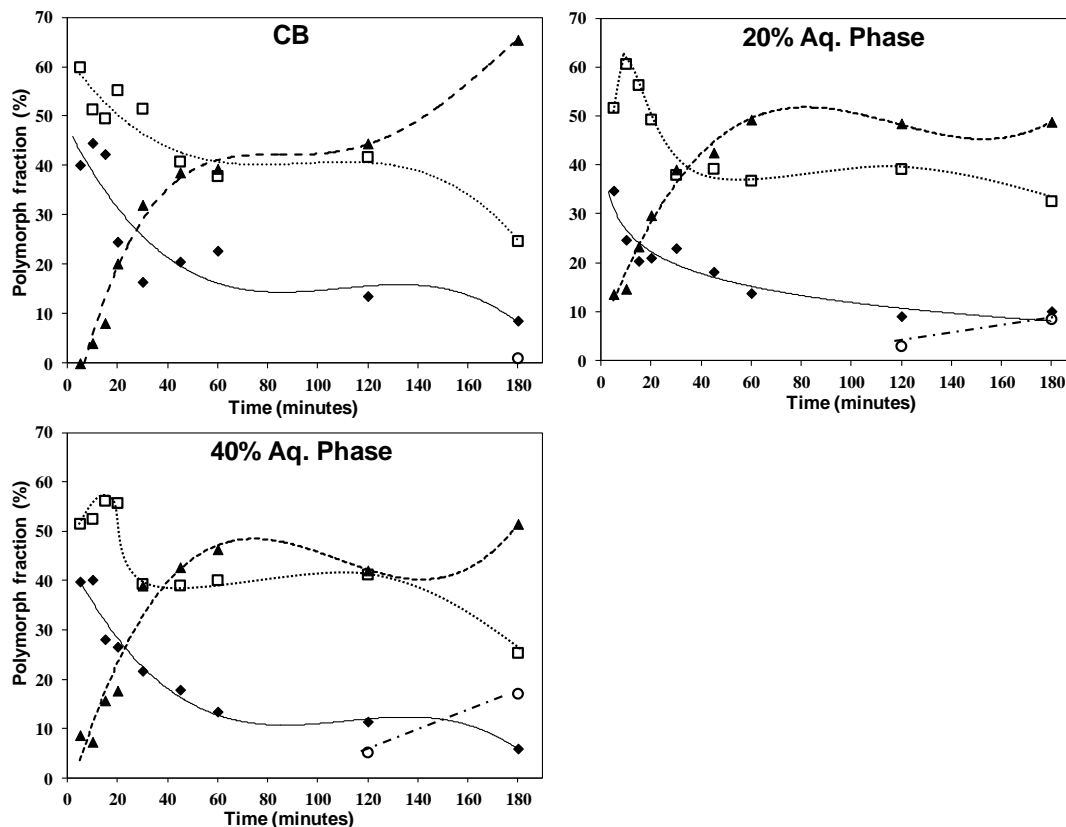


Figure 6.9: Polymorphic evolution of CB systems crystallised at 15 °C. Form II, III, IV, and V are represented by diamond, square, triangles, and circles, respectively. Lines serve only to guide the reader's eye: solid, dotted, dashed, and dashed-dotted line is for Form II, III, IV, and V, respectively.

In the case of emulsions, an overall similar polymorphic transformation could be detected although less clearly, which was attributed to the observed faster polymorphic evolution process. The presence of form IV was detected since the early stage of the annealing process thus explaining the recorded broader peaks (Fig. 6.8). It should be pointed out that for these systems, the same amount of the two β' polymorphs was observed within 30 minutes after the start, with form IV becoming the main one at a time where also the SFC curve had entered the plateau region (Fig. 6.7a). Furthermore, the presence of some form V ($\geq 8\%$) was detected at the end of the experiment together with a decrease of form III. Between the two emulsified systems, the one containing 40% aqueous phase evolved

faster to higher stable forms and contained a larger amount of form V than 20% emulsion, whereas for bulk CB approximately 1% of form V was detected.

6.2.6. Crystallisation at 20 °C

All curves shown in Figure 6.10a have a sigmoid shape characterised by the presence of an induction time where no solid material is detected. This step was followed by a rapid increase in the SFC before levelling off to a plateau value. It can be seen from the cooling profile that all systems had reached the desired temperature within approximately 15 minutes, i.e. within their induction period. Despite the similar curve shape, differences can be easily observed among systems: emulsions were characterised by the smallest induction time (~30 minutes) and entered the plateau region in a time scale within which the SFC of CB was entering its steep increase region (~100 minutes after the start). Bulk CB achieved its plateau SFC value over three hours after the start of the experiment. This result is in disagreement with what referred by Campos *et al.* (2010) who reported that at 20 °C, CB reaches the equilibrium after 120 minutes. Also Dewettinck *et al.* (2004) reported that bulk CB achieved the maximum crystalline fraction within two hours at temperatures between 19 and 23 °C. These differences may be associated with a different experimental set-up adopted here, especially with respect to the applied cooling profile; other variations may rise from the different types of CB used. Nevertheless, it should be noted that for bulk CB both the SFC curve shape and SFC_{\max} (71.0% \pm 0.3) value are comparable to those reported by Foubert *et al.* (2005) (72%), Dewettinck *et al.* (2004) (72.5%), but lower than the value of 78.0% \pm 0.7% reported by Oliver *et al.* (2015). Both emulsions had a SFC_{\max} of 75.0% \pm 0.7% (no difference with bulk CB). The CB system containing 1% PGPR was characterised by an induction time was comparable to that recorded for the emulsions.

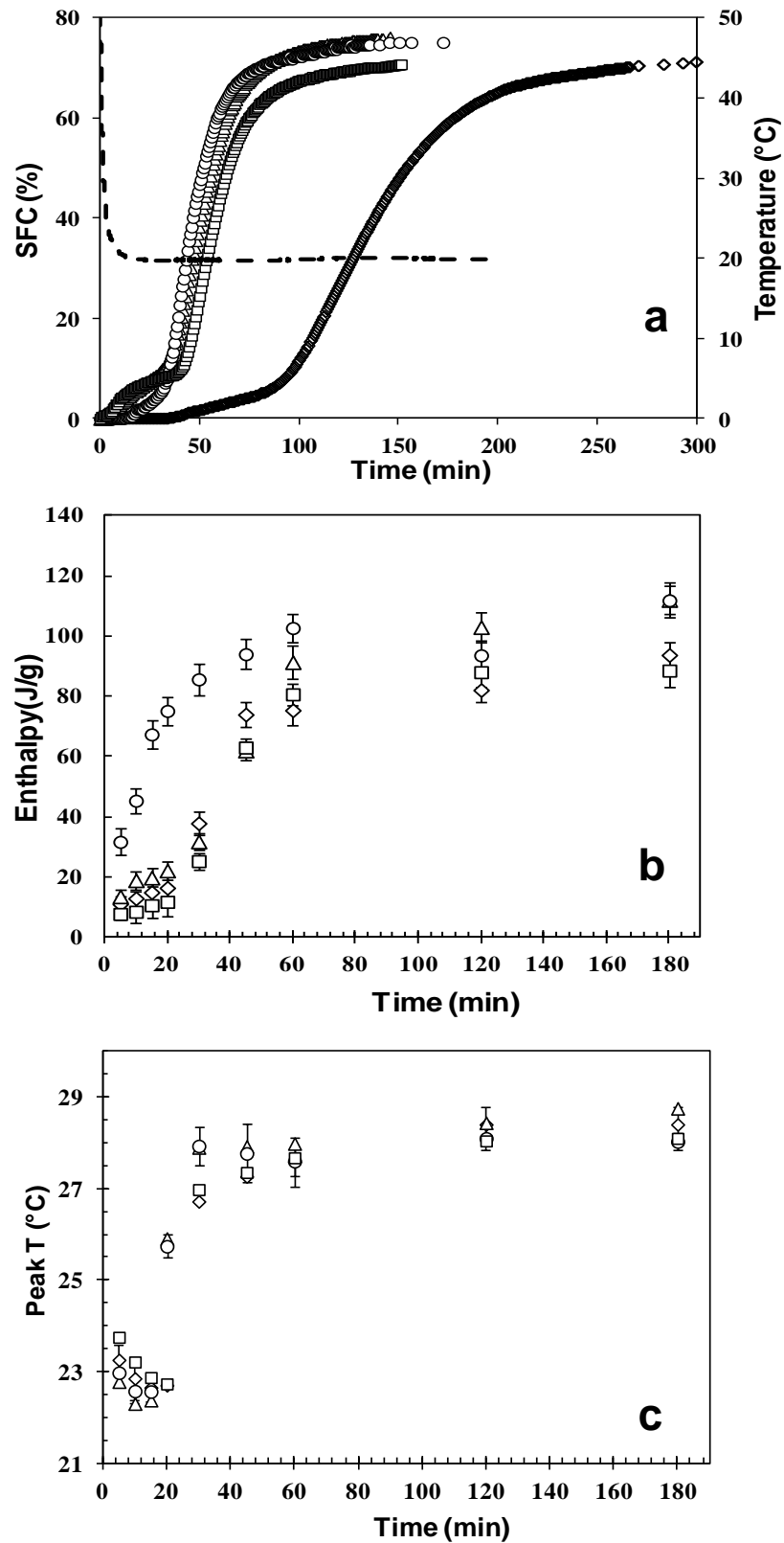


Figure 6.10: SFC curves (a), enthalpy of fusion (b) and melting peak temperatures (c) for CB (\diamond), 20% (Δ) and 40% (\circ) aqueous phase emulsions, and 1% PGPR in CB (\square), respectively, at 20 °C as isothermal crystallisation temperature. Error bars represent the standard deviation and where not shown are smaller than symbols.

In Table 6.5 the parameters obtained from data fitting to the Avrami model have been compiled. As explained in Section 3.2.2.7., the crystallisation data used for the fitting are those belonging to the linear region in a double logarithmic plot, which corresponded to a time range between 35 and 65 minutes, 45 and 75 minutes, and 120 and 150 minutes for emulsions, CB containing 1% PGPR, and bulk CB, respectively. For all systems, a good data fitting was obtained and the Avrami exponent ($n \sim 4$) was comparable among systems and with data in literature (Toro-Vazquez *et al.*, 2004). A value of $n \sim 4$ suggests a mechanism of heterogeneous nucleation from sporadic nuclei. This mechanism implies that the number of nuclei created increases linearly with the time (Yang *et al.*, 2013). Values of k and $t_{1/2}$ (Tab. 6.5) were comparable among emulsions and CB containing 1% PGPR whereas larger values were calculated for CB, thus quantifying the slower crystallisation process occurring in the bulk fat.

Table 6.5: Avrami parameters (n and k) and R^2 of the fitting for SFC data obtained on isothermal crystallisation at 20 °C of CB systems.

Sample	n	k (t^{-n})	$t_{1/2}$ (minutes)	R^2
CB	3.83	5.1×10^{-9}	132.0	0.998
20% Aq. Phase	3.67	4.0×10^{-7}	50.2	0.994
40% Aq. Phase	4.09	9.3×10^{-8}	47.8	0.962
1% PGPR in CB	3.63	2.4×10^{-7}	60.2	0.979

Values of melting enthalpy for the 40% aqueous phase emulsion (Fig. 6.10b) were the highest throughout the annealing time, whereas for the 20% emulsions differences became significant only at a resting period above one hour. No differences were detected between the bulk and 1% PGPR enriched CB. These results are in good agreement with SFC data and confirm that crystallisation occurs faster in emulsified systems than in bulk

fat. In the light of the initial hypothesis and similarly to what discussed for crystallisation at 15 °C, this behaviour can be explained considering that water droplets act as seeds within the fat phase accelerating the solidification process.

In Figure 6.10c the melting points of CB systems are shown. It can be observed that within the first 15 minutes of crystallisation, all the systems are characterised by a main melting point at 23 °C suggesting that the majority of CB had crystallised in form III. However, observation of the corresponding endotherms in Figure 6.12 at the same holding times suggests that all systems may still contain a small proportion of α form (the problem of detecting this form is discussed below). For both emulsified systems an increase in the main melting peak was recorded (Fig. 6.10c) after 20 minutes suggesting the growth of the more stable polymorph IV, whereas for bulk CB and CB containing 1% PGPR a similar shift was observed at 30 minutes. At annealing time longer than 45 minutes, no differences in the peak temperature were observed suggesting that all systems had crystallised mainly in form IV, although some differences in the curves shape can be noted (Fig. 6.11). The final melting temperatures are in agreement with literature data (Toro-Vazquez *et al.*, 2004).

The inability to identify a clear peak corresponding to the α form can be attributed to a number of reasons: (1) crystallisation temperature within α form melting range; (2) limit of the ‘stop-and-return technique’: on re-heating, no stable baseline can be obtained (see Section 3.2.3.2.) as the DSC trace is a result of instantaneous melting of the polymorph and power input of the device; (3) heat induced conversion of α to the β_2' form (form III) on heating; (4) first re-heating step after 5 minutes of annealing: within this time span the polymorphic conversion may have already largely occurred. Also Campos *et al.* (2010) reported the impossibility to observe α polymorph crystallisation using DSC and

conditions comparable to those used here. The authors confirmed the presence of this form using small and wide angles X-ray measurements. Here, the presence of α form at an early stage of the crystallisation process was confirmed by the deconvolution analysis (see below).

In Figure 6.11 the average endotherms for all CB systems are shown. In the first 15 minutes peaks appear rather small and broad revealing the presence of little amounts of crystalline material, which is consistent with SFC data (Fig. 6.10a). For both emulsified systems, the endotherm at 20 minutes appears broad suggesting the presence of form II, III, and IV, with the latter being predominant. For bulk CB and CB with 1% PGPR, the endotherm at the same time point was also broad but form III appeared to be predominant. At longer annealing time, a peak between 25 and 27 °C became clearly visible. This peak was the main one at the end of the crystallisation period. A better understanding of the polymorphic evolution can be gained from results of deconvolution analysis (Figure 6.12). To take into account the contribution from α form, following the melting range proposed van Malssen *et al.* (1999), the fusion point corresponding to this polymorph was centred at 22 °C. However, this implied that it was not possible accurately signalling out the contribution associated with this form.

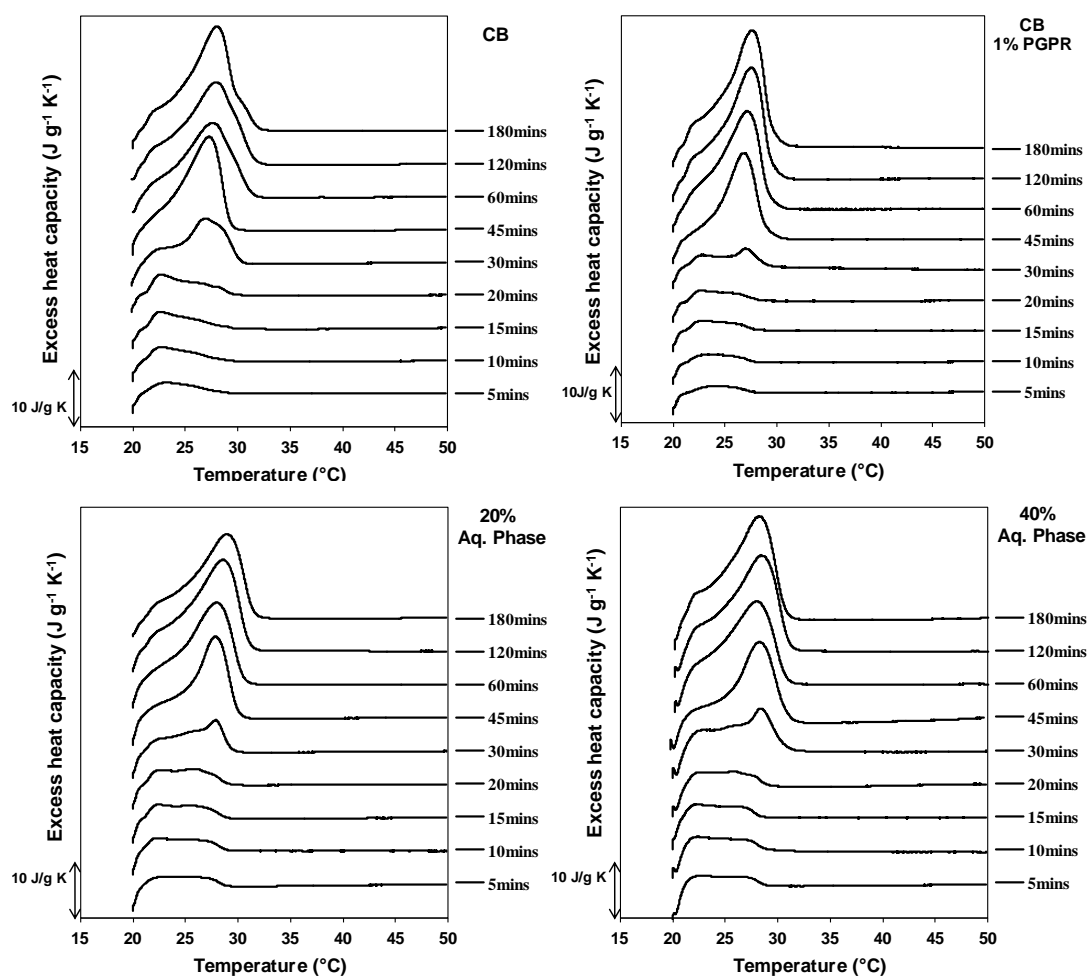


Figure 6.11: Average endothermic curves for CB systems crystallised at 20 °C at all the selected holding times. The time point corresponding to each melting curve and the investigated system are referred in the figure.

Results in Figure 6.12 indicate that form III was the major fraction at the beginning of the crystallisation in all CB systems, with form II representing less than 20% of the total. At 30 minutes of annealing, form IV became the main one for all systems. In bulk CB, it represented approximately 55%, with form III and V accounting for 30% and 10% of the total, respectively, at the end of the crystallisation. In the case of emulsions, similarly to what observed at 15 °C, the development of form IV was limited by the growth of form V, suggesting a faster polymorphic transition. CB enriched with 1% PGPR showed the slowest polymorphic evolution, with form III, IV, and V representing 40%, 50%, and 5%

of the total, respectively. The possible mechanism of polymorphic evolution is described in Section 6.3.2.

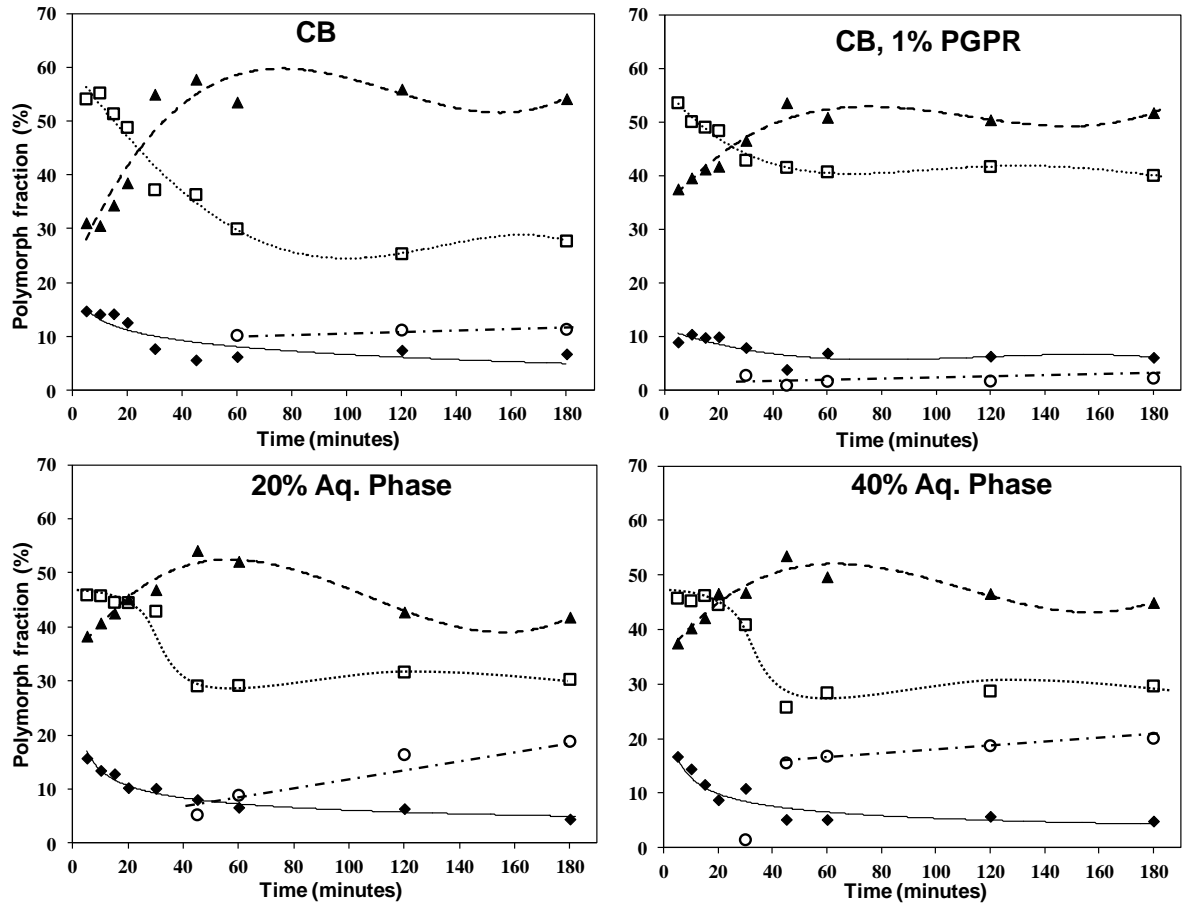


Figure 6.12: Polymorphic evolution of CB systems crystallised at 20 °C. Form II, III, IV, and V are represented by diamond, square, triangles, and circles, respectively. Lines serve only to guide the reader's eye: solid, dotted, dashed, and dashed-dotted line is for Form II, III, IV, and V, respectively.

6.3. Discussion

The shape of SFC curves and the Avrami parameters are recognised to provide information on the phase transition (type of nucleation and phase transition rate are quantified by n and k , respectively) and on the crystal growth mechanism (n value at different temperatures) (Marangoni and McGauley, 2003; Metin and Hartel, 1998). SFC curves were used to quantify the role of microstructure on kinetics of crystallisation in CB systems. Microstructural changes were produced by introducing seeds for

crystallisation in the form of water droplets or by enriching the CB with the emulsifier. Deconvolution analysis of endotherms was used to compare polymorphic evolution among systems.

6.3.1. Effect of water droplets on kinetics of crystallisation

It has been long recognised that CB contains impurities in the form of complex lipids (glycolipids and phospholipids) and saturated TAGs (Davis and Dimick, 1989). These lipids form high melting point crystals which partially phase separate from the monounsaturated TAGs fraction and seed CB crystallisation (Loisel *et al.*, 1998). Therefore, it can be assumed that nucleation occurred *via* a heterogeneous route in all systems and emulsions simply contained a larger number of seeds.

Results suggest that no difference in the crystallisation kinetics occurs when CB systems are rapidly supercooled to 5 or 10 °C: all curves have approximately a hyperbolic shape with no induction time. The n value of ~ 1 suggests an *instantaneous nucleation mechanism*. This latter process implies that all nuclei are formed at the beginning of the crystallisation once the T_{Cr} is reached. The type of nucleation and the absence of differences among systems can be explained considering the degree of supercooling inducing fast nucleation, which masks the seeding effect provided by water droplets. This result is in line with the theoretical description reported by Sato and Ueno (2011).

Results at 15 °C revealed some differences in the crystallisation behaviour of systems. The kinetic constant k and half time of crystallisation $t_{1/2}$ measured for emulsions were higher and lower, respectively, than those for CB suggesting a faster transformation. The Avrami exponent (n) had a value of 2 in all systems. Metin and Hartlel (1998) referred that such value indicates a process characterised by a high initial nucleation rate (*instantaneous nucleation*) and plate-like crystal growth. Here, although crystal

morphology was not studied, considering the degree of supercooling (~ 20 °C), it is reasonable to think that the presence of droplets accelerates the crystallisation process compared to the bulk fat, with the mechanism of crystallisation remaining the same across systems.

Also at 20 °C emulsions crystallised faster than bulk CB (as indicated by the values of k and $t_{1/2}$, Tab. 6.6) but no difference in the Avrami exponent was detected. The increase in the n value to approximately 4 indicates a process of sporadic nucleation, i.e. number of nuclei increasing linearly with the time (Yang *et al.*, 2013). It also suggests that crystal growth evolves from a one- to a multidimensional phenomenon (Wright *et al.*, 2000). The considerably longer induction time observed for bulk CB indicates that the fat phase required longer time to form stable nuclei. CB enriched with 1% PGPR showed similar crystallisation behaviour to emulsions. It is possible that emulsifier molecules may self-structure in the melt and act as seeds for crystallisation. These results suggest that a considerable increase in crystallisation kinetics is produced by only a small number of nuclei and do not scale with seeds number.

From the obtained results, it can be concluded that the initial hypothesis has been verified: emulsified water droplets structured within the fat matrix act as catalytic impurities promoting an overall faster crystallisation process than in bulk CB.

6.3.2. Effect of water droplets on polymorphic evolution

Results of deconvolution analysis revealed a complex polymorphic evolution for all CB systems, with emulsions characterised by a larger fraction of stable forms at all temperatures. In the light of literature data (Loisel *et al.*, 1998a; Lopez *et al.*, 2001), it is reasonable to assume that the first fraction to crystallise is represented by trisaturated TAGs arranged in α conformation. The monounsaturated TAGs, the main CB lipid

fraction ($\geq 80\%$), crystallises at around $15\text{ }^{\circ}\text{C}$ in a complex crystalline arrangement. To this regard, Loisel *et al.* (1998a) investigated the crystallisation behaviour of CB on cooling (and re-heating) at $2\text{ }^{\circ}\text{C}/\text{min}$ from 40 to $0\text{ }^{\circ}\text{C}$: the authors concluded that α form is the first to crystallise and co-exists with liquid-crystals where the saturated chains of the TAGs create organised domains and the unsaturated molecules remain liquid-like. This structural arrangement will be considered below to try to explain the faster polymorphic evolution occurring in emulsions.

With respect to polymorphic evolution, data shown above suggest that at a crystallisation temperature (T_{Cr}) of 5 or $10\text{ }^{\circ}\text{C}$, the fastest crystallising α form is always predominant at the early stage of the solidification process. This is in agreement with the *Ostwald step rule*, which predicts that the polymorph with lowest activation energy of nucleation is the fastest to crystallise, and literature data (Marangoni and McGauley, 2003). At T_{Cr} of 15 and $20\text{ }^{\circ}\text{C}$, α form was not found to be the predominant one, with the result attributed to the limit of the DSC and deconvolution technique.

For T_{Cr} of 5 , 10 , and $15\text{ }^{\circ}\text{C}$, deconvolution analysis highlighted a complex pattern of polymorphic evolution occurring prior and after SFC had entered the plateau region. Data indicate that for all systems form III grows at the expense of α polymorph and evolves into form IV. Furthermore, form II (α) to III transformation occurs simultaneously with further TAGs crystallisation from the melt into α form given the high imposed supercooling ($\geq 20\text{ }^{\circ}\text{C}$) and its lowest activation energy of nucleation. A mechanism of direct crystallisation from melt to form III *via heterogeneous crystallisation* (templating) promoted by the presence of solid material in this conformation can be excluded. Evolution toward form IV occurred after ($T_{\text{Cr}} = 5$ and $10\text{ }^{\circ}\text{C}$) or before ($T_{\text{Cr}} = 15\text{ }^{\circ}\text{C}$) the SFC had reached its maximum (curves had entered the plateau region). In agreement with

Fessas *et al.* (2005), this result confirms that polymorphic evolution is a dynamic process and implies a continuous and gradual transformation from the less to the more stable forms. At these T_{Cr} , only in emulsified systems form V could be detected. These results strongly suggest that CB existing in an emulsified state tend to evolve faster to more stable polymorphs. This is particularly relevant considering that Marangoni and McGauley (2003) stated that CB would remain stable in β' form for 28 days at 15 °C. Here it was found that in emulsified CB, a transition to β form begins to occur within two hours.

To explain the polymorphic evolution at 20 °C, a mechanism similar to that reported by Toro-Vazquez *et al.* (2004) could be hypothesised. These authors considered that the β' polymorph can be formed either from α crystals or from the melt depending on the time-temperature combination. At T_{Cr} of 20 °C, a small fraction of CB crystallises in α form which evolves to β' via a solid state transformation with further crystallisation occurring via *heterogeneous templating nucleation* into β' form. Here, α polymorph had probably been the first to crystallise with evolution to form III occurring prior-during re-heating, so that form III appeared as the main polymorph. At longer times, the fraction of form III increases as solidification of CB occurs directly in this form and (after 30 minutes of annealing) decreases due to form IV growth, suggesting a direct β'_2 to β'_1 evolution. This transformation is in agreement with that described by Fessas *et al.* (2005). Results here are also in agreement with those by Marangoni and McGauley (2003) who showed that crystallisation of β' polymorph directly from the melt gave rise to an n value ≥ 3 as observed here.

To try to explain the faster polymorphic evolution observed in emulsions compared to bulk and 1% PGPR enriched CB, the molecular interfacial arrangement should be

considered. Water droplets are covered by PGPR, which from a non-elastic interface providing stability by steric interactions (Gülseren and Corredig, 2012). Since PGPR cannot co-crystallise with CB TAGs at the investigated temperatures, a liquid layer surrounding the droplets should exist and consist of PGPR molecules, with the hydrophilic head interacting with the water and the tail pointing toward the lipid phase. This implies that PGPR molecules, although liquid, are partially ordered and can interact with TAGs of CB given some structural similarities of the acyl chain. To this respect, Garti *et al.* (1999) have referred that PGPR molecules act as bridges between fat crystals and water, implicitly assuming a certain molecular interaction. The hypothesis of the existence of molecular interaction in the vicinity of droplets interfaces is also in line with results of Wassell *et al.* (2012), who reported that fat crystals close to the droplet interface had their lamellar planes aligned almost parallel to the plane droplet interface. This result was attributed by the authors to hydrophobic interactions between fatty chains of PGPR and TAGs and hydrophilic interactions between PGPR and TAGs glycerol groups. Furthermore, in the light of the obtained results and finding by Loisel *et al.* (1998a), within the investigated temperature range, the TAGs liquid-solid mixture may initially consists of α form and liquid-crystals (structures partially crystallised with the saturated chains forming organised solid domains and the unsaturated chain remaining liquid-like). Given some structural similarities, the unsaturated chain of the TAGs liquid-crystals may interact with the ricinoleic groups of PGPR. Furthermore, α crystals have been shown to be the most surface active crystals (Johansson and Bergensthål, 1995a, b). This result was explained considering that α crystals are characterised by an amorphous structure, with the aliphatic chains oscillating and characterised by a high degree of freedom (Timms, 1984). Therefore, it seems reasonable to hypothesise an interaction in

the vicinity of the interface between PGPR molecules and TAGs crystals both in α form and in a liquid-crystal state. It could be speculated that the interaction between these liquid moieties would promote structural re-arrangements of TAGs molecules, which would result in enhanced polymorphic transition. To this respect, it has been long recognised that the presence of a liquid phase promotes polymorphic evolution toward more stable forms (Timms, 1984). The process hypothesised here is similar to that referred for CB enriched with liquid 25% miglyol (Lopez *et al.*, 2001) or 5% trilinolein (Campos *et al.*, 2010). In both cases the authors concluded that the liquid fatty acid chains (within the network or at the crystals surfaces) would accelerate polymorphic transformation by increasing the molecular re-arrangement and diffusion, thus allowing more stable conformations to be formed. In the scenario presented here, PGPR liquid chains protruding from droplets interface would interact with TAGs molecules increasing their molecular mobility and structural re-arrangement, which results in the development of more stable forms. The evidence that CB enriched with 1% PGPR is characterised by a polymorphic evolution comparable or slower than bulk CB further supports the hypothesis that an interfacial local ordering is needed for accelerating the polymorphic transition.

6.4. Conclusions

Results of SFC analysis for bulk CB were in agreement with data referred in literature at all investigated temperatures. SFC curve and data from kinetic analysis have highlighted differences in the crystallisation behaviour of CB depending on its physical state. When existing as the continuous phase of an emulsion, if a high degree of supercooling was applied ($T_{Cr} \leq 10 \text{ }^\circ\text{C}$), no difference in the kinetics of crystallisation could be observed compared to a bulk fat. At intermediate degree of supercooling ($T_{Cr} \geq 15 \text{ }^\circ\text{C}$), CB in emulsions evolved faster (higher value of k) toward the equilibrium SFC than bulk CB. The similarity in the values of Avrami exponent among systems at all temperatures suggests that the mechanisms of crystallisation are not affected by microstructural changes. Furthermore, the increase to a $n = 4$ at $20 \text{ }^\circ\text{C}$ indicates a change in the dimensions of crystal growth and, perhaps, in the crystallisation of form III directly from the melt, similarly to what is observed in milk fat (Wright *et al.*, 2000).

With respect to CB systems polymorphism, the large number of DSC curves, and their deconvolution analysis, has allowed gaining a good understanding of polymorphic evolution depending on CB physical structure. Data obtained for bulk CB were in agreement with those published by Fessas *et al.* (2005) and with other literature data. Within the investigated temperature range, in all samples CB crystallised in the metastable forms α (II) and β'_2 (III) (at $20 \text{ }^\circ\text{C}$) at the early stage of the annealing process. Emulsified CB always showed to evolve faster toward higher stable forms and a significant fraction of form V was detected toward the end of the resting period. It was hypothesised that faster polymorphic transitions result from the interaction at the interface between α arranged CB (mixed with liquid crystals) and PGPR: the presence of liquid moieties at the droplets interfaces promotes polymorphic transformation by

increasing molecular mobility and re-arrangement of TAGs in the vicinity of the interface.

Chapter 7. Conclusions and future recommendations

7.1. Conclusions

Water-in-cocoa butter emulsions are a novel food ingredient that is suggested as a route for the reduction of fat in chocolate. Results discussed in this thesis represent an important advancement in the development of a reduced-fat chocolate with textural-sensorial properties comparable to a full-fat product. The following sections detail the main conclusions drawn from the findings discussed in each results chapter.

7.1.1. Effect of processing and formulation on the microstructural properties of water-in-cocoa butter emulsions

The first objective of this thesis was to gain a better understanding of the role of processing and formulation on emulsions microstructural properties, in order to optimise the process proposed in literature (Norton and Fryer, 2012). To achieve this goal, emulsions with two different aqueous phase percentages (10 and 20%) were produced using either the entire margarine line (as described in the literature) or a scraped surface heat exchanger as a single unit (SSHE, i.e. the first mixer of the margarine line), and microstructural properties of each were compared. This investigation resulted in two main outcomes: (i) emulsions prepared using the SSHE alone have an average droplet size ($d_{3,2}$) smaller than that obtained for emulsions produced with the entire margarine line; (ii) tempering of the emulsions occurs only on using the SSHE alone. These results suggest that shear applied in the pin stirrer (i.e. the second mixer of the margarine line) increases the size of the droplets formed in the SSHE and cannot promote CB crystallisation into the desired polymorphic form V. Therefore, it was suggested that the use of the PS should be avoided. From a process engineering point of view, the use of the SSHE alone allows a significant reduction in terms of energy consumption and time required for emulsification.

With respect to role of formulation, by combining interfacial tension profiles with results obtained for experiments at different PGPR concentrations, it was concluded that 0.5% (wt%) is the minimum PGPR concentration to obtain droplets with an average $d_{3,2}$ below 5 μm (required for microbiological stability). Furthermore, results obtained at different emulsification temperatures clearly indicate that fat crystals play a key role for both droplet break-up and stabilisation. Fat crystals contribute to stability by growing into a bulk network, which immobilises the droplets, and by behaving as Pickering particles. After emulsification, the interfacially adsorbed crystals grow together (i.e. sinter) to form a continuous crystalline fat shell encasing the water. Using cryo-SEM, the presence of a crystalline shell was shown for different emulsifier concentrations, and even in absence of added emulsifier, thus further confirming that fat crystals are effective to provide droplet stability. Finally, cryo-SEM visualisation of fractured droplets indicated that shell thickness is approximately 250 nm suggesting it is made up of several layer of TAGs lamellae.

7.1.2. Effect of microstructure on the large deformation behaviour of cocoa butter systems

In order to evaluate the possibility of replacing part of the CB with water and to understand the role of droplets on CB mechanical properties, the large deformation behaviour of CB systems was investigated using uniaxial compression test.

Results obtained by the analysis of bulk CB revealed that its mechanical behaviour is determined by the crystallisation conditions: when rapidly crystallised under shear and cooling in the SSHE, many small crystals are formed, which on post-processing sinter together and determine CB brittle behaviour. Under slow cooling, and in absence of any externally applied force, crystals can grow more and sintering is expected to occur over a

longer time scale. As a result, statically crystallised CB behaves like a plastic dispersion of crystals in liquid oil. These results suggest that difference between the two materials ultimately depends on the number solid of bonds: on increasing the number of solid bonds, both elasticity (E_{app}) and hardness (i.e. the stress to failure) increase.

With respect to emulsion behaviour, in agreement with the initial hypothesis, it was observed that a higher water content (and therefore more droplets-structural defects) weakens the structure, leading to reduced material strength (here both in term of stress and work to fracture) and strain to fracture, compared to a bulk CB phase. This result can be explained considering that water droplets are only partially sintered with the surrounding network and other weak interactions, such as van der Waals forces, contribute to network stabilisation. The presence of droplet-matrix solid bonds was suggested by the fact that the E_{app} and BM values remain constant up to 30% of aqueous phase. Furthermore, microstructure visualisation using cryo-SEM suggested that droplets are not completely bonded to the network. At deformations greater than the (small) linear region, a phenomenon of stress concentration occurs in the vicinity of the droplets and, since droplets are less connected to the surrounding matrix than the bulk crystals ('partially sintered' as mentioned above), fracture can occur more easily. Breaking of the solid bonds between interfacial and network crystals determines droplet-matrix debonding (i.e. fracture initiation). As only weak van der Waals forces are left to support the structure, these can be easily overcome by the applied stress and fracture propagation occurs. Furthermore, the distribution of droplets through the matrix would provide a "favourable pathway" for fracture propagation. This hypothesised mechanism would explain the lower energy of fracture required for emulsions compared to bulk CB.

With respect to results obtained for emulsions with different droplet sizes, the E_{app} and BM remained constant whereas fracture parameters (stress, strain, and work to fracture) decreased at increasing droplet size, suggesting that larger defects weaken the structure more.

All of the systems showed a strain hardening behaviour: the mechanical energy to be supplied for fracture to occur increases with increasing compressive rate. The highest work to failure was measured for bulk CB at all rates. Nevertheless, the same elastic energy was stored in all systems, suggesting that differences in the work to fracture arise from differences in the number of structural defects and mechanisms of energy dissipation.

7.1.3. Crystallisation in water-in-cocoa butter emulsions

In Chapter 6 the effect of droplets on the crystallisation behaviour of CB systems was investigated. It was hypothesised that the presence of droplets would act as heterogeneous nuclei, increasing the rate of crystallisation. In order to evaluate the effect of the droplets, the systems were initially melted (50 °C) to destroy the existing crystals and then crystallised at four temperatures ($T_{Cr} = 5, 10, 15, 20$ °C). For experiments at 5 and 20 °C, CB enriched with 1% PGPR was also studied. NMR droplet size measurements confirmed that emulsions remained stable on re-melting (i.e. droplet size did not change). The crystallisation process was followed by pNMR and data fitted to the Avrami model, while the polymorphism was investigated *via* DSC and curve deconvolution.

Results show that at high level of supercooling (i.e. at crystallisation temperature of 5 and 10 °C) no difference in the crystallisation behaviour occurred between CB and emulsions. However, at $T_{Cr} \geq 15$ °C emulsions crystallised faster than bulk CB suggesting that

emulsions droplets increase the rate of crystallisation. Results were explained considering that at low temperatures it is the high degree of supercooling that determines crystallisation, with impurities (i.e. the droplets) having negligible effect. The values of the Avrami exponent (n) increased with increasing T_{Cr} from 1 to 4 for all systems (suggesting crystal growth evolved from a “one” to a “multidimensional” process). Nevertheless, no difference in the n value was observed among systems suggesting that the mechanism of nucleation did not change due to the presence of water droplets.

With respect to the polymorphic behaviour, it was observed that emulsions evolved faster than CB toward more stable polymorphic forms at all temperatures. This result was explained hypothesising a mechanism of “facilitated TAGs structural re-arrangement” in the vicinity of the interface: the presence at the water interface of partially organised liquid PGPR moieties and of α arranged CB TAGs (and, by speculation, also of liquid crystals) enhances molecular mobility and structural re-arrangement, increasing the rate of polymorphic evolution (similarly to what occurs in a melt-mediated polymorphic transformation). Furthermore, the evidence that a CB system enriched with 1% PGPR did not exhibit any difference in terms of polymorphic evolution compared to bulk CB, suggests that a certain degree of ordering (here provided by the interface) may be necessary to increase polymorphic transformation.

7.2. Future recommendations

In this thesis the SSHE has showed to be an effective tempering-emulsifying device for the production of stable emulsions containing up to 40% aqueous phase. However, to significantly decrease the fat content in chocolate, it may be necessary to further increase the fraction of dispersed phase. As shown in Chapter 4, it was not possible to produce emulsions containing 60% aqueous phase, either using the SSHE alone or the entire margarine line. A phase inversion approach may be undertaken in the future to produce emulsions containing high aqueous phase percentage. Future work may also consider using lower amount of PGPR (as regulation limits its use) in combination with other 'label friendly' emulsifiers (e.g. lecithin or monoglycerides). Furthermore, the use of emulsifiers that are able to crystallise at the interface (such as mono- and di-glycerides) may represent an opportunity to increase the droplet-matrix interactions. Since these emulsifiers crystallise, they may promote the development of more droplet-matrix solid bonds, thus reducing the weakening effect discussed in Chapter 5 following the addition of water droplets. By increasing the number of solid bonds, it is hypothesised here that the mechanical properties of emulsions at fracture may become similar to that of the bulk phase.

To confirm and further advance results shown here with respect to polymorphism, future work may investigate the polymorphic evolution of emulsions using DSC combined with X-ray analysis. Furthermore, synchrotron macro-beam may be used to investigate *in situ* emulsified-TAGs interactions in the vicinity of the interface.

Appendices

Appendix 1: Matlab Script

The Matlab script used for conversion of force-deformation data in engineering stress-strain data was the following:

```
clear; clc; close all;

filename='CBratesM.xlsx';

[x info] = xlsfinfo(filename);

raw=cell(1,numel(info));

n_camp=zeros(1,numel(info));

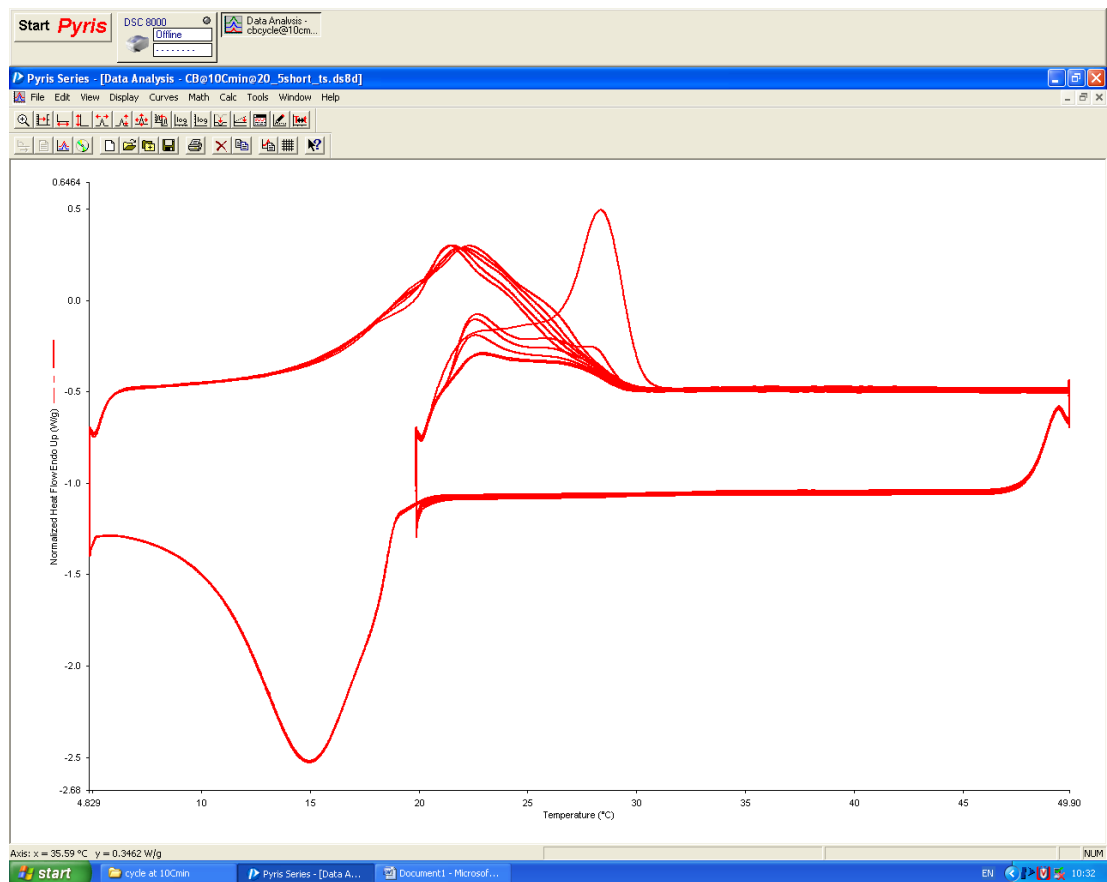
for i = 1:numel(info)
    raw{i}=xlsread(filename,i);
    [n m]=size(raw{i});
    n_camp(i)=m/5;
end
k=0;
S=1;
for i=1:n_camp(S)
    c1=raw{S}(:,k+i:k+i+1); % k+1: measured force; k+i+1: distance on
compression
    r=0.008; % radius in metres
    A=pi*r^2; % area in m^2
    Hi=0.025; % intial height in m
    Fmax=max(c1(:,1));
    Mindex = find(c1(:,1) == Fmax);
    c1(Mindex:end,:)=[];
    c1(:,2)=c1(:,2)/1000;
    h_t=Hi-c1(:,2.);
    eng_strain=(Hi-h_t)/Hi;
    eng_stress=c1(:,1)/A; % in N/m^2
    stress_to_failure(i)=max(eng_stress);
    index = find(eng_stress == eng_to_failure(i));
    strain_to_failure(i)= eng_strain(index);
    fig=figure;
    plot(eng_strain, eng_stress, '.')
    title(cat(2,'sample num ',num2str(i))) % puts a title on fig
    [x, y] = getpts(fig);
    figure(2)
    h=plot(eng_strain,eng_stress, '.',x,y,'r');
    set(h(2), 'linewidth',3)
    pause
    %plot(eng_strain(1000:3000),eng_stress(1000:3000))
    %slope=polyfit(eng_strain(1000:3000), eng_stress(1000:3000),1);
    %slope=slope(1); % slope of linear region
```

```
slope(i)=diff(y)-diff(x) % Young's modulus in N/m^2 = Pa
% work_to_failure(i)=trapz(eng_strain,eng_stress) % in N/m^2
work_to_failure(i)=trapz(eng_strain,eng_stress) % in J/m^2
k=k+4;
close all
clc
end
save(cat(2,filename(1:end-
5),'_',num2str(S),'.mat'),'slope','work_to_failure','strain_to_failure',
'stress_to_failure')
```

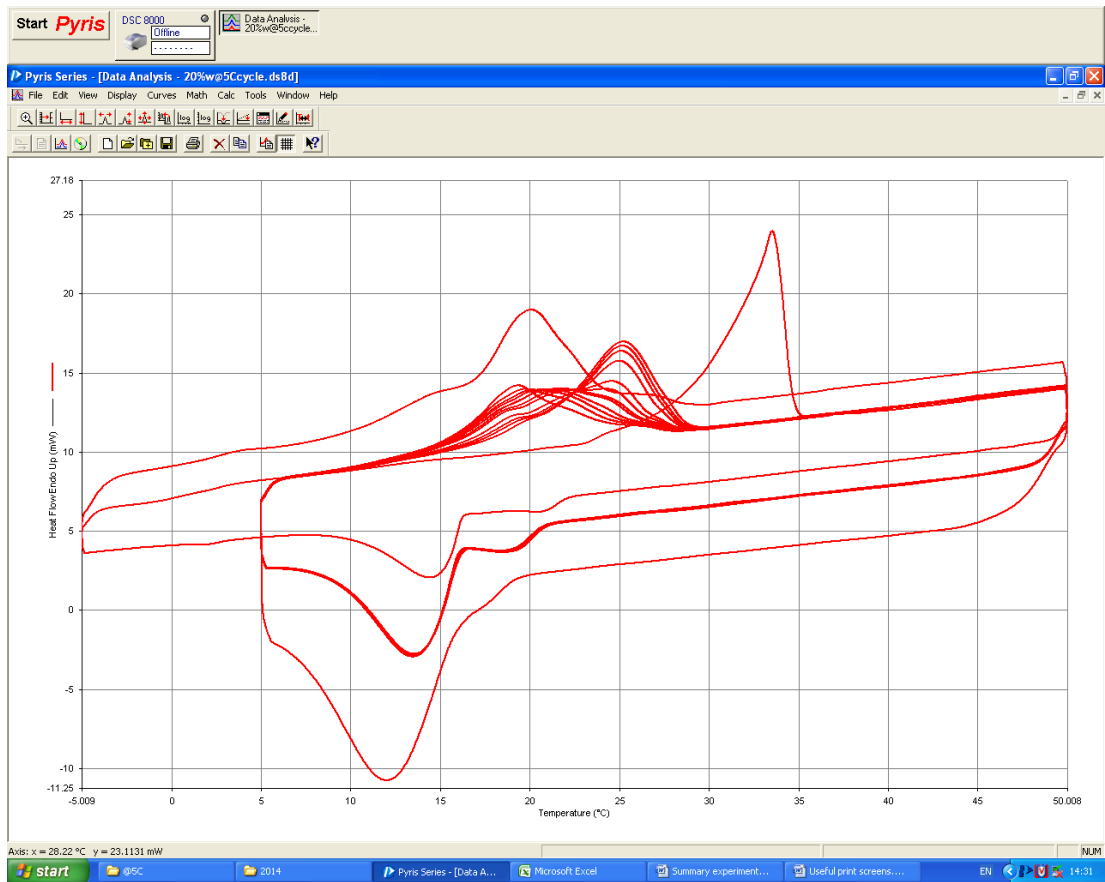
Appendix 2

Examples of curves obtained using the stop-and-return method showing the complete overlapping of traces. Images are print-screens of experiments, prior to any data manipulation. These results suggest that system remain stable.

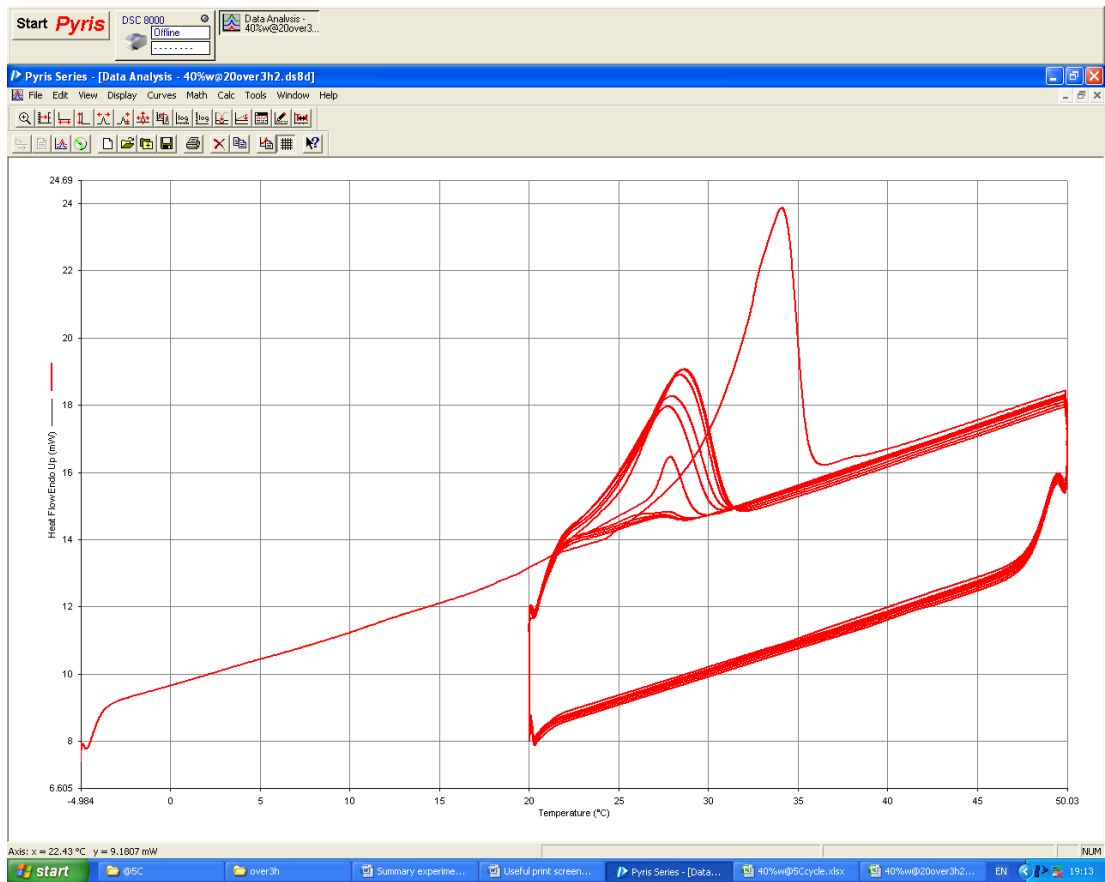
Bulk cocoa butter crystallised at 5 and 20 °C up to 45 minutes



Emulsion containing 20% aqueous phase crystallised at 5 °C for up to 180 minutes



Emulsion containing 40% aqueous phase crystallised at 20 °C for up to 180 minutes



References

- ACEVEDO, N. C., PEYRONEL, F. & MARANGONI, A. G. 2011. Nanoscale structure intercrystalline interactions in fat crystal networks. *Current Opinion in Colloid & Interface Science*, 16, 374-383.
- AFOAKWA, E. O., PATERSON, A., FOWLER, M. & RYAN, A. 2009. Matrix effects on flavour volatiles release in dark chocolates varying in particle size distribution and fat content using GC–mass spectrometry and GC–olfactometry. *Food Chemistry*, 113, 208-215.
- ARIMA, S., UEJI, T., UENO, S., OGAWA, A. & SATO, K. 2007. Retardation of crystallization-induced destabilization of PMF-in-water emulsion with emulsifier additives. *Colloids and Surfaces B: Biointerfaces*, 55, 98-106.
- ARIMA, S., UENO, S., OGAWA, A. & SATO, K. 2009. Scanning Microbeam Small-Angle X-ray Diffraction Study of Interfacial Heterogeneous Crystallization of Fat Crystals in Oil-in-Water Emulsion Droplets. *Langmuir*, 25, 9777-9784.
- AVRAMI, M. 1939. Kinetics of Phase Change. I General Theory. *The Journal of Chemical Physics*, 7, 1103-1112.
- AVRAMI, M. 1940. Kinetics of Phase Change. II Transformation-Time Relations for Random Distribution of Nuclei. *The Journal of Chemical Physics*, 8, 212-224.
- BALTSAVIAS, A., JURGENS, A. & VLIET, T. V. 1997. FACTORS AFFECTING FRACTURE PROPERTIES OF SHORT-DOUGH BISCUITS. *Journal of Texture Studies*, 28, 205-219.
- BERGENSTÅHL, B. 2008. Physicochemical Aspects of an Emulsifier Functionality. In: HASENHUETTL, G. & HARTEL, R. (eds.) *Food Emulsifiers and Their Applications*. Springer New York.
- BINKS, B. P. 2002. Particles as surfactants—similarities and differences. *Current Opinion in Colloid & Interface Science*, 7, 21-41.
- BINKS, B. P. & CLINT, J. H. 2002. Solid Wettability from Surface Energy Components: Relevance to Pickering Emulsions. *Langmuir*, 18, 1270-1273.
- BOODE, K. & WALSTRA, P. 1993. Partial coalescence in oil-in-water emulsions 1. Nature of the aggregation. *Colloids and Surfaces A: Physicochemical and Engineering Aspects*, 81, 121-137.
- BOODE, K., WALSTRA, P. & DE GROOT-MOSTERT, A. E. A. 1993. Partial coalescence in oil-in-water emulsions 2. Influence of the properties of the fat. *Colloids and Surfaces A: Physicochemical and Engineering Aspects*, 81, 139-151.
- BROOKS, B. W. & RICHMOND, H. N. 1994. Phase inversion in non-ionic surfactant—oil—water systems—II. Drop size studies in catastrophic inversion with turbulent mixing. *Chemical Engineering Science*, 49, 1065-1075.
- BRUNELLO, N., MCGAULEY, S. E. & MARANGONI, A. 2003. Mechanical properties of cocoa butter in relation to its crystallization behavior and microstructure. *LWT - Food Science and Technology*, 36, 525-532.
- CALZADA, J. F. & PELEG, M. 1978. MECHANICAL INTERPRETATION OF COMPRESSIVE STRESS-STRAIN RELATIONSHIPS OF SOLID FOODS. *Journal of Food Science*, 43, 1087-1092.
- CAMPOS, R., OLLIVON, M. & MARANGONI, A. G. 2010. Molecular Composition Dynamics and Structure of Cocoa Butter. *Crystal Growth & Design*, 10, 205-217.
- CHAPMAN, D. 1962. The Polymorphism of Glycerides. *Chemical Reviews*, 62, 433-456.

- CHRONAKIS, L. S. & KASAPIS, S. 1995. A rheological study on the application of carbohydrate-protein incompatibility to the development of low fat commercial spreads. *Carbohydrate Polymers*, 28, 367-373.
- CISNEROS ESTEVEZ, A., TORO-VAZQUEZ, J. F. & HARTEL, R. W. 2013. Effects of Processing and Composition on the Crystallization and Mechanical Properties of Water-in-Oil Emulsions. *Journal of the American Oil Chemists' Society*, 90, 1195-1201.
- COOK, K. L. K. & HARTEL, R. W. 2010. Mechanisms of Ice Crystallization in Ice Cream Production. *Comprehensive Reviews in Food Science and Food Safety*, 9, 213-222.
- DARLING, D. F. 1982. Recent advances in the destabilization of dairy emulsions. *Journal of Dairy Research*, 49, 695-712.
- DAVIS, T. & DIMICK, P. 1989. Isolation and thermal characterization of high-melting seed crystals formed during cocoa butter solidification. *Journal of the American Oil Chemists Society*, 66, 1488-1493.
- DEMAN, J. M. & BEERS, A. M. 1987. FAT CRYSTAL NETWORKS: STRUCTURE AND RHEOLOGICAL PROPERTIES. *Journal of Texture Studies*, 18, 303-318.
- DEWETTINCK, K., FOUBERT, I., BASIURA, M. & GODERIS, B. 2004. Phase Behavior of Cocoa Butter in a Two-Step Isothermal Crystallization. *Crystal Growth & Design*, 4, 1295-1302.
- DHONSI, D. & STAPLEY, A. G. F. 2006. The effect of shear rate, temperature, sugar and emulsifier on the tempering of cocoa butter. *Journal of Food Engineering*, 77, 936-942.
- DI BARI, V., NORTON, J. E. & NORTON, I. T. 2014. Effect of processing on the microstructural properties of water-in-cocoa butter emulsions. *Journal of Food Engineering*, 122, 8-14.
- DICKINSON, E. 2012. Use of nanoparticles and microparticles in the formation and stabilization of food emulsions. *Trends in Food Science & Technology*, 24, 4-12.
- DOUAIRE, M., DI BARI, V., NORTON, J. E., SULLO, A., LILLFORD, P. & NORTON, I. T. 2014. Fat crystallisation at oil-water interfaces. *Advances in Colloid and Interface Science*, 203, 1-10.
- DUMONT, E., FAYOLLE, F. & LEGRAND, J. 2000. Flow regimes and wall shear rates determination within a scraped surface heat exchanger. *Journal of Food Engineering*, 45, 195-207.
- EL-HAMOUZ, A., COOKE, M., KOWALSKI, A. & SHARRATT, P. 2009. Dispersion of silicone oil in water surfactant solution: Effect of impeller speed, oil viscosity and addition point on drop size distribution. *Chemical Engineering and Processing: Process Intensification*, 48, 633-642.
- FESSAS, D., SIGNORELLI, M. & SCHIRALDI, A. 2005. Polymorphous transitions in cocoa butter. *Journal of Thermal Analysis and Calorimetry*, 82, 691-702.
- FOUBERT, I., DEWETTINCK, K., JANSSEN, G. & VANROLLEGHEM, P. A. 2006. Modelling two-step isothermal fat crystallization. *Journal of Food Engineering*, 75, 551-559.
- FOUBERT, I., DEWETTINCK, K. & VANROLLEGHEM, P. A. 2003a. Modelling of the crystallization kinetics of fats. *Trends in Food Science & Technology*, 14, 79-92.
- FOUBERT, I., FREDRICK, E., VEREECKEN, J., SICHIEEN, M. & DEWETTINCK, K. 2008. Stop-and-return DSC method to study fat crystallization. *Thermochimica Acta*, 471, 7-13.

- FOUBERT, I., VANROLLEGHEM, P. A. & DEWETTINCK, K. 2003b. A differential scanning calorimetry method to determine the isothermal crystallization kinetics of cocoa butter. *Thermochimica Acta*, 400, 131-142.
- FOUBERT, I., VANROLLEGHEM, P. A. & DEWETTINCK, K. 2005. Insight in model parameters by studying temperature influence on isothermal cocoa butter crystallization. *European Journal of Lipid Science and Technology*, 107, 660-672.
- FOUBERT, I., VANROLLEGHEM, P. A., VANHOUTTE, B. & DEWETTINCK, K. 2002. Dynamic mathematical model of the crystallization kinetics of fats. *Food Research International*, 35, 945-956.
- FRASCH-MELNIK, S., NORTON, I. T. & SPYROPOULOS, F. 2010. Fat-crystal stabilised w/o emulsions for controlled salt release. *Journal of Food Engineering*, 98, 437-442.
- FREDRICK, E., VAN DE WALLE, D., WALSTRA, P., ZIJVELD, J. H., FISCHER, S., VAN DER MEEREN, P. & DEWETTINCK, K. 2011. Isothermal crystallization behaviour of milk fat in bulk and emulsified state. *International Dairy Journal*, 21, 685-695.
- FREDRICK, E., WALSTRA, P. & DEWETTINCK, K. 2010. Factors governing partial coalescence in oil-in-water emulsions. *Advances in Colloid and Interface Science*, 153, 30-42.
- FRIBERG, S., LARSSON, K. & SJOBLOM, J. 2003. *Food Emulsions*, CRC Press.
- GABBOTT, P. 2008. *Principles and applications of thermal analysis*, Blackwell Pub.
- GAONKAR, A. 1989. Interfacial tensions of vegetable oil/water systems: Effect of oil purification. *Journal of the American Oil Chemists' Society*, 66, 1090-1092.
- GAONKAR, A. G. 1992. Effects of salt, temperature, and surfactants on the interfacial tension behavior of a vegetable oil/water system. *Journal of Colloid and Interface Science*, 149, 256-260.
- GARTI, N., ASERIN, A., TIUNOVA, I. & BINYAMIN, H. 1999. Double emulsions of water-in-oil-in-water stabilized by α -form fat microcrystals. Part 1: Selection of emulsifiers and fat microcrystalline particles. *Journal of the American Oil Chemists' Society*, 76, 383-389.
- GARTI, N., BINYAMIN, H. & ASERIN, A. 1998. Stabilization of water-in-oil emulsions by submicrocrystalline α -form fat particles. *Journal of the American Oil Chemists' Society*, 75, 1825-1831.
- GHOSH, S. & ROUSSEAU, D. 2009. Freeze-thaw stability of water-in-oil emulsions. *Journal of Colloid and Interface Science*, 339, 91-102.
- GHOSH, S. & ROUSSEAU, D. 2011. Fat crystals and water-in-oil emulsion stability. *Current Opinion in Colloid & Interface Science*, 16, 421-431.
- GHOSH, S. & ROUSSEAU, D. 2012. Triacylglycerol Interfacial Crystallization and Shear Structuring in Water-in-Oil Emulsions. *Crystal Growth & Design*, 12, 4944-4954.
- GHOSH, S., TRAN, T. & ROUSSEAU, D. 2011. Comparison of Pickering and Network Stabilization in Water-in-Oil Emulsions. *Langmuir*, 27, 6589-6597.
- GÜLSEREN, İ. & CORREDIG, M. 2012. Interactions at the interface between hydrophobic and hydrophilic emulsifiers: Polyglycerol polyricinoleate (PGPR) and milk proteins, studied by drop shape tensiometry. *Food Hydrocolloids*, 29, 193-198.
- GUNES, D. Z., CLAIN, X., BRETON, O., MAYOR, G. & BURBIDGE, A. S. 2010. Avalanches of coalescence events and local extensional flows – Stabilisation or destabilisation due to surfactant. *Journal of Colloid and Interface Science*, 343, 79-86.
- HALL, S., COOKE, M., EL-HAMOUI, A. & KOWALSKI, A. 2011a. Droplet break-up by in-line Silverson rotor-stator mixer. *Chemical Engineering Science*.

- HALL, S., COOKE, M., PACEK, A. W., KOWALSKI, A. J. & ROTHMAN, D. 2011b. Scaling up of silverson rotor–stator mixers. *The Canadian Journal of Chemical Engineering*, 89, 1040-1050.
- HEERTJE, I. 1993. MICROSTRUCTURAL STUDIES IN FAT RESEARCH. *Food Structure*, 12, 77-94.
- HEERTJE, I. 2014. Structure and function of food products: A review. *Food Structure*, 1, 3-23.
- HEERTJE, I., VANEENDENBURG, J., CORNELISSEN, J. M. & JURIAANSE, A. C. 1988. THE EFFECT OF PROCESSING ON SOME MICROSTRUCTURAL CHARACTERISTICS OF FAT SPREADS. *Food Microstructure*, 7, 189-193.
- HEMMINGA, M. A. 1992. Introduction to NMR. *Trends in Food Science & Technology*, 3, 179-186.
- HERRERA, M. L. & HARTEL, R. W. 2000. Effect of processing conditions on crystallization kinetics of a milk fat model system. *Journal of the American Oil Chemists' Society*, 77, 1177-1188.
- HIMAWAN, C., STAROV, V. M. & STAPLEY, A. G. F. 2006. Thermodynamic and kinetic aspects of fat crystallization. *Advances in Colloid and Interface Science*, 122, 3-33.
- HODGE, S. M. & ROUSSEAU, D. 2005. Continuous-phase fat crystals strongly influence water-in-oil emulsion stability. *Journal of the American Oil Chemists' Society*, 82, 159-164.
- IVANOV, I. B., DANOV, K. D. & KRALCHEVSKY, P. A. 1999. Flocculation and coalescence of micron-size emulsion droplets. *Colloids and Surfaces A: Physicochemical and Engineering Aspects*, 152, 161-182.
- JOHANSSON, D. & BERGENSTÅHL, B. 1995a. Sintering of fat crystal networks in oil during post-crystallization processes. *Journal of the American Oil Chemists' Society*, 72, 911-920.
- JOHANSSON, D. & BERGENSTÅHL, B. 1995b. Wetting of fat crystals by triglyceride oil and water. 2. adhesion to the oil/water interface. *Journal of the American Oil Chemists' Society*, 72, 933-938.
- JOHANSSON, D., BERGENSTÅHL, B. & LUNDGREN, E. 1995. Wetting of fat crystals by triglyceride oil and water. 1. The effect of additives. *Journal of the American Oil Chemists' Society*, 72, 921-931.
- JOHNS, M. L. 2009. NMR studies of emulsions. *Current Opinion in Colloid & Interface Science*, 14, 178-183.
- KABALNOV, A., WEERS, J., ARLAUSKAS, R. & TARARA, T. 1995. Phospholipids as Emulsion Stabilizers. 1. Interfacial Tensions. *Langmuir*, 11, 2966-2974.
- KHANNA, Y. P., TAYLOR, T. J. & CHOMYN, G. 1988. A new differential scanning calorimetry based approach for the estimation of thermal conductivity of polymer solids and melts. *Polymer Engineering & Science*, 28, 1034-1041.
- KLOEK, W., VAN VLIET, T. O. N. & WALSTRA, P. 2005a. LARGE DEFORMATION BEHAVIOR OF FAT CRYSTAL NETWORKS. *Journal of Texture Studies*, 36, 516-543.
- KLOEK, W., VAN VLIET, T. O. N. & WALSTRA, P. 2005b. MECHANICAL PROPERTIES OF FAT DISPERSIONS PREPARED IN A MECHANICAL CRYSTALLIZER. *Journal of Texture Studies*, 36, 544-568.
- KLOEK, W., WALSTRA, P. & VAN VLIET, T. 2000a. Crystallization kinetics of fully hydrogenated palm oil in sunflower oil mixtures. *Journal of the American Oil Chemists' Society*, 77, 389-398.

- KLOEK, W., WALSTRA, P. & VAN VLIET, T. 2000b. Nucleation kinetics of emulsified triglyceride mixtures. *Journal of the American Oil Chemists' Society*, 77, 643-652.
- KROG, N. & LARSSON, K. 1992. Crystallization at Interfaces in Food Emulsions – A General Phenomenon. *Lipid / Fett*, 94, 55-57.
- LARSSON, K. 1966. CLASSIFICATION OF GLYCERIDE CRYSTAL FORMS. *Acta Chemica Scandinavica*, 20, 2255-&.
- LAUKE, B. & FU, S.-Y. 2013. Aspects of fracture toughness modelling of particle filled polymer composites. *Composites Part B: Engineering*, 45, 1569-1574.
- LAVIGNE, F., BOURGAUX, C. & OLLIVON, M. 1993. Phase transitions of saturated triglycerides. *J. Phys. IV France*, 03, C8-137-C8-140.
- LE RÉVÉREND, B. J. D., TAYLOR, M. S. & NORTON, I. T. 2011. Design and application of water-in-oil emulsions for use in lipstick formulations. *International Journal of Cosmetic Science*, 33, 263-268.
- LEE, L. L., NIKNAFS, N., HANCOCKS, R. D. & NORTON, I. T. 2013. Emulsification: Mechanistic understanding. *Trends in Food Science & Technology*, 31, 72-78.
- LEMENAND, T., DUPONT, P., VALLE, D. D. & PEERHOSSAINI, H. 2013. Comparative efficiency of shear, elongation and turbulent droplet breakup mechanisms: Review and application. *Chemical Engineering Research and Design*, 91, 2587-2600.
- LENS, P. N. L. & HEMMINGA, M. A. 1998. Nuclear magnetic resonance in environmental engineering: Principles and applications. *Biodegradation*, 9, 393-409.
- LEVINE, S., BOWEN, B. D. & PARTRIDGE, S. J. 1989. Stabilization of emulsions by fine particles I. Partitioning of particles between continuous phase and oil/water interface. *Colloids and Surfaces*, 38, 325-343.
- LOISEL, C., KELLER, G., LECQ, G., BOURGAUX, C. & OLLIVON, M. 1998a. Phase transitions and polymorphism of cocoa butter. *Journal of the American Oil Chemists' Society*, 75, 425-439.
- LOISEL, C., KELLER, G., LECQ, G., LAUNAY, B. & OLLIVON, M. 1997. Tempering of chocolate in a scraped surface heat exchanger. *Journal of Food Science*, 62, 773-780.
- LOISEL, C., LECQ, G., KELLER, G. & OLLIVON, M. 1998b. Dynamic crystallization of dark chocolate as affected by temperature and lipid additives. *Journal of Food Science*, 63, 73-79.
- LUCASSEN-REYNDERS, E. H. & TEMPEL, M. V. D. 1963. STABILIZATION OF WATER-IN-OIL EMULSIONS BY SOLID PARTICLES¹. *The Journal of Physical Chemistry*, 67, 731-734.
- LUYTEN, H. & VAN VLIET, T. 1995. FRACTURE PROPERTIES OF STARCH GELS AND THEIR RATE DEPENDENCY. *Journal of Texture Studies*, 26, 281-298.
- LUYTEN, H., VAN VLIET, T. & WALSTRA, P. 1992. COMPARISON OF VARIOUS METHODS TO EVALUATE FRACTURE PHENOMENA IN FOOD MATERIALS. *Journal of Texture Studies*, 23, 245-266.
- MACMILLAN, S. D., ROBERTS, K. J., ROSSI, A., WELLS, M. A., POLGREEN, M. C. & SMITH, I. H. 2002. In Situ Small Angle X-ray Scattering (SAXS) Studies of Polymorphism with the Associated Crystallization of Cocoa Butter Fat Using Shearing Conditions. *Crystal Growth & Design*, 2, 221-226.
- MALEKY, F. & MARANGONI, A. G. 2008. Process development for continuous crystallization of fat under laminar shear. *Journal of Food Engineering*, 89, 399-407.

- MARANGONI, G., A., MCGAULEY & E., S. 2003. Relationship between crystallization behavior and structure in Cocoa butter. 3, 14.
- MARANGONI, A. 1998. On the use and misuse of the avrami equation in characterization of the kinetics of fat crystallization. *Journal of the American Oil Chemists' Society*, 75, 1465-1467.
- MARANGONI, A. G. 2000. Elasticity of high-volume-fraction fractal aggregate networks: A thermodynamic approach. *Physical Review B*, 62, 13951-13955.
- MARANGONI, A. G. 2002. Special issue of FRI—Crystallization, structure and functionality of fats. *Food Research International*, 35, 907-908.
- MARANGONI, A. G., ACEVEDO, N., MALEKY, F., CO, E., PEYRONEL, F., MAZZANTI, G., QUINN, B. & PINK, D. 2012. Structure and functionality of edible fats. *Soft Matter*, 8, 1275-1300.
- MÁRQUEZ, A. L., MEDRANO, A., PANIZZOLO, L. A. & WAGNER, J. R. 2010. Effect of calcium salts and surfactant concentration on the stability of water-in-oil (w/o) emulsions prepared with polyglycerol polyricinoleate. *Journal of Colloid and Interface Science*, 341, 101-108.
- MAZZANTI, G., GUTHRIE, S. E., SIROTA, E. B., MARANGONI, A. G. & IDZIAK, S. H. J. 2003. Orientation and Phase Transitions of Fat Crystals under Shear. *Crystal Growth & Design*, 3, 721-725.
- MCCLEMENTS, D. J. 2005. *Food emulsions: principles, practices, and techniques*, CRC.
- MCCLEMENTS, D. J. 2007. Critical Review of Techniques and Methodologies for Characterization of Emulsion Stability. *Critical Reviews in Food Science and Nutrition*, 47, 611-649.
- MCCLEMENTS, D. J. 2010. Emulsion Design to Improve the Delivery of Functional Lipophilic Components. *Annual Review of Food Science and Technology*, 1, 241-269.
- MCCLEMENTS, D. J. 2012a. Crystals and crystallization in oil-in-water emulsions: Implications for emulsion-based delivery systems. *Advances in Colloid and Interface Science*, 174, 1-30.
- MCCLEMENTS, D. J. 2012b. Nanoemulsions versus microemulsions: terminology, differences, and similarities. *Soft Matter*, 8, 1719-1729.
- MCCLEMENTS, D. J. & RAO, J. 2011. Food-Grade Nanoemulsions: Formulation, Fabrication, Properties, Performance, Biological Fate, and Potential Toxicity. *Critical Reviews in Food Science and Nutrition*, 51, 285-330.
- METIN, S. & HARTEL, R. 1998. Thermal analysis of isothermal crystallization kinetics in blends of cocoa butter with milk fat or milk fat fractions. *Journal of the American Oil Chemists' Society*, 75, 1617-1624.
- NADIN, M., ROUSSEAU, D. & GHOSH, S. 2014. Fat crystal-stabilized water-in-oil emulsions as controlled release systems. *LWT - Food Science and Technology*, 56, 248-255.
- NARINE, S. S. & MARANGONI, A. G. 1999a. Fractal nature of fat crystal networks. *Physical Review E*, 59, 1908-1920.
- NARINE, S. S. & MARANGONI, A. G. 1999b. Mechanical and structural model of fractal networks of fat crystals at low deformations. *Physical Review E*, 60, 6991-7000.
- NIELSEN, S. S. 2010. *Food Analysis*, Springer.

- NIKNAFS, N., SPYROPOULOS, F. & NORTON, I. T. 2011. Development of a new reflectance technique to investigate the mechanism of emulsification. *Journal of Food Engineering*, 104, 603-611.
- NORTON, A. B., COX, P. W. & SPYROPOULOS, F. 2011. Acid gelation of low acyl gellan gum relevant to self-structuring in the human stomach. *Food Hydrocolloids*, 25, 1105-1111.
- NORTON, I., FRYER, P. & MOORE, S. 2006. Product/Process integration in food manufacture: Engineering sustained health. *AIChE Journal*, 52, 1632-1640.
- NORTON, I. T., SPYROPOULOS, F. & COX, P. W. 2009a. Effect of emulsifiers and fat crystals on shear induced droplet break-up, coalescence and phase inversion. *Food Hydrocolloids*, 23, 1521-1526.
- NORTON, J. & FRYER, P. 2012. Investigation of changes in formulation and processing parameters on the physical properties of cocoa butter emulsions. *Journal of Food Engineering*.
- NORTON, J. E., FRYER, P. J., PARKINSON, J. & COX, P. W. 2009b. Development and characterisation of tempered cocoa butter emulsions containing up to 60% water. *Journal of Food Engineering*, 95, 172-178.
- O'SULLIVAN, J., ARELLANO, M., PICHOT, R. & NORTON, I. 2014. The effect of ultrasound treatment on the structural, physical and emulsifying properties of dairy proteins. *Food Hydrocolloids*, 42, Part 3, 386-396.
- OLIVER, L., SCHOLTEN, E. & VAN AKEN, G. A. 2015. Effect of fat hardness on large deformation rheology of emulsion-filled gels. *Food Hydrocolloids*, 43, 299-310.
- PACKER, K. & REES, C. 1972. Pulsed NMR studies of restricted diffusion. I. Droplet size distributions in emulsions. *Journal of Colloid and Interface Science*, 40, 206-218.
- PAWLIK, A., COX, P. W. & NORTON, I. T. 2010. Food grade duplex emulsions designed and stabilised with different osmotic pressures. *Journal of Colloid and Interface Science*, 352, 59-67.
- PELEG, M. 2006. On fundamental issues in texture evaluation and texturization—A view. *Food Hydrocolloids*, 20, 405-414.
- PÉREZ-MARTÍNEZ, D., ALVAREZ-SALAS, C., CHARÓ-ALONSO, M., DIBILDOX-ALVARADO, E. & TORO-VAZQUEZ, J. F. 2007. The cooling rate effect on the microstructure and rheological properties of blends of cocoa butter with vegetable oils. *Food Research International*, 40, 47-62.
- PÉREZ-MARTÍNEZ, D., ALVAREZ-SALAS, C., MORALES-RUEDA, J. A., TORO-VAZQUEZ, J. F., CHARÓ-ALONSO, M. & DIBILDOX-ALVARADO, E. 2005. The effect of supercooling on crystallization of cocoa butter-vegetable oil blends. *Journal of the American Oil Chemists' Society*, 82, 471-479.
- PICHOT, R. 2012. Stability and characterisation of emulsions in the presence of colloidal particles and surfactants. Ph.D., University of Birmingham.
- PICHOT, R., SPYROPOULOS, F. & NORTON, I. T. 2009. Mixed-emulsifier stabilised emulsions: Investigation of the effect of monoolein and hydrophilic silica particle mixtures on the stability against coalescence. *Journal of Colloid and Interface Science*, 329, 284-291.

- PICHOT, R., SPYROPOULOS, F. & NORTON, I. T. 2010. O/W emulsions stabilised by both low molecular weight surfactants and colloidal particles: The effect of surfactant type and concentration. *Journal of Colloid and Interface Science*, 352, 128-135.
- PICHOT, R., SPYROPOULOS, F. & NORTON, I. T. 2012. Competitive adsorption of surfactants and hydrophilic silica particles at the oil–water interface: Interfacial tension and contact angle studies. *Journal of Colloid and Interface Science*, 377, 396-405.
- PICKERING, S. U. 1907. Emulsions. *Journal of the Chemical Society*, 91, 2001-2021.
- POVEY, M. J. W. 2014. Crystal nucleation in food colloids. *Food Hydrocolloids*, 42, Part 1, 118-129.
- RAMSDEN, W. 1903. Separation of Solids in the Surface-Layers of Solutions and 'Suspensions' (Observations on Surface-Membranes, Bubbles, Emulsions, and Mechanical Coagulation). -- Preliminary Account. *Proceedings of the Royal Society of London*, 72, 156-164.
- RAO, C. S. & HARTEL, R. W. 2006. Scraped Surface Heat Exchangers. *Critical Reviews in Food Science and Nutrition*, 46, 207-219.
- ROBINS, M. M. 2000. *Lipid emulsions* 2000.
- ROHM, H. 1993. RHEOLOGICAL BEHAVIOUR OF BUTTER AT LARGE DEFORMATIONS. *Journal of Texture Studies*, 24, 139-155.
- ROUSSEAU, D. 2000. Fat crystals and emulsion stability — a review. *Food Research International*, 33, 3-14.
- ROUSSEAU, D. 2013. Trends in structuring edible emulsions with Pickering fat crystals. *Current Opinion in Colloid & Interface Science*, 18, 283-291.
- ROUSSEAU, D., GHOSH, S. & PARK, H. 2009. Comparison of the Dispersed Phase Coalescence Mechanisms in Different Tablespreads. *Journal of Food Science*, 74, E1-E7.
- ROUSSEAU, D., ZILNIK, L., KHAN, R. & HODGE, S. 2003. Dispersed phase destabilization in table spreads. *Journal of the American Oil Chemists' Society*, 80, 957-961.
- SAKAMOTO, M., OHBA, A., KURIYAMA, J., MARUO, K., UENO, S. & SATO, K. 2004. Influences of fatty acid moiety and esterification of polyglycerol fatty acid esters on the crystallization of palm mid fraction in oil-in-water emulsion. *Colloids and Surfaces B: Biointerfaces*, 37, 27-33.
- SATO, K. 2001. Crystallization behaviour of fats and lipids — a review. *Chemical Engineering Science*, 56, 2255-2265.
- SATO, K., BAYÉS-GARCÍA, L., CALVET, T., CUEVAS-DIARTE, M. À. & UENO, S. 2013. External factors affecting polymorphic crystallization of lipids. *European Journal of Lipid Science and Technology*, 115, 1224-1238.
- SATO, K. & UENO, S. 2011. Crystallization, transformation and microstructures of polymorphic fats in colloidal dispersion states. *Current Opinion in Colloid & Interface Science*, 16, 384-390.
- SATO, K., UENO, S. & YANO, J. 1999. Molecular interactions and kinetic properties of fats. *Progress in Lipid Research*, 38, 91-116.
- SCHANTZ, B. & ROHM, H. 2005. Influence of lecithin–PGPR blends on the rheological properties of chocolate. *LWT - Food Science and Technology*, 38, 41-45.
- SCHUBERT, H. & ENGEL, R. 2004. Product and formulation engineering of emulsions. *Chemical Engineering Research and Design*, 82, 1137-1143.

- SONWAI, S. & MACKLEY, M. R. 2006. The effect of shear on the crystallization of cocoa butter. *Journal of the American Oil Chemists' Society*, 83, 583-596.
- STANG, M., SCHUCHMANN, H. & SCHUBERT, H. 2001. Emulsification in High-Pressure Homogenizers. *Engineering in Life Sciences*, 1, 151-157.
- STAUFFER, C. E. 2005. Emulsifiers for the Food Industry. *Bailey's Industrial Oil and Fat Products*. John Wiley & Sons, Inc.
- STEJSKAL, E. O. & TANNER, J. E. 1965. Spin Diffusion Measurements: Spin Echoes in the Presence of a Time-Dependent Field Gradient. *The Journal of Chemical Physics*, 42, 288-292.
- SULLO, A., ARELLANO, M. & NORTON, I. T. 2014. Formulation engineering of water in cocoa – Butter emulsion. *Journal of Food Engineering*, 142, 100-110.
- SVANBERG, L., AHRNÉ, L., LORÉN, N. & WINDHAB, E. 2011. Effect of sugar, cocoa particles and lecithin on cocoa butter crystallisation in seeded and non-seeded chocolate model systems. *Journal of Food Engineering*, 104, 70-80.
- TADROS, T., IZQUIERDO, P., ESQUENA, J. & SOLANS, C. 2004. Formation and stability of nano-emulsions. *Advances in Colloid and Interface Science*, 108–109, 303-318.
- TALBOT, G. 2009. Chocolate Temper. *Industrial Chocolate Manufacture and Use*. Wiley-Blackwell.
- TANG, D. & MARANGONI, A. 2006a. Microstructure and fractal analysis of fat crystal networks. *Journal of the American Oil Chemists' Society*, 83, 377-388.
- TANG, D. & MARANGONI, A. G. 2006b. Quantitative study on the microstructure of colloidal fat crystal networks and fractal dimensions. *Advances in Colloid and Interface Science*, 128–130, 257-265.
- TANG, D. & MARANGONI, A. G. 2007. Modeling the rheological properties and structure of colloidal fat crystal networks. *Trends in Food Science & Technology*, 18, 474-483.
- TIMMS, R. E. 1984. Phase behaviour of fats and their mixtures. *Progress in Lipid Research*, 23, 1-38.
- TORO-VAZQUEZ, J., PÉREZ-MARTÍNEZ, D., DIBILDOX-ALVARADO, E., CHARÓ-ALONSO, M. & REYES-HERNÁNDEZ, J. 2004. Rheometry and polymorphism of cocoa butter during crystallization under static and stirring conditions. *Journal of the American Oil Chemists' Society*, 81, 195-202.
- UENO, S., HAMADA, Y. & SATO, K. 2003. Controlling Polymorphic Crystallization of n-Alkane Crystals in Emulsion Droplets through Interfacial Heterogeneous Nucleation. *Crystal Growth & Design*, 3, 935-939.
- VAN AKEN, G. A. & VISSER, K. A. 2000. Firmness and Crystallization of Milk Fat in Relation to Processing Conditions. *Journal of Dairy Science*, 83, 1919-1932.
- VAN BOEKEL, M. A. J. S. & WALSTRA, P. 1981. Stability of oil-in-water emulsions with crystals in the disperse phase. *Colloids and Surfaces*, 3, 109-118.
- VAN DUYNHOVEN, J. P. M., GOUDAPPEL, G. J. W., VAN DALEN, G., VAN BRUGGEN, P. C., BLONK, J. C. G. & EIJKELENBOOM, A. P. A. M. 2002. Scope of droplet size measurements in food emulsions by pulsed field gradient NMR at low field. *Magnetic Resonance in Chemistry*, 40, S51-S59.
- VAN DUYNHOVEN, J. P. M., MAILLET, B., SCHELL, J., TRONQUET, M., GOUDAPPEL, G.-J. W., TREZZA, E., BULBARELLO, A. & VAN DUSSCHOTEN, D. 2007. A rapid benchtop NMR

- method for determination of droplet size distributions in food emulsions. *European Journal of Lipid Science and Technology*, 109, 1095-1103.
- VAN LANGEVELDE, A., VAN MALSSSEN, K., PESCHAR, R. & SCHENK, H. 2001. Effect of temperature on recrystallization behavior of cocoa butter. *Journal of the American Oil Chemists' Society*, 78, 919-925.
- VAN MALSSSEN, K., PESCHAR, R. & SCHENK, H. 1996. Real-time X-ray powder diffraction investigations on cocoa butter. I. temperature-dependent crystallization behavior. *Journal of the American Oil Chemists' Society*, 73, 1209-1215.
- VAN MALSSSEN, K., VAN LANGEVELDE, A., PESCHAR, R. & SCHENK, H. 1999. Phase behavior and extended phase scheme of static cocoa butter investigated with real-time X-ray powder diffraction. *Journal of the American Oil Chemists' Society*, 76, 669-676.
- VAN PUTTE, K. & VAN DEN ENDEN, J. 1974. Fully automated determination of solid fat content by pulsed NMR. *Journal of the American Oil Chemists Society*, 51, 316-320.
- VAN VLIET, T. 1996. Large deformation and fracture behaviour of gels. *Current Opinion in Colloid & Interface Science*, 1, 740-745.
- VAN VLIET, T. 2002. On the relation between texture perception and fundamental mechanical parameters for liquids and time dependent solids. *Food Quality and Preference*, 13, 227-236.
- VAN VLIET, T. & WALSTRA, P. 1995. Large deformation and fracture behaviour of gels. *Faraday Discussions*, 101, 359-370.
- VANHOUTTE, B., DEWETTINCK, K., FOUBERT, I., VANLERBERGHE, B. & HUYGHEBAERT, A. 2002. The effect of phospholipids and water on the isothermal crystallisation of milk fat. *European Journal of Lipid Science and Technology*, 104, 490-495.
- WALSTRA, P. 1993. Principles of emulsion formation. *Chemical Engineering Science*, 48, 333-349.
- WALSTRA, P. 2002. *Physical Chemistry of Foods*, CRC Press.
- WASSELL, P., OKAMURA, A., YOUNG, N. W. G., BONWICK, G., SMITH, C., SATO, K. & UENO, S. 2012. Synchrotron Radiation Macrobeam and Microbeam X-ray Diffraction Studies of Interfacial Crystallization of Fats in Water-in-Oil Emulsions. *Langmuir*, 28, 5539-5547.
- WILLE, R. & LUTTON, E. 1966. Polymorphism of cocoa butter. *Journal of the American Oil Chemists' Society*, 43, 491-496.
- WILSON, R. & SMITH, M. 1998. Human Studies on Polyglycerol Polyricinoleate (PGPR). *Food and Chemical Toxicology*, 36, 743-745.
- WINDHAB, E. J., DRESSLER, M., FEIGL, K., FISCHER, P. & MEGIAS-ALGUACIL, D. 2005. Emulsion processing—from single-drop deformation to design of complex processes and products. *Chemical Engineering Science*, 60, 2101-2113.
- WOOSTER, T. J., GOLDING, M. & SANGUANSRI, P. 2008. Impact of Oil Type on Nanoemulsion Formation and Ostwald Ripening Stability. *Langmuir*, 24, 12758-12765.
- WRIGHT, A., HARTEL, R., NARINE, S. & MARANGONI, A. 2000. The effect of minor components on milk fat crystallization. *Journal of the American Oil Chemists' Society*, 77, 463-475.
- YANG, D., HRYMAK, A. & KEDZIOR, S. 2013. Kinetics of Isothermal Crystallization of Hydrogenated Castor Oil-in-Water Emulsions. *Journal of the American Oil Chemists' Society*, 90, 1743-1750.

ZHANG, J., DAUBERT, C. R. & FOEGEDING, E. A. 2005. Fracture Analysis of Alginate Gels. *Journal of Food Science*, 70, e425-e431.